ANALYSIS AND DESIGN OF ULTRASOUND PHASED ARRAYS FOR HYPERTHERMIA CANCER THERAPY

BY

MOHAMMED SALAMEH IBBINI

Dipl., Universite de Caen, 1978
M.S., University of Colorado, 1980

THESIS

Submitted in partial fulfillment of the requirements
for the degree of Doctor of Philosophy in Electrical Engineering
in the Graduate College of the
University of Illinois at Urbana-Champaign, 1988

Urbana, Illinois

ANALYSIS AND DESIGN OF ULTRASOUND PHASED ARRAYS FOR HYPERTHERMIA CANCER THERAPY

Mohammed Salameh Ibbini, Ph. D.
Department of Electrical and Computer Engineering
University of Illinois at Urbana-Champaign 1988
Charles Cain, Advisor

Acoustic phased arrays, which can be focused and steered electronically, offer an attractive alternative to the mechanically scanned focused ultrasound systems currently in use in hyperthermia cancer therapy. However, both electrical and mechanical scannings require a very intense focal spot which could increase the risk of unwanted nonthermal effects such as cavitation. In addition, hot spots proximal to the tumor may occur because of the near-field beam overlapping due to scanning. This thesis introduces a new method which will allow the direct synthesis, without scanning, of the more diffuse heating patterns useful in hyperthermia. Two quite different phased arrays are theoretically evaluated as hyperthermia applicators: a concentric ring array (CRA), and an NxN square-element array.

The new synthesis method is based on the conjugate phase and amplitude matching techniques often used in optics.The field conjugation method (FCM), theoretically capable of tailoring the ultrasonic power deposition to virtually any tumor geometry without scanning, offers also the possibility of simultaneously focusing at different locations. The multiple focusing feature is combined with a new phasing technique involving angular phase rotation to eliminate hot spots that are often associated with the synthesis of annular patterns.

A concentric-ring array was chosen because of its ability to directly produce annular patterns with a minimum number of array elements. However, computer simulations demonstrated that the use of directly synthesized annular intensity profiles for heating could be severely limited due to the formation of undesired hot spots along the array axis. A new method, based on combining the multiple focusing feature and a simple mechanical movement of the applicator, is proposed as a means of heating different size tumors at various depths.

While a concentric-ring array is limited to the synthesis of annular and spot foci, an NxN square-element array is investigated as a means of synthesizing heating patterns with or without circular symmetry. Simulated heating patterns produced by the FCM are compared to those produced by electronic scanning. Although the two techniques result in equivalent power deposition patterns, the SPTP focal intensity associated with the FCM is substantially lower than that used for scanning. A method is also proposed to combine the FCM with electronic scanning to produce more complicated diffuse heating patterns. The advantage of this method is to minimize the number of scan points and, hence, to use a lower SPTP intensity. Moreover, an 8X8 square-element phased array prototype built and radiation patterns produced by single and multiple elements were measured, and agreed well with theoretically predicted patterns..

To evaluate the different applicators, the steady-state bioheat transfer equation was solved using a finite difference technique. The simulated temperature distributions associated with different power deposition patterns demonstrate the potential of the field conjugation technique for the design of diffuse heating patterns for hyperthermia cancer therapy.

DEDICATION

Dedicated to the soul of my father, Salameh Ali Ibbini, whose love, support, and encouragement for me were, unlike his life, unlimited.

ACKNOWLEDGEMENTS

The author is indebted to his advisor, Professor Charles A. Cain, for his time, suggestions, and especially his moral support provided during this project. Thanks to Professor Leon A. Frizzell and Dr. Shin-Ichiro Umemura for their very helpful discussions. Thanks are also extended to Professors W. O'Brien and S. Lee for serving on my committee. Thanks are due to my brother, Emad, for his exemplary moral support he provided, particularly during the last 18 months of this work. Wanda Elliot, Billy McNeill, Joe Cobb, and Robert Cicone deserve many thanks for their help and assistance. My appreciation goes to the NCSA staff and students for their help and assistance which made the computer simulations on their supercomputer (CRAYX-MP48) very enjoyable. Special thanks to all the Bioacoustics Research Laboratory staff and students who made the laboratory an excellent work environment. The continuous support and love provided by my family will always be remembered. The biggest thanks of all goes to my wife, Etaf, and my children, Emad and Esam, for putting up with me during the different stages of this thesis. In particular, Etaf's effort to put up with me and with Esam, while he was patient in the hospital, during six months of this work, is to be remembered.

This work was funded in part by Grant CA44124 from the National Institute of Health, an award from Hitachi Central Research Laboratory, Hitachi, LTD, Tokyo, Japan, and Grant ECS870001 from the National Center for Supercomputer Applications (NCSA) at the University of Illinois.

TABLE OF CONTENTS

CHAPTER 1

INTRODUCTION

The use of hyperthermia, or elevated temperature, in the treatment of malignant tissues was initiated by the Roman and Greek physicians more than twenty centuries ago [1,2]. However, attitude toward hyperthermia went through different stages of optimism and pessimism within the last few decades [3]. The resurgent interest in hyperthermia cancer therapy today is probably due to an increased number of investigators confirming the higher sensitivity of malignant and tumorous tissue to induced heat compared to that of normal tissue [4-7]. While it is now well established that tumor cells are more sensitive to heat than normal tissue cells, the difference between these sensitivities is not very well known but believed to be rather small [8]. This last statement emphasizes the importance of a precise control of the induced heat if hyperthermia is to be recognized as an efficient and safe cancer treatment. An ideal hyperthermia treatment would consist of raising the tumor temperature to therapeutic levels while keeping the surrounding tissue temperature level below thresholds that can cause damage to normal tissue.

Different modalities can be used to induce heat in tissue noninvasively. Among those modalities are EM waves, radio frequency current, and ultrasound energy. However, ultrasound may be the modality of choice for the treatment of deep seated tumors. In fact, the small size of its wavelength and its relatively low attenuation in tissue, at the frequencies of interest (0.3-3.0 MHz), make ultrasound superior to any other noninvasive modality for the production of localized heat at depth [9]. Another advantage of ultrasound is that it does not require special arrangements such as shielding and the use of particular measures to ensure the safety of the operating technicians as opposed to other modalities. A serious problem with ultrasound is its impedance mismatch at tissue-gas and tissue-bone interfaces. The ultrasonic energy is almost totally reflected (99%) at a tissue-air interface, while about 50%

reflection occurs at the interface between tissue and bone. Moreover, the ultrasonic absorption coefficient in bone is many times greater than that in tissue, and hence, bone or air cavities make some body regions inaccessible to noninvasive ultrasound.

Unfocused ultrasound can be used to heat superficial tumors but cannot produce therapeutic gain at depth [10]. Focused transducers can be used to concentrate the ultrasonic energy into a small region deep in the body. However, the small size of the resulting focal spot makes it difficult to heat typical size tumors without some manipulation. This problem can be resolved by mechanically translocating the applicator so that the focal spot is swept over a desired path, a technique known as mechanical scanning. Several mechanical scanning systems are currently in clinical use [11-13]. Mechanical scanning, while demonstrating the possibility of localized focused treatment at depth, suffers generally from a lack of speed, allowing only a crude control of power deposition and a complex and cumbersome patient-machine interface due to the mechanical movement of a transducer which must be continuously coupled to the tissue.

Phased arrays, which can be focused and steered electronically, offer an attractive alternative to the mechanical scanning of focused systems. This could be attributed in part to the speed and flexibility of electronic control systems which, while complex, can be implemented remotely from the applicator aperture. Electronic scanning offers the advantage of eliminating the need of any mechanical movement of the transducer, allowing a more precise electronic control, and permitting the scanning of very irregular heating patterns as compared to the simple ones achieved by mechanical scanning. A number of phased array configurations have been investigated [14-16].

Both electronic and mechanical scanning require the use of high spatial-peak temporal-peak focal intensity ultrasound. This requirement is crucial to compensate for the short dwell time (time spent at each scan point) to eliminate thermal ripples. Recently, phased array applicators of particular configurations were proposed which were capable of directly synthesizing diffuse intensity profiles without electrical or mechanical scanning [17].

This thesis will introduce a new general method which is expected to allow the direct synthesis of optimal laterally diffuse intensity profiles. As a demonstration, two quite different array configurations are examined, a concentric-ring and a square-element NxN phased array.

In Chapter 2, a method based on phase and amplitude matching concepts will be proposed as a means of directly synthesizing many heating patterns useful in hyperthermia. Besides its capability of producing conventional foci (intense focal spots), the field conjugation method can potentially be used to directly tailor the heating pattern to the geometry of the tissue to be heated. The method can also be used to produce multiple foci at different locations which can be useful in different hyperthermia applications (i.e., heating of large tumors). The direct synthesis of diffuse heating patterns is achieved by splitting the array focal intensity over a larger volume and, hence, a focal intensity lower than those associated with scanning can be used. The method can also be used in clinical situations where tissue inhomogeneity might decrease the focusing capability of conventional focusing systems which primarily use geometrical concepts in establishing the relative excitation phase for each array element.

The capability of a concentric-ring array of producing power deposition patterns useful for hyperthermia applications is analyzed in Chapter 3. The applicator geometry was chosen for its capability of producing 3-D focusing volumes with a minimum number of elements compared to the large number of elements generally required by 2-D phased arrays. While computer simulations demonstrate the possibility of producing conventional (spot foci) and annular foci uniquely by adjusting the electronic control circuitry, a new technique combining mechanical and electrical scanning is proposed as a means of producing optimal heating patterns that probably cannot be produced by either type of scanning separately.

A square-element NxN phased array is then chosen to produce intensity profiles that cannot be produced by a concentric-ring applicator. In particular, patterns with or without circular symmetry are synthesized and analyzed. The direct synthesis technique is then compared to electronic scanning of an intense focal spot and shown to be a potential alternative to scanning. A combination of electronic scanning and direct synthesis techniques is also proposed and some resulting heating patterns are simulated.

Investigated in Chapter 5 is the thermal response associated with some power deposition patterns of Chapter 3. To obtain the temperature distributions, a geometrical thermal model of the tumor and surrounding tissue is adopted and the method of finite difference with over-relaxation is used to solve the 2-D radially symmetrical bioheat equation.

A 3-D thermal model is proposed in Chapter 6 and the finite difference with over-relaxation technique is used to solve the 3-D bioheat transfer equation in rectangular coordinates. An evaluation of the direct technique as a means of synthesizing different heating patterns using an NxN square-element applicator is offered. Temperature distributions resulting from direct synthesis, electronic scanning, and their combinations are simulated and discussed.

The fabrication process of an 8x8 square-element phased array prototype is described in Chapter 7. In particular, practical problems such as PZT handling, impedance matching, and electronic control are discussed. The frequency response of the PZT-8 ceramic electrical impedance is measured and the resonance frequency is determined. Experimental data of a preliminary study of the array radiation patterns are presented and compared to theoretically predicted simulations.

This thesis is concluded in Chapter 8 with some suggestions for future research in hyperthermia cancer therapy applicators design.

CHAPTER 2

DIRECT SYNTHESIS OF DIFFUSE INTENSITY PROFILE PATTERNS USING A FIELD CONJUGATION TECHNIQUE

2.1 Introduction

Heating the periphery of a poorly perfused tumor is more efficient than uniform heating throughout the treated volume if the goal is to obtain a uniform temperature distribution within the tumor tissue [10]. By delivering enough energy at the edges of the tumor to compensate for the heat losses to surrounding normal tissues by conduction or convection, the temperature of the whole tumor volume might be raised evenly to a therapeutic level ($\geq 42°$ C).

Several techniques are currently used to deposit the ultrasonic energy at the tumor periphery. These techniques range from simply aiming several unfocused transducers at points around the tumor periphery to scanning an intense focal spot along the tumor border using sophisticated electronics. Fessenden et al. proposed a system consisting of six unfocused transducers mounted in a spherical shell section and driven at slightly different frequencies [18]. This arrangement is capable of producing a waist of focal points around the tumor. Moreover, a specially designed lens, to deposit the ultrasonic energy around the tumor periphery, was simultaneously proposed by Lele [19] and Beard et al. [20]. Lele also proposed a similar design to heat the tumor periphery and its center as well. This later design can be used to heat well perfused or larger tumors (diameter > 20 mm) for which heating the periphery might prove inadequate.

Figure 2.1a) is a schematic of the geometry of the multitransducer system developed at Stanford (Fessenden) while Figures 2.1b) and c) illustrate a cross section of the specially designed lenses proposed by Lele. The main disadvantage of the multitransducer system and the specially designed lenses is their inflexibility for treatment of different tumor geometries

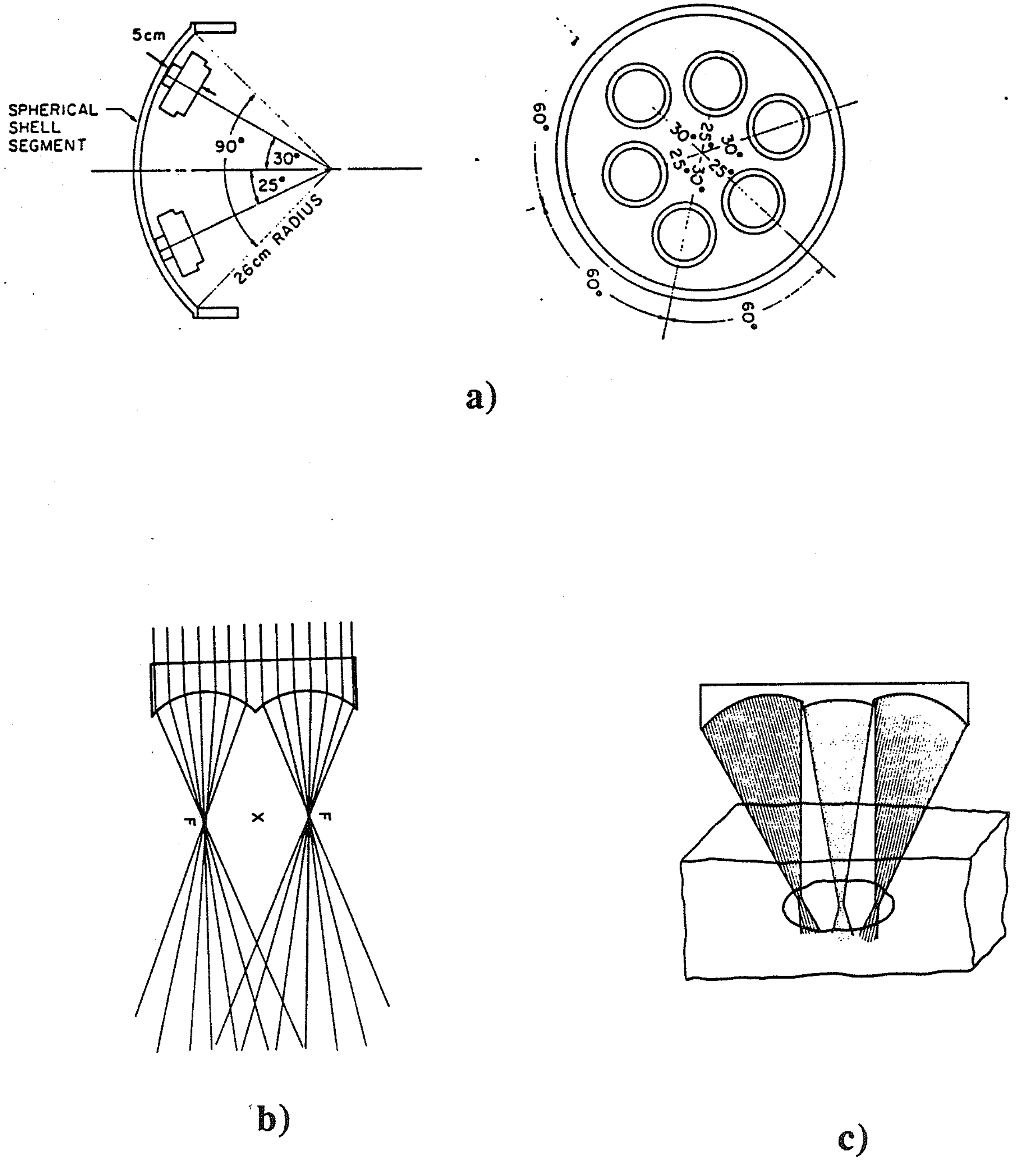

Figure 2.1. a) The geometrical configuration of the Stanford system [18], b) specially designed lens capable of producing annular foci [20], and c) specially designed lens proposed by Lele [19].

or tumor depths. In fact, these transducers are often designed to accommodate tumors with certain geometries at specific depths and their adjustment to different tumor specifications might involve tilting (or even displacing) the transducers and/or increasing (decreasing) the bolus (coupling medium) thickness. These adjustments could increase the complexity of the patient-machine interface and, consequently, a new design is needed to allow the treatment of tumors of different sizes or at different depths.

Dynamic scanning of an intense focal spot offers an alternative to specially designed transducers. An intense focal spot is first produced and then swept along a prescribed path, often around the tumor periphery, by mechanical or electrical means.

Mechanical scanning consists of using a focused transducer to produce an intense focal spot, and the transducer is then translocated by some mechanical arrangement [21]. On the other hand, electrical scanning consists of producing an intense focal spot by adjusting the electrical phase of the signal applied to each element of a phased array (multielement-transducer), The resulting focus is then swept over a prescribed trajectory by simply adjusting the electronic control [16,22].

Both types of scanning require a very short dwell time (time spent at each scanning point) to obtain proper heating of the treated volume while keeping the temperature fluctuation to a minimum level. The requirement of a short dwell time implies the use of a very high intensity ultrasound in order to deliver the proper thermal dose. The use of high intensity ultrasound might increase the risk of undesired nonthermal effects such as cavitation [23]. In addition, mechanical scanning suffers from lack of speed resulting in a relatively crude control of heating patterns and from the need for a cumbersome coupling medium which complicates the patient-machine interface during the treatment.

In the following section, a method is proposed which allows the direct generation of an optimal heating pattern without scanning. Moreover, the method will allow simultaneous focusing at more than one site, a feature that may be used to heat simultaneously different parts of the treatment volume. Establishing the phase and amplitude of the driving signals required to synthesize the desired heating pattern (annular, elliptical, multiple foci, etc.) is accomplished using simple geometrical considerations. The essence of the method is a direct application of the reciprocity theorem combined with phase and amplitude matching techniques often used in optics [24,25]. Similar methods have been used in the design of microwave applicators [26,27,28]. The method lends itself admirably to many types of transducers including planar and nonplanar arrays [16,29]. First, a mathematical presentation of the method is given. Second, different versions of the method will be presented and advantages and limitations of the technique will be pointed out.

In summary, the method will provide a means of directly synthesizing different heating patterns without scanning, heating simultaneously different parts of a large tumor, and reducing the ultrasound intensity to levels lower than those used in scanning while achieving the required time-averaged intensity gain [30].

2.2 The Field Conjugation Method (FCM)

The essence of the proposed method is an application of the reciprocity theorem combined with the conjugate phase and amplitude matching technique. In general, one assumes a source at the desired focal location and calculates the field produced by the assumed source at the center of each element of the array. Finally, the values of the complex amplitude of the field are conjugated and used as excitation for the different array elements.

To generate multiple foci with different amplitudes, the procedure is repeated for every focus independently, complex amplitudes of the fields are then calculated, multiplied by the appropriate scaling factor, conjugated, and then summed to lead to the final expression necessary for the excitation of each element. The amplitude of each focus is controlled by adjusting the scaling factor associated with that focus.

2.2.1 Formulation of the problem

The synthesis problem considered here is to produce M foci of different amplitudes using a phased array of N elements. As an illustration, Figure 2.2 shows the elements S_1, S_2, ..., S_N arranged along the same line in the source plane. However, the method is not restricted to any geometrical configuration and can be applied to nonplanar arrays as well.

2.2.2 The field conjugation method (FCM)

The method is first presented in general form. A mathematical presentation based on matrix notation is then adopted. The matrix notation, while not essential for the development of the method, will help in adapting the synthesis procedure to the use of digital computers. Furthermore, this same presentation can be used in the formulation of an optimization problem where a desired criterion index (power deposition, intensity gain, etc.) is to be optimized while the excitation signal is constrained to remain within some specified limits. A matrix presentation will prove useful for applying optimization techniques. The FCM can be described as follows:

<u>Step 1</u>: Consider a source at a point P in the focal plane (desired focus) and let it radiate back toward the surface of the array. The source excitation is assumed to be a time-harmonic signal of the form A exp(jωt), where t, ω, and A are the time, the frequency in rad/sec, and a real scaling factor, respectively. However, in a later section, the source excitation signal will be modified by introducing a phasing term to eliminate some undesired hot spots.

<u>Step 2:</u> Compute the field F_{11} at the center of element S_1 in the source plane due to the assumed source at point P. Calculate the fields F_{12}, F_{13},..., F_{1N} at the center of S_2, S_3,...S_N, respectively. An Nx1 vector V_1 is then formed:

$$V_1 = (F_{11} \quad F_{12} \quad \dots \quad \dots \quad F_{1N})^T$$

where T is the transpose.

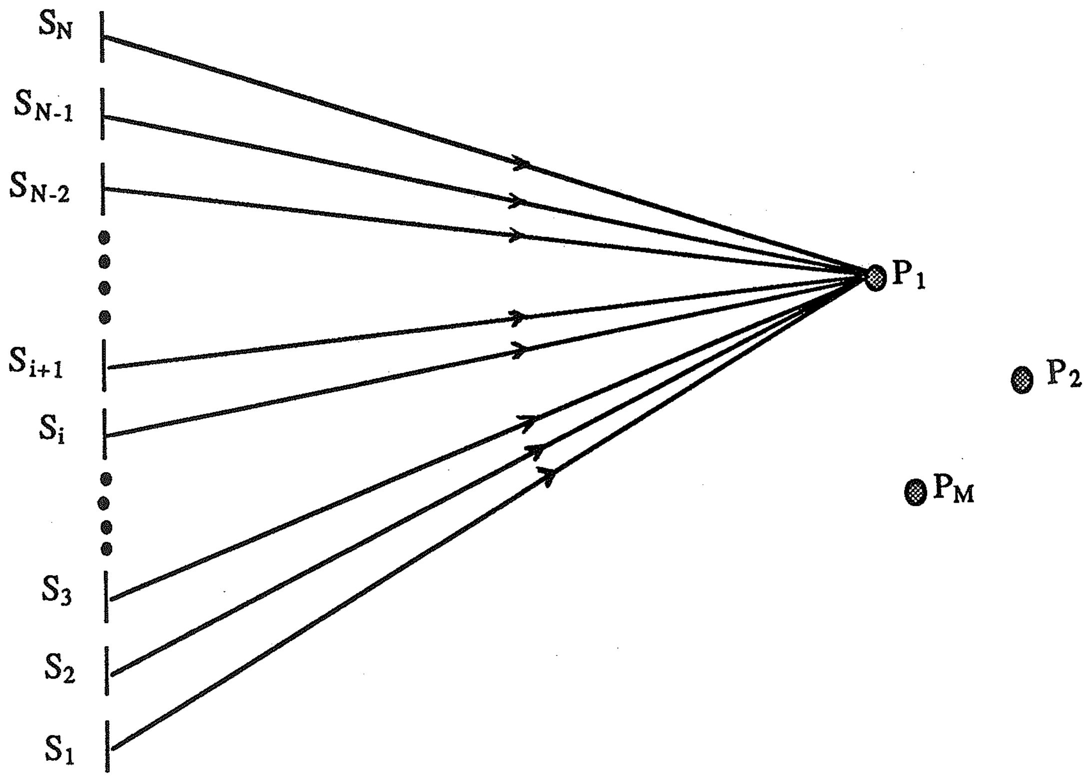

Figure 2.2. A schematic of the field conjugation technique. The assumed sources are designated by $P_1, P_2, \ldots, P_M$ and the array elements are arranged in linear fashion for simplicity.

Step 3: The same procedure (step 2) is then repeated for the different desired foci P_2, P_3,..., P_M and form the vectors V_2, V_3,..., V_M as follows:

$$V_2 = (F_{21} \quad F_{22} \quad \cdots \quad \cdots \quad F_{2N})^T$$

$$V_3 = (F_{31} \quad F_{32} \quad \cdots \quad \cdots \quad F_{3N})^T$$

$$\vdots$$

$$V_M = (F_{M1} \quad F_{M2} \quad \cdots \quad \cdots \quad F_{MN})^T$$

The notation F_{ik} means a complex field at the location S_i due to a source with a harmonic excitation A_k placed at location P_k.

Step 4: The NxM matrix F is then formed.

$$F = \begin{bmatrix} F_{11} & F_{21} & \cdots & \cdots & F_{M1} \\ F_{12} & F_{22} & \cdots & \cdots & F_{M2} \\ \cdots & \cdots & \cdots & \cdots & \cdots \\ \cdots & \cdots & \cdots & \cdots & \cdots \\ F_{1N} & F_{2N} & \cdots & \cdots & F_{MN} \end{bmatrix}$$

Step 5: The conjugate matrix F^* is then formed by substituting each component in the matrix F by its conjugate.

$$F^* = \begin{bmatrix} F_{11}^* & F_{21}^* & \dots & \dots & F_{M1}^* \\ F_{12}^* & F_{22}^* & \dots & \dots & F_{M2}^* \\ \dots & \dots & \dots & \dots & \dots \\ \dots & \dots & \dots & \dots & \dots \\ F_{1N}^* & F_{2N}^* & \dots & \dots & F_{MN}^* \end{bmatrix}$$

Step 6: The signal needed to excite each element of the array is then computed by summing the components of the corresponding row of the matrix F*.

$$I = \begin{bmatrix} I_1 \\ I_2 \\ \cdot \\ \cdot \\ I_N \end{bmatrix} = \begin{bmatrix} \sum_1^M F^*_{i1} \\ \sum_1^M F^*_{i2} \\ \cdot \\ \cdot \\ \sum_1^M F^*_{iN} \end{bmatrix}$$

[I] is the excitation vector where $I_1, I_2, \dots, I_N$ are the complex signals needed to excite the elements $S_1, S_2, \dots, S_N$, respectively.

2.2.3 Direct synthesis of intensity profile patterns

The FCM, like other phasing techniques, can be used to produce an intense focal spot that can be swept along a prescribed trajectory leading to some desired field intensity patterns. However, the ultimate goal of the method is to directly synthesize heating patterns overlaying tumor geometry by direct deposit of ultrasonic energy where it is needed, without scanning. An attractive feature of the FCM is its ability to reconstruct a desired intensity profile by examining the field produced by a "fictitious" source of shape and size similar to those of the desired profile at the center of each array element.

In its very elementary form, the method consists of assuming a source of shape and size similar to those of the intensity profile to be synthesized at the desired location and applying the procedure described in Section 2.2. As an illustration, Figure 2.3a) shows the simultaneous synthesis of an annular ring and an elliptical pattern at a certain distance from the applicator (arbitrary two-dimensional array). A similar pattern can be produced by substituting the spatially continuous assumed source by N discrete point sources appropriately distributed over the contour of the desired pattern. The number of the assumed point sources and their relative spacings are governed by the dimension of the focal spot produced by the array and the size of the desired pattern. Figure 2.3b) illustrates the procedure for the synthesis of a focal ring.

The direct synthesis of heating patterns, like scanning the periphery of a tumor, requires the predetermination of the size, shape, and the location of the tissue volume to be heated. In a clinical situation, this can be accomplished prior to the treatment using an imaging system which could in some cases be a part of the therapeutic system.

2.2.4 The rotating field conjugation method (RFCM)

The synthesis method, presented in the previous section, is characterized by its ease of application which allows the production of a complex field pattern by assuming a source of an appropriate shape. However, the method can lead, in some cases, to particularly strong secondary foci along the axis of symmetry. The formation of these foci is the result of the constructive interference of the acoustic waves along the axis due to the reconstructive nature of the field conjugation method. The method assumes N point sources distributed appropriately over the periphery of the desired ring (see Figure 2.3b)). The N fictitious sources are assumed to vibrate in phase as described in Section 2.2. Moreover, the acoustic path between an arbitrary point on the main axis and any assumed source is the same due to the circular symmetry. This means that the acoustic waves will interfere constructively over the main axis to reconstruct the desired annular pattern.

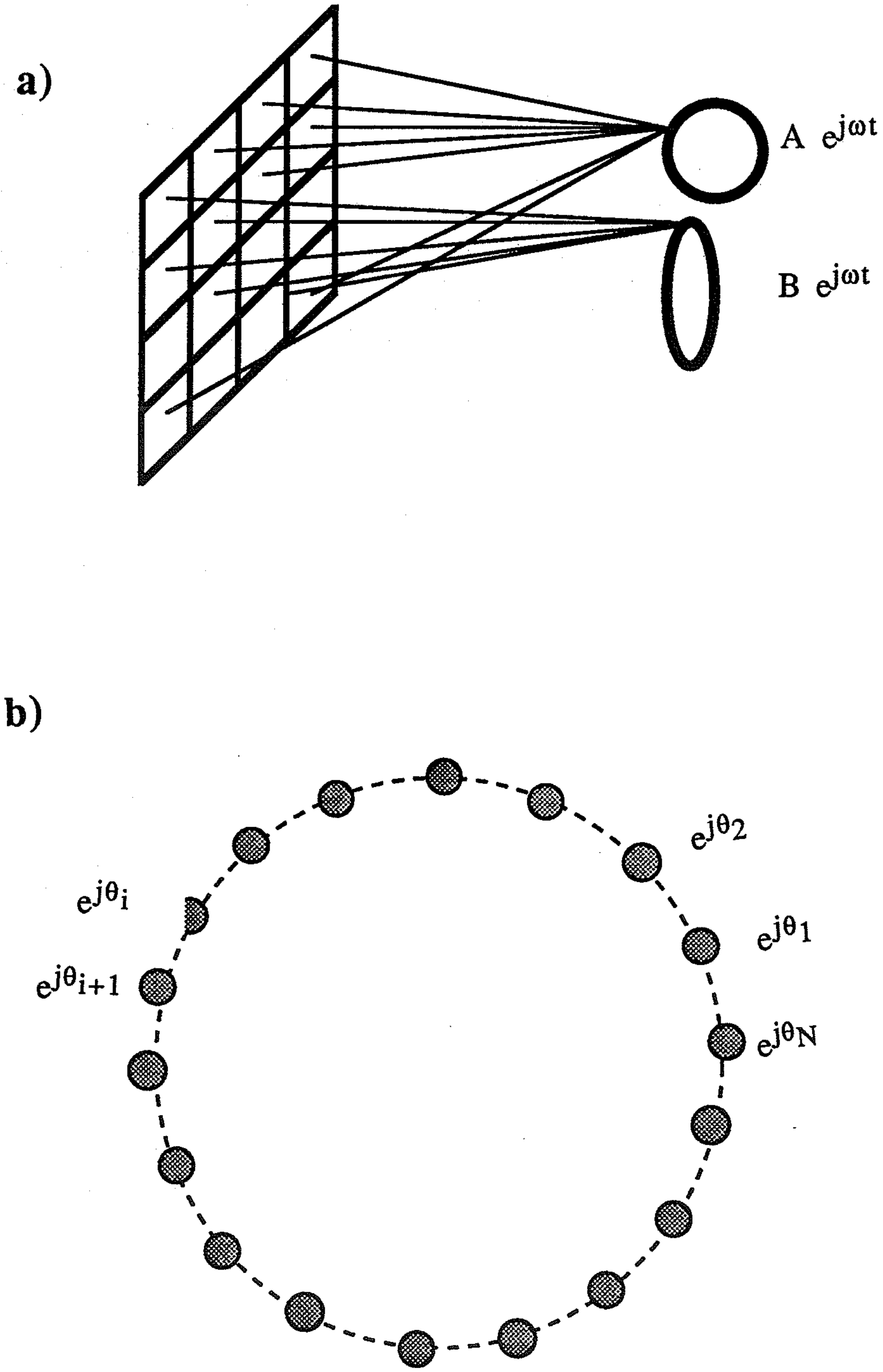

Figure 2.3. Application of the FCM to synthesize different intensity profiles. a) Synthesis of annular and elliptical intensity profiles using spatially continuous shapes and b) synthesis of an annular pattern using N point sources.

This problem can be resolved by introducing an appropriate phasing function to the excitation of each assumed source as will be shown in the following paragraphs. It is demonstrated that the problem of the formation of secondary foci on the axis is completely eliminated in some cases (i.e., annular and disk-shaped patterns). However, the problem is only alleviated in some other cases such as the synthesis of elliptical patterns.

The number of the necessary point sources (or small disk-shaped ones) and their distribution depend on the geometry of the the desired pattern and that of the focal spot produced by the array. It is often appropriate to choose the spacing in such a way that a minimal interference occurs between the individual half power focal spots resulting in the focal plane. This implies that the spacing between assumed sources should be at least of the order of the focal-spot size. An estimate of the number of the required point sources is obtained by dividing the length of the periphery (i.e., $2\pi R$ for an annular ring of radius R) by a length slightly larger than the transverse size of the 3 dB region of the focal spot characteristic of the array. The necessary phasing terms are then calculated by computing the expression of the field resulting on the main axis and forcing its value to zero by choosing the appropriate phase necessary for every vibrating source.

The procedure is illustrated for two cases of interest, annular rings and elliptically shaped patterns. The distributions of the assumed point sources over the periphery of an annular ring of radius R is illustrated in Figure 2.3b). These assumed sources are then excited by signals of the form $\exp j(\omega t+\theta_1)$, $\exp j(\omega t+\theta_2)$,..., $\exp j(\omega t+\theta_N)$ where θ_1, θ_2,..., θ_N are the individual phases to be determined. The calculation of the resulting field, at an arbitrary point q along the main axis, is then performed as follows:

$$P= A \sum_{i=1}^{N} \exp(j\theta_i) \frac{\exp(-jkr_i)}{r_i} \qquad (2.1)$$

where r_i is the distance separating the point q and the source i, k is the propagation constant of the medium, and A is a proportionality constant. The time dependency of Eq. (2.1) was dropped for simplicity. The pressure field expression becomes

$$P= A \sum_{i=1}^{N} \exp(j\theta_i) \frac{\exp(-jk\sqrt{R^2+z^2})}{\sqrt{R^2+z^2}} \tag{2.2}$$

where R and z are the distances separating the center of the annular ring from the source i and the point q, respectively. It is clear from above that only θ_i depends on the position of the element and hence, the summation becomes

$$P= A \frac{\exp(-jk\sqrt{R^2+z^2})}{\sqrt{R^2+z^2}} \sum_{i=1}^{N} \exp(j\theta_i) \tag{2.3}$$

By choosing $\theta_i = i\theta_0$ in the above expression, the summation can be performed as follows:

$$P= A \frac{\exp(-jk\sqrt{R^2+z^2})}{\sqrt{R^2+z^2}} \frac{\exp(j\theta_0)-\exp(j(N+1)\theta_0)}{1-\exp(j\theta_0)} \tag{2.4}$$

The technique consists of forcing the field to be zero along the axis by choosing an appropriate θ_0. This condition can be achieved by choosing $N\ \theta_0 = 2m\pi$ and $\theta_0 \neq 2p\pi$ simultaneously (m and p are integers). Finally, the required phasing angle can be written as $\theta_i = i\,\frac{2\pi}{N}$ where i and N are the indexes of the assumed source S_i and the total number of sources, respectively.

The above calculation shows that by choosing $\theta_1 = \frac{2\pi}{N}$, $\theta_2 = \frac{4\pi}{N}$,...,$\theta_N = 2\pi$, the secondary foci on the main axis are eliminated. A similar calculation, in the case of elliptically shaped pattern synthesis, can be performed as follows:

$$P = A \sum_{i=1}^{N} \exp(j\theta_0) \frac{\exp(-jkr_i)}{r_i} \tag{2.5}$$

By assuming the ellipse parameters to be a,b and ϕ such that $\frac{x^2}{a^2}+\frac{y^2}{b^2}=1$ and ϕ is the angle between the vector (x,y) and the horizontal axis (see Figure 2.4), then r_i can be expressed as;

$$r_i=\sqrt{a^2\cos^2\phi_i+b^2\sin^2\phi_i+z^2} \tag{2.6}$$

and by considering the trigonometric identity, $\cos^2\phi-\sin^2\phi=\cos2\phi$, r_i becomes

$$r_i=\sqrt{a^2+b^2+z^2}\sqrt{1+\frac{a^2-b^2}{a^2+b^2+z^2}\cos2\phi_i} \tag{2.7}$$

and by noticing that $\frac{a^2-b^2}{a^2+b^2+z^2}<<1$, Eq. (2.5) becomes

$$P=A\frac{\exp(-jk\sqrt{a^2+b^2+z^2})}{\sqrt{a^2+b^2+z^2}}\sum_{i=1}^{N}\exp(j\theta_i-jk\frac{a^2-b^2}{2(a^2+b^2+z^2)}\cos2\phi_i) \tag{2.8}$$

Equation 2.8 is identically zero if $\sum_{m=1}^{N}\exp^{jm\beta}=0$ with $m\beta=\theta_m-k\frac{a^2-b^2}{2(a^2+b^2+z^2)}\cos2\phi_m$ and by using the result of the circular case, the necessary phase of element m is

$$\theta_m=\frac{2\pi}{N}m+k\frac{a^2-b^2}{2(a^2+b^2+z^2)}\cos2\phi_m \tag{2.9}$$

Unlike the result reached for the annular case, the resulting expression here depends on z, and hence, it is necessary to specify the depth at which the secondary focus is to be eliminated. In a simulation situation, one needs to determine the field along the axis of the array without the phasing term; then z is chosen to eliminate the highest observed secondary foci along the axis. This technique will be demonstrated in Chapter 4.

2.3 The driving amplitude control required by the FCM

The FCM requires not only a driving phase but also a driving amplitude control for every array element. As an illustration, the phase and the amplitude distributions of the signal needed to excite a point-source linear array of 15 elements are given in Table 2.1.

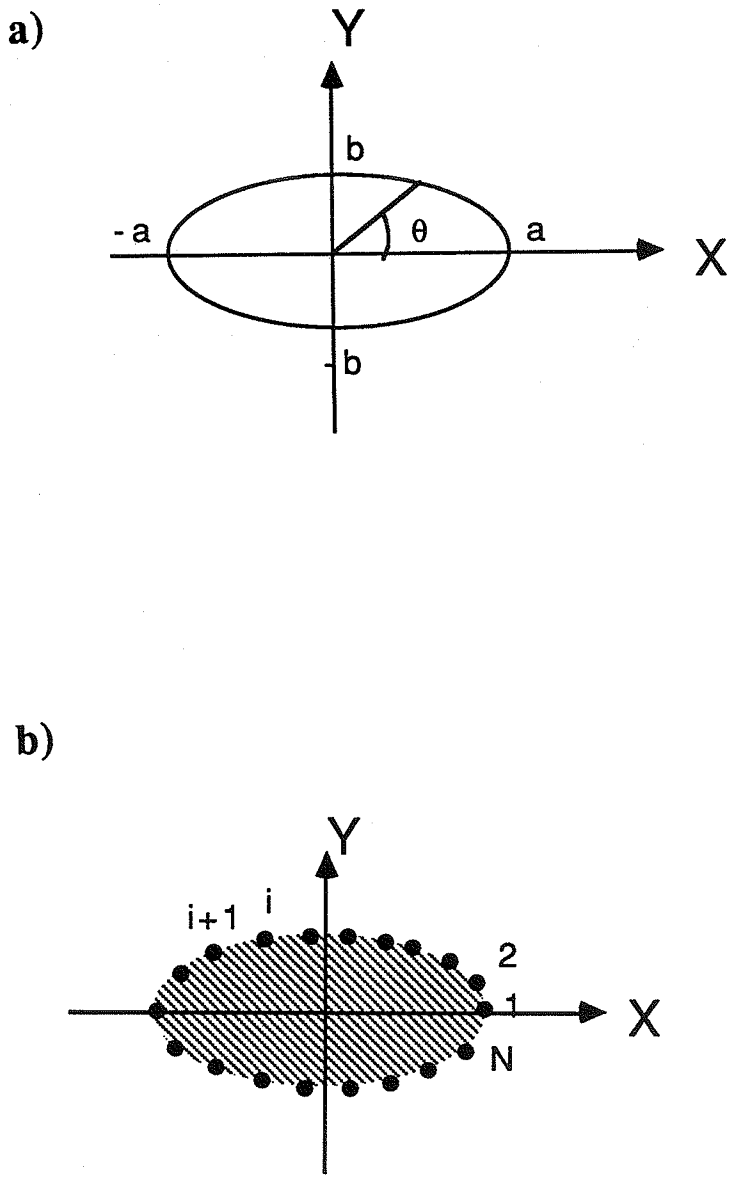

Figure 2.4. Synthesis of an elliptical pattern. a) A schematic of an ellipse and b) geometrical arrangement of the assumed N point sources in the focal plane.

These distributions were obtained by assuming a point source at a point p along the axis of the array as illustrated in Figure 2.5a). The amplitudes were normalized to the maximum amplitude required by the method. The medium is assumed lossless ($\alpha = 0$) for this example.

Table 2.1

Relative Amplitude and Phase Associated with the Pattern of Figure 2.5

Element	Amplitude	Phase in rad
1	0.65	3.21
2	0.71	2.43
3	0.761	1.81
4	0.83	1.21
5	0.89	0.71
6	0.94	0.32
7	0.98	0.08
8	1.00	0.00

The phase and relative amplitude for elements 9, 10,..., 15 are the same as those of elements 7, 6,..., 1 due to the symmetry of the synthesized pattern. Table 2.1 was obtained for d= one wavelength and D= 6d (see Figure 2.5a)). Figure 2.5b) shows the normalized amplitude distribution required for this simple case of synthesis. It can be seen that the required amplitudes are shaded strongly toward the center with relatively low amplitudes toward the edges of the array. The same conclusion can be reached for the case where the beam is steered to an arbitrary point off-axis except that the amplitudes will be shaded strongly toward the nearest point source to the point p' as shown in Figures 2.6a) and b). It is interesting to notice that this kind of shading is commonly used in underwater ultrasonic array design to control the directivity and side lobes, as will be discussed. However, the amount of maximum power that the array can provide is also affected by the amplitude shading and needs to be considered. In the following, the effect of the amplitude shading on

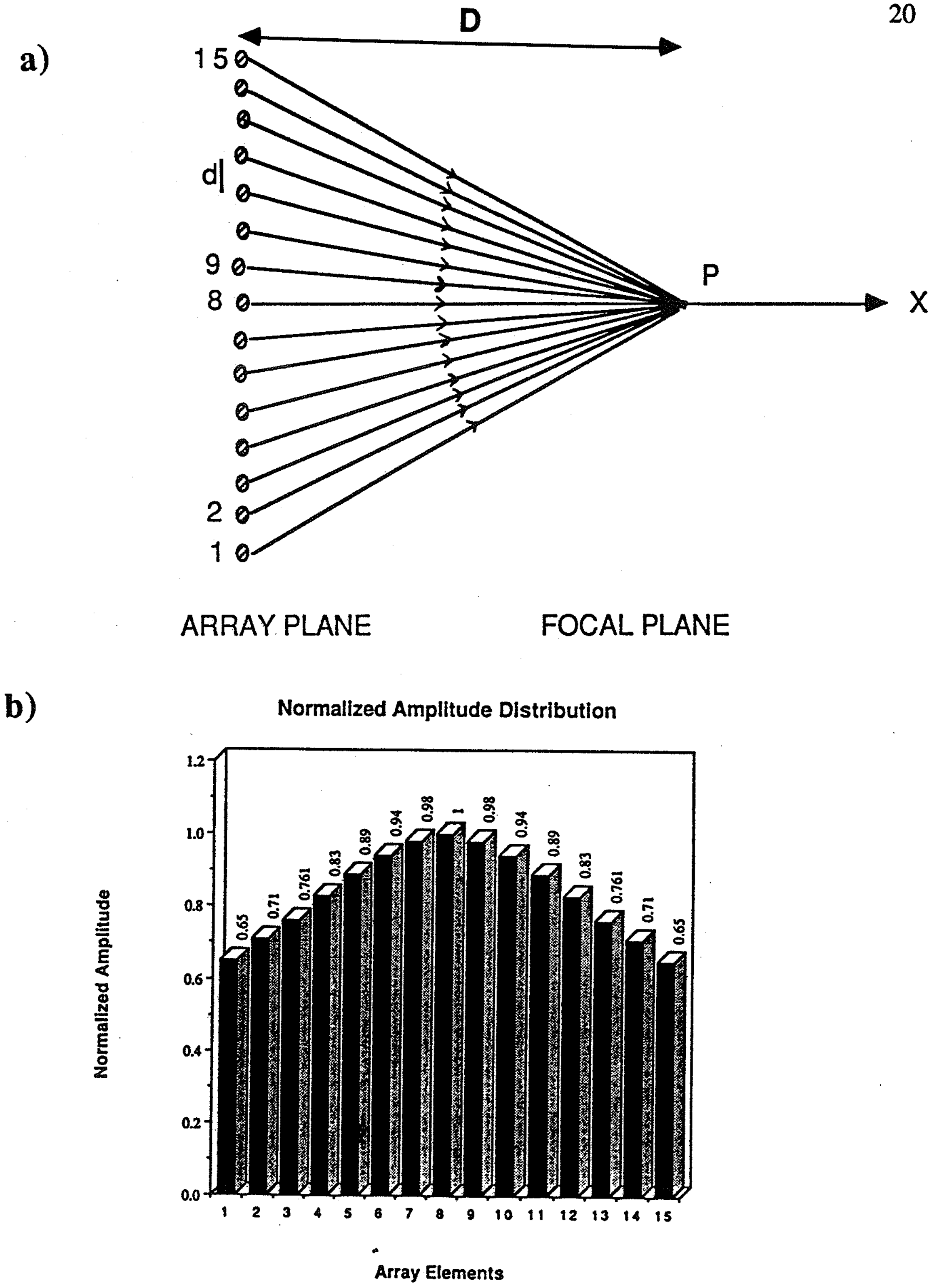

Figure 2.5. The driving amplitude control required by the FCM. a) A linear array of point sources focused along its axis and b) the normalized amplitude distribution of the excitation signal required for the synthesis of a).

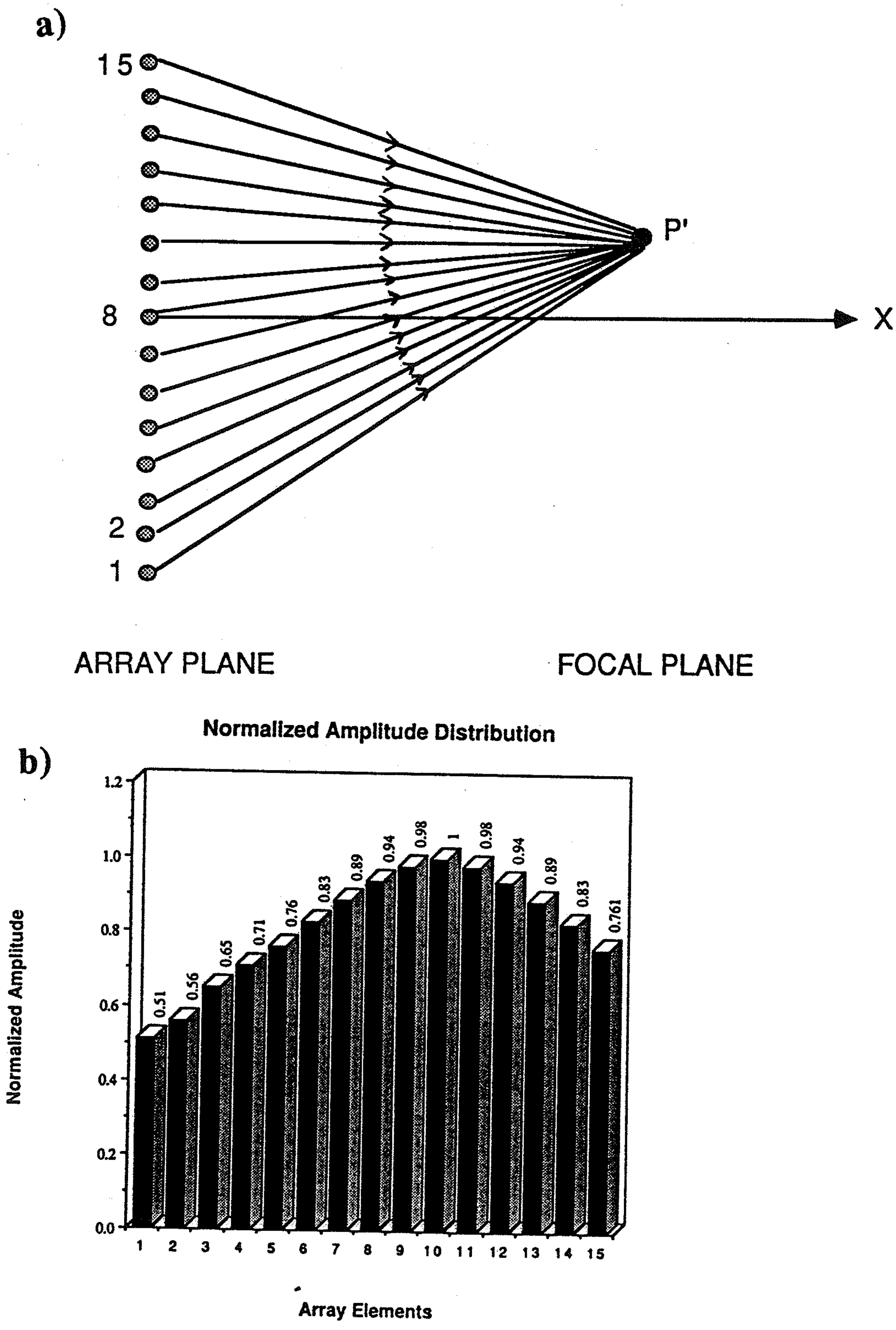

Figure 2.6. The driving amplitude control required by the FCM. a) The array of Fig. 2.5 steered to a point p' off axis and b) the required normalized amplitude distribution.

the directivity and the maximum power available along with some other issues are considered.

2.3.1 Effect of the amplitude shading on the directivity of the array

Amplitude shading has been used widely to achieve some degree of control over the patterns produced by sonar arrays. The shading consists of adjusting the amplitude of the received signal to provide maximum sensitivity [31]. In most cases, shading is accomplished with maximum amplitude toward the center and least amplitude toward the outer elements [31,32,33]. As noticed earlier, the FCM results in a similar shading and, consequently, an illustration of the effect of shading on the directivity of the array is attempted in the following paragraphs.

A linear array of point sources with uniform spacing is considered for the demonstration. Although this situation might be too simple to simulate any case of interest, it is believed that the results will provide a better understanding of the effect of shading on the patterns produced by multitransducer applicators. Figure 2.7 illustrates the geometry of the considered array.

The far field approximation of the pattern produced by this array in a direction relative to an arbitrary point q is given by

$$P = P_0 \sum_{i=1}^{2N} u_i \exp(-jk(r \text{ x } r_i)) \qquad (2.10)$$

where u_i is the strength of the point source i, r is a unit vector pointing toward the point q, r_i is a vector originating from the center toward the position of the source i, k is the propagation constant of the medium, and x is the cross product. P_0 is a normalization factor to make P equal unity along the axis of maximum pressure (array axis in this example).

In the following, it is assumed that the number of elements is 2N (the case of 2N+1 can be treated similarly) and that $u_1= u_{2N}$, $u_2= u_{2N-1},\ldots, u_{N-1}= u_{N+2}$, $u_N= u_{N+1}$. The

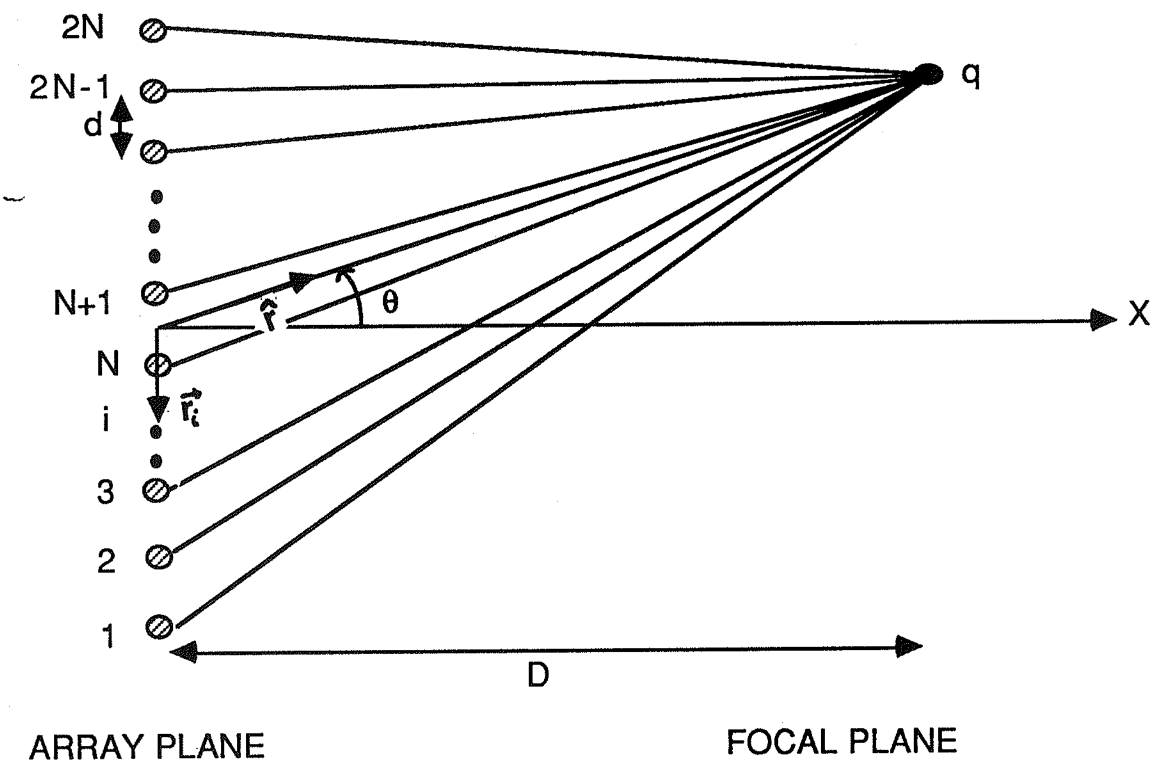

Figure 2.7. A point-source linear array of 2N elements steered to an arbitrary point q in the focal plane.

normalization factor is then found to be $(1/\sum_{1}^{N} 2u_i)$ and the expression of the far field pattern becomes

$$P = 2P_0 \sum_{i=1}^{N} u_i \cos[(2i-1)\frac{kd\sin\theta}{2}] \tag{2.11}$$

To illustrate the effect of the amplitude shading on the side lobes, point-source linear arrays of four and ten elements are considered for different weighting functions ($u_1, u_2, \ldots, u_n$). These two cases were chosen because of the different nature of side lobes as a function of the element number (array length). As could be expected, the number of the side lobes increases with the number of elements, but their relative amplitudes decrease (with respect to the main lobe amplitude). The simulations of the resulting patterns were performed for a uniform source-to-source spacing (0.5 λ).

Different weighting functions (amplitude shading) were assumed for the simulations. Figure 2.8 illustrates the resulting patterns for shading function (2, 1, 1, 2), (1, 1, 1, 1), (1, 2, 2, 1), and (1, 4, 4, 1). It is observed that an increase or decrease in the amplitude of side lobes may result depending on the scheme used for amplitude shading. If shading is accomplished with maximum amplitude toward the array edges, the relative amplitude of the side lobes is increased (compared to the nonshading case) as illustrated in Figure 2.8. On the other hand, shading with maximum amplitude toward the center results in suppressing the side lobes while widening the main lobe. Similar observations result from simulating the case of a 10-point-source linear array as shown in Figure 2.9. By comparing the different patterns with that resulting from the nonshading case (1, 1, 1, 1, 1), it is clear that the particular amplitude shading required by the FCM may help suppress some side lobes. However, grating lobes (of amplitude equivalent to that of the main lobe) seem to be insensitive to amplitude shading, as illustrated in Figure 2.10, which is obtained for a uniform spacing of a full wavelength.

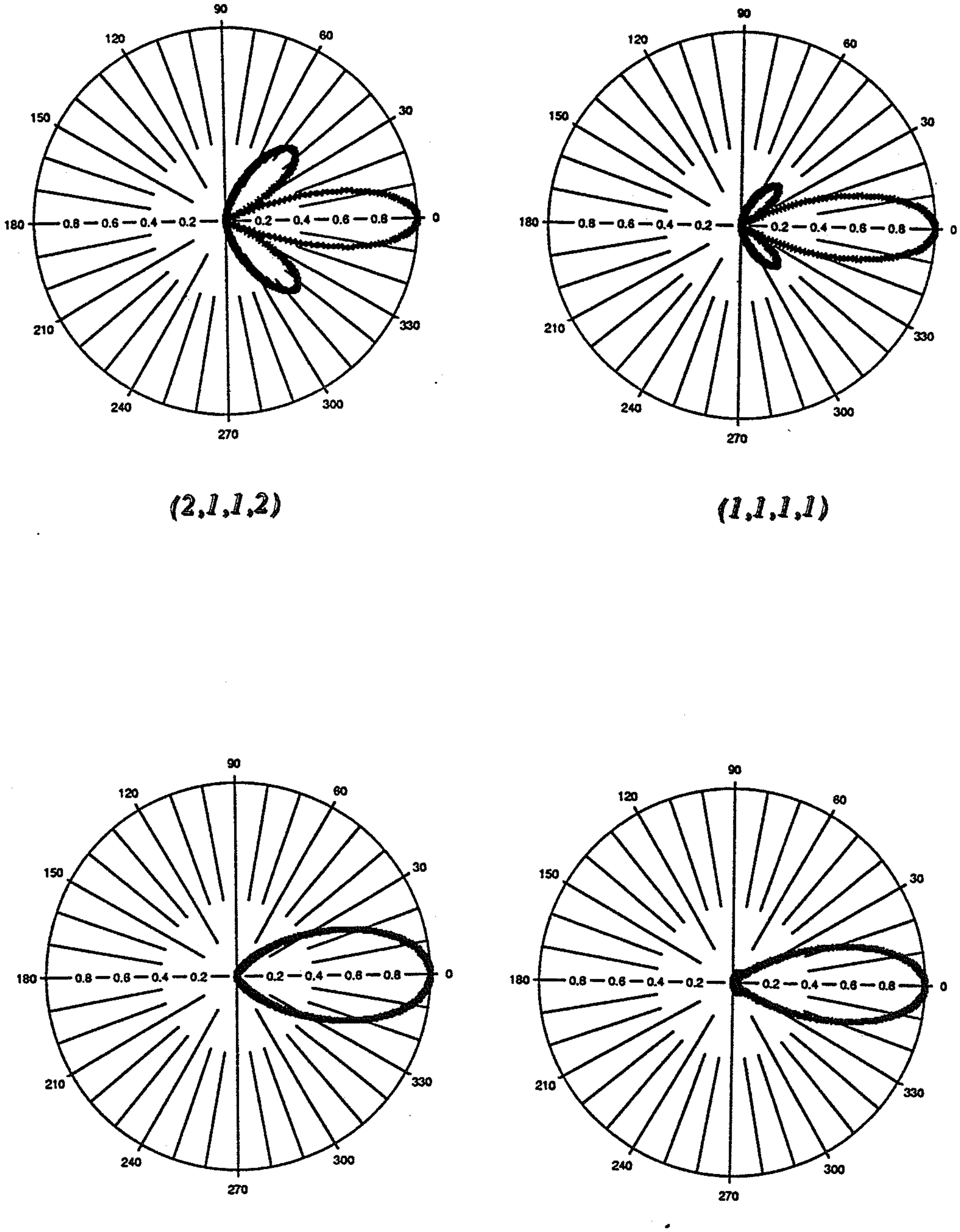

(2,1,1,2)

(1,1,1,1)

(1,2,2,1)

(1,4,4,1)

Figure 2.8. Effect of the amplitude shading on side lobes. The assumed linear array consists of 4 elements of a strength function (u_1,u_2,u_3,u_4). Different patterns each associated with a strength function as shown.

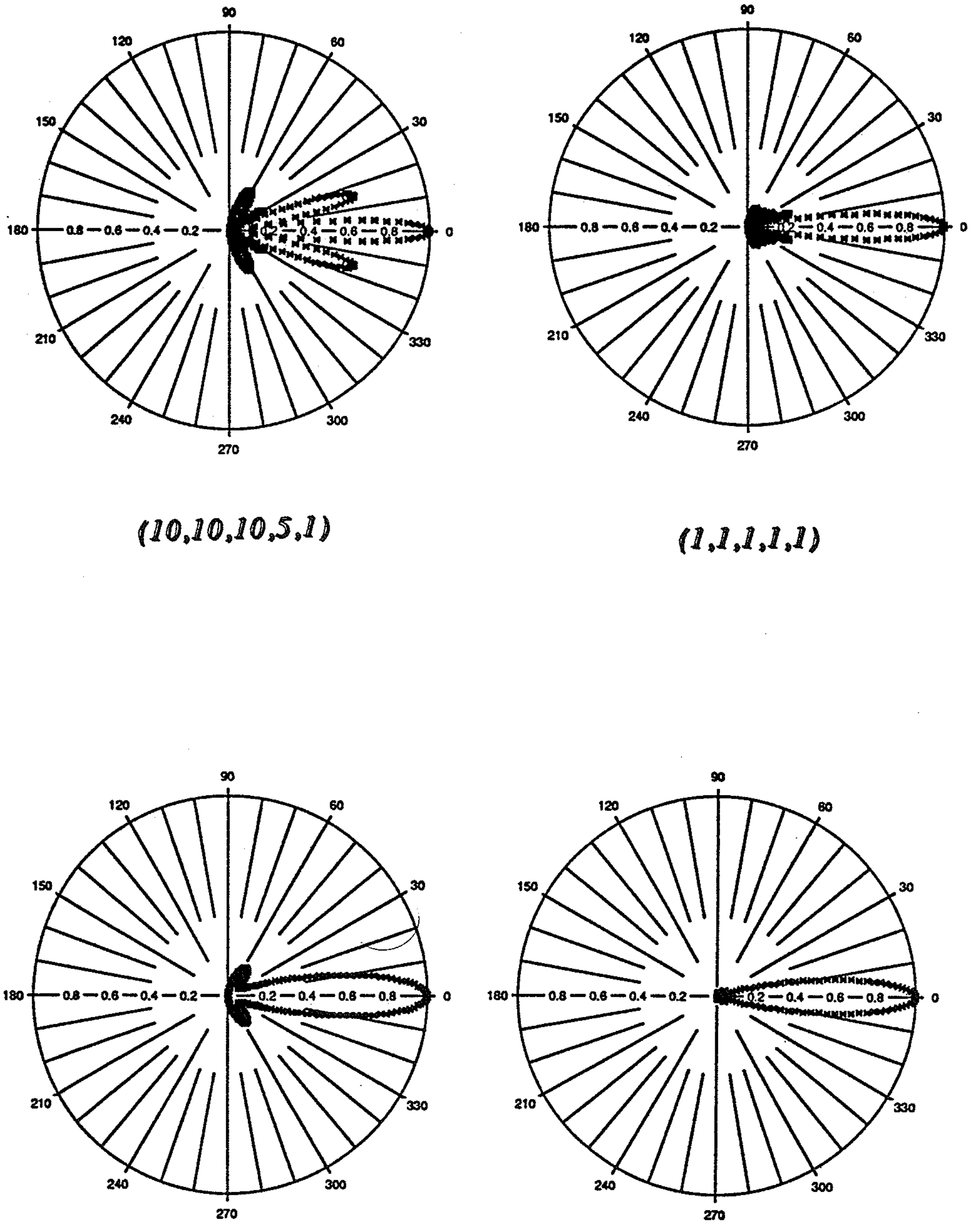

(10,10,10,5,1)

(1,1,1,1,1)

(1,1,1,10,10)

(1,2,3,4,5)

Figure 2.9. Effect of the amplitude shading on side lobes. A point-source linear array of 10 elements is used. The elements are symmetrical with respect to the axis and hence, the strength function is of the form (u_1,u_2,u_3,u_4,u_5). Different patterns each associated with a strength function are illustrated.

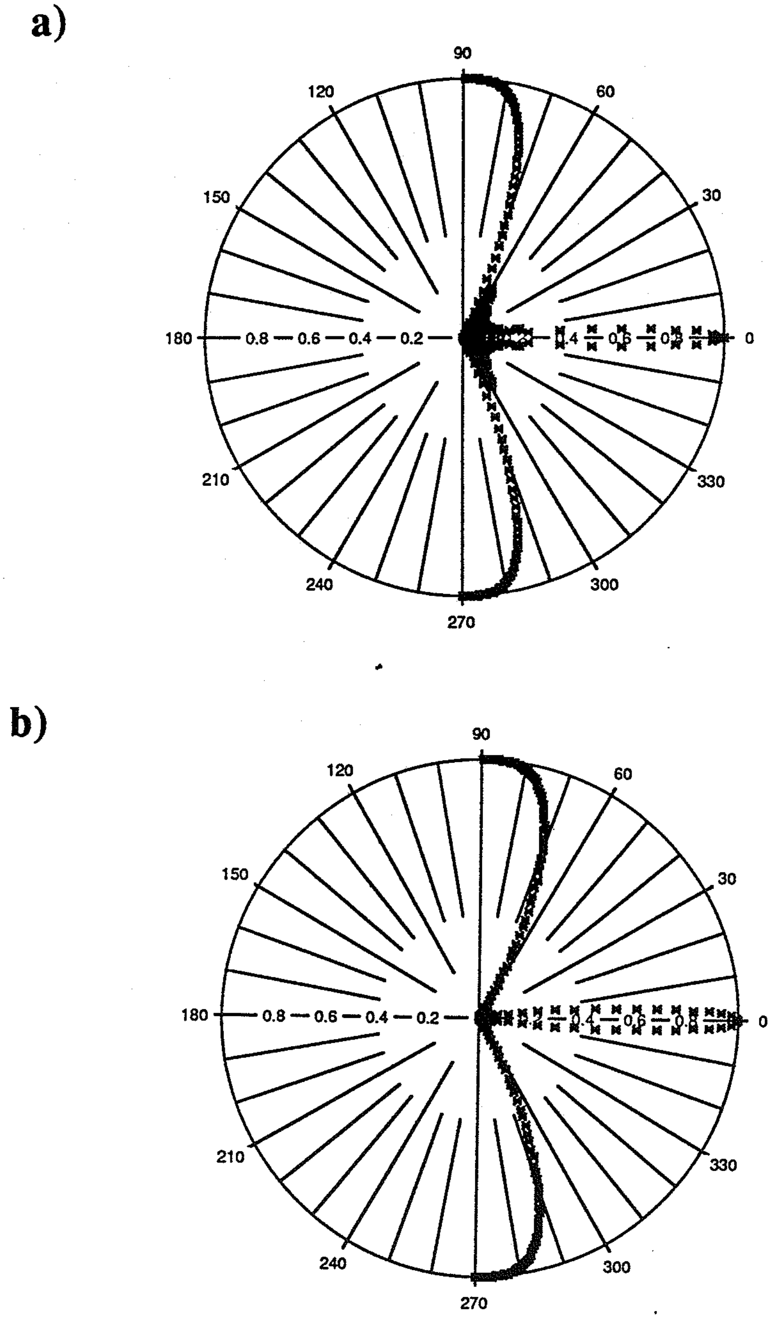

Figure 2.10. Effect of the amplitude shading on side lobes. a) Pattern associated with a nonshaded case and b) pattern associated with a shaded case.

2.3.2 Effect of the amplitude shading on the maximum power produced by the array

The power delivered by a vibrating source is proportional to the square of its surface velocity and, consequently, it is assumed that the maximum power that can be extracted from an array is achieved if each element is vibrating at its maximum velocity tolerable by the transducer material. This observation indicates that due to the amplitude shading of the FCM, the resulting power is always less than that which would have resulted under the assumption of uniform excitation amplitude.

Figure 2.11a) shows the normalized driving amplitude distribution resulting when the FCM was used to synthesize a focal spot along the axis of a 20-element concentric-ring applicator. The analysis of the concentric-ring array is presented in Chapter 3, and Figure 2.11 will be subject to a deeper analysis at that point. It is obvious from Figure 2.11a) that while some elements are excited with relatively high amplitude signals (i.e., elements 1,2,...,7), other elements are merely vibrating with relatively low amplitudes (i.e., elements 15,16,...,20). This amplitude distribution influences the array maximum power capability as some elements will be delivering their maximum power while others are only delivering a fraction of it. For the sake of example, the annular elements of the concentric-ring array are assumed to be of equal effective surface (variable element widths).

The effect of the amplitude shading on the array power can be measured by defining a parameter to characterize each driving amplitude distribution. A simple parameter can be obtained by summing the squares of all normalized amplitudes and dividing the resulting sum by the number of elements. The resulting parameter will be called the " amplitude shading factor" and is actually an indication of the relative average power produced, when the FCM is used, versus that which would have resulted from a uniform amplitude excitation. The amplitude shading factor derived in this section assumes equal area elements. However, a more precise definition will be given in Chapter 3 to account for the cases of elements with different effective surface areas as well. The definition given in Chapter 3 will be slightly different and will be adopted for the remainder of the thesis.

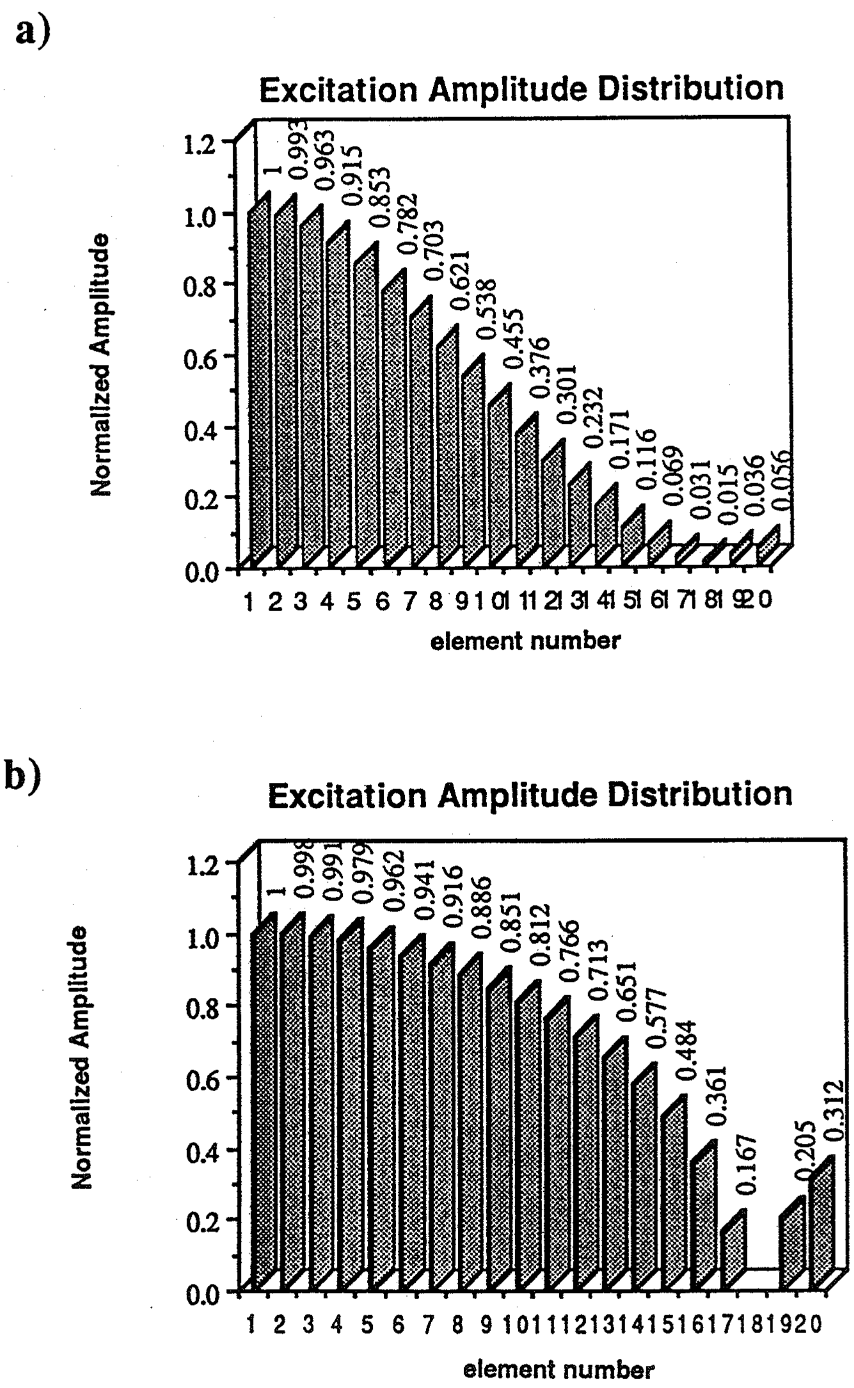

Figure 2.11. Effect of amplitude shading on the maximum power produced by an array. a) Amplitude distribution of the excitation signal as required by the FCM and b) a logarithmically scaled amplitude distribution.

The amplitude shading factor relative to the distribution shown in Figure 2.11a) was found to be 0.337, which might be low for some practical applications. However, it is possible in some cases to improve the amplitude shading factor by modifying the scaling of the amplitude distribution. In some cases, one needs to shorten the dynamical range between the different amplitudes while keeping the general behavior of the distribution close to the original one. One possible approach is to logarithmically scale all amplitudes after dividing them by the lowest amplitude of the original distribution. The division is meant to avoid negative numbers that arise if the logarithm of numbers smaller than unity is attempted. The resulting numbers are then normalized to their maximum and used as driving amplitudes. Figure 2.11b) shows the normalized amplitude distribution resulting from the application of this procedure to the distribution shown in Figure 2.11a). The amplitude shading factor for this logarithmic scaled distribution is found to be 0.61 compared to 0.337 obtained above. This technique will be extensively used in the following chapters. In some simple cases such as simple focusing (point or diffuse focus), it is also possible to drive the array with constant amplitude control while using only the phase control resulting from the FCM as will be shown in Chapter 4.

As will be shown in Chapters 3 and 4, the amplitude shading will prove useful in alleviating the problems associated with the secondary foci formation beyond the focal plane. In particular, for extreme cases where masking the outer elements of the array is proposed [17], the FCM seems to lead to a better power deposition pattern as demonstrated in Chapter 3.

2.4. Conclusions

The field conjugation method was proposed as a means of directly synthesizing the more diffuse intensity profiles without scanning. In other cases where scanning is necessary, the multiple focusing feature of the FCM could potentially simplify scanning by reducing the number of scan points and/or lowering the focal intensity which is often a concern in scanning techniques.

The method can be used to synthesize very complicated intensity profiles which might be used in hyperthermia, imaging and other applications as well. Although the driving amplitude control might appear as an added complexity to already complicated electronics associated with phase control, the required hardware is essentially the same except for the addition of a digital counter, as will be illustrated in Chapter 7.

CHAPTER 3

ANALYSIS AND DESIGN OF A CONCENTRIC-RING ARRAY

3.1 Introduction

Many ultrasonic systems currently in clinical use employ a single large aperture focused transducer. The focal spot produced by this transducer is too small to heat even the smallest tumor; hence, it is translocated over a desired trajectory (often around the tumor periphery) by some mechanical arrangement. The disadvantages of this technique were mentioned earlier. Systems using multiple transducers arranged in a certain geometrical fashion have also been reported. These systems are based on the use of the overlapping ultrasonic beams which can be controlled by positioning the individual transducers. However, those systems are cumbersome and require a large acoustical window. Moreover, excessive pain can result and often lead to a premature termination of the treatment [18,34]. This problem can be attributed in large part to the absence of the ability to precisely control or modify the power deposition pattern during the treatment. Heating of bone distal to the tumor is a particularly difficult problem which can limit the treatment.

A potential alternative is the use of ultrasonic phased arrays in which the control is mainly electronic and can be built remotely from the applicator allowing a simpler patient-machine interface. Moreover, the associated sophistication in electronics and transducer array configuration should permit more precise control of the heating pattern, and would allow modification of the pattern during treatment, without the need to mechanically move the applicator.

A disadvantage of 2-D phased arrays technology is the need for a large number of transducer elements which increases the complexity of the associated electronic control circuitry [35]. Although this may no longer be a severe limitation due to advances in microelectronics and power amplifier design, it is always preferable to minimize the number of array elements. In this chapter, the concentric ring array (CRA) is analyzed and the synthesis of different field patterns is simulated using the field conjugation method of Chapter 2. Because of its circular symmetry, the CRA does not require a large number of elements. Moreover, this array is chosen because of its ability to produce 3-D volume heating at different depths. Conventional focusing (intense focal spot) as well as annular intensity profiles are synthesized. The synthesis of multiple foci, conventional and annular, is demonstrated. The advantages and disadvantages of the method are discussed and compared to those of other techniques. Finally, a method based on a simple mechanical scanning of multiple conventional foci (on the main axis) is proposed as a means of heating small and moderate sized tumors deep in the body. The possibility of heating the back and the front of the tumor simultaneously is also demonstrated through computer simulations.

3.2 Geometrical Configuration of the Array

A concentric-ring applicator has been chosen as one array configuration for further study because it allows 3-D volume focusing of the acoustic power at variable depths. Moreover, this configuration is expected to produce circular heating patterns of different diameters simply by adjusting the amplitude and the phase of the driving signal.

Two concentric-ring configurations with the same active surface area and the same number of elements are investigated. The goal is to choose the most appropriate one for simulations and, ultimately, for implementation. In what follows, an applicator diameter of 12 cm is considered for simulations. The applicator size has been chosen to ensure the delivery of adequate acoustic power (more than 350 watts) [36,37] while being within the limits imposed by the acoustical window available for ultrasonic use in the body. It is also desired to keep the number of annular elements as low as possible to reduce the cost of associated phasing and amplifier electronics. For the sake of simplicity of analysis, the small gap between adjacent annular elements will be neglected and the whole surface of the applicator will be considered active. The two configurations under investigation are the concentric-ring array with a constant-electrode surface area and that with a constant-electrode width.

3.2.1 The equal surface area element array

In this configuration, the effective surface area of every annular element is kept the same. Figure 3.1 illustrates the configuration of the array. The elements S_1, S_2,. , S_N are of the same active surface S, and d_1, d_2,. , d_N are the widths of the elements S_1, S_2,. ., S_N, respectively. It is noticed that the outermost elements are considerably thinner than the innermost ones. This is due to the fact that, in this configuration, the annular element width is inversely proportional to the radius.

The acoustical power extracted from a piezoelectric element is proportional to its active surface and hence, every element will deliver the same acoustical power. Because the widths d_1, d_2,. ,d_N are all different for this geometry, the width-to-thickness ratio of each ceramic element will be different and, consequently, a different operating frequency is needed for each electrode. This could significantly increase the cost of the driving electronics.

Another drawback of this configuration is the need for a very large number of annular elements to achieve annular focusing. This is due to the large width of the innermost elements, compared to the outermost ones, which cannot be steered easily by adjusting the driving phase. Thus, the innermost element widths need to be kept small enough ($<\lambda$) to achieve focusing. The requirement of small width innermost elements implies the division of the applicator into very small equal areas and, consequently, a large number of elements.

As an illustration, a 12 cm diameter applicator is considered. Twenty annular elements, each of a surface area of 5.65 cm^2, are assumed. For the sake of simplicity, the spacing between adjacent elements is neglected and the total surface was simply divided by the number of annular elements. The widths of some of the resulting outer and innermost annular elements are given in Table 3.1. It should be noticed that, while the outermost element width (d_{20}) is 2.5 mm, the innermost element width (d_1) is 13.5 mm. For an

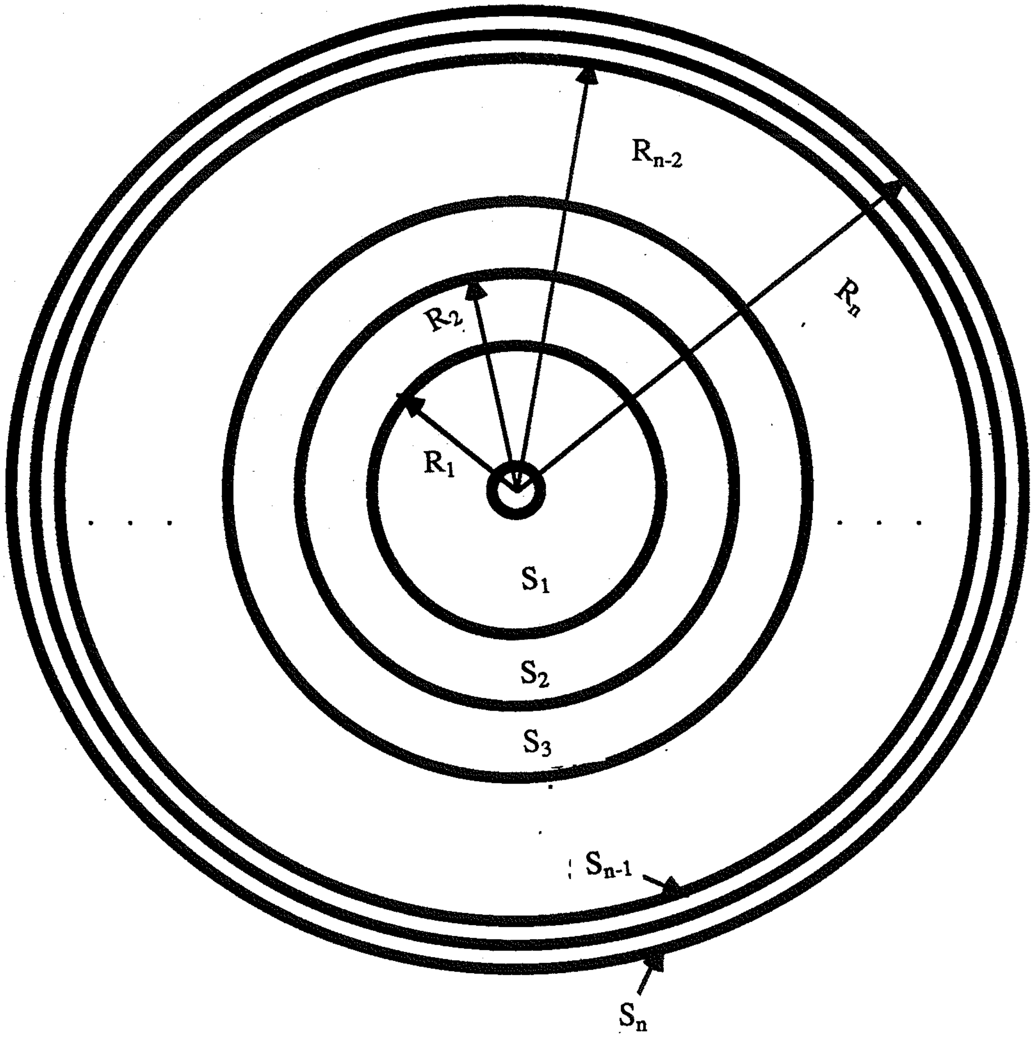

Figure 3.1. Geometrical configuration of a constant area per element concentric-ring array.

Table 3.1.
Outer and Innermost Electrodes Widths for 20-Element Array

innermost electrodes	electrode width in mm	outermost electrodes	electrode width in mm
1	13.45	16	1.77
2	5.60	17	1.70
3	4.40	18	1.65
4	3.70	19	1.60
5	3.20	20	1.50

Table 3.2.
Outer and Innermost Electrodes Width for an 80-Element Array

innermost electrodes	electrode width in mm	outermost electrodes	electrode width in mm
1	6.60	76	0.39
2	2.75	77	0.38
3	2.13	78	0.38
4	1.80	79	0.38
5	1.61	80	0.37

operating frequency of 500 kHz and assuming a sound velocity of 1500 m/s (in tissues), some of the innermost elements are much wider than the wavelength in the medium. Because of these wide elements, steering the sound beam to the desired focal location, by assuming a constant driving phase over the wide electrode, will prove very difficult. Figure 3.2 shows the normalized intensity along a longitudinal axis passing through the focus when synthesizing an annular ring of 30 mm radius at 80 mm depth. This intensity pattern demonstrates that no focus is achieved at the desired location (z=80 mm). However, when the number of elements is increased to 80 (surface area is decreased to 1.41 cm^2 for each element), focusing at the desired location is achieved as demonstrated in Figure 3.3. The widths of the annular electrodes are given in Table 3.2.

It is obvious that reducing the widths of the innermost elements, while resulting in better focusing, leads to a higher number of electrodes and to extremely thin outermost elements which might be impractical for implementation (see Table 3.2). Due to these major drawbacks, no further attention is given to this configuration and the investigation will use the configuration of the equal width element array.

3.2.2 Equal width element array

In this configuration, the width of each annular electrode is kept the same, i.e., $d_1= d_2= d_3=...= d_n$. Figure 3.4 illustrates the geometry of the applicator. As mentioned earlier, the step between adjacent elements is neglected and the center-to-center spacing is considered to be equal to the width of a single element.

The advantage of this configuration is that the width-to-thickness ratio is the same for all annular elements. Therefore, the same resonance frequency is used to drive all electrodes. Moreover, the number of elements can be kept reasonably small to reduce the complexity of the associated electronics. Finally, the realization of such a configuration is simplified since it does not require cutting annular elements of extremely small widths.

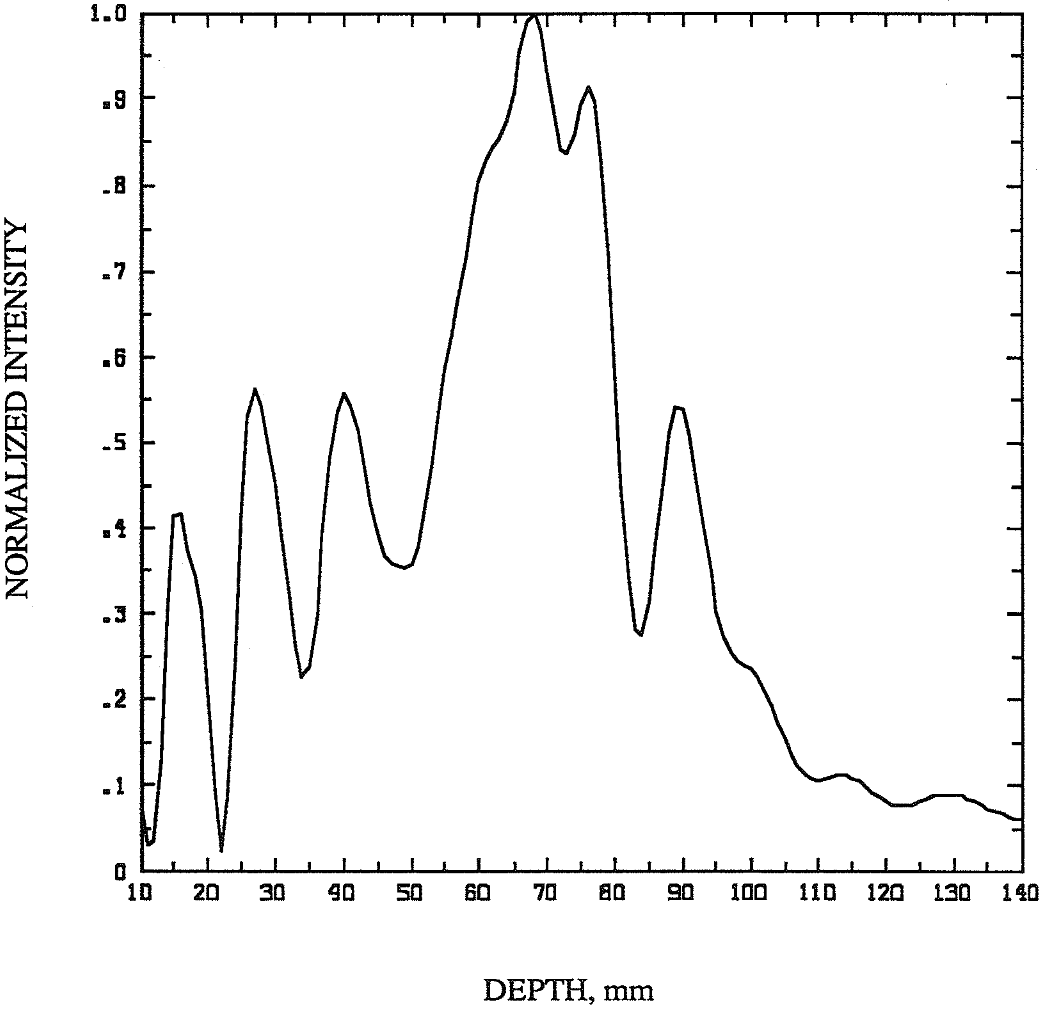

Figure 3.2. Relative field intensity of a constant-electrode surface CRA versus z position. The pattern resulted from attempting to focus the array at (o,o,80) along the axis. The number of elements is 20.

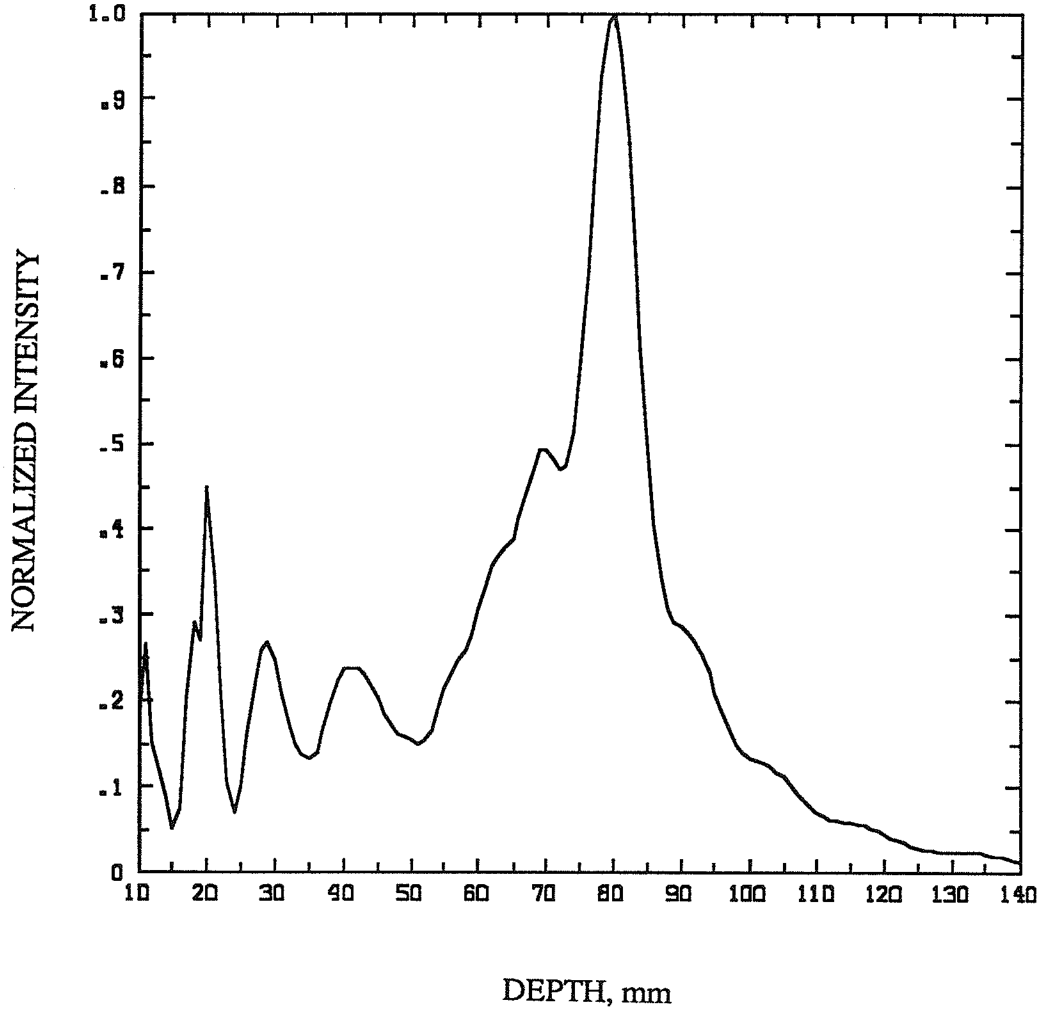

Figure 3.3. Relative field intensity resulting from increasing the number of elements of Fig. 3.2 to 80. Intensities are normalized to that of the focus.

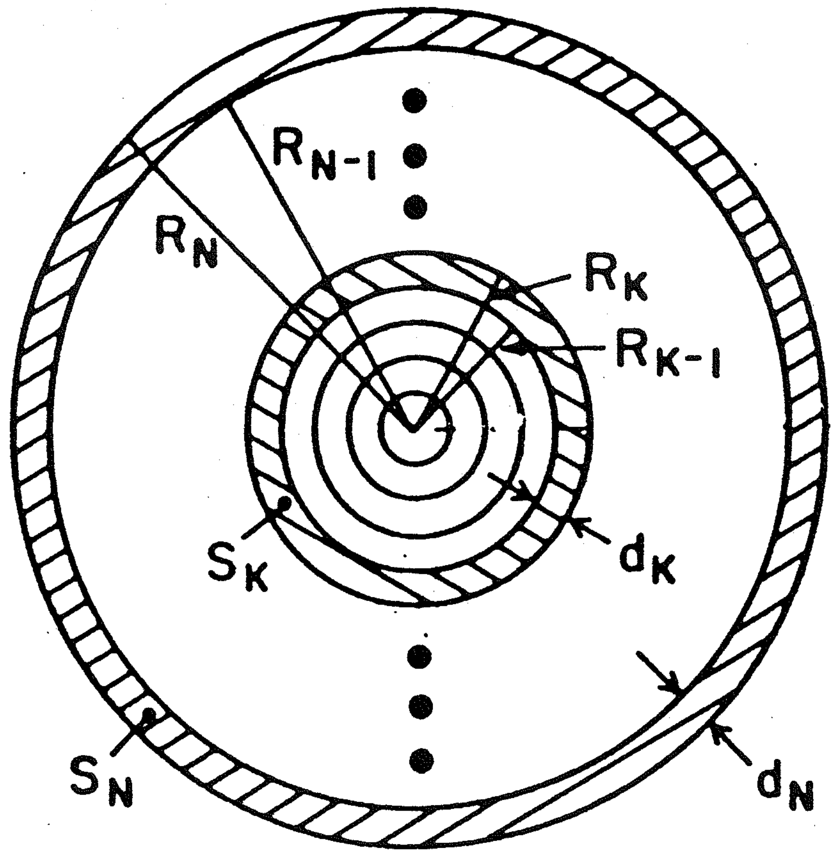

Figure 3.4. Geometrical configuration of an equal-width element concentric-ring array.

As a comparison, the normalized intensity as a function of the depth along the axis of the focus (R=30 mm) is shown in Figure 3.5. The pattern is obtained for the 12 cm diameter applicator divided into 20 annular elements, each of a 3 mm width. In conclusion, this configuration is chosen for further study and for application of the FCM in the following sections.

3.3 Modeling of the Acoustic Field

The Sommerfield-Rayleigh diffraction integral can be evaluated numerically to obtain the pressure field, due to the array, at an arbitrary point in space. This integral can be handled in a straightforward manner as a double summation in cylindrical coordinates. However, because of the rapid change in the phase term exp(jkr), the summation increment needs to be very small and the computation time increases accordingly. To achieve the calculation in a reasonable computation time, the method of equidistant areas described in [38] is modified for the calculation of the field produced by a CRA. The advantage of the method is the transformation of the double integral into a simple one that can be handled easily by digital computers. A summary of the method is given below.

The field produced by the CRA at an arbitrary point P is the sum of the contributions of all annular elements computed at P. A complex surface velocity u_i is associated with the the annular element i. The field due to the element i is then given by

$$P = \frac{j\rho ck}{2\pi} \sum_{i=1}^{N} \int_{S_i} u_i \frac{e^{jKr_i}}{r_i} ds_i \tag{3.1}$$

where N is the number of the annular elements, ds_i and s_i are the incremental and the total surface areas, respectively. Also, r_i is the distance between the element ds_i and the point where the field is to be evaluated. The surface velocity is assumed uniform over the annular

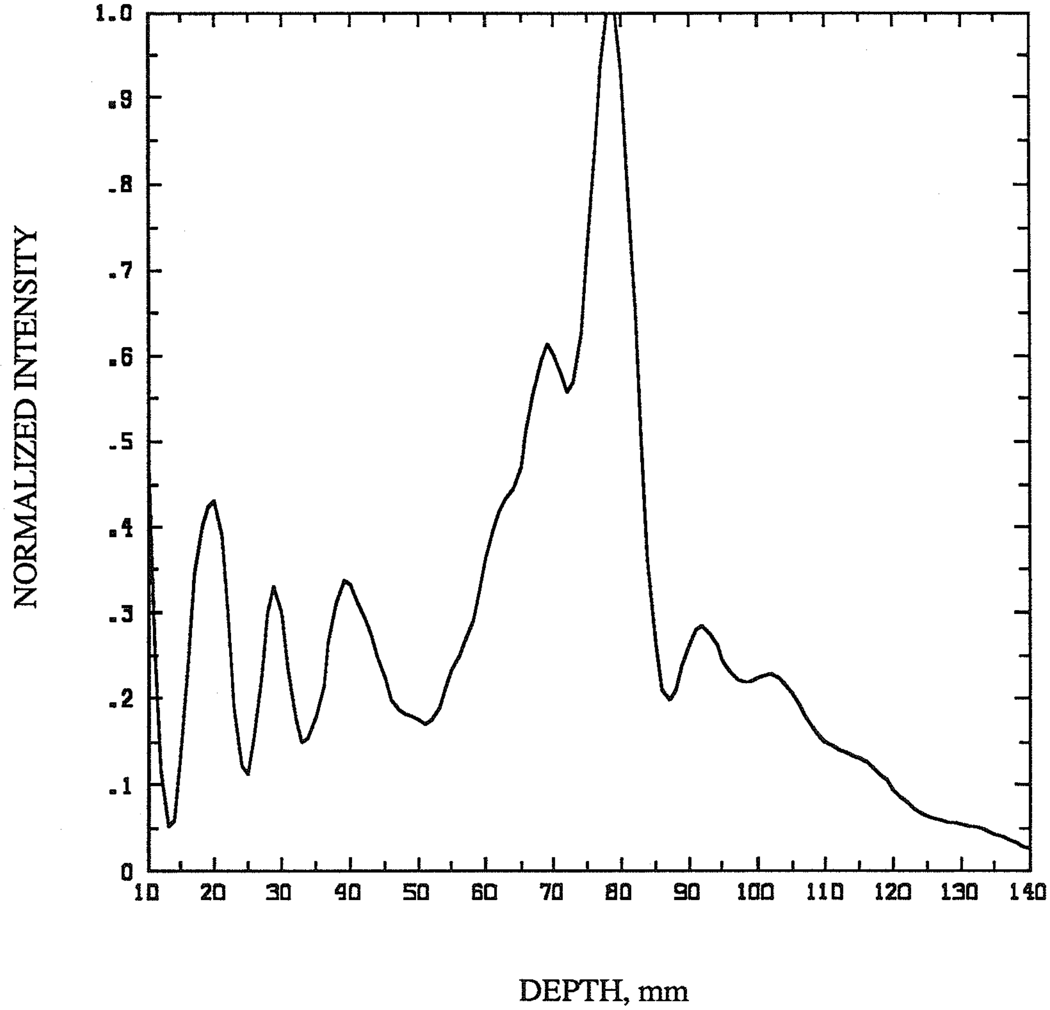

Figure 3.5. Normalized field intensity versus z position resulting from focusing a 20 equal-width element array at point (0,0,80).

element surface, and the problem is that of calculating a surface integral as suggested by Eq. (3.1).

In the above integral, the propagation constant K is assumed complex to account for medium attenuation ($K= k+j\alpha$). To transform the double integral into a simple one, the incremental area is taken as the area over which r_i is sensibly the same. This incremental area is determined by projecting the point P onto the plane of annular element surface and, using geometrical concepts, to evaluate the equidistant areas. To illustrate this, an annular element of inner and outer radii R_1 and R_2 is considered . It is desired to evaluate the field at point P as illustrated in Figure 3.6a) where the point P is projected on P', situated in the plane of the transducer. The equidistant areas are then determined as the intersection between the annular element surface and all the annular strips centered at P' as illustrated in Figure 3.6b).

It is obvious from the illustration that the number of incremental areas (equidistant areas) depends on the width of the annular strips and, hence, the precision of the method can be improved by making the strip width very small. However, the choice of the strip width should be a trade-off between the required accuracy and the computation time. Finally, the double integral is transformed to a simple one given by

$$P_i = \sum_{m=1}^{M} \Delta A_m \frac{\exp(jkr_m)}{r_m} \tag{3.2}$$

where ΔA_m is the area common to the electrode and the annular strip m, r_m is the distance between the point P and the mth annular strip, and M is the total number of annular strips needed to cover the whole electrode surface.

Once the expression P_i is computed for all annular electrodes (i=1, 2, 3,..., N), then the total pressure due to the array is handled as a simple sum. The final expression is given by

$$P = \frac{j\rho ck}{2\pi} \sum_{i=1}^{N} P_i \tag{3.3}$$

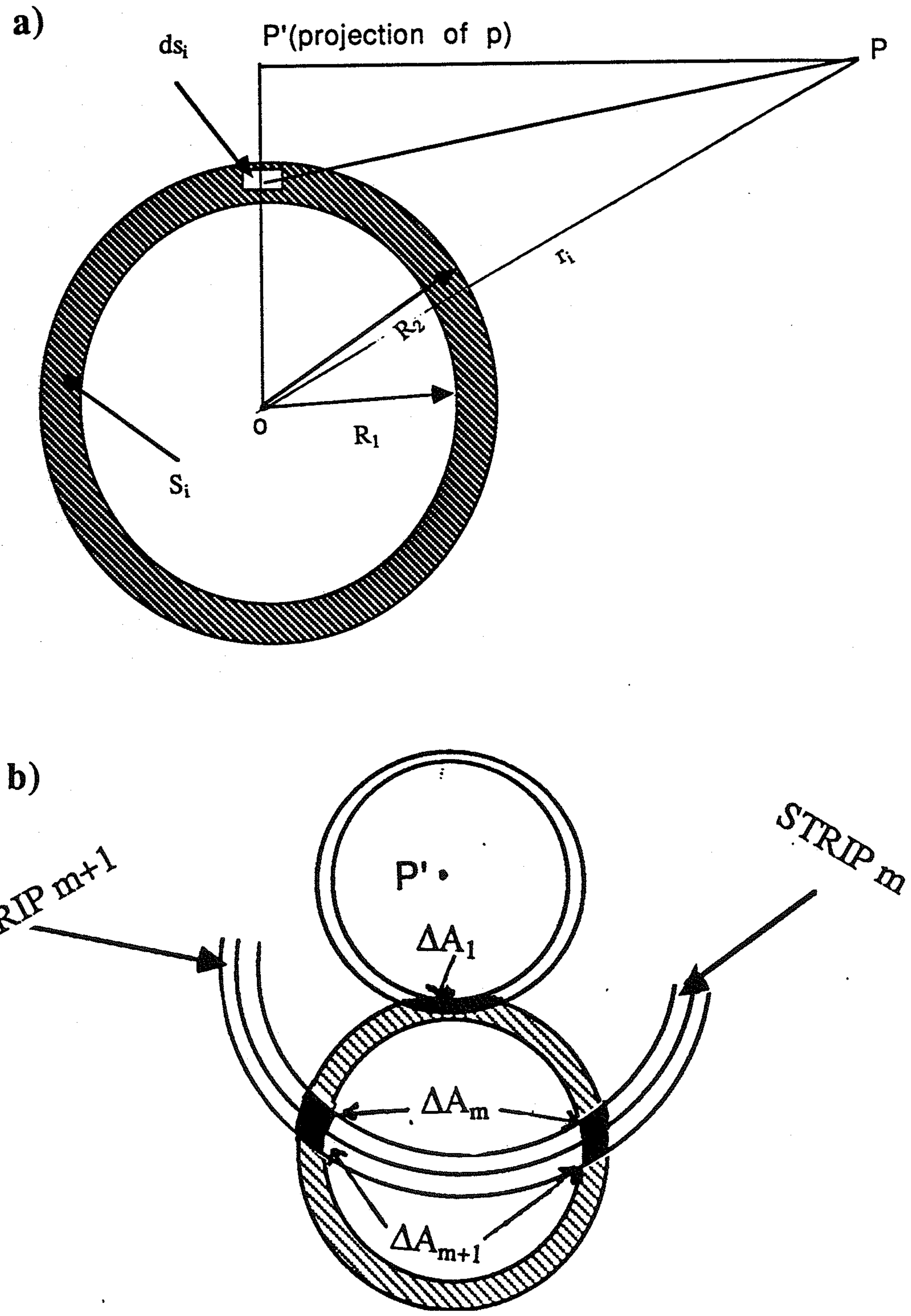

Figure 3.6. Equidistant-areas method. a) A schematic used for the calculation of the pressure field at point P due to an annular ring source and b) determination of the incremental areas.

It is clear that the accuracy of the method depends essentially on the width of the considered annular strips. To choose an appropriate width, our calculations were compared to those obtained by Zemanek for the case of a disk transducer [39]. This case was simulated by considering all electrodes vibrating with the same complex velocity, and the results showed perfect agreement for increments on the order of 1/8 wavelength.

3.4 Synthesis Using the FCM

The general approach consists of assuming a source of annular shape at the desired location, the field due to this source being then computed at the midwidth point of each annular element. Finally, these values are conjugated and used as excitation signals to the corresponding electrodes. However, it is sometimes necessary to modify the procedure slightly to optimize the desired pattern (i.e., elimination of hot spots, etc.). These modifications often deal with the nature of the assumed source and merely require the modification of the software to obtain different heating patterns.

In this section, the general approach is first presented, simulations of some heating patterns obtained by this approach are then given, and a comparison with some existing methods is then discussed.

3.4.1 Synthesis of annular heating patterns using the FCM

An annular source is first assumed at the desired focal plane. The field due to this source is then calculated at the midwidth point of each annular array element. These values are conjugated and the resulting complex expressions are used as excitation signals to the corresponding array elements. Figure 3.7 illustrates the configuration of the assumed source with respect to the array.

This method can be used to synthesize single and multiple annular heating patterns. The annular pattern obtained by assuming a ring of a 40 mm radius at an 80 mm depth is illustrated in Figures 3.8 and 3.9. Figure 3.8 is the surface plot of the patterns resulting in

a) CONCENTRIC-RING ARRAY

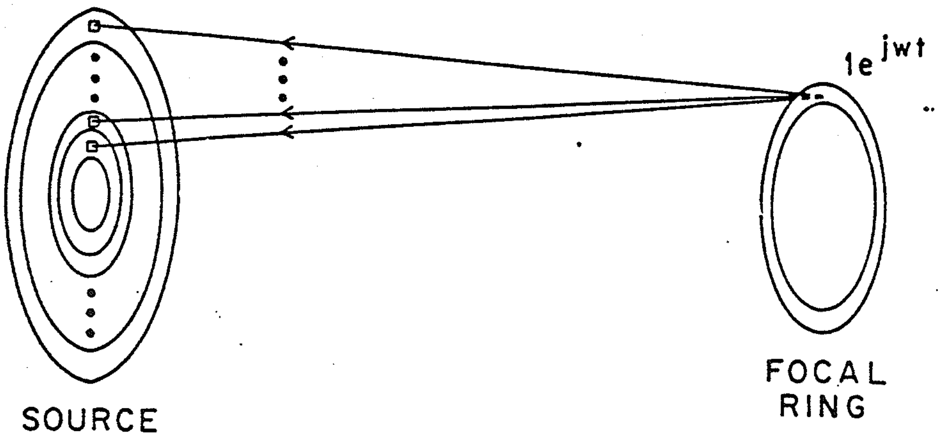

b) CROSS SECTION

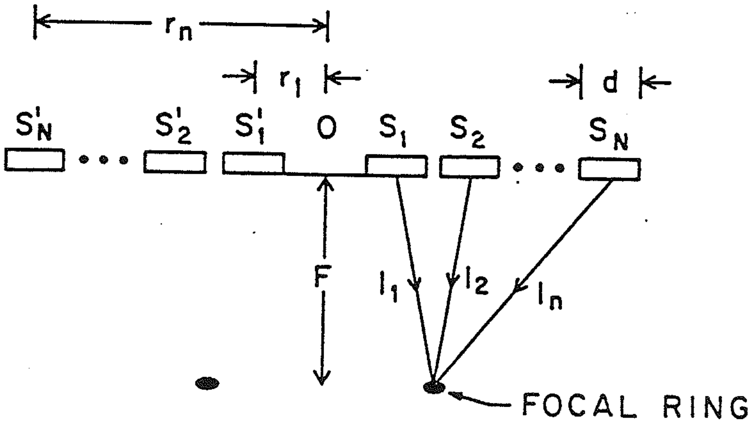

Figure 3.7. Synthesis of annular pattern using the FCM. a) A general view and b) a cross section.

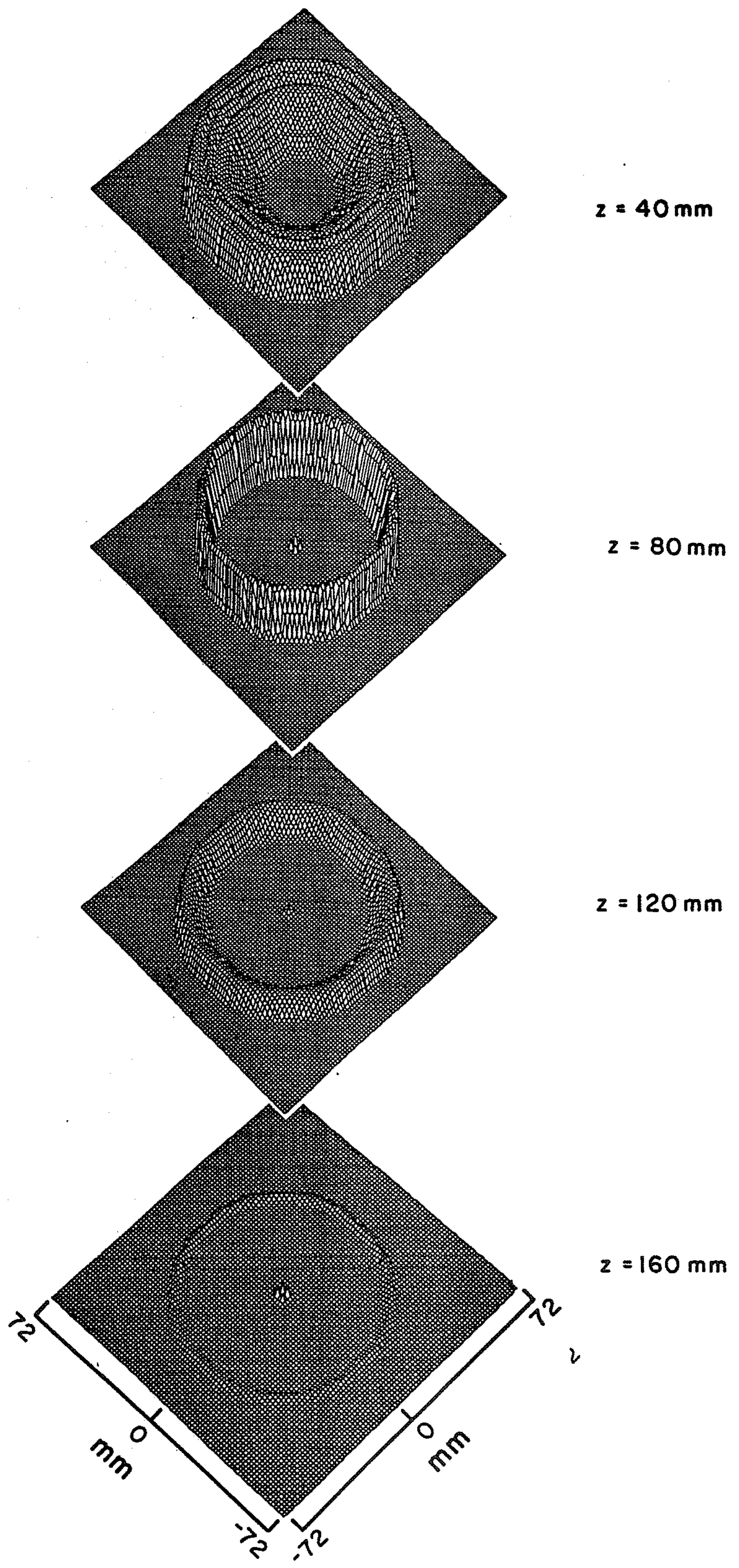

Figure 3.8. Synthesis of an annular pattern of 40 mm radius at z=80 mm. Surface plot of the resulting pattern in 4 transverse planes, parallel to the array surface, at different depths.

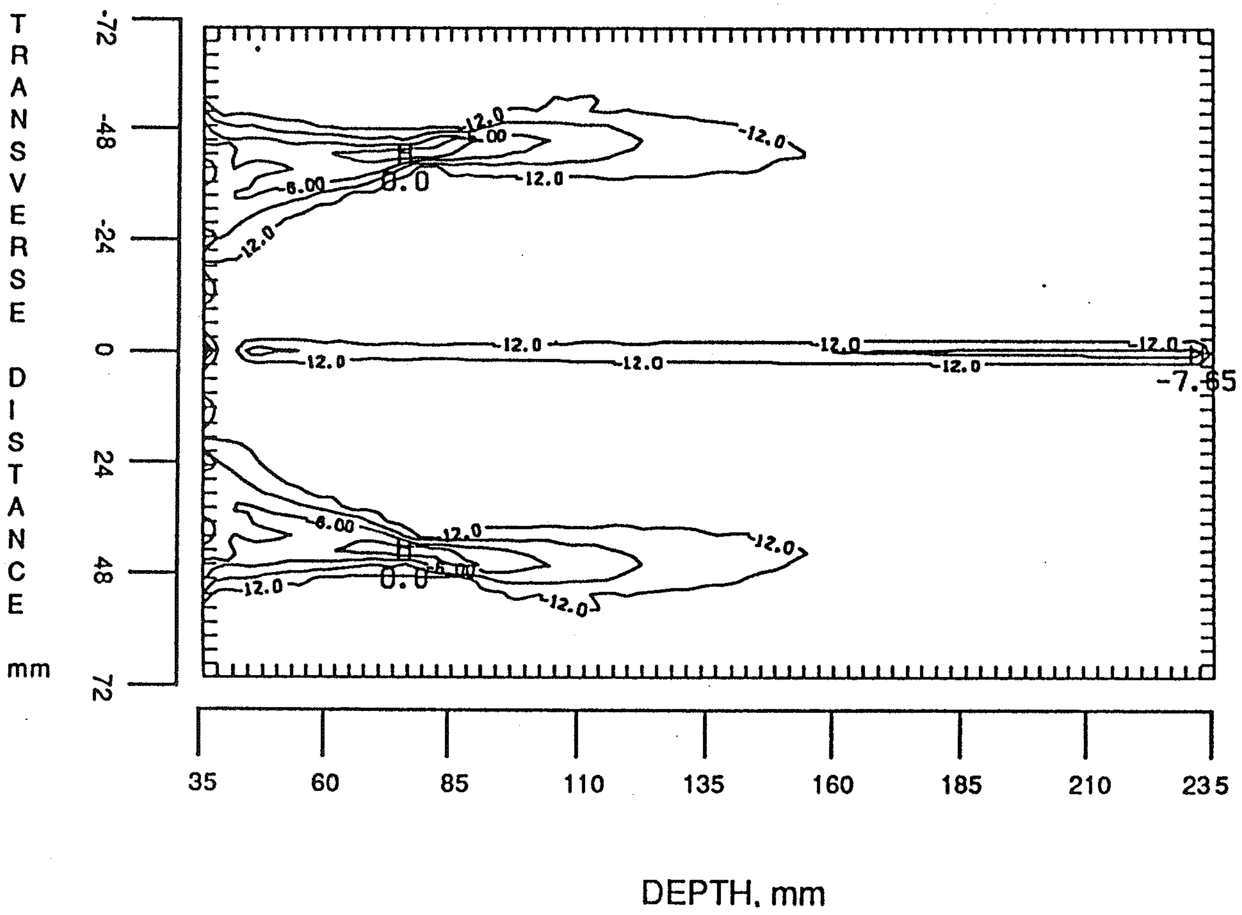

Figure 3.9. Synthesis of an annular pattern of 40 mm radius at 80 mm depth.
a) A contour plot of the pattern in the (r,z) plane with a contour increment of 3 dB.

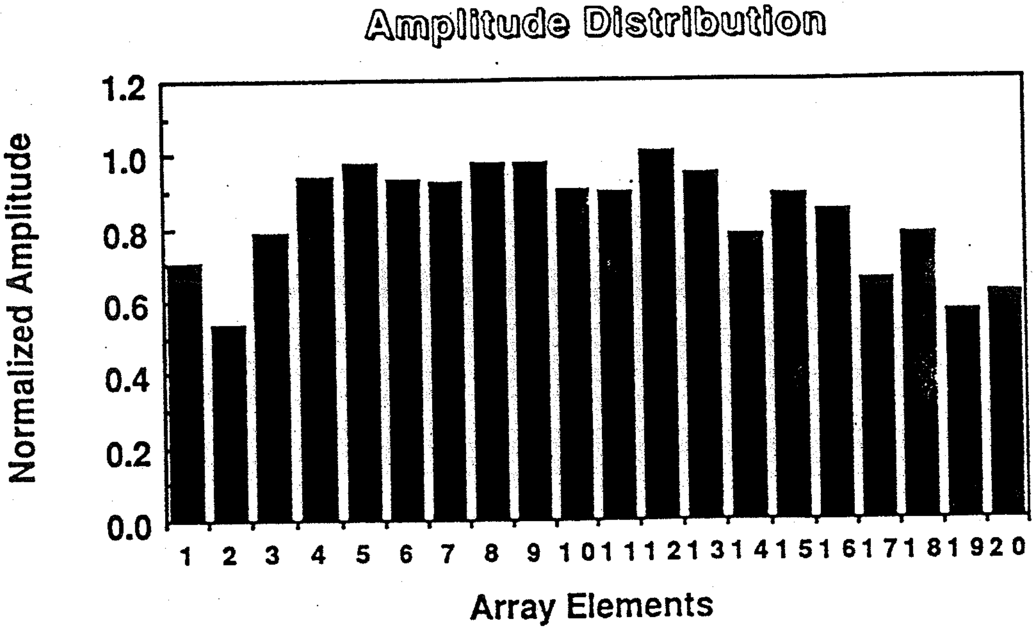

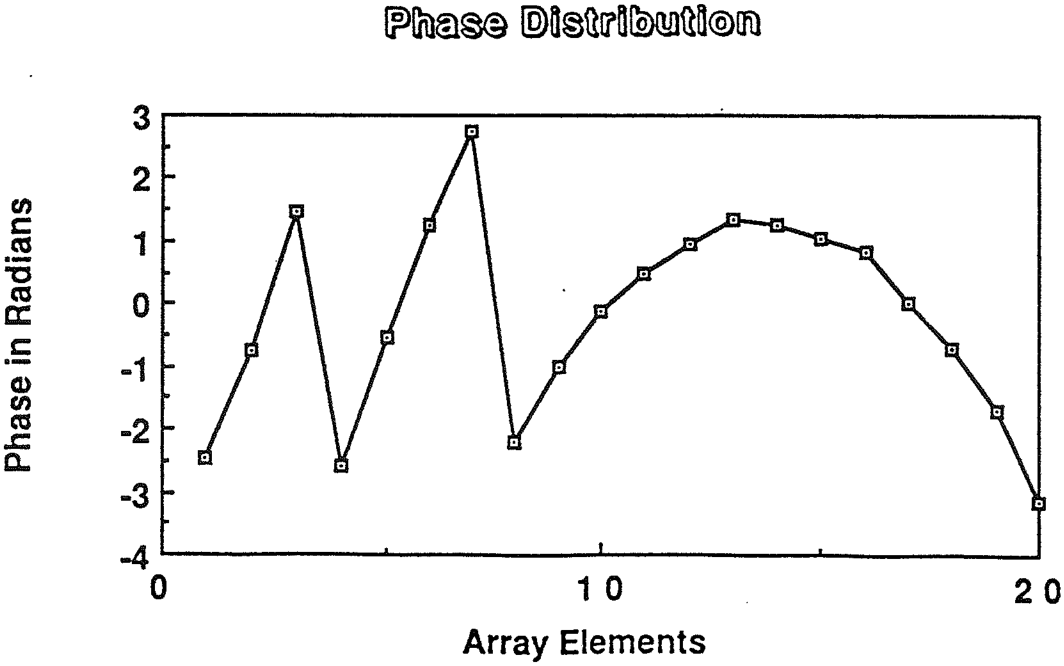

Figure 3.9. b) amplitude and phase distributions required for the synthesis of the above pattern.

four transverse planes including the focal plane (z= 80 mm) while Figure 3.9a) is a contour plot of the heating pattern in a plane containing the primary axis of the array. The width of the assumed ring was 5 mm. The phase and amplitude of the signals necessary to excite each of the elements are illustrated in Figure 3.9b).

The FCM can also be used to generate spot foci (conventional focusing) on the main axis. To do that, one assumes a point source at the desired location on the main axis. This can also be done by assuming a full disk shaped source of a small radius (< wavelength) at the desired main axis location. Figure 3.10a) is a contour plot of the pattern obtained by assuming a disk shape (4 mm diameter) at 100 mm from the array. Figure 3.10b) is a surface plot of the same pattern as seen in the focal plane (z= 100). The advantage of assuming a disk shaped small source over a point source is the production of a more diffuse focal spot compared to that resulting from a point source.However, the depth of field of the focal region is also increased and hence, the radius of the assumed source should be kept small.

Multiple foci on the main axis can be produced by assuming a disk shaped source (or a point source) at the location of each focus and adjusting the scaling factor to obtain the desired amplitude. Figure 3.11a) is a contour plot of the power deposition pattern resulting from simultaneously focusing at two depths (z= 60 and 130 mm). An elongated focal region can be generated by shortening the distance separating the two foci to allow their 3 dB focal regions to overlap. Figure 3.11b) is an elongated focus on the axis, obtained by simultaneously focusing at z= 85 and 100 mm, respectively. Figure 3.12 demonstrates the multiple focusing feature of the method by simultaneously focusing at three locations distributed along the main axis. The pattern is obtained by assuming a disk shaped source at z= 55, 100, and 160 mm from the applicator surface. The number of foci is obviously limited by the lower limit of the power necessary to produce therapeutic heating. These issues will be examined in Chapter 5 in which the resulting temperature distributions are investigated.

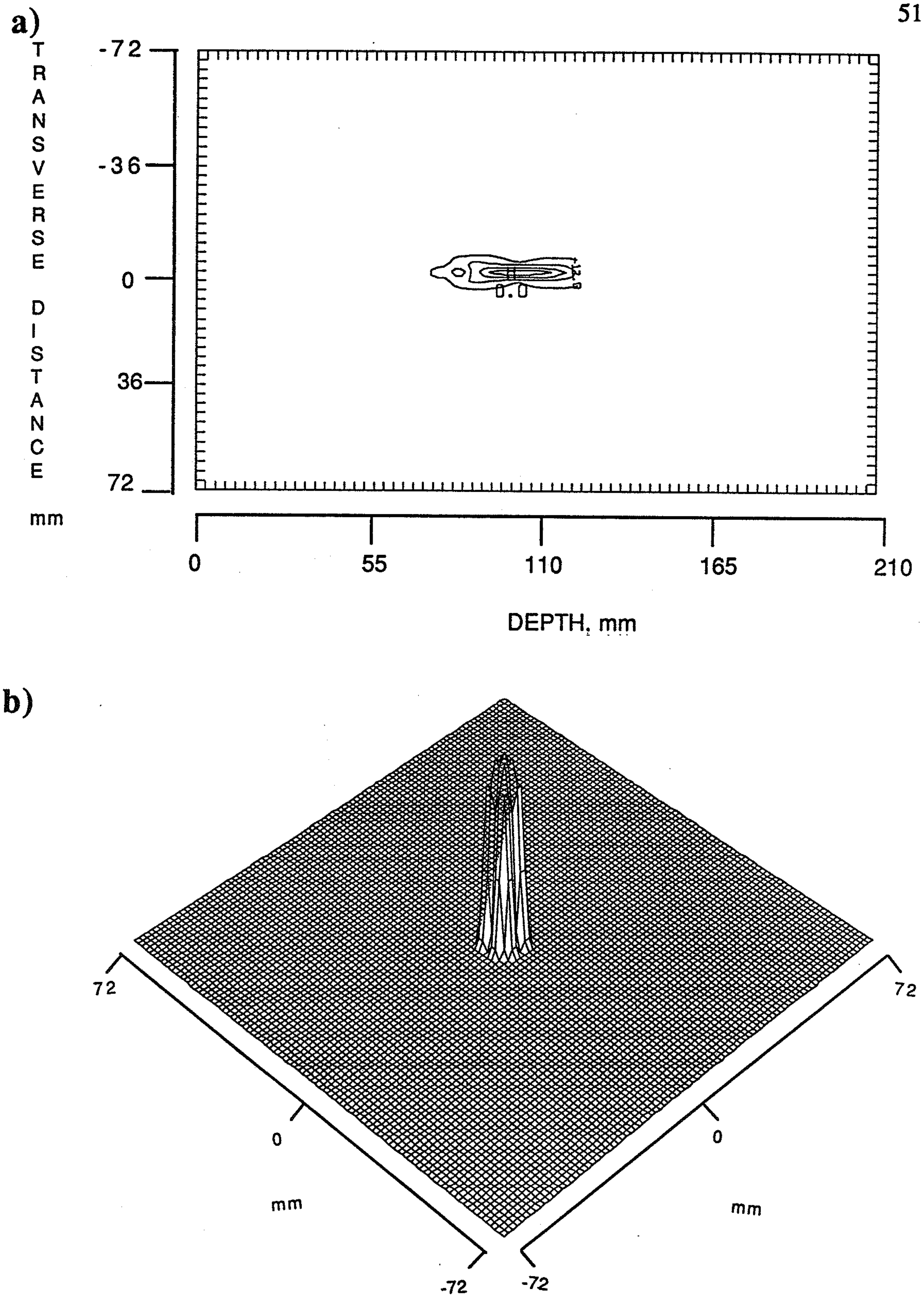

Figure 3.10. Simple focus at (0,0,80). a) A contour plot of the pattern in the (r,z) plane with a contour interval of 3 dB and b) a surface plot of the pattern in the focal plane (z=80).

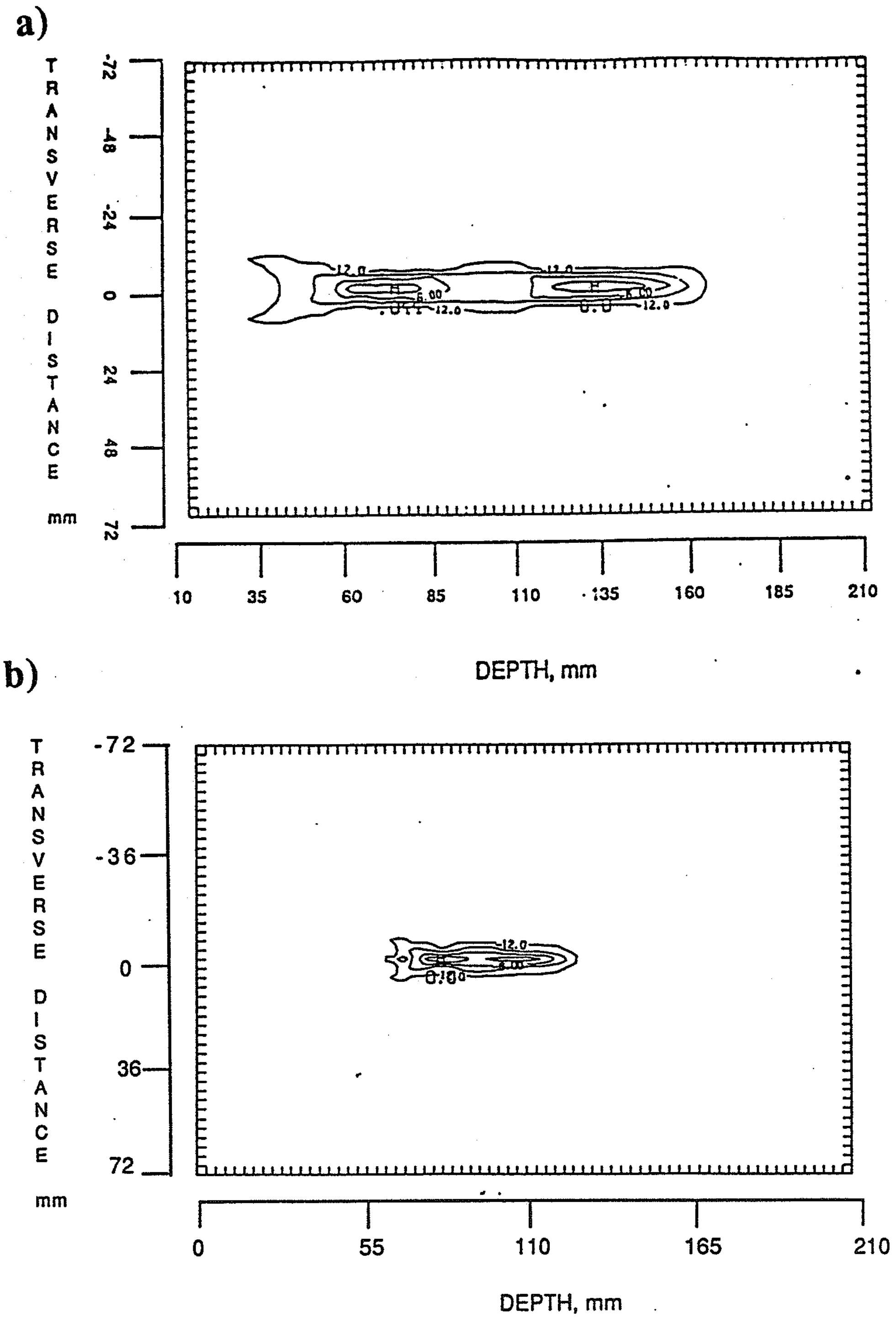

Figure 3.11. Multiple foci along the CRA axis. a) A contour plot of the pattern resulting when the array is simultaneously focused at (0,0,65) and (0,0,130), respectively, and b) a contour plot of the pattern resulting from simultaneously focusing at (0,0,80) and (0,0,105), respectively. Contours are given in increments of 3 dB.

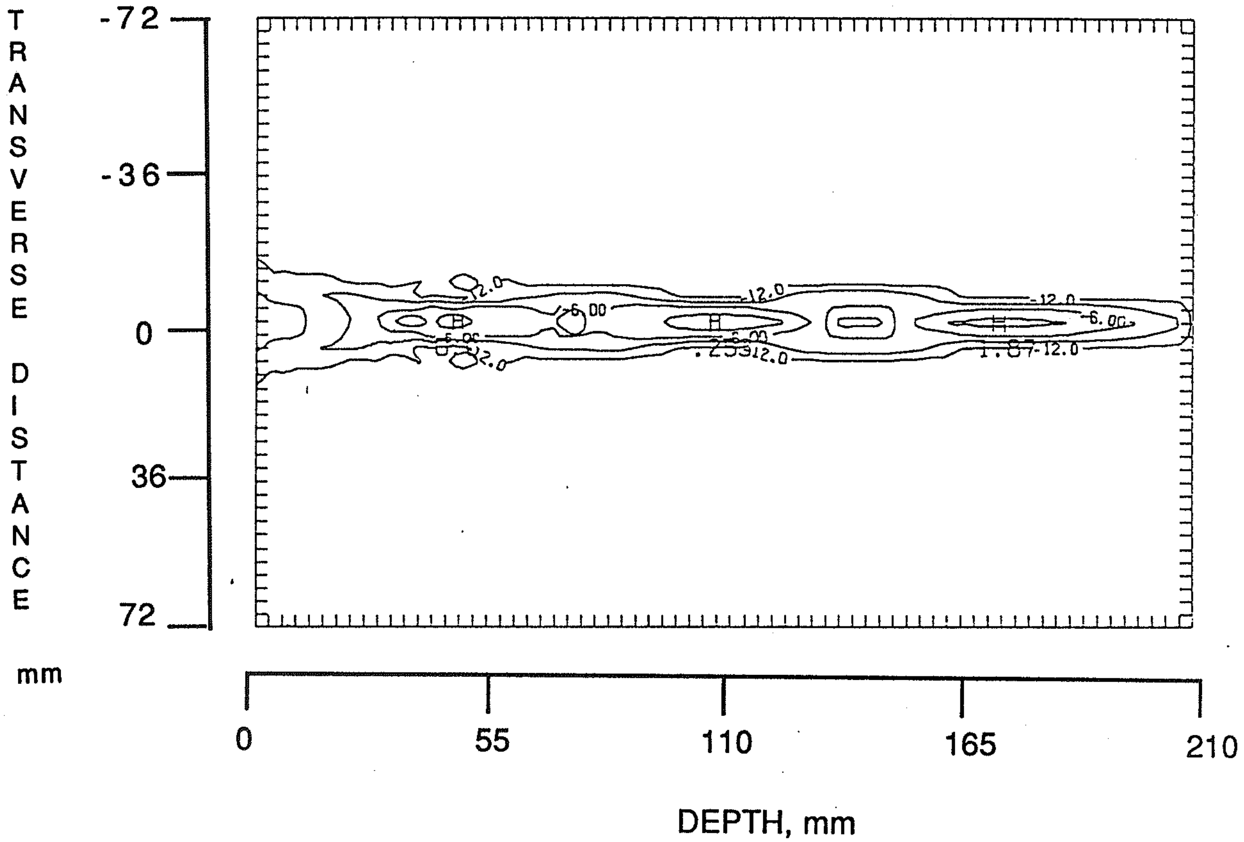

Figure 3.12. Multiple foci along the CRA axis. a) A contour plot of the pattern produced by simultaneously focusing at (0,0,55), (0,0,105), and (0,0,160) along the array axis. All intensities are normalized to that of the focus and contours are given at levels of 3 dB.

The synthesis of multiple annular rings is also demonstrated. Figures 3.13a) and b) illustrate the pattern obtained in the focal plane(z= 80 mm) from the synthesis of two annular rings and three annular rings, respectively.

Because of the circular symmetry of the assumed source, a high intensity region is produced on the main axis in the proximity of the transducer. This results from the constructive interference of the acoustic waves when interfering on the main axis. In fact, because of the symmetry of the applicator and that of the assumed source, acoustic waves interfer on the main axis with the same phase. Figure 3.14 is an illustration of the axial intensity resulting from the synthesis of a 40 mm radius ring at 80 mm depth. All intensities are normalized to that of the focus and then converted to the dB scale. It is noticed that the high intensity on the main axis exceeds the focal intensity and, hence, needs to be considered when using the FCM.

By using simple geometrical considerations, the formation of the sharp intensity and its extension on the main axis can be predicted. Figure 3.15 is a cross section of the CRA and the assumed annular source in the focal plane. By tracing only the acoustic rays emanating from the outermost and innermost elements to the opposite side of the assumed source, it can be noticed that the rays will consolidate along the segment BC on the main axis. An approximation of this extension can be computed easily by comparing the triangles ABC and DEC; therefore

$$\frac{r}{R}=\frac{F-d}{d} \tag{3.4}$$

$$d=\frac{R}{R+r}F \tag{3.5}$$

where r, R, d, and F are the synthesized annular ring radius, the applicator radius, the extension of the high intensity over the main axis, and the focal depth, respectively.

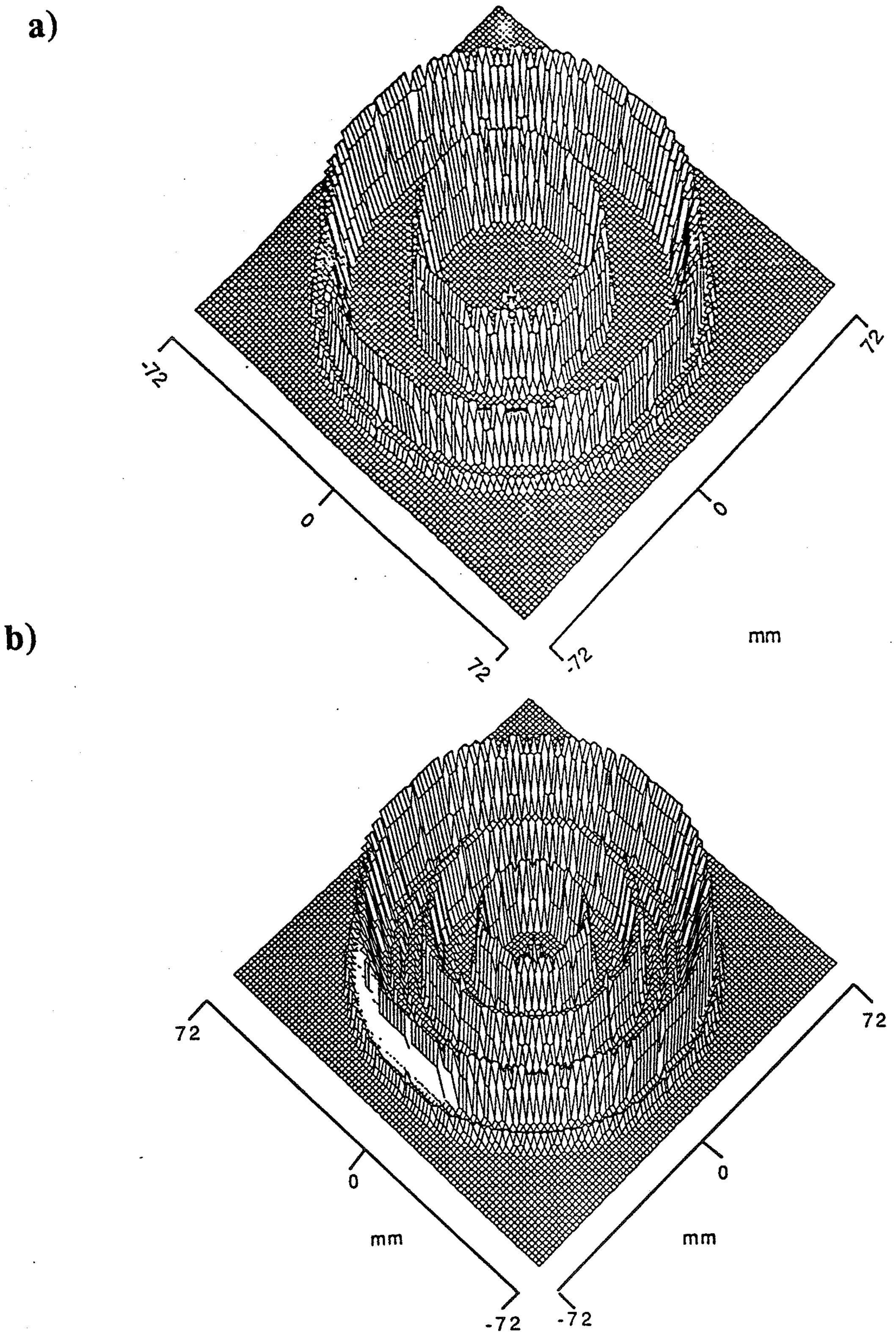

Figure 3.13. Multiple foci synthesis. a) A surface plot of two concentric annular foci of radii 30 and 45 mm, respectively. b) A surface plot of three concentric annular foci of 20,30, and 45 mm radii at 80 mm depth.

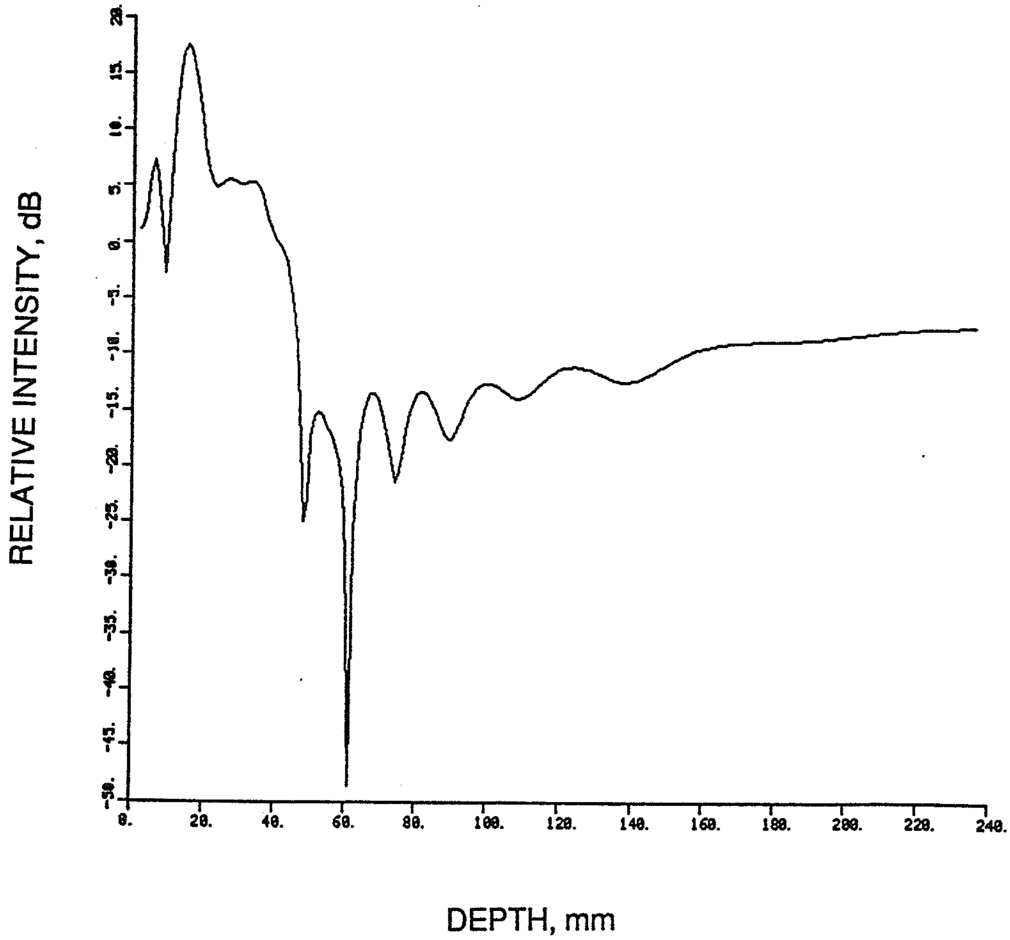

Figure 3.14. A plot of the relative intensity versus z (depth) . All intensities are normalized to the intensity evaluated at the focal site.

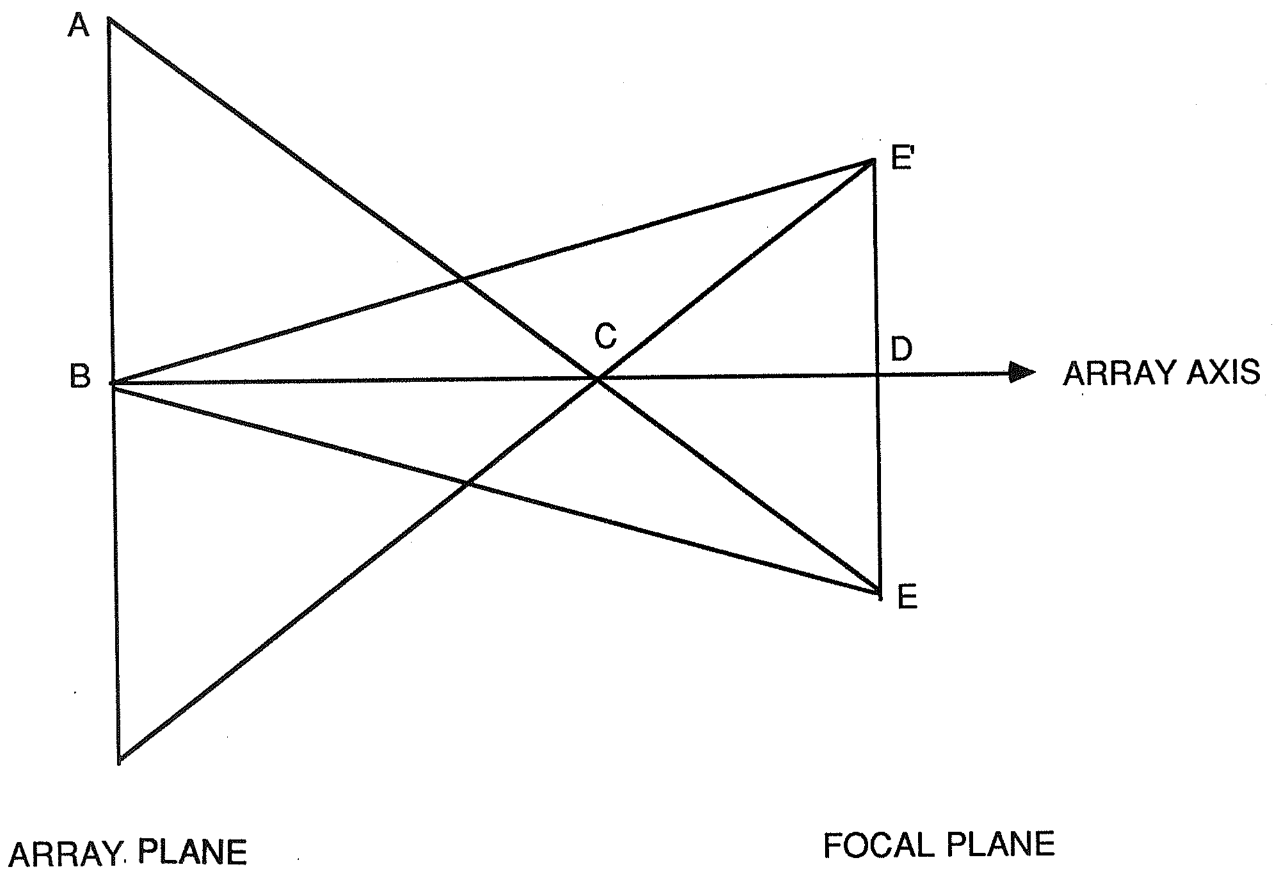

Figure 3.15. A schematic of a cross sectional view of the position of an assumed source, for the synthesis of an annular pattern via the FCM, with respect to the array.

This simple calculation indicates that the sound interference will cause a high intensity region on the main axis extending between the transducer and the point C as shown in Figure 3.15. Equation (3.5) shows that the radius of the focal ring needs to be at least equal to that of the applicator to limit the high intensity extension (on the main axis) to approximately half of the focal depth. However, the radius of the focal ring needs to be smaller than that of the applicator in order to obtain a reasonable gain at the focal site and, consequently, the undesired high intensity region will always extend to more than half of the focal depth.

This problem can be partially resolved by cooling the surface of the skin of the treated volume or by using a suitable bolus to contain the high intensity extension out of the patient body. However, the latter solution tends to limit the usable focal depth to a fraction of the designed one.

A more efficient solution is to create another pattern such that the interference of the two patterns is destructive at least over some part of the main axis. This can be produced by synthesizing an annular focal ring of a slightly different diameter and at a very close depth. The excitation signal of the new assumed ring should be identical to that used for the excitation of the original source except for its phase. In fact, if the original ring is excited with a signal $A \exp(j\phi)$, then the new annular source is excited by a signal $A\ e^{j(\phi-\pi)}$.

This procedure is best illustrated by an example. If a focal ring of a 40 mm radius at an 80 mm depth is to be synthesized, the approach consists of thinking of the problem as a multiple foci synthesis of two rings of 40 and 41 mm radius at 80 and 79 mm depth, respectively. The FCM is then applied by assuming two rings of 40 and 41 mm at the appropriate location. These assumed rings are then excited by identical signals except for a phase difference of π (i.e., $A\ e^{j(\phi-\pi)}$). This procedure will lead to destructive interference along a part of the main axis, and the extension of the high intensity axial region is reduced. Figure 3.16a) illustrates the normalized intensity resulting on the primary axis when the outlined procedure is used. It is noticed that the high intensity extension is limited to less

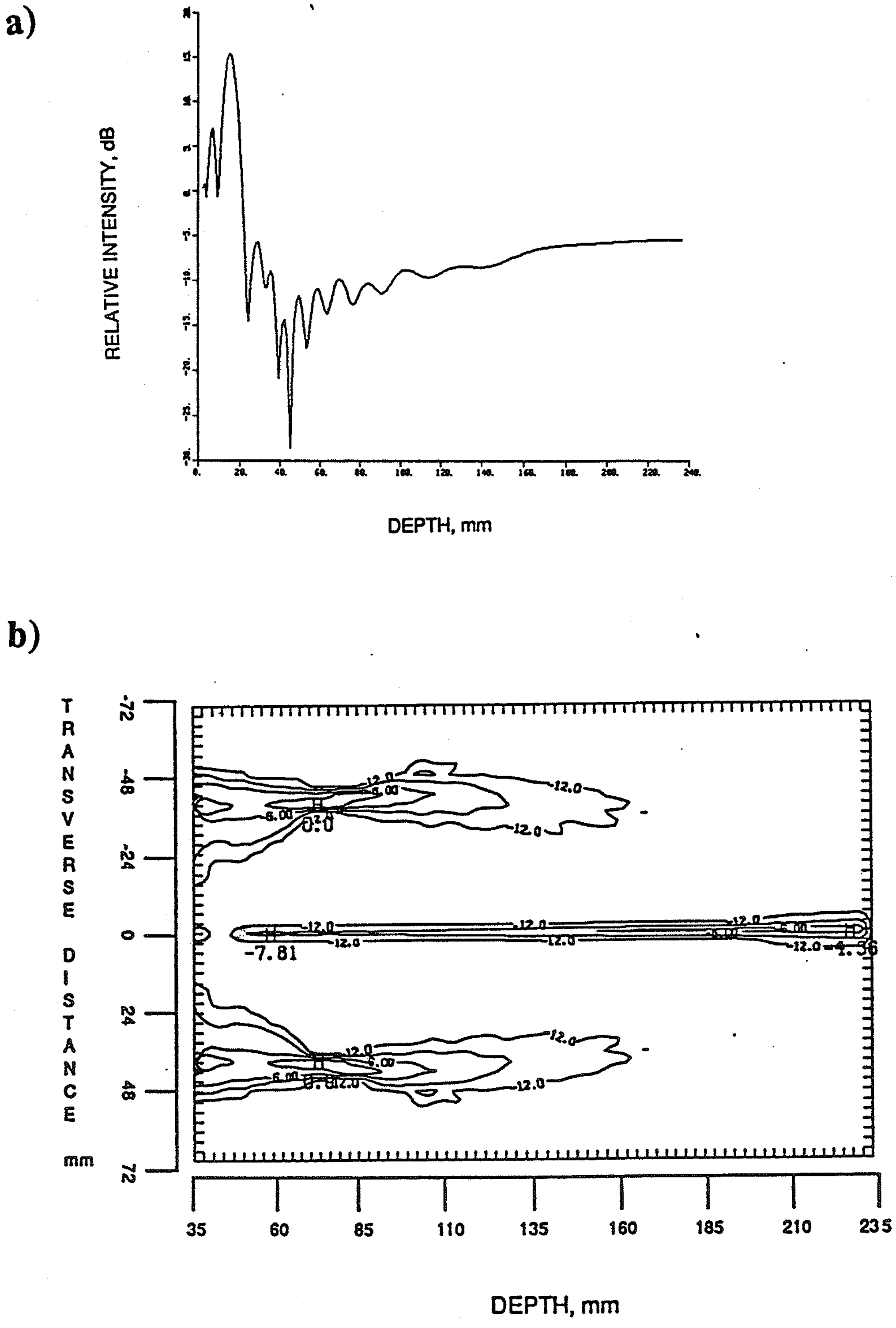

Figure 3.16. a) A plot of relative intensity in dB along the axis as a function of z (depth). Intensity is normalized to the intensity evaluated at the focal site. b) A contour plot of a pattern produced by assuming two "rings" of slightly different sizes with surface velocities 180^0 out of phase. The procedure is used to reduce the intensity of secondary foci along the main axis.

than 2 cm compared to the 5 cm extension obtained earlier (see Figure 3.14). Figure 3.16b) is a contour plot of the resulting heating pattern in the (r,z) plane.

3.4.2 Synthesis of an annular focal pattern using a pseudo-direct approach.

The high intensity extension on the main axis of the array is explained by the interference of the acoustic waves constructively on the main axis. In fact, because of the circular symmetry of the assumed source, the sound beams consolidate along the main axis, and, consequently, a high intensity region results in the proximity of the transducer. However, because of the circular symmetry of the applicator, the array is constrained to produce annular patterns even if the assumption of an annular source is replaced by assuming a point source placed arbitrarily on a point on the periphery of the desired ring. In fact, by assuming a point source placed at a point P on the periphery of the desired annular ring, the FCM is then used to calculate the phase and amplitude of the excitation signal as explained earlier. However, due to the circular geometry of the applicator, the excitation signal will result in an annular heating pattern with the desired radius. The name pseudo-direct is due to the similarity between this method and a direct approach which is frequently used in the literature. The direct approach is summarized in the following paragraphs as a reference.

As proposed in [15,17], the method consists of calculating the phase delay necessary to be applied to each annular element such that the resulting field converges at a point P. As illustrated in Figure 3.17a), the delay is computed by calculating the distances separating point P from the annular elements S_1, S_2,. , S_N which are then divided by the sound velocity in tissues to find the time delay. The result is finally converted to phase delay as follows:

$$\Phi_i = \frac{2\pi f \sqrt{F^2 + (r-id)^2}}{C} \tag{3.6}$$

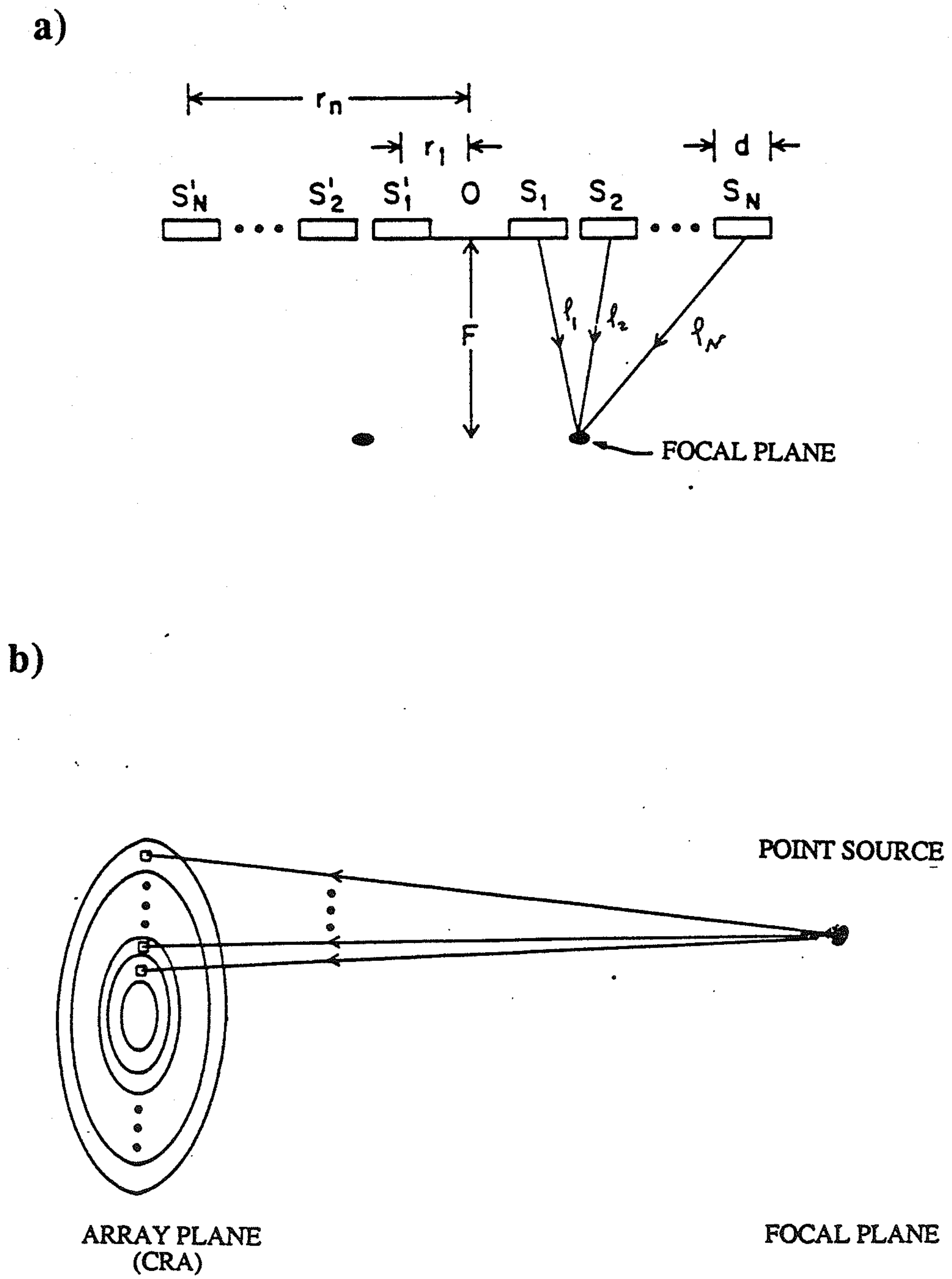

Figure 3.17. A schematic of the pseudo-direct synthesis technique. a) A cross section view and b) a general view of the position of the assumed source with respect to the array.

Once each element is excited with the proper signal, the pattern in the focal plane is an annular ring of radius r (distance separating the point P from the main axis). In the remainder of this chapter, this will be referred to as the direct phasing method.

It is obvious that a slight modification of the FCM, as explained earlier, will lead to heating patterns similar to those obtained by the direct phasing method. The main difference between the original FCM and this procedure is with respect to the assumed source. In fact, while the assumed source in the FCM is an annular ring, the one assumed here is a point source. Figure 3.17b) is a schematic illustration of the array and a point source placed at a point P. The point P is chosen arbitrarily on the periphery of the ring to be synthesized. The effect of this point source is then computed at the center of each annular element of the array. These values are finally conjugated and used as excitation signals to the proper array elements.

The annular patterns obtained using this technique are similar to those obtained by the direct phasing method because both methods assume a point source and neglect the effect of the farthest side of the array. The power deposition pattern of synthesizing a 40 mm radius ring at an 80 mm depth using the pseudo-direct method is illustrated in Figures 3.18. Figure 3.18a) is the surface plot of the heating pattern in six transverse planes including the focal plane at z= 80 mm, while Figure 3.18b) is a contour plot of the pattern obtained in the (r,z) plane. The driving phase and amplitude as calculated by the pseudo-direct method are given in Figure 3.18c).

In summary, the synthesis of annular heating patterns can be achieved using the FCM and the pseudo-direct techniques. An outline of a direct phasing method was then presented. In a later section, the direct and pseudo-direct methods will be compared to the FCM, and advantages and limitations of each will be discussed.

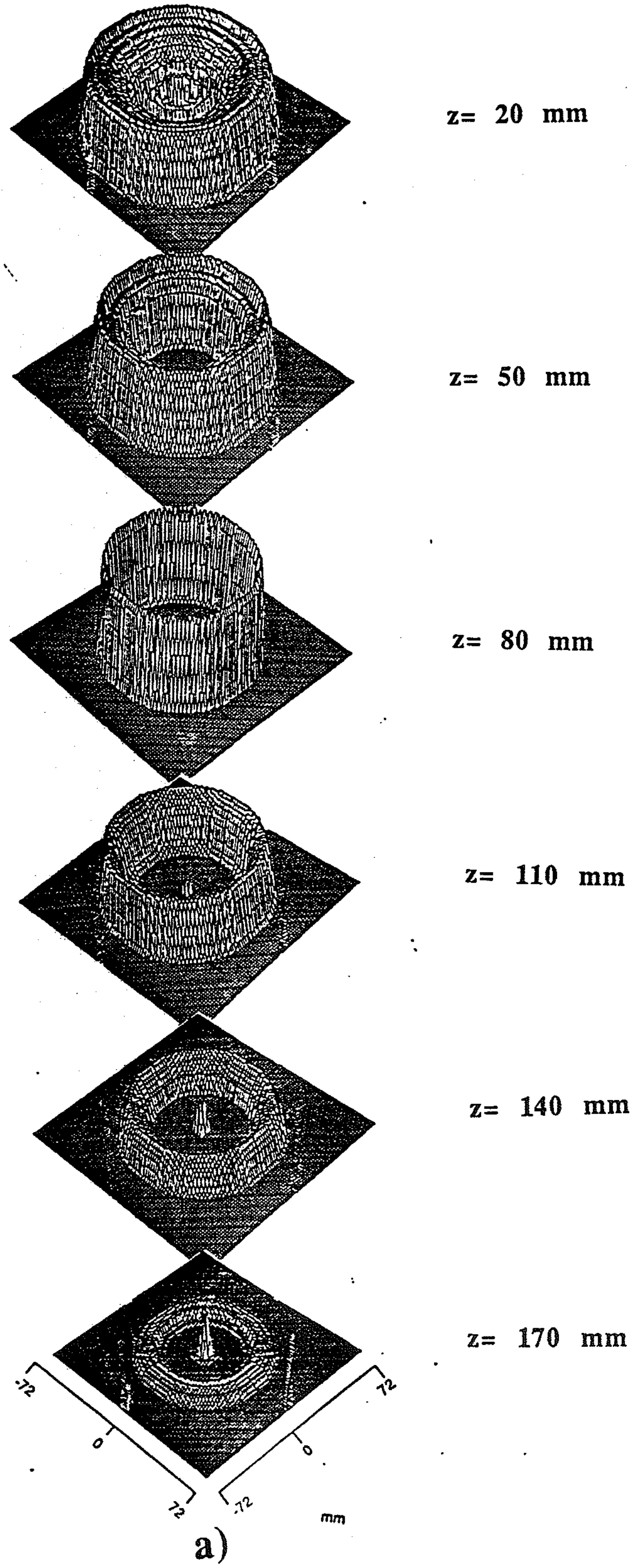

Figure 3.18. a) A surface plot of an annular pattern produced by the pseudo-direct technique . The pattern is of a 40 mm radius at an 80 mm depth. Several transverse planes at different depths are shown.

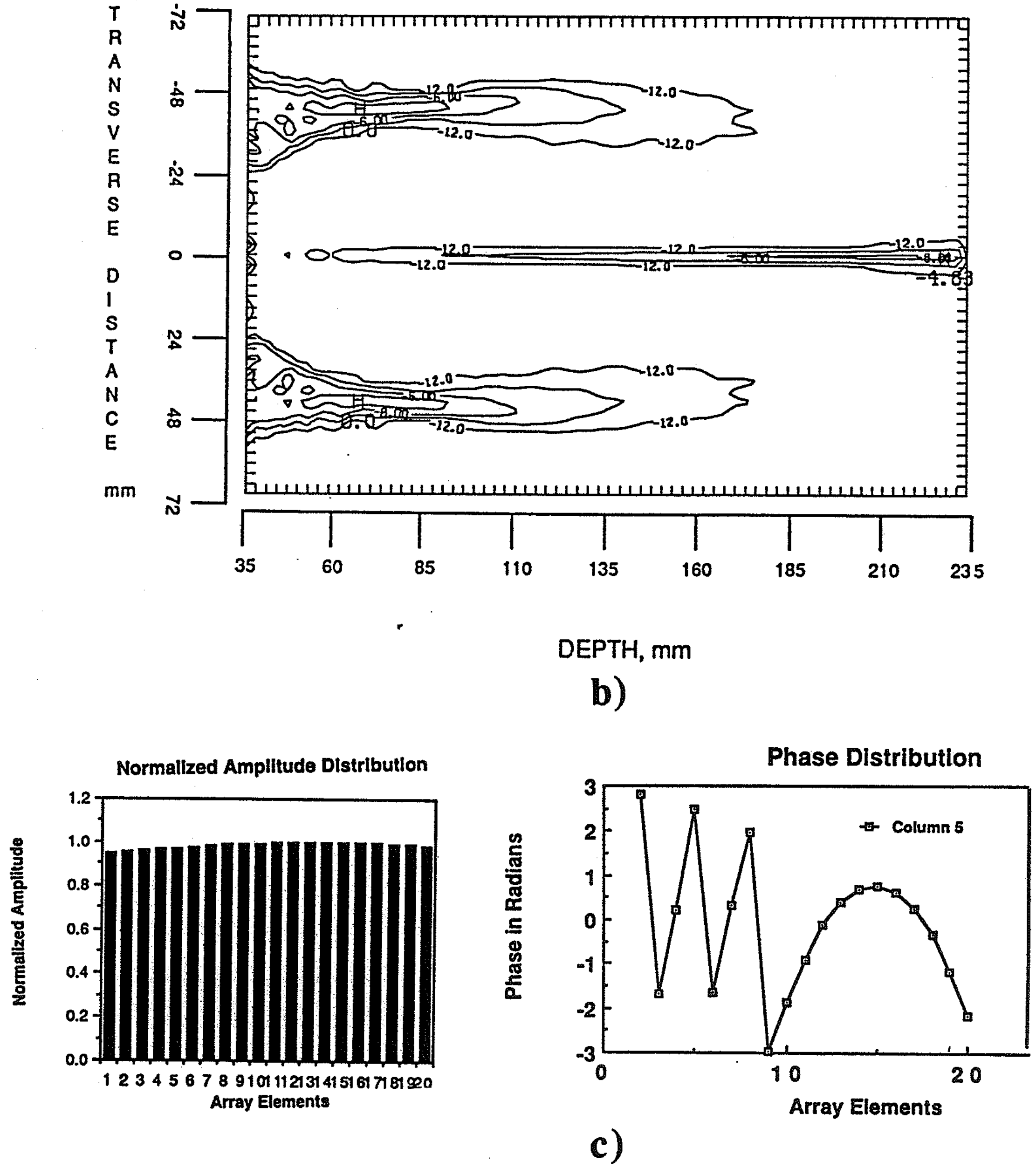

b)

c)

Figure 3.18. b) A contour plot of the pattern of a) in the (r,z) plane. The contours are given at intervals of 3 dB. c) Magnitude and phase distributions of the required excitation signal.

3.5 The Design Parameters

3.5.1 Geometrical considerations

Due to the particular symmetry of the applicator and that of the synthesized patterns (annular rings), we have observed that undesired hot spots (secondary foci) might result on the main axis in some cases. In this section, an attempt is made to understand the origin of these undesirable hot spots and some useful approaches to reduce the effect of such undesired heating are discussed.

When synthesizing annular rings using a CRA, the direct phasing method leads to a secondary focus on the main axis beyond the focal plane. This secondary focus had been observed by Huu and Hartemann [15] and later described by Cain and Umemura [17].

The FCM also leads to a similar secondary focus in some cases, but with a lower intensity than those produced by the direct phasing method. To make a meaningful comparison, the secondary focus intensity was normalized in both cases to the peak intensity produced at the annular focus. The observed difference in the normalized secondary focus intensities between the two methods is due to the amplitude shading of the driving signal required by the FCM and to the nature of the assumed sources.

For the same synthesis parameters (annular ring radius, frequency, depth, etc.), the normalized secondary focus resulting from the application of the FCM is about 4 dB less than that resulting from the direct phasing method. Figure 3.19a) illustrates the heating pattern obtained in the (r,z) plane for the synthesis of a 40 mm radius ring at an 80 mm depth using the FCM, while Figure 3.19b) is the same pattern synthesized using the direct phasing method. It should be noticed that the secondary focus intensity, in Figure 3.19a), is about 8 dB less than that of the annular focus. Figure 3.19b) shows that ,for the same case, the secondary focus intensity produced by the direct phasing method is about 4.5 dB less than that of the annular focus. However, the effect of these secondary focus intensities will be further reduced by blood perfusion in the normal tissues. This issue will be discussed in Chapter 5 when the resulting temperature distributions are calculated.

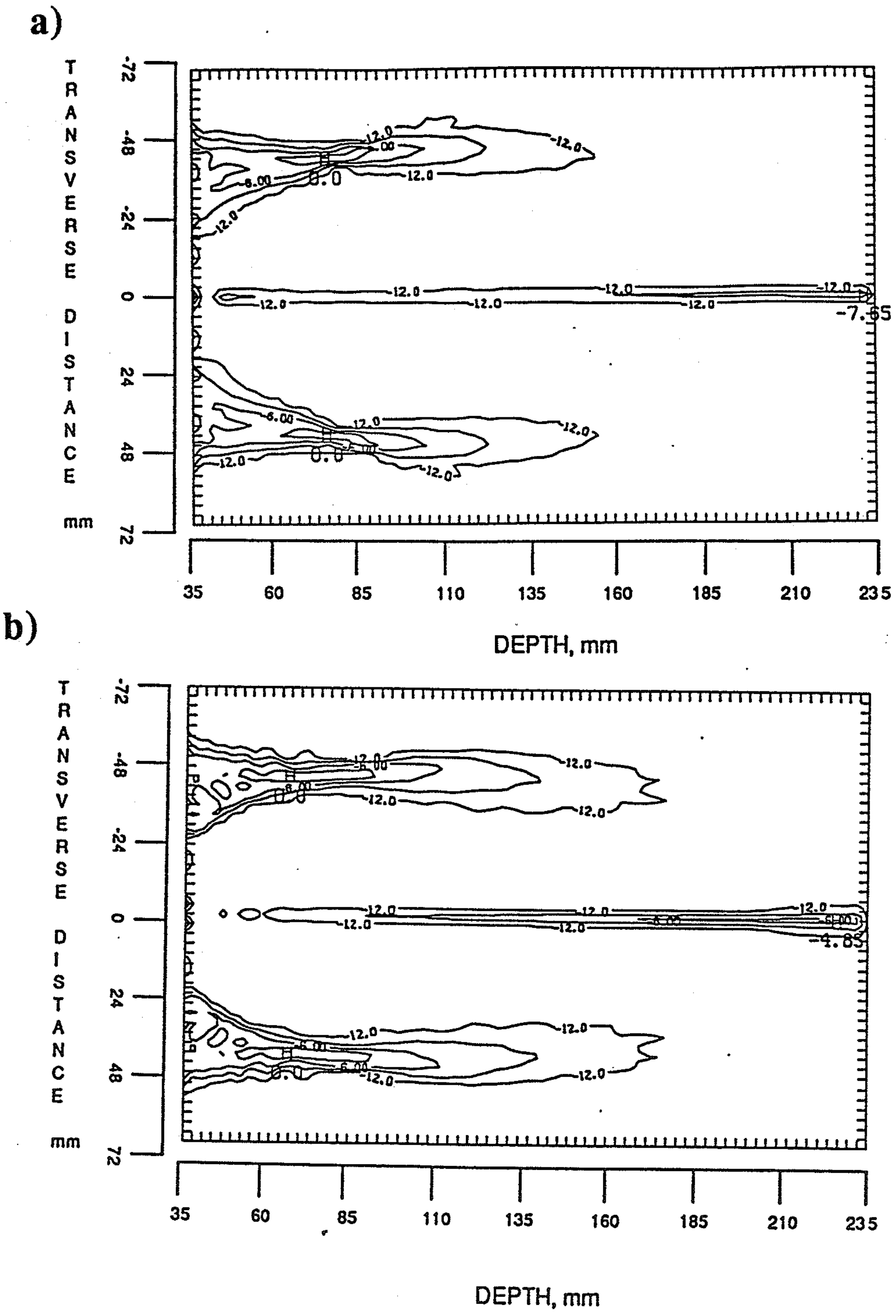

Figure 3.19. Comparison between the FCM and the pseudo-direct method. a) a contour plot in the (r,z) plane of an annular pattern of 40 mm radius at 80 mm depth synthesized by the FCM and b) the same pattern synthesized using the pseudo-direct method.

The problem becomes more serious when the array is used to synthesize annular patterns with smaller diameters. In fact, to avoid significant secondary foci, the radius of the synthesized pattern should be kept larger than that which divides the array surface into two equal areas. This half-area radius R_s is precisely equal to the applicator radius divided by $\sqrt{2}$. This is due to the fact that when the synthesized radius is smaller than R_s, more than half of the applicator energy (extracted energy is proportional to the surface area) will be steered toward the main axis beyond the focal plane, as illustrated in Figure 3.20a). Hence, a strong secondary focus appears at point F' beyond the annular focus.

This interpretation is in accordance with that given by Beard et al. [20]. In fact, when the synthesized radius is less than or equal to R_s, the situation is similar to that which would have resulted from a specially designed lens, illustrated in Figure 3.20b).

For a radius greater than R_s, more than half the energy extracted from the applicator is steered toward the outside of the annular focus as shown in Figure 3.21a). In the latter case, the situation is similar to that which would have resulted from the lens presented in Figure 3.21b).

The effect of the masking procedure proposed in [17], to reduce the secondary focus intensity, is to actually reduce the effective applicator radius to satisfy the requirement that the synthesized radius should be of the order of R_s of the array. More specifically, the direct phasing method was used to synthesize a focal ring of a radius of 30 mm at an 80 mm depth using an applicator of a 60 mm radius [17]. The resulting secondary focus intensity, beyond the focal plane, exceeded that of the annular focus. This result could have been predicted because the synthesized radius is far less than R_s of the applicator (R_s=42 mm). However, the authors proposed to mask the outer 5 annular rings which would reduce the effective applicator radius to 45 mm and, consequently, reduce R_s to 31.8 mm. The contour plot of the pattern obtained by masking the outermost 15 mm width ring, using the direct phasing method, is reproduced and presented in Figure 3.22a). Figure 3.22b) is the pattern obtained using the FCM as a means of synthesis. Figure 3.22a) suggests that while masking reduces

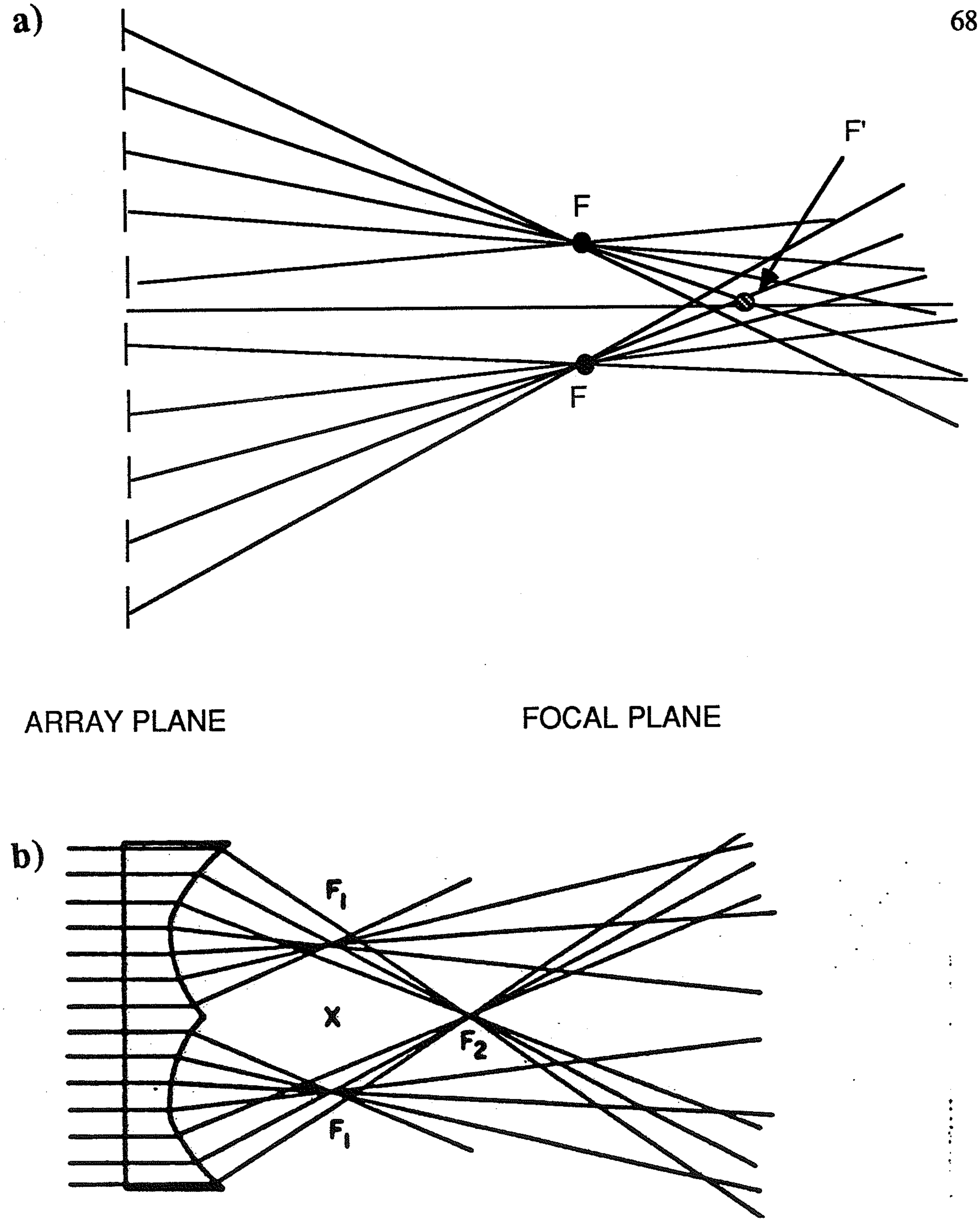

Figure 3.20. a) A schematic of synthesis of an annular pattern of small radius ($R \leq R_s$). A secondary foci is developed at point F'. b) Formation of a secondary foci beyond the focal plane of a specially designed concave lense.

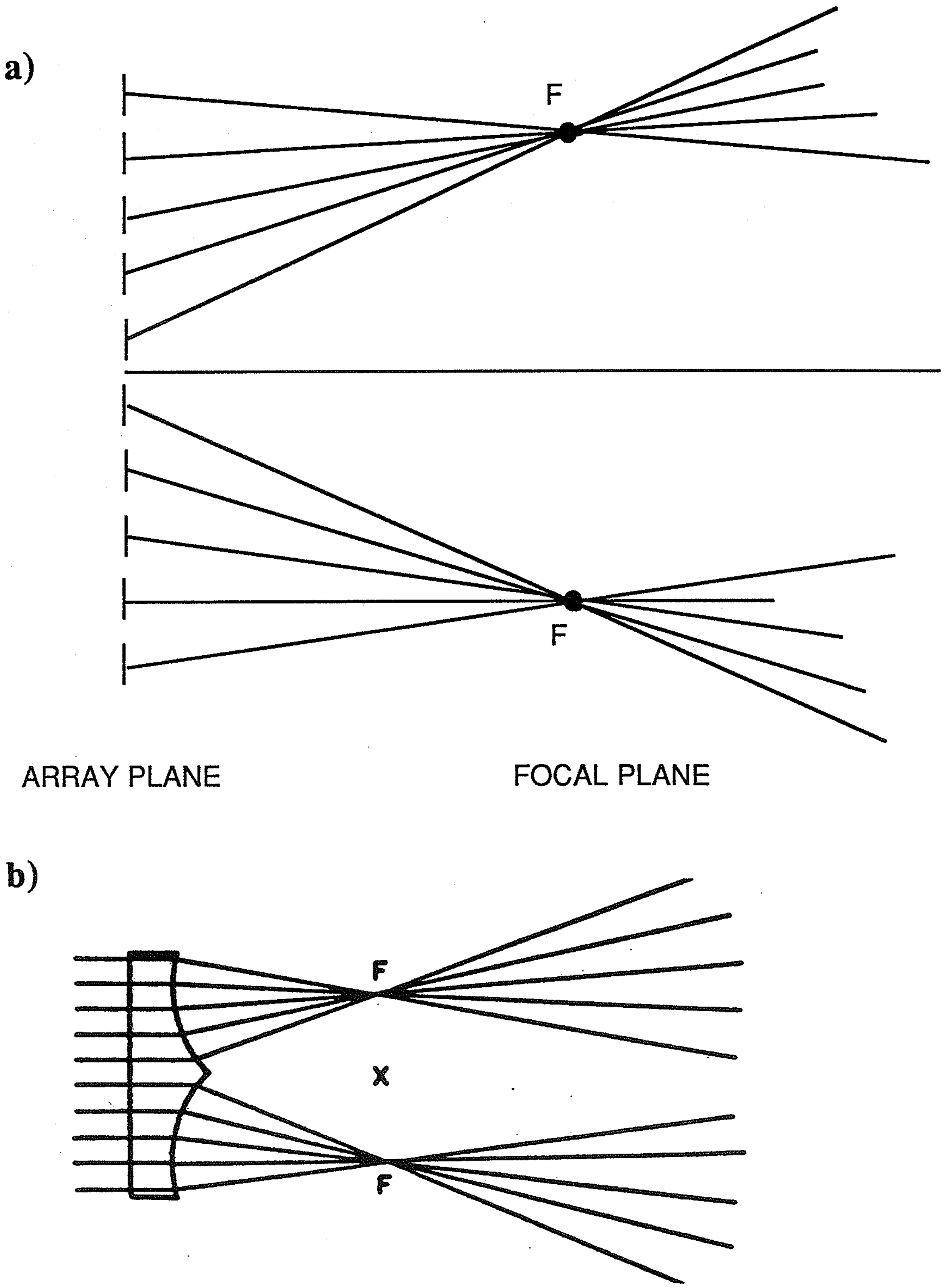

Figure 3.21. a) A schematic of a large size annular pattern synthesis. b) A similar type of pattern produced by a specially designed lense.

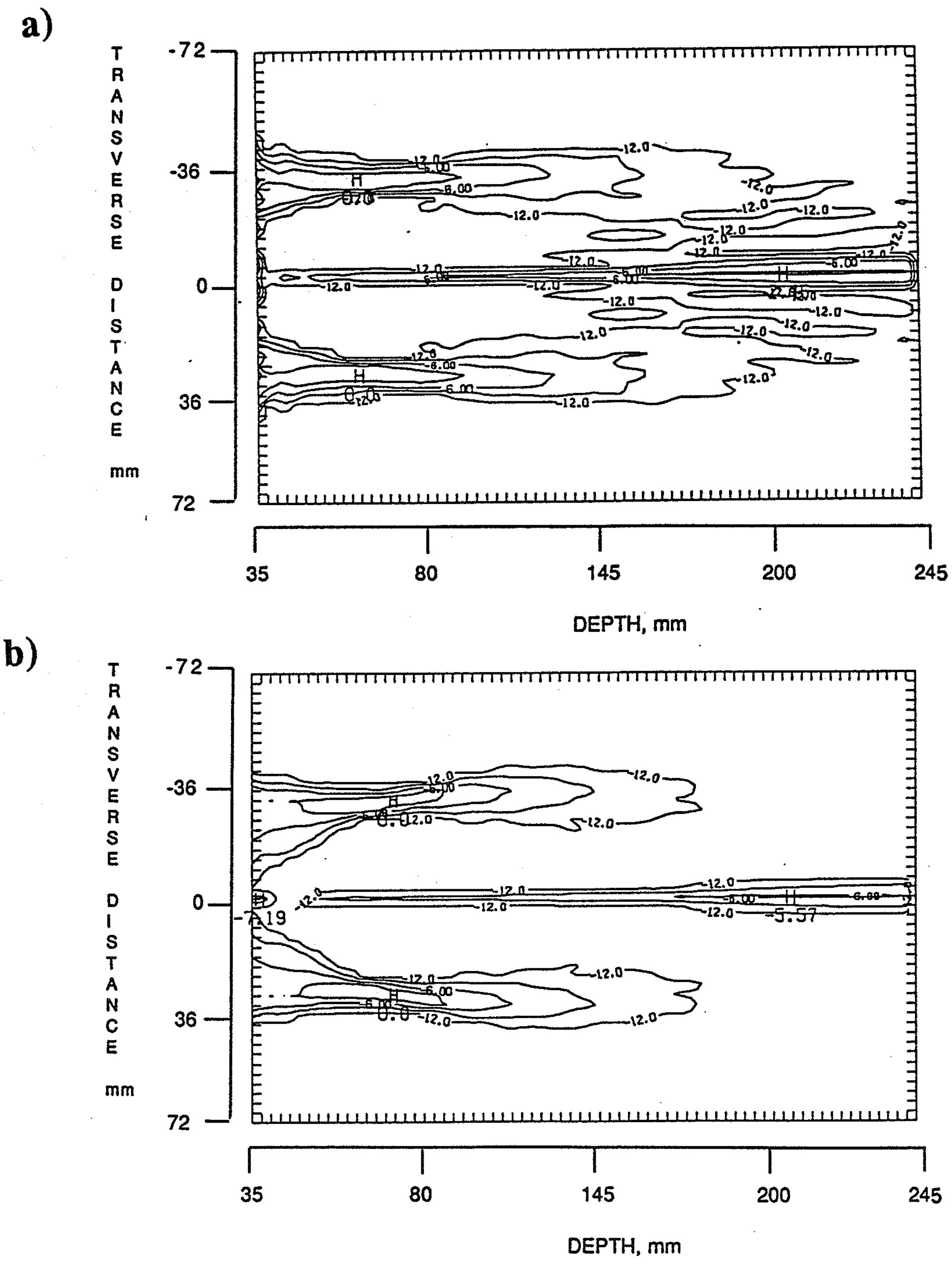

Figure 3.22. Reduction of the secondary foci intensity. a) A contour plot of the synthesis of a 30 mm radius annular pattern at 80 mm depth using the direct method. The secondary foci, beyond the focal plane, intensity was reduced by masking the 5 outer elements as proposed in [17]. b) The same pattern synthesized using the FCM (no masking).

the secondary foci intensity, it also leads to a substantial surface heating and, consequently, cannot be considered an efficient solution.

In conclusion, the preceding analysis suggests that a potential problem might result when synthesizing annular heating patterns of a radius smaller than R_s because of the formation of a secondary focus beyond the focal plane. A higher frequency might be used to reduce the intensity of the secondary focus beyond the focal plane. However, the possible depth of treatment would be shorter due to the attenuation effect.

3.5.2 The driving amplitude control of the annular elements

In general, focusing is achieved by exciting each element of a phased array by an appropriate signal. The excitation signal is established by calculating the length of the path separating the center of each element from the desired focus location. This length is then divided by the sound velocity in tissue, and the resulting time delay is converted to the necessary phase delay for each element. However, the FCM establishes not only the necessary phase delay but also the amplitude of the signal needed for each array element. The requirement of amplitude control, although easy to be implemented electronically, might lower the amount of acoustic power extracted from array, in some cases, to a limit where heating the tumor might become difficult, if not impossible.

To illustrate the problem of amplitude control, a heating pattern is generated by assuming an annular focal ring of a 40 mm radius at an 80 mm depth from the surface of the CRA. For this example, the width of the assumed ring is taken to be 1 mm.

The amplitude of the required signal is illustrated in Figure 3.23a). The required driving phase is shown in Figure 3.23b) which suggests that while some annular elements are driven with relatively high amplitude signals (e.g., 4, 5, 6), others are excited with very small amplitude signals (e.g., 2, 8, 12, 15, 18, 20). This observation means that some elements are delivering their maximum power while others are merely supplying a fraction of

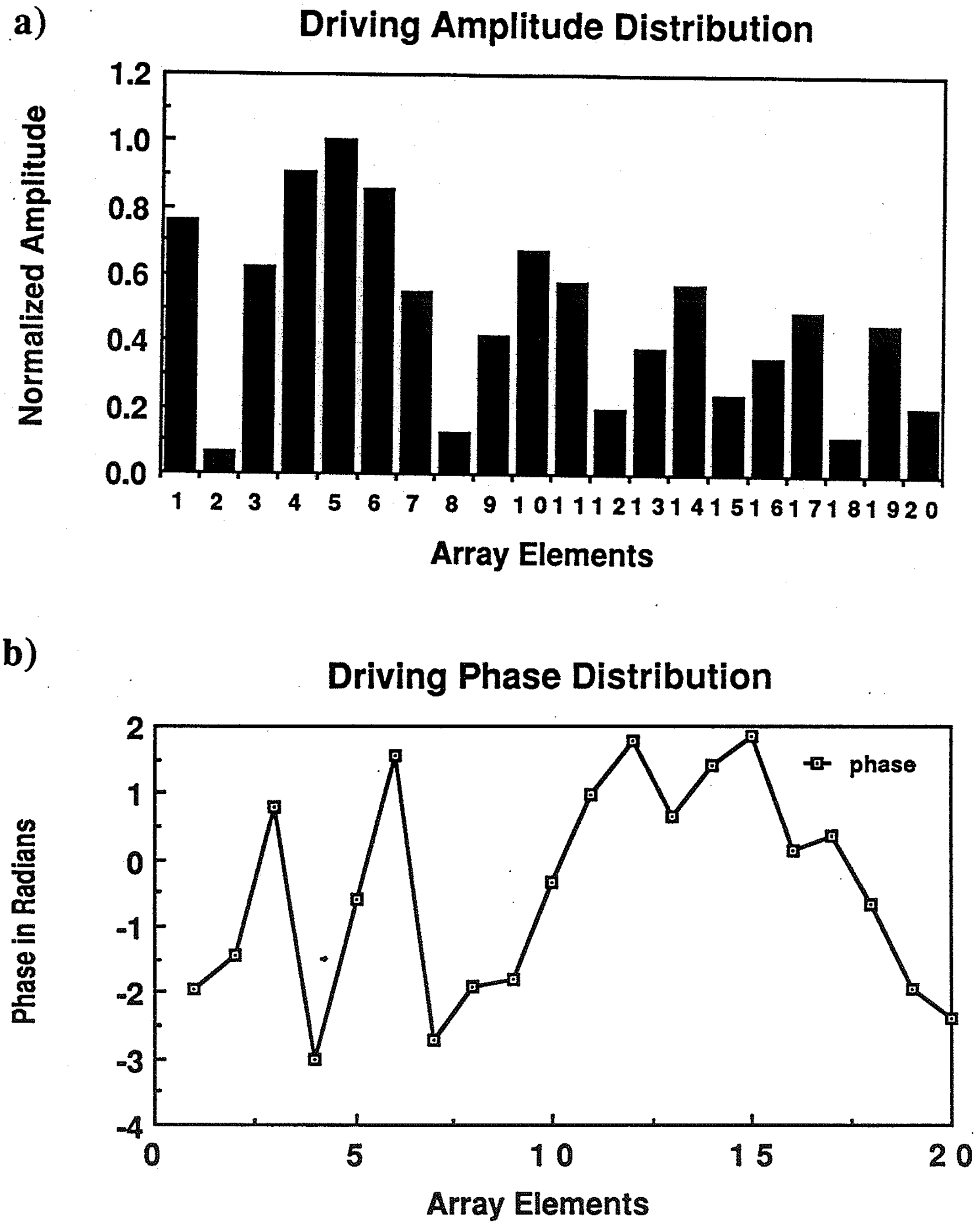

Figure 3.23. Phase and amplitude distributions of the driving signal as required by the FCM. a) The normalized amplitude distribution and b) phase distribution. The assumed source is an annular ring of 40 mm at 80 mm depth.

it. The amplitude of the excitation signals, established by the FCM, needs to be optimized in order to allow the array elements to deliver enough power to induce therapeutic heating.

The amplitude of the driving signal depends on many factors, among which are tumor size, depth, the number of synthesized rings, and the width of the focal ring. It is then necessary to define a standard quantity to enable the therapist to judge how efficiently the array is excited and to estimate the maximum amount of power that can be extracted from the array for a given signal amplitude distribution.

Intuitively, such a standard quantity should take into account the power delivered by every annular element, for a given magnitude distribution, to that which would have resulted if the elements were uniformly driven to deliver their maximum power. However, because the surface areas of the annular elements are different, an averaging procedure over the applicator surface is necessary. We will call such a standard quantity "the amplitude shading factor" and define it as follows:

$$\varepsilon = 1 - \frac{\sum_{i=1}^{N} (A_i)^2 S_i}{A^2 S} \qquad (3.7)$$

In the above equation, A_i and S_i are the amplitude of the driving signal of element i and its surface area, respectively. Also, A is the maximum excitation magnitude allowed by the ceramics and S is the total effective surface of the applicator. It is to be emphasized that for a fixed driving amplitude excitation (A_i=A=constant and $\sum_{i=1}^{N} S_i = S$), the amplitude shading factor as calculated by Eq. (3.7) is zero .

The amplitude shading factor is an important quantity in determining the gain of the array as will be discussed in Section 3.5.4. Simulations show that, for a specified treatment depth and tumor diameter, an optimum value of the amplitude shading factor can be obtained by adjusting the width of the assumed focal ring. To illustrate this point, a focal ring of a 30 mm radius at an 80 mm depth was synthesized for different widths of fictitious annular sources. The width of the assumed ring was varied from 2 to 15 mm and the driving amplitude was calculated. Figure 3.24 illustrates the driving amplitude for each width. The amplitude shading coefficient is then calculated and given below:

Ring width in mm	Amplitude Shading
1	0.84
2	0.83
4	0.65
5	0.37
7.5	0.47
10	0.54
12	0.58
15	0.63
18	0.66
20	0.70

3.5.3 Choice of the annular ring width

In the previous section, it was shown that an optimum amplitude shading factor can be obtained by choosing the appropriate width of the assumed focal ring. Unfortunately, the amplitude shading factor is only one factor among many others that need to be considered in synthesizing an optimum heating pattern. Among those factors are the length of the focal region (depth of field), the intensity of the undesired hot spot (secondary foci) beyond the focal plane, and the high intensity region which appears on the main axis near the transducer. These different factors need to be considered when choosing the width of the assumed annular ring.

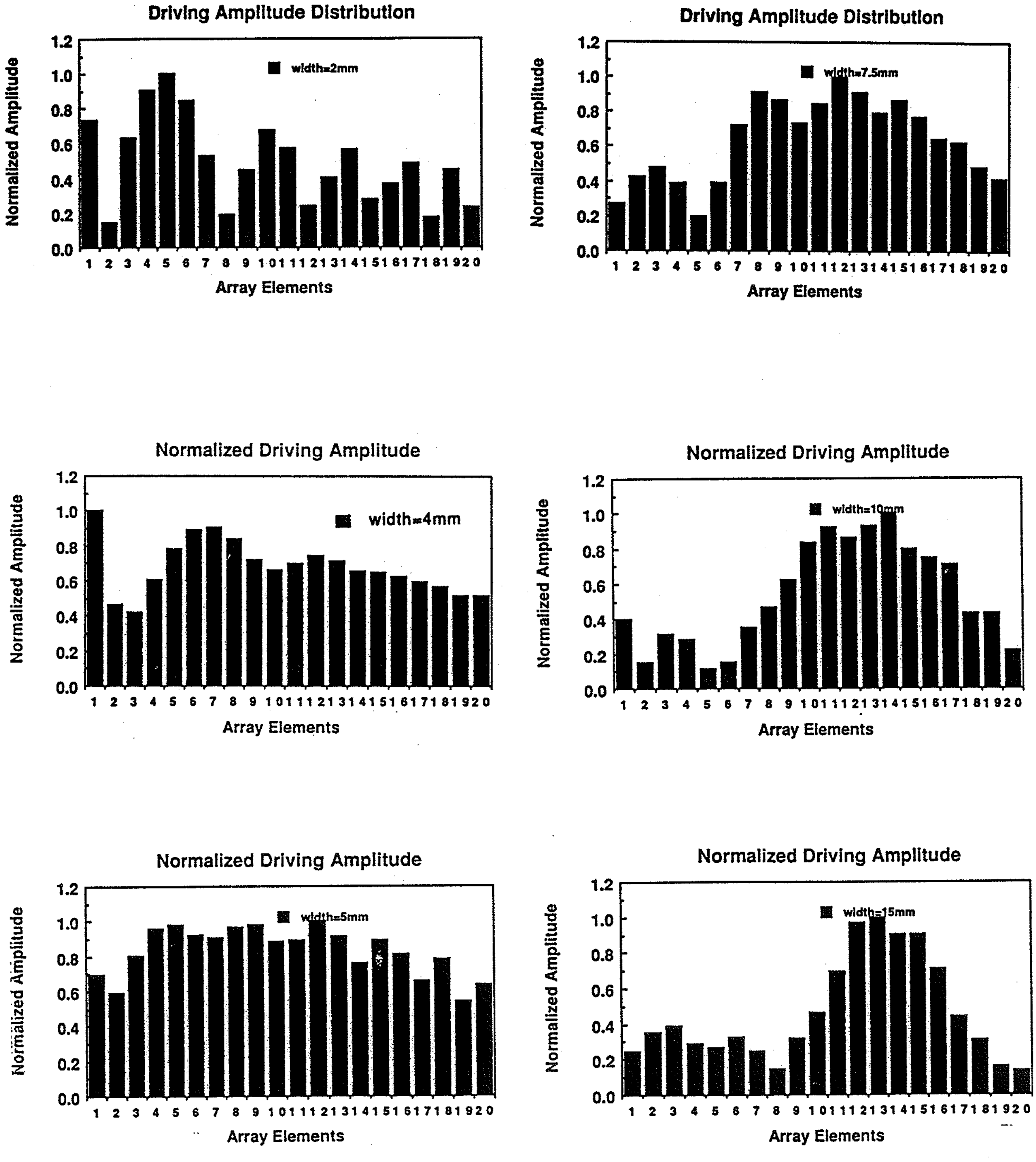

Figure 3.24. The normalized amplitude distribution as a function of the assumed annular source width. A 40 mm radius annular ring was assumed at 80 mm depth. The ring width was varied while keeping all other parameters fixed.

As demonstrated in Section 3.5.2, the choice of a 1 mm width annular ring of a 40 mm radius had led to a very high amplitude shading factor, which would limit the power output of the array to a small fraction of its maximum power output. On the other hand, when assuming annular rings with large widths (> 3λ), a substantial surface heating results, as demonstrated in Figures 3.25a) and b). Figure 3.25 is a contour plot of the pattern obtained from an attempt to synthesize a ring of 12 and 30 mm width, respectively. It is then necessary to determine an optimal range of focal widths which will maximize the power deposition at the tumor site without excessive surface heating while, at the same time, minimize the undesired hot-spot intensities. Moreover, the optimal focal width should result in a minimum amplitude shading factor in order to achieve therapeutic heating.

Simulations are conducted to solve this optimization problem with multiple constraints. Figure 3.26 illustrates the focal patterns obtained for annular ring widths ranging from 0.3 to 10λ (λ is the wavelength) at an operating frequency of 500 kHz. The synthesized annular ring is of a 30 mm radius at an 80 mm depth. Figure 3.27 is the surface plot of the pattern obtained when a full disk shaped source, of 60 mm radius, is assumed in the focal plane.

Although well behaved focal patterns result for all different widths, including the full disk shaped one, the corresponding contour plots in the longitudinal plane (r,z) suggest that surface heating occurs for a large width (> 3λ) as illustrated in Figure 3.25. Moreover, the driving amplitude control associated with thin rings (< λ) results in a high shading coefficient (see Section 3.4.2). Furthermore, a lower secondary focus intensity, when compared to that of the annular focus, results for annular sources with larger widths. This reduction of the secondary focus intensity is due to the splitting of the focused energy over a wider surface in the focal plane and consequently, the secondary focus (beyond the focal plane) is smoothed out.

In conclusion, the width of the assumed annular ring should not be very large in order to avoid surface heating. However, a very thin annular ring results in a high amplitude

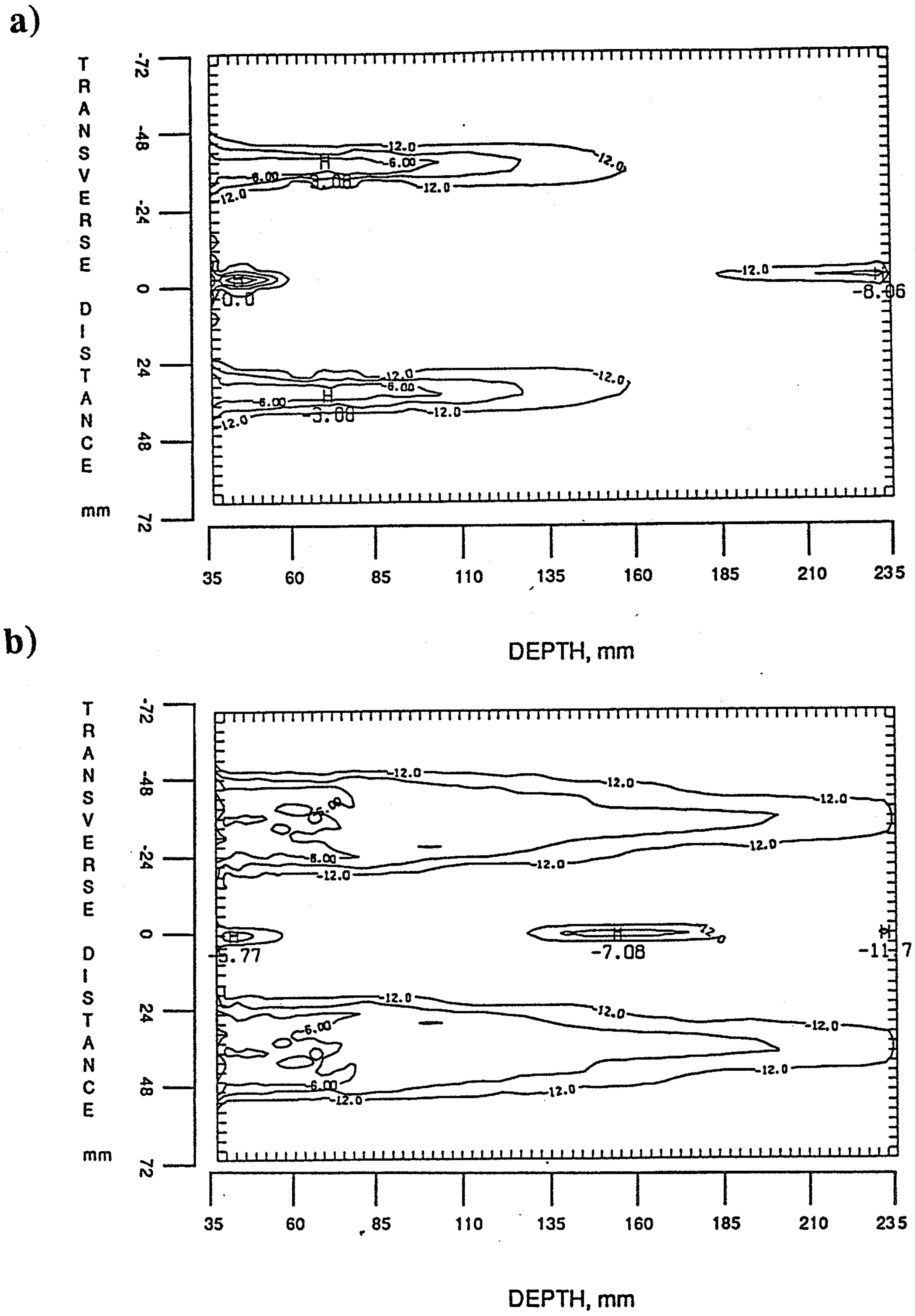

Figure 3.25. Surface heating resulting from large width annular rings. a) A contour plot of the pattern resulting when assuming a "ring" of 12 mm width in the focal plane (z= 80 mm) and b) resulting from assuming a 30 mm width annular source at 80 mm from the array surface.

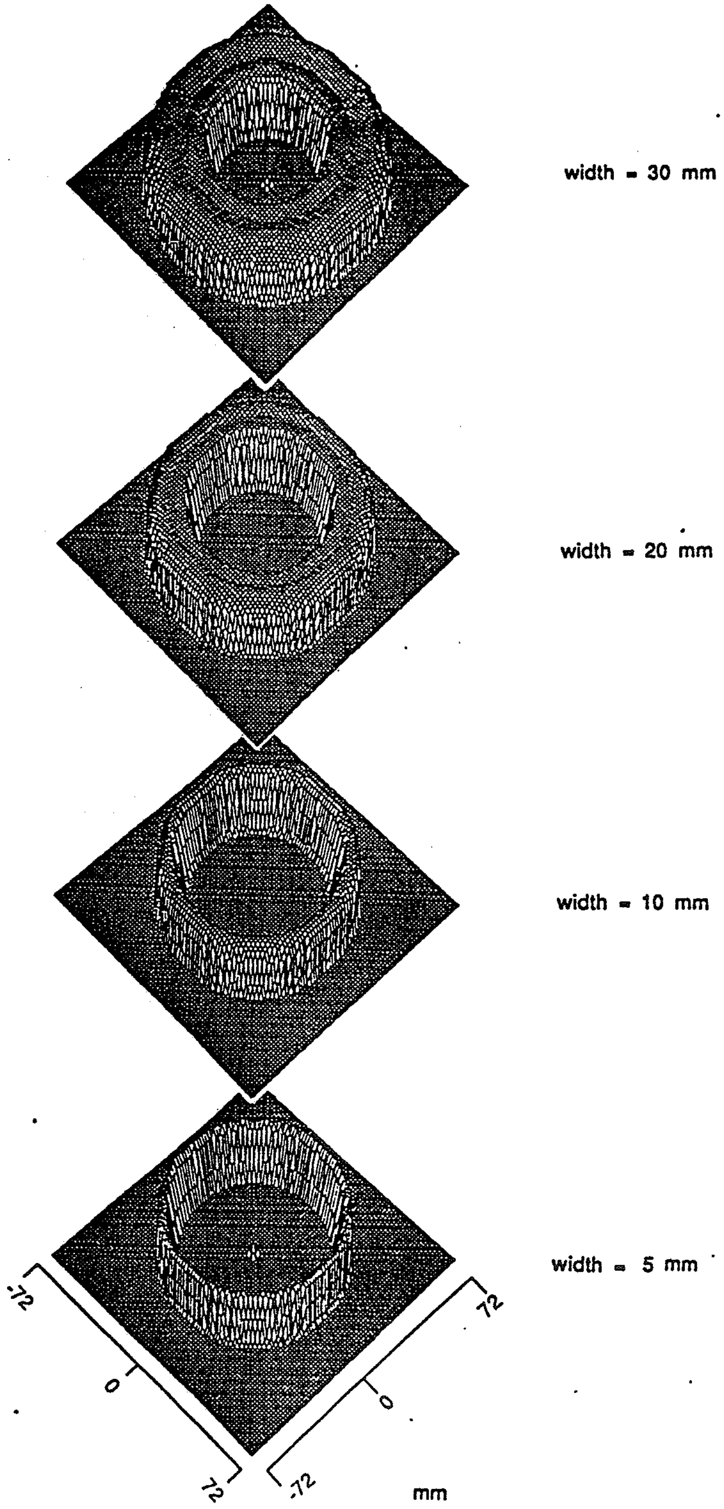

Figure 3.26. A surface plot of the the focal pattern (z=80) of a 30 mm radius annular ring synthesized using different width sources. Pattern resulting from 5, 10, 20, and 30 mm width rings are illustrated.

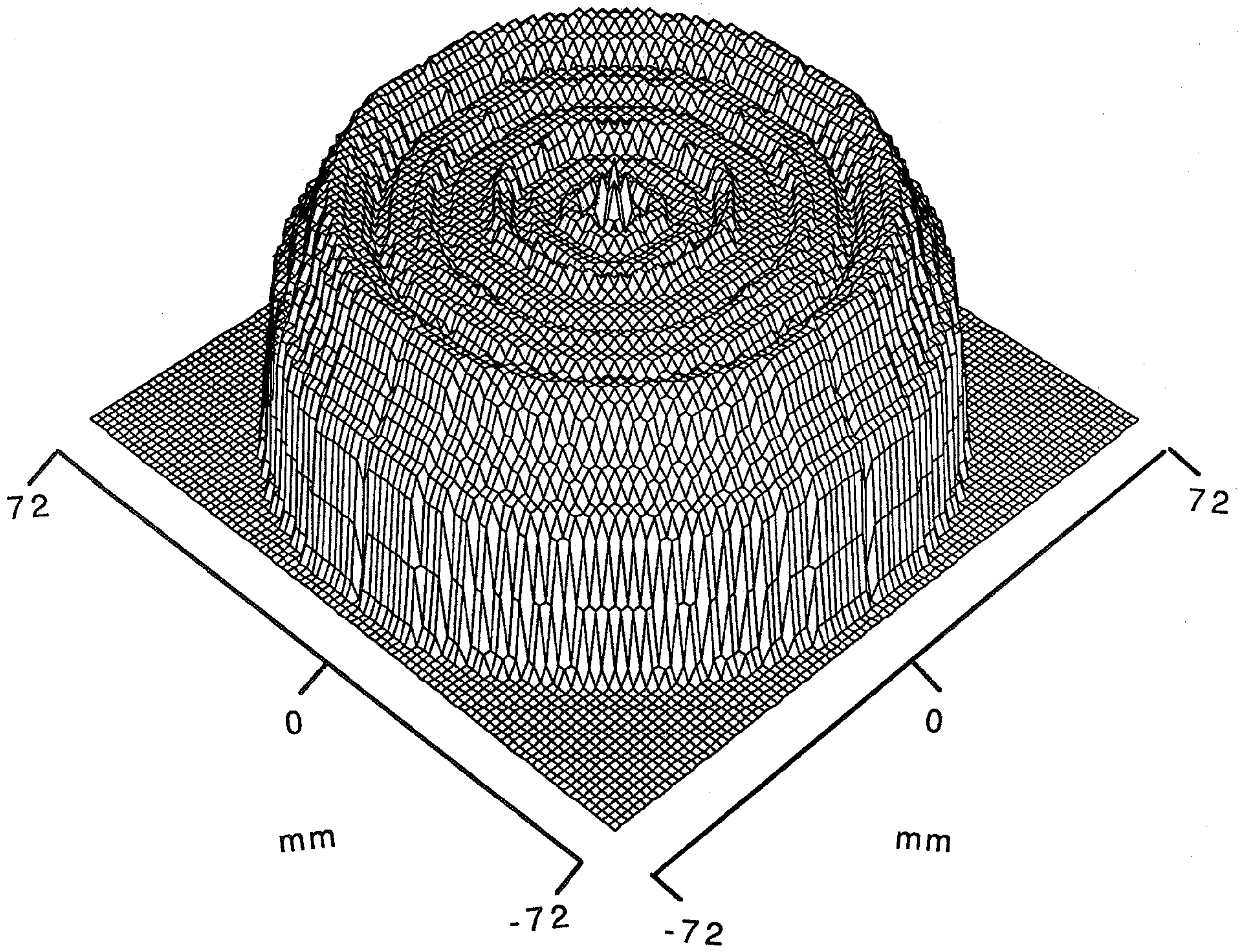

Figure 3. 27. A surface plot of the focal intensity profile (z=80) of a complete disk-shaped pattern. The pattern was synthesized by assuming a 60 mm radius disk (same size as the applicator) at 80 mm distance from the array surface.

shading coefficient and, consequently, a poor maximum extracted power. Simulations demonstrate that, for the synthesized focal depth and pattern radius, an optimum pattern was obtained for an annular source of a 5 mm width. It is necessary to conduct a similar series of simulations, for each case of synthesis, to determine the optimum width to be considered as this width depends necessarily on the synthesis parameters.

3.5.4 Array Gain

The intensity gain is defined as the ratio of the peak intensity at the focal site to that at the applicator surface (or at the skin surface). For a plane wave, this can be expressed as

$$G = \frac{I_z}{I_0} = e^{-2\alpha z} \tag{3.8}$$

where I_z and I_0 are the acoustic intensities evaluated at the tumor site and at the applicator surface respectively, α is the attenuation factor in NP/cm/MHz and z is the treatment depth in centimeters.

It is obvious that the value of G in Eq. (3.8) can only decrease exponentially for increasing depth. Moreover, its value is equal to unity at the surface $z= 0$ and less than unity for $z>0$ and, consequently, no gain is achieved by using plane waves. However, gain at depth can be achieved using focused transducers. For a focused transducer, the gain is obtained by the reduction of the cross-sectional area traversed by the sound beam [12]. Then Eq. (3.8) can be modified to account for the focusing effect as follows:

$$G = \frac{I_z}{I_0}\left(\frac{A_s}{A_t}\right) \tag{3.9}$$

where G is the intensity gain, A_s and A_t are the cross-sectional areas traversed by the sound beam at the skin surface and at the tumor site, respectively.

Equation (3.9) assumes that the effective surface of the applicator is driven by a constant amplitude control, which is not a valid assumption for the synthesis using the FCM.

This is due to the driving amplitude control required by the method. Hence, Eq. (3.9) needs to be modified to account for the amplitude shading factor. This is done as follows:

$$G = \frac{A_s}{A_t}(1-\varepsilon)\, e^{-2\alpha z} \tag{3.10}$$

It is obvious that for a fixed amplitude signal, Eq. (3.10) is reduced to Eq. (3.9), as expected ($\varepsilon = 0$). The frequency dependence of the gain factor is implicit and can appear by using

$$\alpha = \alpha_0 f \tag{3.11}$$

Equation (3.11) is a linear approximation of the empirical relation $\alpha = \alpha_0 (f)^h$, where α_0 is the attenuation in NP/cm at 1 MHz, f is the frequency in MHz, and h is a real number (h ~(0.8-1.3) for biological tissues) [40].

Finally, by using Eqs. (3.11) and (3.10), one gets

$$G = \frac{A_s}{A_t}(1-\varepsilon)\, e^{-2\alpha_0 f z}$$

and an explicit formula for the CRA gain can be derived by considering simple triangular similarities in Figure 3.28.

$$x = \frac{(F-d)R + r\, d}{F} \tag{3.12}$$

$$A_s = \pi \left[\frac{(F-d)R + r\, d}{F}\right]^2 \tag{3.13}$$

where As is the cross-sectional area traversed by the sound beam at the skin surface. By assuming a synthesized ring of width D, the cross-sectional area of the focal region is

$$\frac{A_s}{A_t} = \left[\frac{(F-d)R + r\, d}{F}\right]^2 \frac{1}{2Dr} \tag{3.14}$$

Using the simple geometrical presentation illustrated in Figure 3.28, an explicit expression for A_s/A_t as a function of the design parameters results. In the geometrical

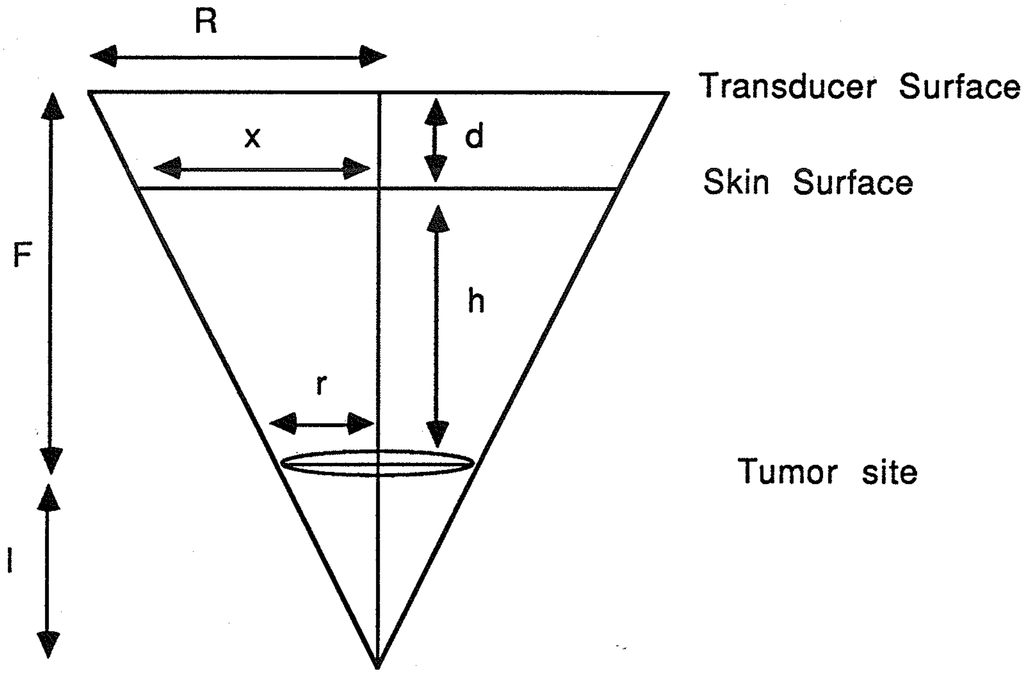

Figure 3.28. Geometry used in the CRA gain calculation.

illustration, R is the CRA radius, r is the tumor cross-sectional radius, d is the coupling medium (bolus) thickness, F is the focal depth, and h is the tumor depth from the skin surface. Finally, the CRA gain can be expressed as

$$G = \left[\frac{(F-d)R+r\,d}{F} \right]^2 \frac{(1-\varepsilon)}{2Dr} e^{-2\alpha_0 f\,(F-d)} \tag{3.15}$$

3.6 Analysis of the FCM : Advantages and Limitations

The ability of the CRA to produce conventional focusing (intense focal spot) on the main axis is well known [15]. Moreover, the ability of this configuration to produce annular heating patterns was investigated in [17]. In both cases, the synthesis method (referred to as the direct phasing method) consisted of establishing the driving phase necessary for each element by directly computing the distance separating the element center from the desired focus.

The field conjugation method, in addition to its ability to produce conventional and annular focusing, offers some unique advantages over the direct phasing method. These advantages include the generation of multiple foci and the production of annular rings with variable widths. Multiple focusing, if used appropriately, can be used to heat the back of the tumor as well as the front by carefully placing the treated volume between two foci. Moreover, focal rings with variable widths can be used to heat tumors with higher blood flow. Furthermore, it has been demonstrated that appropriate widths result in a lower secondary focus intensity compared to those produced by the direct phasing method.

In this section, the FCM is investigated and the characteristics of the conventional and annular heating patterns are compared to those produced by the direct phasing method.

3.6.1 Conventional focusing on the main axis.

By assuming a point source at the desired location on the primary axis, or by considering a small disk shaped source at the desired focal location, the FCM procedure is applied and the phase and amplitude of the driving signal are established.

Figure 3.10 is a contour plot of a conventional focus at a 100 mm depth from the applicator surface. The assumed source is a small disk of a 4 mm diameter placed at z=100 mm on the primary axis.

To investigate the characteristics of simple focusing on the main axis, the resulting focal region (3 dB region) was checked for different design parameters and the results confirmed those published by Huu and Hartemann [15]. Two different sets of simulations were conducted. In the first series of simulations, the F-number (F= focal distance/aperture diameter) was kept constant for different focal depths and the axial and lateral extensions of the focal region were measured. Those extensions were defined as the length and width of the 3 dB region, respectively. To obtain a constant F-number for different focal depths, the effective number of annular rings (effective applicator size) was adjusted to the desired focal depth. The simulation results are given in Table 3.3 for focal depths ranging from 50 to 120 mm and a constant f-number (0.96-1.06). Table 3.3 demonstrates the possibility of heating similar small volumes (~1cm^3) at different depths by varying the number of effective annular rings.

A second series of simulations consisted of varying the F-number while keeping the focal depth constant (z=120 mm). The F-number was varied by adjusting the number of excited annular elements (applicator diameter) for the same focal depth. Table 3.4 illustrates the data obtained for F-number varying from 0.8 to 1.5 for a constant focal depth. Under these conditions, the resulting focal region volumes ranged from 1 to 3 cm^3.

Table 3.3

Focal Region Dimensions for a Fixed F-number

Number of excited electrodes	Focal depth (F_d) in mm	F-Number $F= (F_d/R)$	Depth of field in mm	Lateral width of focal region in mm
8	50	0.96	20.9	3.37
10	60	1.00	23.9	3.38
12	70	1.02	23.1	3.61
13	80	0.97	23.0	3.60
15	90	1.00	24.0	3.62
17	100	1.02	24.0	3.62
18	110	0.97	23.5	3.61
20	120	1.00	24.5	3.6

Table 3.4

Focal Region Dimensions for Different Values of the F-number

Number of exited electrodes	F-Number F=Fd/R	Depth of field in mm	Lateral width of focal region in mm
20	1.00	24.5	3.66
18	1.10	31.5	4.01
16	1.20	32.0	4.20
15	1.3	36.2	4.57
14	1.42	41.3	4.75
13	1.53	44.5	4.83

Multiple focusing can also be produced by assuming point sources (or small disks) at the desired locations along the main axis. Elongated focal regions can be produced to accommodate special tumor geometries (see Section 3.4.1). In addition, heating the back as well as the front of a small tumor can be synthesized by producing separate foci at different depths as illustrated in Section 3.4.1.

3.6.2 Annular focal patterns.

By assuming an annular-shaped source at the location where an annular focal ring is to be produced, the driving signal needed to excite the different array electrodes can be established using the FCM. The size, width, and depth of the synthesized pattern are governed by those of the assumed source. Two methods of synthesis were discussed in this chapter: the FCM and the pseudo-direct method.

While the pseudo-direct method is somewhat similar to the direct phasing method, the FCM has two advantages over the direct phasing method. The first advantage is a more localized focal region (3 dB region) compared to that obtained by the direct phasing method. This property is the result of the assumption of a full annular ring as a fictitious source, in the focal plane, as compared to that of a point source. More precisely, the direct phasing method considers only the effect of the nearest side of the array to calculate the necessary phasing for each element. However, if the direct phasing method were modified to account for the farthest side of the array, a high intensity region (near the transducer), similar to that observed for the FCM, would have resulted. Figure 3.19a) illustrates the pattern obtained using the FCM to synthesize an annular ring of a 40 mm radius at an 80 mm depth. The extension of the 3 dB region (depth of field) is about 21 mm (7 λ) compared to the 51 mm (17 λ) length obtained by the direct phasing method as illustrated in 3.19b. Figure 3.18b) is the contour plot of the same pattern using the pseudo-direct method. The length of the 3 dB region is about 42 mm, which is twice the length of that produced by the FCM, but still shorter than that produced by the direct approach.

The second advantage is with respect to the hot spot (secondary focus) appearing on the main axis, beyond the focal plane in some cases. The normalized secondary focus produced by the FCM is at least 3.5 dB lower than those produced by the direct or pseudo-direct techniques for the same specifications. Figures 3.19a) and b) illustrate the pattern obtained from the synthesis of a 40 mm radius ring at an 80 mm depth using the FCM and the direct method, respectively. It is demonstrated that while the secondary focus intensity resulting from the FCM is about 7.5 dB less than that of the annular focus, the direct phasing method leads to about a 4.5 dB difference, which might prove inadequate to avoid distal bone heating.

One disadvantage associated with the FCM is the formation of a high intensity extension over a part of the main axis near the transducer. As mentioned earlier, this can be resolved by accounting for the high intensity region to fall within the coupling medium (bolus). However, this solution tends to limit the practical treatment depth to a few centimeters. Another solution consists of substituting the pseudo-direct method for the FCM by to reduce the high intensity extension. Furthermore, it was shown that the synthesis of small diameter annular patterns ($r < R_s$) would produce a strong secondary focus on the axis beyond the focal plane. To overcome these limitations, a method based on the combination of multiple focusing on the main axis with a simple mechanical movement of the applicator is proposed in the following section.

3.7 Simple and Multiple Focusing on the Main Axis Combined with Mechanical Scanning as a Means of Heating Deep Seated Tumors.

3.7.1 Motivation

The CRA configuration, investigated throughout this chapter, is well suited for the production of annular heating patterns. Two methods were proposed to directly synthesize annular foci, the FCM and the pseudo-direct method. The FCM, while capable of producing heating patterns judged as more suitable (secondary focus intensity, depth of field,...,etc.) than those produced by other methods, is limited to the treatment of superficial tumors, as shown earlier. This limitation is due to the formation of a high intensity region prior to the focal plane as demonstrated in Section 3.4.1. In addition, a significant secondary focus might result beyond the focal plane if the direct or the pseudo-direct phasing method is used for the synthesis. This problem is more serious when the synthesis of focal rings of a smaller radius ($r< R_s$) is attempted. The production of annular heating patterns of large diameters ($r > R_s$) might not produce adequate time averaged intensity gain to produce therapeutic heating. In conclusion, annular heating patterns are expected to produce therapeutic effects at shallow depths (up to 5 cm for the applicator considered throughout this chapter).

Focusing on the primary axis results in very localized focal regions at depths ranging from very shallow to extremely deep in the body. In addition, multiple foci at different depths can be produced simultaneously as discussed in Section 3.4.1. However, the resulting focal regions are extremely small and cannot be used to heat even small tumors without some electrical or mechanical manipulation. To resolve this problem, it is proposed to produce a simple (or multiple) focusing on the main axis, and to mechanically scan the resulting focal spot (spots) over a predetermined trajectory. This technique has many advantages over the mechanical scanning of a fixed focus transducer. The advantages include the possibility of easily varying the depth of treatment, the capability of producing multiple focusing on the main axis at different depths which can be scanned simultaneously, and the elimination of any possibility of intervening tissue heating due to the highly localized focal regions produced on the primary axis. These different issues are discussed in detail in the following paragraphs to justify the combination of mechanical and electrical scanning which might appear very unusual.

The depth of the treatment can be adjusted electronically by simply varying the phase of the driving signal. This feature will allow the treatment of tumors at depths ranging from shallow to very deep in the body. This would have to be handled, in the case of a focused transducer, by varying the thickness of the coupling medium (bolus), which would result in a more complicated transducer-patient interface.

Scanning of multiple foci on the main axis leads to unique heating patterns that cannot be obtained by scanning a fixed focus transducer. Among these patterns is heating the back, as well as the front, of a large tumor by simultaneously focusing at two depths and scanning the resulting pattern. This probably would have been achieved, in the case of traditional mechanical scanning, by the use of several transducers (arranged in different planes), which is complex, cumbersome and requires a complicated coupling medium (bolus).

By examining the contour plot of the pattern obtained by focusing at z= 100 mm on the main axis as illustrated in Figure 3.10a), it is clear that the focal region (the 3 dB region) extends to less than 13 mm while the power deposition intensity drops more than 10 dB in less than 5 mm away from this region. This very localized power deposition will allow the scanning of the tumor periphery without the risk of excessively heating the intervening tissues as frequently observed when using large focused transducers.

3.7.2 Method

The method consists of generating a focal spot (or multiple focal spots) along the array axis by electronically adjusting the phase and amplitude distribution to the array elements.This stationary field intensity profile is characterized by its spatial-peak temporal-peak (SPTP) value which coincides with the peak intensity at the focus (foci) when the array is focused at a point (points) along its main axis. However, the SPTP and the peak intensity at the focus could be different for other applications such as annular focusing which might lead, in some cases, to secondary foci with intensities higher than those evaluated at the focal site (i.e., near the transducer surface or far beyond the focal plane) as demonstrated earlier. The SPTP intensity is defined as the absolute maximum field intensity in time and space which might or might not be at the focal site as stated earlier. The stationary field intensity pattern is then scanned mechanically over a desired trajectory (or surface) , i.e., single or multiple concentric rings. The mechanical scanning is assumed to be uniform and fast enough to avoid thermal ripples. The effect of scanning can be simulated by convoluting the stationary field intensity pattern resulting from the electronic focusing with a surface function h(r) as defined in [12],

$$h(r) = \{ 1 \quad \text{for } r \text{ within the surface A and identically zero elsewhere} \tag{3.16}$$

where r is the radial distance from the main axis and A is the surface area of the scanned region, the scanned field intensity that results from scanning the stationary field profile $I_0(r)$ over a surface s is obtained by performing the following convolution integral [12],

$$I(r) = A^{-1} \int_S I_0(r-r')\, h(r')\, d^2r' \tag{3.17}$$

where h(r) is as defined above, s is the scanned surface, and d^2r is an elementary surface over s.

To simulate the mechanical scanning over an annular surface of inner and outer radius r_1 and r_2, respectively, it is only necessary to modify h(r) and S of Eq. (3.17) as follows:

$$h(r) = \{ 1 \qquad r_1 \leq r \leq r_2 \text{ and zero elsewhere} \tag{3.18}$$

with s is now the surface of the annular region and the time-averaged field intensity is simulated by evaluating Eq. (3.17).

3.7.3 Simulations and results

In the following simulations, a concentric-ring applicator of 20 annular elements is assumed. The annular elements are of an individual width of 3 mm each with center-to-center spacing of 4 mm. An operating frequency of 500 kHz was chosen to allow a deep penetration of ultrasound in tissue-like media (> 10 cm). The tissue attenuation coefficient and the ultrasound velocity in tissue-like media were taken to be 1 dB/cm/MHz and 1500 m/s, respectively.

The CRA was first focused at Z=70 mm along its main axis. The contour plot of the field intensity pattern in the (r,Z) plane is shown in Figure 3.29a). Figure 3.29b) is the normalized amplitude distribution needed for this synthesis as established by the FCM. The amplitude shading factor for this distribution was computed and found to be 0.69. This amplitude shading factor was improved by applying the logarithmic scaling procedure as explained in Chapter 2. The new amplitude distribution is shown in Figure 3.29c). This new distribution resulted in an amplitude shading factor of 0.39. The spatial-peak temporal-peak (SPTP) focal intensity gain is found to be 22.3 dB. This focal intensity gain was also evaluated using Eq. (3.15) and found to be 23.4 dB. An SPTP focal intensity of 638 W/cm^2 is computed at the focal site assuming that the annular electrodes are capable of producing a surface intensity of 4 W/cm^2. To simulate scanning, the convolution integral was evaluated for a disk-shaped surface of 35 mm radius. The resulting field intensity pattern is shown in Figure 3.30a). The scanned field intensity gain of the resulting pattern is 5.95 dB. However, when the convolution integral was evaluated over an annular ring of inner and outer radii of 9 and 15 mm, respectively, the annular heating pattern of Figure 3.30b) was produced. The scanned field intensity gain evaluated at the focal site was 15.09 dB. These patterns will be used as inputs to the BHTE, and their associated temperature distributions will be discussed in Chapter 5.

An elongated focus is also generated by simultaneously focusing at 60 and 80 mm (along the axis) from the array surface. The contour plot of the resulting field intensity pattern is illustrated in Figure 3.31a). An SPTP focal intensity of approximately 432 W/cm^2 was evaluated compared to 648 W/cm^2 for the previous case. The convolution integral was

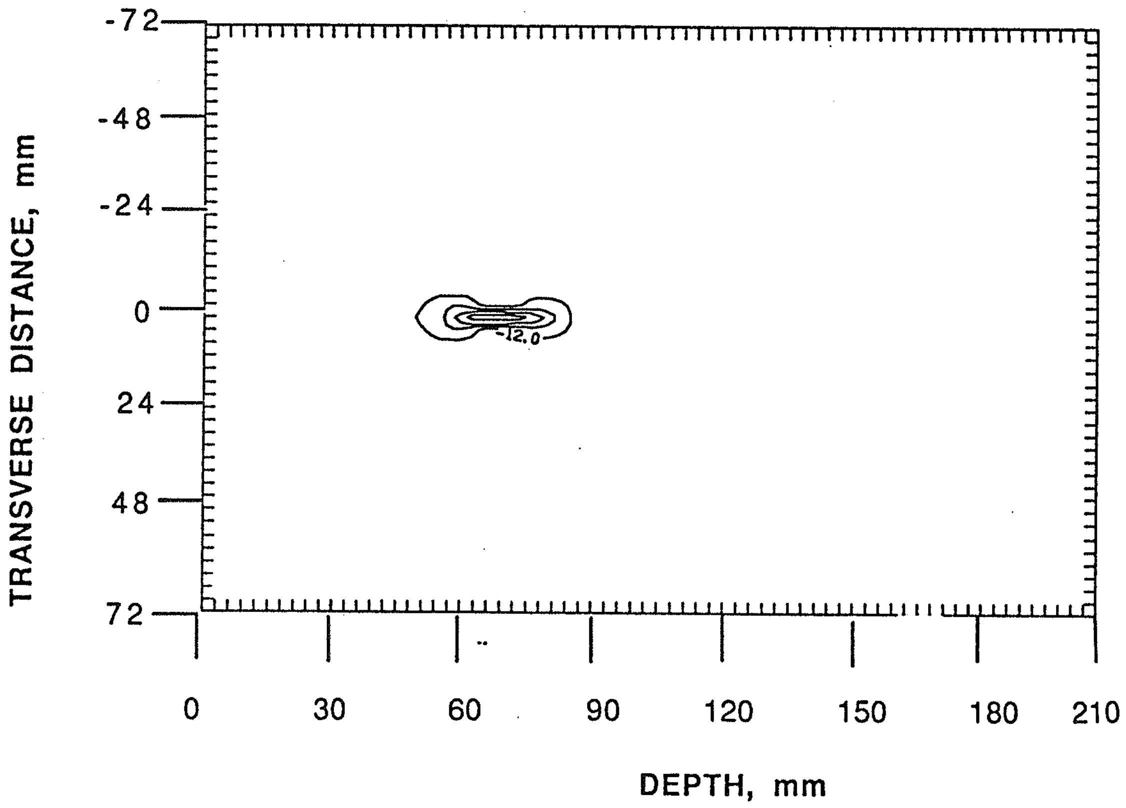

Figure 3.29. Synthesis of a conventional foci along the axis. a) A contour plot of the pattern resulting from focusing at (0,0,70) along the array axis. The lowest contour level is -12 dB and contours are given at 3 dB intervals.

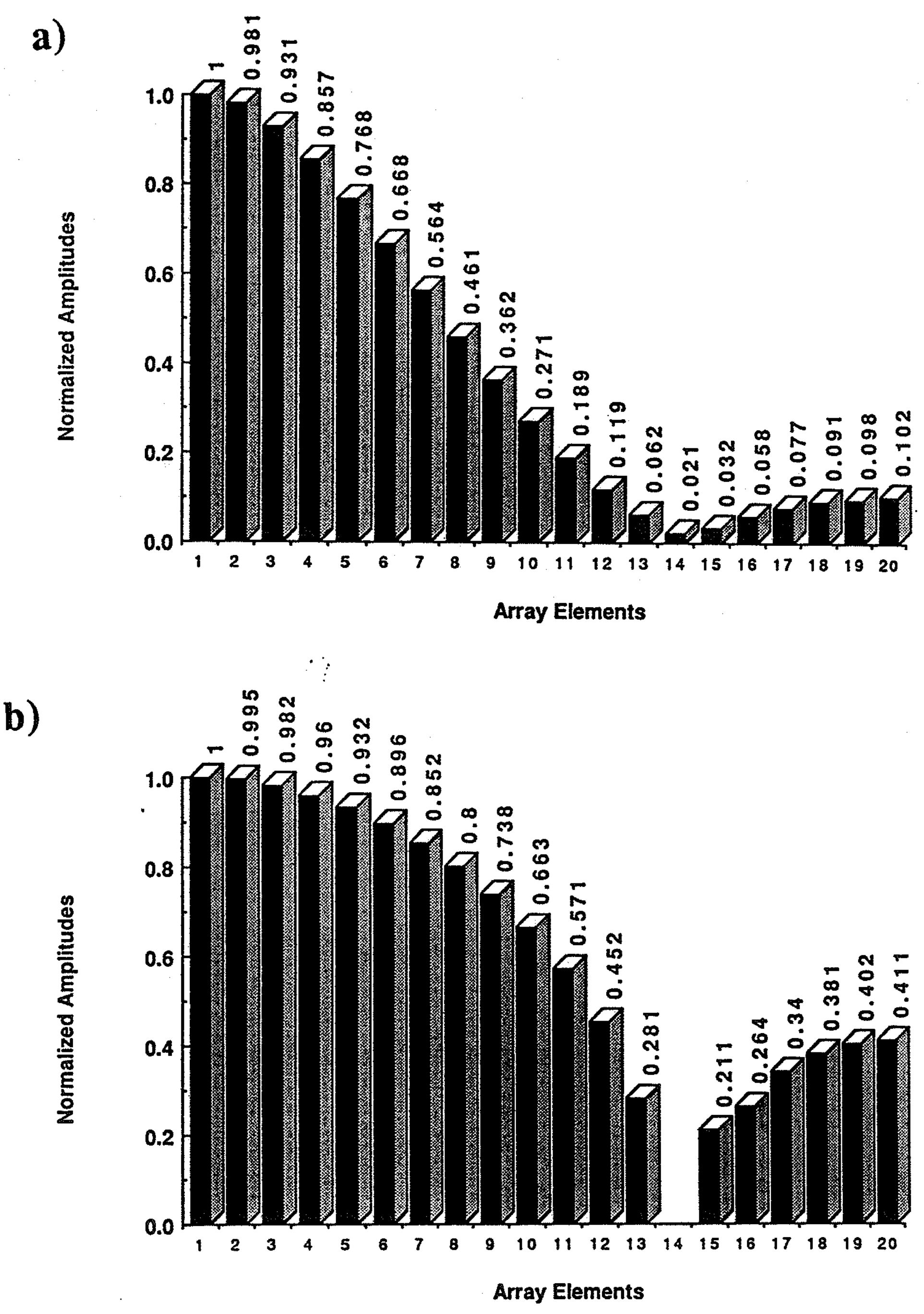

Figure 3.29. b) Normalized amplitude distribution of the excitation signal required by the FCM for the synthesis of (a) and b) is the normalized driving amplitude distribution logarithmically scaled as described in Chapter 2.

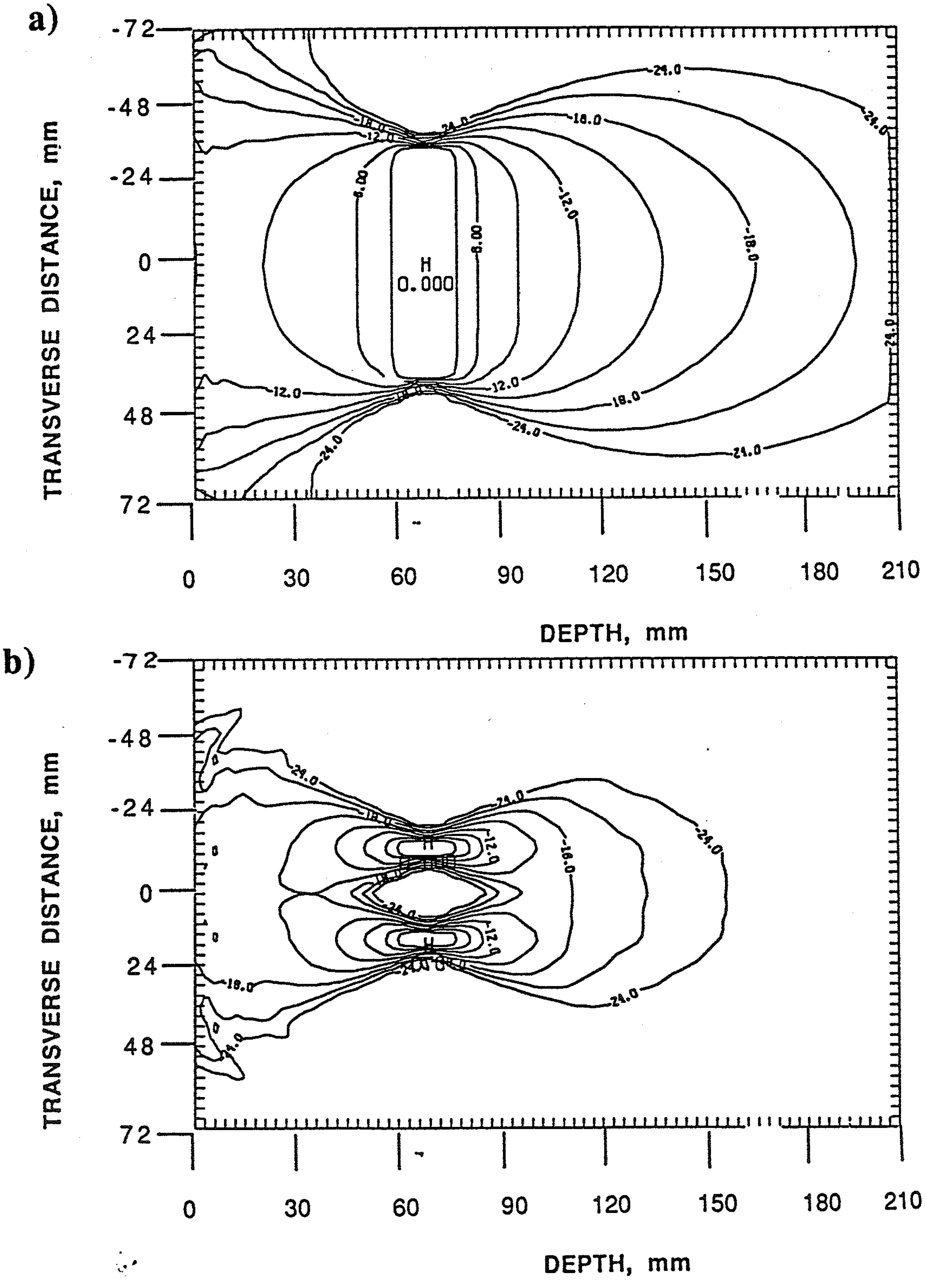

Figure 3.30. Simulated intensity profiles resulting from mechanical scanning. a) Scanned field (time-averaged) intensity over a disk 35 mm radius and b) is the time-averaged intensity produced by scanning the array over an annular ring of 9 and 15 mm, respectively. Lowest contour level is -24 dB and contours are given at intervals of 3 dB.

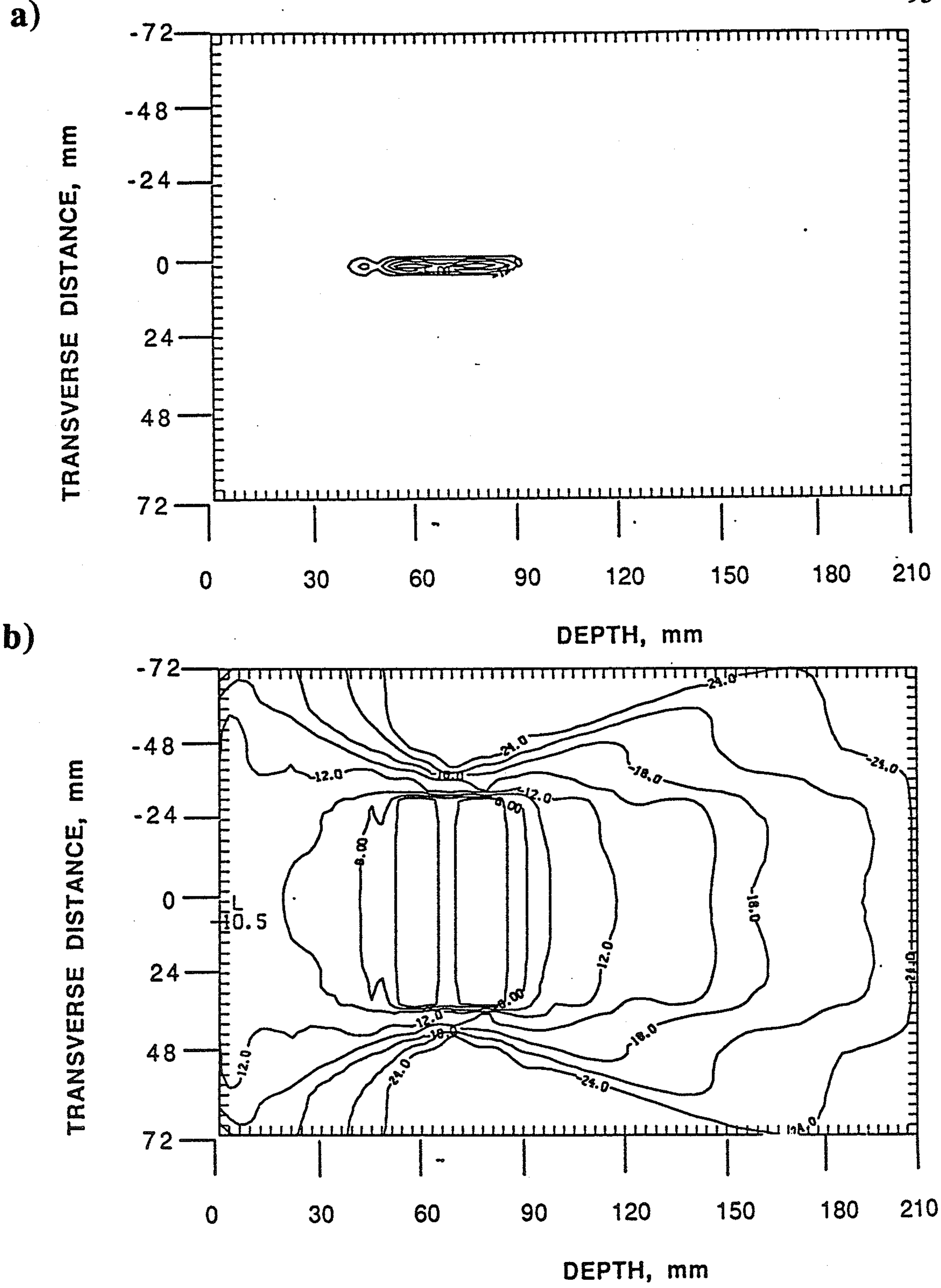

Figure 3.31. Simulated intensity profiles resulting from mechanical scanning . a) Elongated foci resulting from simultaneously focusing at (0,0,60) and (0,0,80). b) The time-averaged intensity profile of the pattern produced by scanning a) over a disk of 30 mm radius.

then used to evaluate the scanning of this pattern over a disk-shaped surface of 30 mm radius. The resulting scanned field intensity profile is shown in Figure 3.31b). The thermal response associated with this pattern will be investigated in Chapter 5.

As a demonstration of heating simultaneously different volumes, the pattern obtained by simultaneously focusing at 60, 68 and 90 mm is scanned (by performing the convolution integral) over a disk of an 18 mm radius and the field intensity profile is shown in Figure 3.32. The SPTP focal intensity used to achieve this pattern is 187.77 W/cm^2 compared to over 400 W/cm^2 in the previous cases.

To demonstrate the possibility of heating very deep seated tumors, the FCM was used to synthesize a focal spot at 180 mm (over the axis) from the applicator surface as illustrated in Figure 3.33. An elongated focal region resulted due to the high focal number of the pattern. An SPTP intensity gain of 13.3 dB was evaluated at the focal site. The convolution integral was then evaluated over a ring of inner and outer radii of 12 and 18 mm, respectively, and the field intensity profile is shown in Figure 3.34a). Finally, the convolution integral was evaluated over a disk of a 10 mm radius and the resulting field intensity profile is shown in Figuire 3.34b). An evaluation of these different patterns, based on their associated thermal response, will be given in Chapter 5.

3.8 Conclusions

Throughout this chapter, the application of the FCM to the analysis and design of a concentric-ring array was investigated. The configuration was chosen because of its ability to produce 3-D focusing volumes while using a minimum number of annular electrodes. Two synthesis methods based on a field conjugation concept were investigated: the FCM and the pseudo-direct method. These methods were used to synthesize multiple foci on the

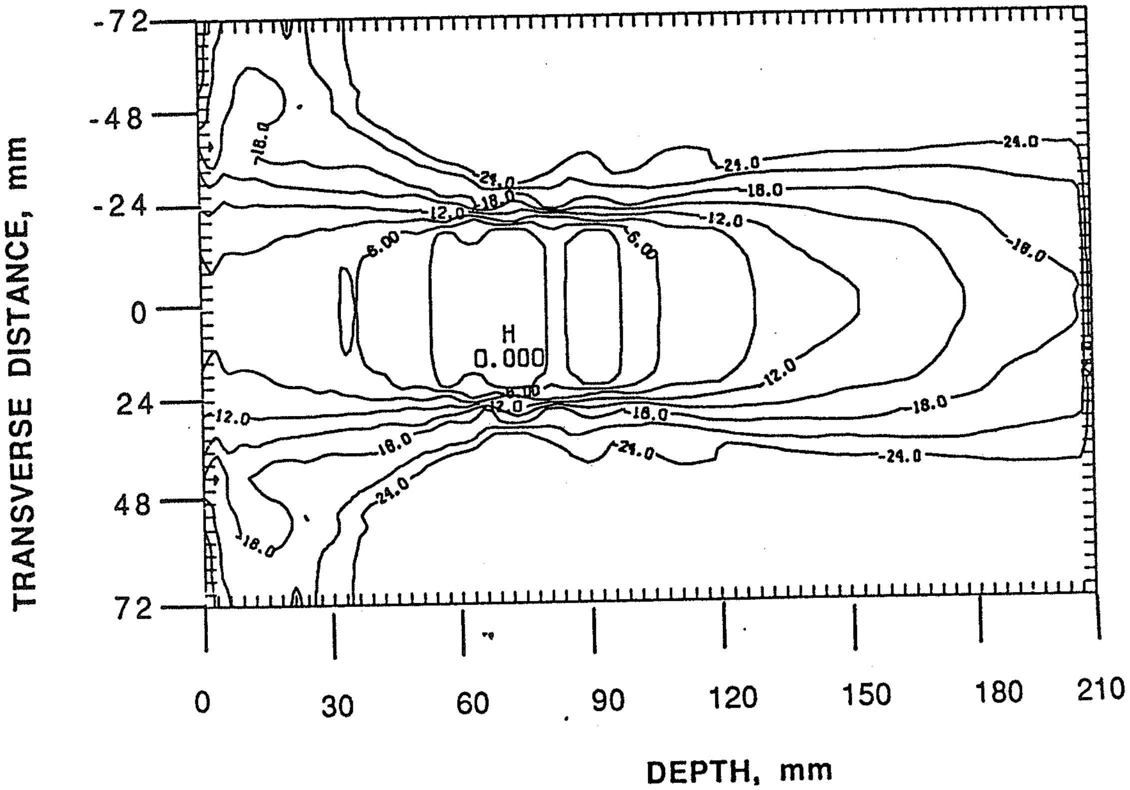

Figure 3.32. Mechanical scanning of multiple foci pattern. The array was simultaneously focused at (0,0,60), (0,0,68), and (0,0,90) along the axis. The resulting pattern was mechanically scanned over a disk of 18 mm radius. The lowest contour level is -24 db with contour intervals of 3 dB.

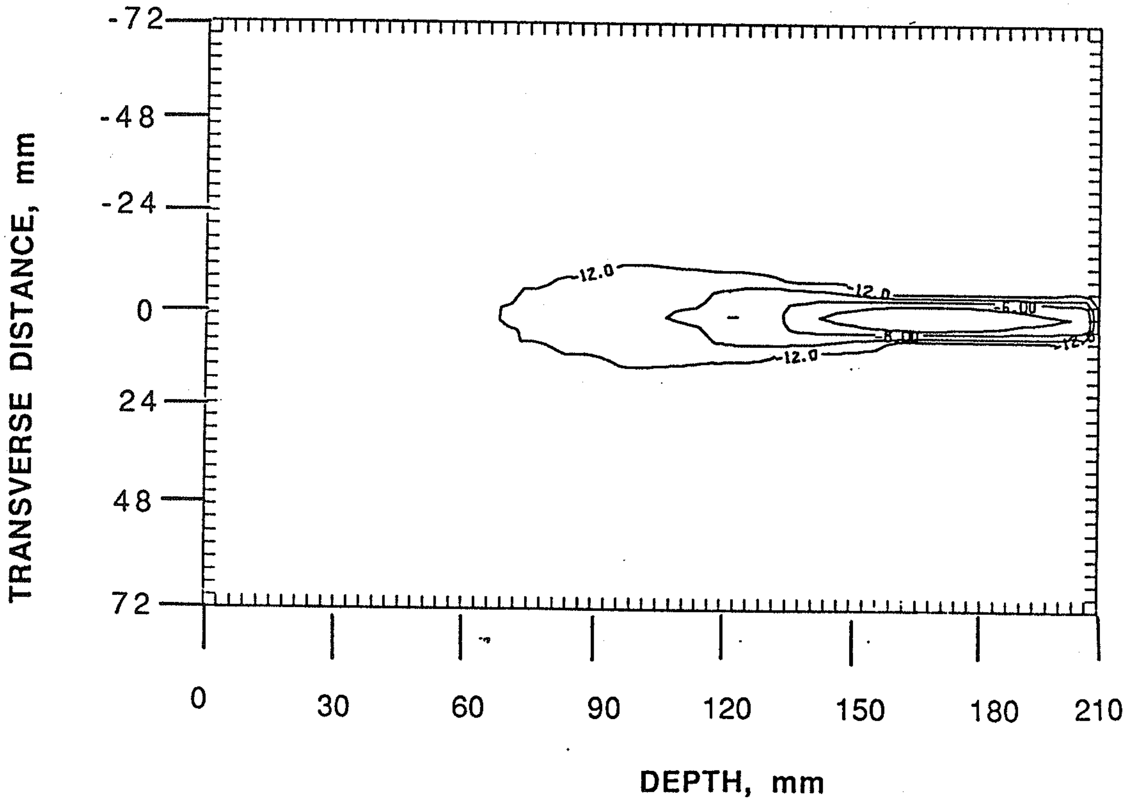

Figure 3.33. Synthesis of simple focus at depth. A contour plot of the pattern resulting from focusing at (0,0,180) along the array axis. The 3 dB region elongation is due to the large F-number of the pattern.

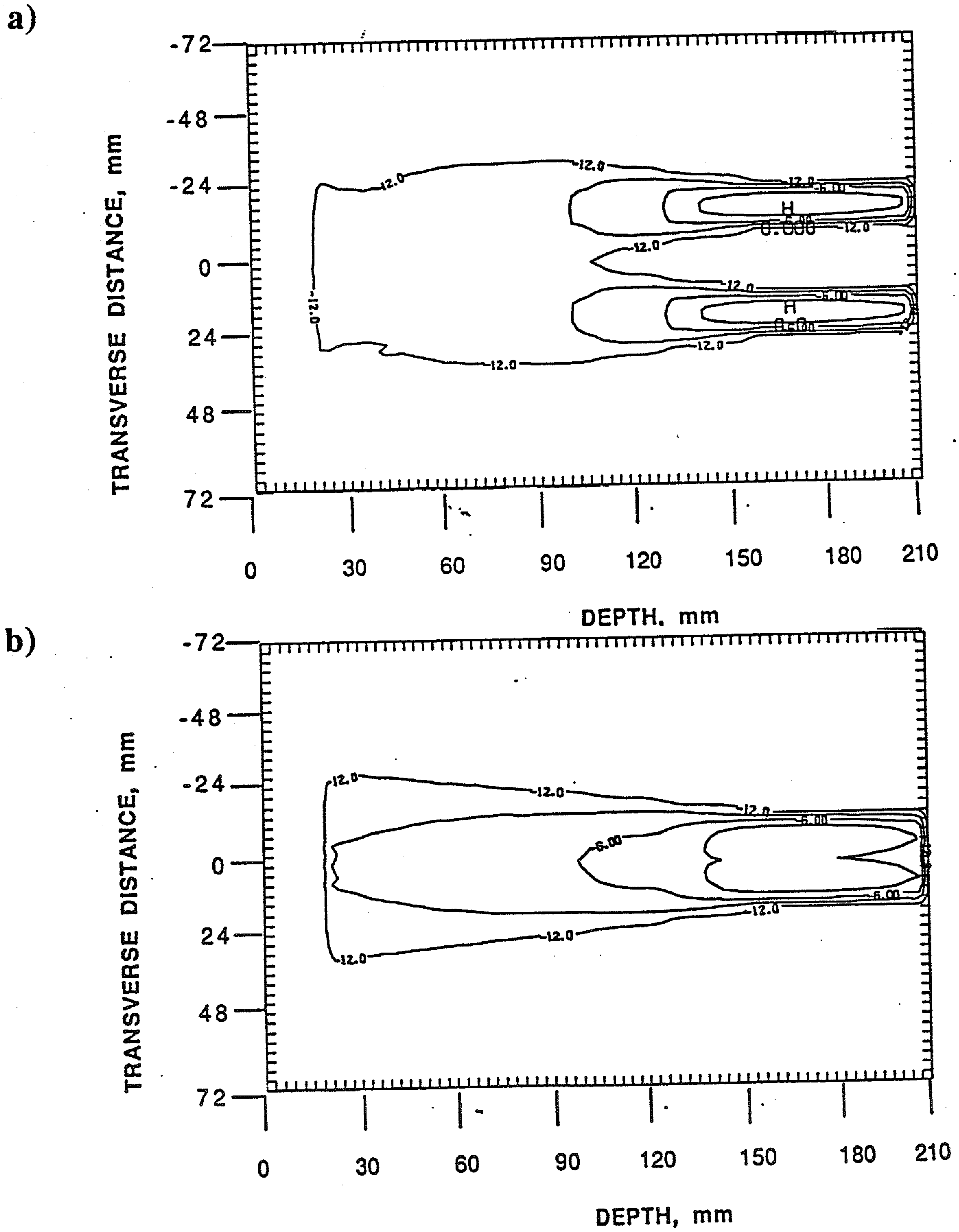

Figure 3.34. Deep seated tumors heating using mechanical scanning. a) Time-averaged intensity profile resulting from scanning the pattern of Fig. 3.32 over an annular ring. b) The time-averaged intensity profile resulting when the scan surface is a disk of 10 mm radius.

main axis as well as annular intensity profiles of different dimensions. In some cases, the method's performance was compared to that of the direct phasing method described in [15,17]. The advantages and limitations of each method were then discussed. In particular, it was shown that focusing on the main axis resulted in a very localized power deposition (very small 3 dB region). Also, the multiple focusing feature was used to produce simultaneous on-axis foci at different depths. Annular focusing was shown to be possible. The synthesis of multiple annular foci was shown, and focal rings of different widths were also simulated. A strong secondary focus was observed on the main axis, far beyond the focal plane, when the synthesis of small radii ($r < R_s$) was attempted. The formation of such a strong secondary focus might impose severe limitations on the use of CRA to treat small tumors.

To overcome these limitations, it is proposed to use the multiple focusing on the main axis combined with a simple mechanical movement of the transducer. The proposed technique was then simulated on the computer and heating patterns ranging from small to large annuli were produced. Moreover, heating the back of the tumor as well as the front simultaneously was shown to be possible. The temperature distributions associated with different power deposition patterns will be investigated in Chapter 5.

CHAPTER 4

ANALYSIS AND DESIGN OF AN NxN SQUARE-ELEMENT ULTRASONIC PHASED ARRAY

4.1 Introduction

The field conjugation method (FCM) is characterized by its ability to directly synthesize arbitrary heating patterns overlaying tumor geometry without electrical or mechanical scanning, a technique that should prove very useful in hyperthermia applications. Furthermore, the multiple focusing feature of the method offers the possibility of simultaneously heating different parts of the treated volume (i.e., back of the tumor, etc.). Broadening the focal region by simultaneously focusing at two or more neighboring locations might be used to simplify the electronic scanning by reducing the number of scan points and would allow the use of lower spatial-peak temporal-peak (SPTP) focal intensities [30].

The direct synthesis of heating patterns, to tailor the ultrasonic power deposition to virtually any tumor geometry can be achieved by assuming a source of the appropriate shape at the desired location. The FCM is then used to establish the required driving phase and amplitude distributions for all array elements.

The multiple focusing feature is achieved by assuming point sources (or small disk shaped sources) at every desired location, and the FCM is then applied to determine the required excitation signals. By splitting the focal intensity among different foci, it is possible to directly heat, or eventually to scan, a tumor while keeping the SPTP focal intensity level far below thresholds for nonthermal effects such as cavitation.

The capability of a concentric-ring array to produce annular intensity profiles was demonstrated throughout the last chapter. The possibility of focusing the applicator to a point, or multiple points, along its main axis was demonstrated. While the beam could be steered to any location along the main axis, deflecting the beam from the axis would result in annular patterns because of the applicator geometry. Thus it was concluded that the intensity profiles produced by the CRA are limited to annular shapes and to focal spots along the axis. Moreover, the analysis of annular intensity profiles, as given in Chapter 3, lead to the conclusion that mechanical scanning of the CRA might be necessary to produce optimal diffuse heating patterns.

In this chapter, a new array configuration is proposed to overcome the CRA limitations and to allow the investigation of more features of the FCM. The configuration, an NxN square-element array, is chosen to permit the synthesis of different field intensity profiles with arbitrary circular and noncircular symmetry. Patterns ranging from annular to elliptical and from a simple focal point to a complete "line focus" will be demonstrated. Besides potential uses in hyperthermia applications, these intensity profiles might also prove useful in other ultrasound applications as well. Section 4.6 will demonstrate the overall flexibility of the method.

In what follows, a numerical method used to compute the sound field is explained followed by the derivation of analytical expressions for the far-field radiation pattern of a square radiating surface and of an NxN array. The field conjugation method is then used to directly synthesize different intensity profiles. The versatility of the method is demonstrated through the use of the rotational field conjugation method (RFCM) version of the technique to eliminate the secondary foci which were shown to seriously limit the annular patterns produced by the CRA configuration. The direct synthesis is then compared to dynamic scanning of an intense focal spot. The multiple focusing feature can also be used to directly deposit the ultrasonic energy around an arbitrarily shaped periphery or closed path. In some cases, this technique is used to simplify scanning by reducing the number of required scan points and by using a lower SPTP intensity. Advantages and limitations of these phasing methods and the NxN applicator geometry are discussed.

4.2 The NxN Square-Element Array

4.2.1 The array configuration

Figure 4.1a) shows the geometrical configuration of the NxN square-element array. The applicator consists of NxN square elements each of width W. The center-to-center spacing between elements is d. The total side width of the array is D ($N=\frac{D}{d}$). The center of the array coincides with the center of the coordinate system (0, 0, 0). For clarity, the surface of the array is assumed to be in the plane z=0. Figure 4.1a) shows the extension of the array from $-\frac{D}{2}$ to $\frac{D}{2}$ in the X and Y directions. The elements are designated by S_{ij} where i is the element index in the X direction and j is its index in the Y direction ($1\leq i,j\leq N$).

4.2.2 Choice of the square element width

The NxN square-element configuration requires a substantially larger number of elements than those required by the concentric-ring applicator. This number of elements needs to be minimized in order to simplify the associated driving electronics. The number of array elements is determined by the largest element size that results in the synthesis of a desired pattern without significant grating lobes. A series of computer simulations was conducted to determine an appropriate upper limit on the size of the individual square-element. In these simulations, element width was varied between 0.5 λ and 3.0 λ while keeping other parameters unchanged. For the different patterns discussed in this chapter (element width = 1.5 λ), grating lobe intensity levels were always at least 11 dB below the focal intensity. As an illustration, the focal pattern obtained by simultaneously focusing at 20 points uniformly distributed over the periphery of a 20 mm radius annular ring at 100 mm depth is shown in Figure 4.1b). The synthesis of annular patterns using the RFCM will be discussed in a Sections 4.5 through 4.8 and the focal pattern is merely used as an illustration in this section. On the other hand, when the width was increased to 2λ,

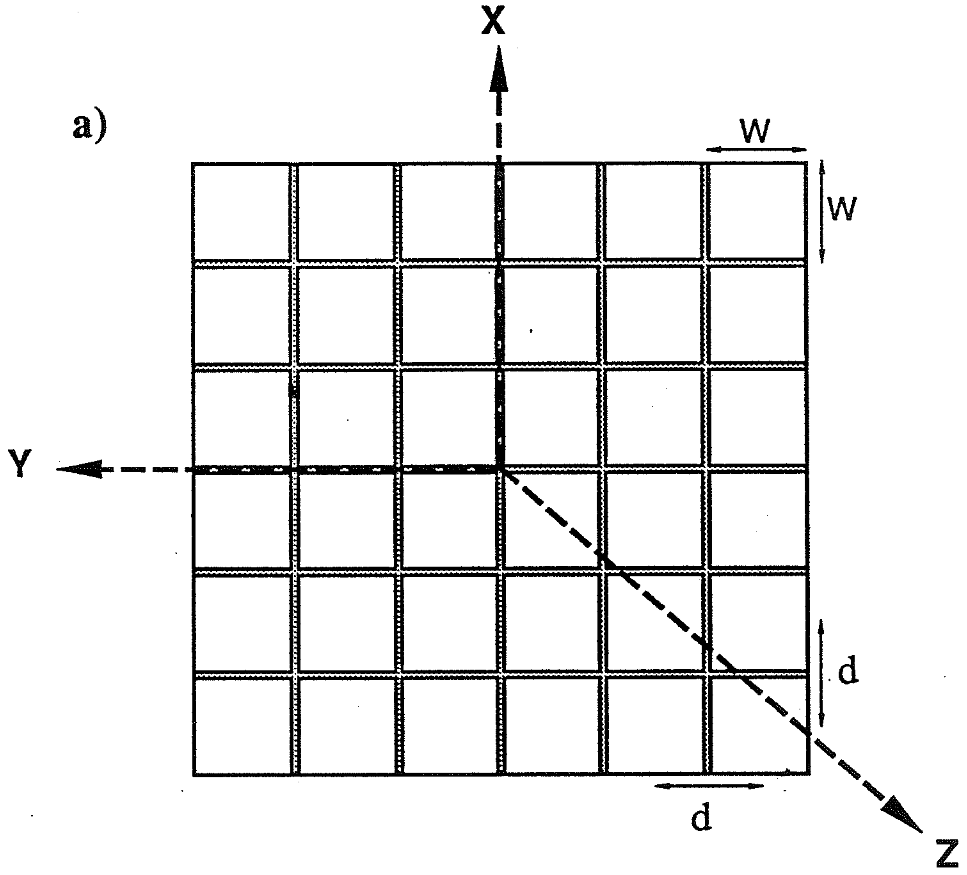

Figure 4.1 a) Geometrical configuration of a square-element NxN phased array. Individual elements are of W width and center-to-center spacing d. Total side length is D.

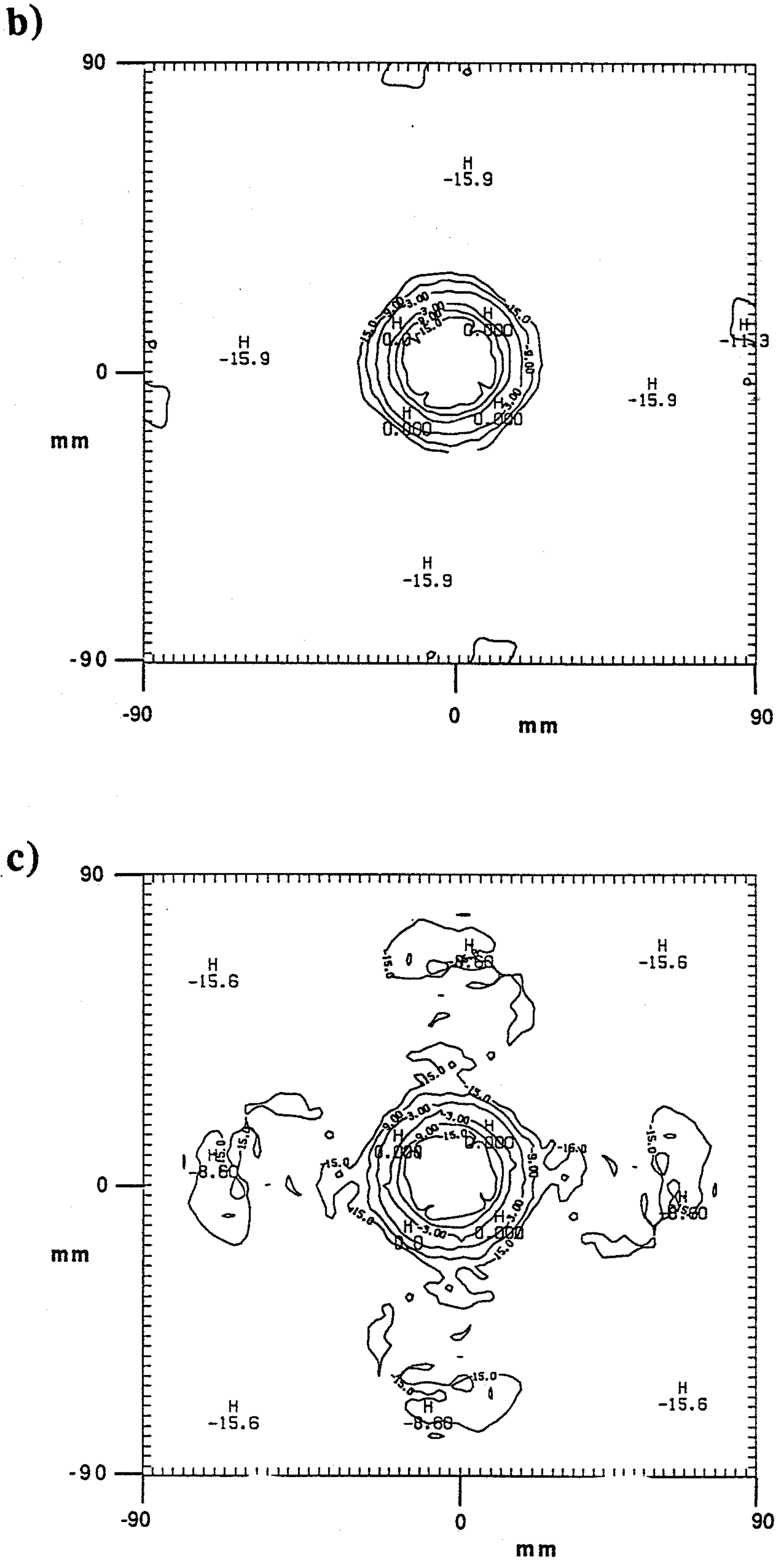

Figure 4.1. b) A contour plot of the focal pattern produced by focusing at 20 points uniformly spaced over the periphery of a 20 mm radius ring. The array is of 20x20 elements of individual width 1.5 wavelength. c) The same pattern as in b) but produced by 15x15 elements array. The element width is two wavelengths.

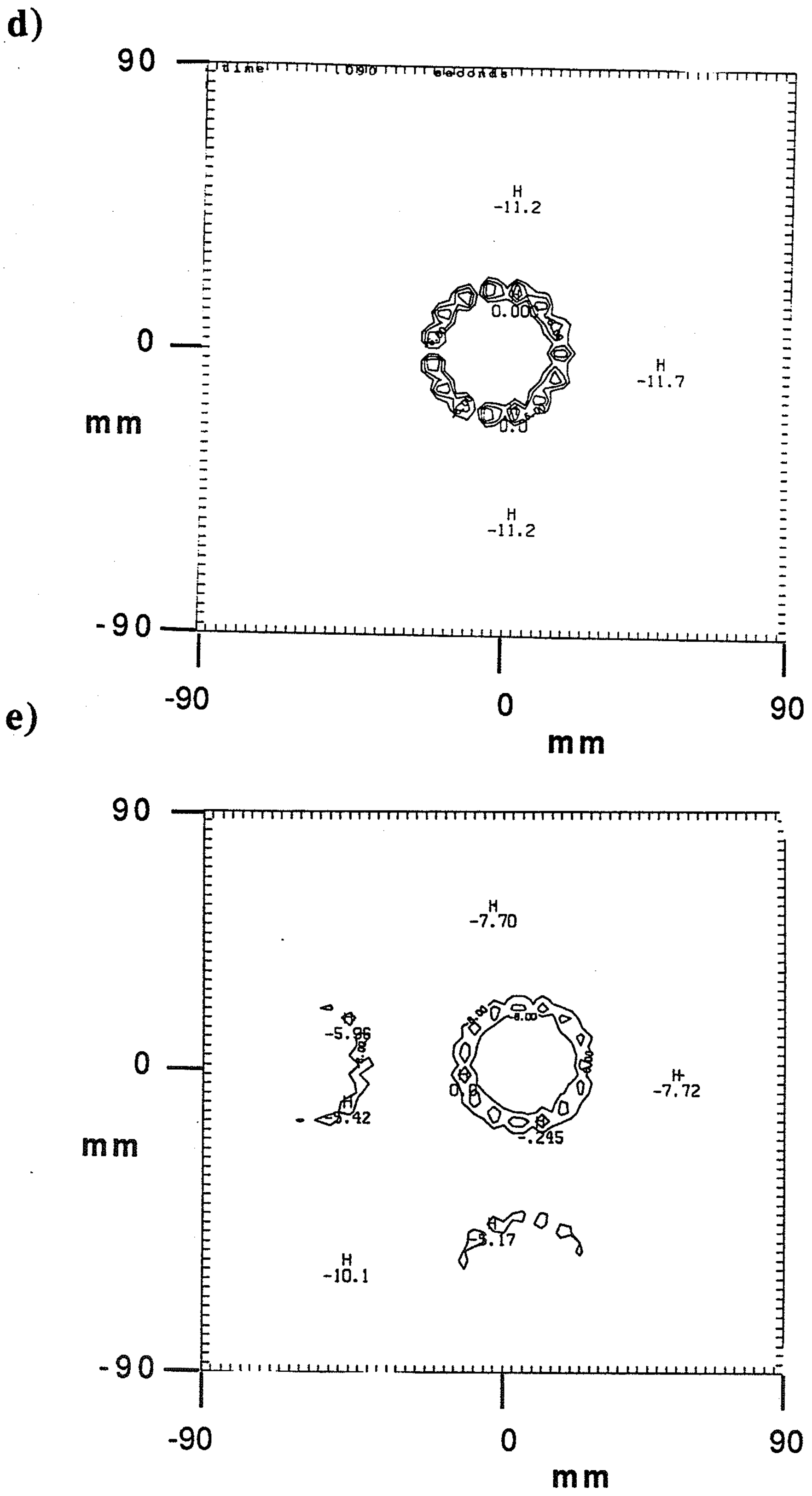

Figure 4.1 d) A contour plot of the focal pattern resulting from electronically scanning a ring of 20 mm radius (see text). The focal spot was synthesized using the FCM and e) is the resulting pattern when the amplitude distribution (FCM) was substituted by uniform amplitude excitation.

synthesis of the same pattern resulted in grating lobes only 9 dB below the focal intensity, as illustrated in Figure 4.1c). This might be acceptable for most hyperthermia applications. Unlike scanning techniques where grating lobe levels change with the translocations of the focal spot, the grating lobe levels remain fixed for each distributed pattern that is synthesized using the FCM. Furthermore, a focal spot was synthesized using the FCM and electronically swept over 15 points uniformly distributed over a circular trajectory of 20 mm radius (details of the electronic scanning technique are given in Section 4.7). Figure 4.1d) illustrates the resulting scanned field intensity profile in the focal plane(z= 100 mm). The pattern results in grating lobe levels of about 11 dB less than the focal intensity peak. However, when the array elements were uniformly excited (uniform excitation amplitudes), the same pattern resulted in an increase of the grating lobe levels of about 5 dB, as shown in Figure 4.1e). Based on the above simulations, an element width of 1.5 λ was chosen for all computer simulations discussed in this chapter. The total array width is then 100 mm (20x20 elements).

4.3 Modeling of the Acoustic Field

A general problem in the analysis and design of phased arrays is that of evaluating the applicator resulting pressure field at an arbitrary point in the space. This calculation is indispensable to allow the investigation of the effect of different design parameters on the field produced by the applicator. These investigations are crucial in the choice of an optimum set of design parameters based on the characteristics of the simulated field. The determination of such an optimal set of design parameters reduces substantially the time and cost involved in the fabrication process.

In Chapter 3, a numerical method (equidistant areas) based on symmetry considerations was used for the field computations. The use of the equidistant areas was motivated by the circular symmetry of the applicator. However, the rectangular geometry of the NxN configuration makes the application of the equidistant areas method difficult and inappropriate; hence, another numerical technique is needed.

The calculation of the field produced by an array is reduced to that of evaluating the field due to one of its radiating elements set in an infinite baffle. Moreover, Hygen's principle reduces the calculation further to that of summing the contributions of all infinitesimal elements of areas (ds=dx dy) constituting the radiating surface. The partial pressure produced by an elementary surface ds radiating with a complex surface velocity u is given by

$$dp = \frac{j\rho ck}{2\pi}(u\,ds)\,\frac{e^{j(\omega t-kr)}}{r}\,e^{-\alpha r} \tag{4.1}$$

where ρ is the density of the medium, c is the sound velocity in the medium, k is the wave number ($k=\frac{2\pi}{\lambda}$), α is the pressure attenuation coefficient, u is the surface velocity of the elementary surface ds, and r is the distance separating ds and the point q where the field is to be calculated. By superposing all the contributions of elementary areas, the total pressure of a radiating surface s is

$$p = \frac{j\rho ck}{2\pi}\int_s u(x_0,y_0)\,\frac{e^{-(\alpha+jk)r}}{r}\,ds \tag{4.2}$$

where s is the area of the effective radiating surface, (x_0,y_0) refers to the (x,y) plane at the rectangular element surface (z= 0). The time-harmonic term ($e^{j\omega t}$) is dropped for simplicity and is assumed in the remainder of this chapter.

Several numerical methods can be used to handle the surface integral of Eq. (4.2). An excellent comparison between different numerical techniques is given in Reference [41].

The comparison is based on the required computation time and the number of field points needed for accuracy. The rectangular radiator method [42] was shown to be the most efficient method for handling rectangular geometry. In the remainder of this chapter, the rectangular radiator technique will be used to evaluate the field produced by the array while the equidistant areas method (see Chapter 3) is used to handle the computation of fields produced by sources with circular symmetry (i.e., fictitious sources of annular or disk shapes). A summary of the rectangular radiator method is given below [41,42].

The method consists of dividing the array elements into subelements of individual areas ΔA and calculating the fields produced by those elements under certain assumptions. The subelements are chosen to be a part of only one array element and should not contain any of the interelement spacing. The number of those subelements is m and the center of subelement n is denoted by (x_n,y_n). Figure 4.2 illustrates the geometry used for the calculations. The pressure field is given by

$$P = \frac{j\rho ck}{2\pi} \sum_{n=1}^{m} U_n \int_{-\frac{\Delta h}{2}}^{\frac{\Delta h}{2}} \int_{-\frac{\Delta w}{2}}^{\frac{\Delta w}{2}} \frac{e^{-(\alpha+jk)r}}{r}\, dx_0\, dy_0 \tag{4.3}$$

where Δw and Δh are the side and the height of subelement n. The distance r is given by

$$r = \sqrt{z^2 + (x-x_n-x_o)^2 + (y-y_n-y_0)^2} \tag{4.4}$$

and by changing the variables

$$x' = x-x_n \quad \text{and} \quad y' = y-y_n \tag{4.4'}$$

the distance r can be written as

$$r = \sqrt{R^2 - 2y_0y' - 2x_0x' + x_0^2 + y_0^2} \tag{4.5}$$

$$R^2 = z^2 + x'^2 + y'^2 \tag{4.5'}$$

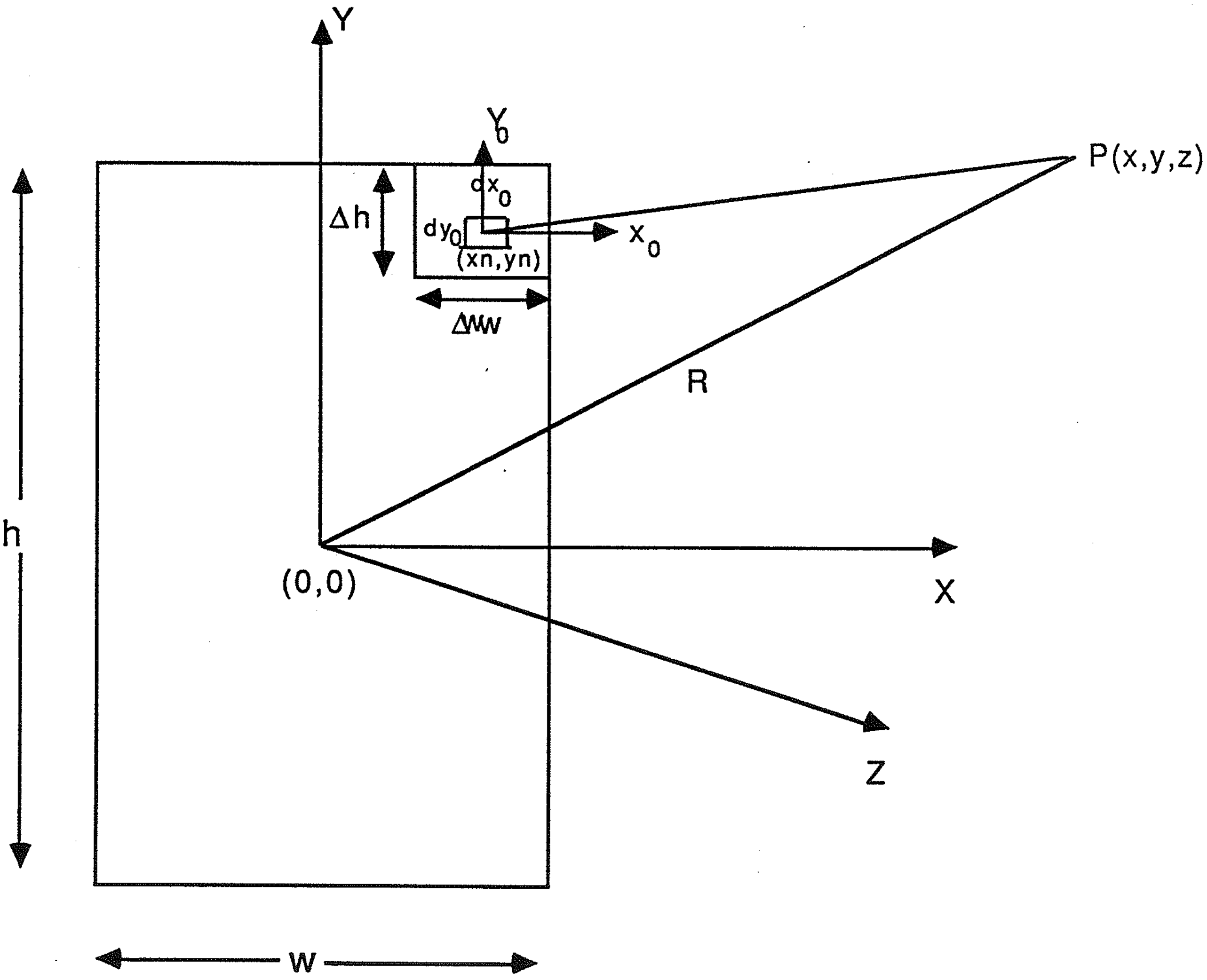

Figure 4.2. Geometry of a rectangular source as considered for the rectangular radiators method computations.

Equation (4.5) can be further simplified if one assumes that $x_0^2 + y_0^2 << R^2$ and uses Taylor series expansion, r can then be expressed as

$$r = R\left(1 - \frac{x_0x' + y_0y'}{R^2}\right) \tag{4.6}$$

and using this expression to substitute for r in the exponential argument of Eq. (4.3) and R in the denominator, one gets

$$P = \frac{j\rho ck}{2\pi} \sum_{n=1}^{m} Un \, \frac{e^{-(\alpha+jk)R}}{R} \int_{-\frac{\Delta w}{2}}^{\frac{\Delta w}{2}} e^{j\frac{kx'x_0}{R}} dx_0 \int_{-\frac{\Delta h}{2}}^{\frac{\Delta h}{2}} e^{j\frac{ky'y_0}{R}} dy_0 \tag{4.7}$$

where the two integrals are obviously independent and can be evaluated analytically. Equation (4.7) can finally be written as

$$P = \frac{j\rho ck}{2\pi} \sum_{n=1}^{m} U_n \, \frac{e^{-(\alpha+jk)R}}{R} \operatorname{sinc}\left(\frac{ky'\Delta h}{2R}\right) \operatorname{sinc}\left(\frac{kx'\Delta w}{2R}\right) \Delta w \, \Delta h \tag{4,8}$$

and it is Eq. (4.8) that can be easily handled by computer as the double integral of Eq. (4.3) has been transformed to a simple summation over n (notice that $y'=y-y_n$ and $x'=x-x_n$). This expression, however, is only valid under the assumptions made in obtaining Eq.(4.7). These assumptions are known as the far-field assumptions and summarized hereafter

$$\frac{k(x_0^2 + y_0^2)}{2R} = \frac{\pi(x_0^2 + y_0^2)}{\lambda R} << \pi \tag{4.9}$$

$$\frac{1}{r} = \frac{1}{R} \tag{4.10}$$

where Eq. (4.9) was used in approximating the exponential argument and Eq. (4.10) in approximating the denominator of Eq. (4.7), respectively. The variables x_0 and y_o are upper limited by $\frac{\Delta w}{2}$ and $\frac{\Delta h}{2}$, respectively, and consequently, Eq. (4.9) can be substituted by

$$k\frac{(\Delta w)^2}{8R}+k\frac{(\Delta h)^2}{8R} << \pi \qquad (4.11)$$

and Eq. (4.11) is verified if the two following conditions are

$$k\frac{(\Delta w)^2}{8R} << \pi \text{ and } k\frac{(\Delta h)^2}{8R} << \pi \qquad (4.12)$$

Finally, one should notice that Eq. (4.10) is included in Eq. (4.12) which can further be simplified by substituting R by z to give

$$z >> \frac{k(\frac{\Delta w}{2})^2}{2\pi} \quad \text{and } z >> \frac{k(\frac{\Delta h}{2})^2}{2\pi} \qquad (4.13)$$

and to ensure the verification of these two conditions, a constant C can be defined such that,

$$\Delta w,\Delta h \leq \sqrt{\frac{8\pi z}{kC}} \qquad (4.14)$$

It can be noticed from Eq. (4.14) that the restriction on the subelement size is relaxed as the distance of the point (where the field is to be calculated) from the array surface (z) increases. This relaxation of the subelement size continues until a limit case is reached where z is so large that Δw= w and Δh= h. This relaxation of the subelement size makes the method suitable for the calculation of the field at different depths. In the different computer simulations of this chapter, the value of the far-field constant C was chosen to be 16. Using this value, it was possible to perform the computation of the pressure field over a grid of (61X61) points (transverse plane z=100 mm) in 63s using the CRAY X-MP48. A Fortran code (TRANS) is given in Appendix A.

4.4 The Far-Field Radiation Pattern of the NxN Array

While the field produced by the NxN square-element array is rather complicated, a simple expression can be derived under the assumptions generally known as the far-field approximations (Section 4.3). In the previous section, an accurate numerical technique was proposed to calculate the field at any distance from the array surface. In this section, an analytical expression of the array pattern under the far-field assumptions will be derived. The analytical expression is only valid for points situated in the far-field of the applicator and will not be useful for the distance range considered in this thesis. However, the derivation of such an analytical expression might lead to a better understanding of the effect of some design parameters (i.e., spacing, element width, aperture size, etc.) on the array radiation pattern. The derivation of the far-field pattern is accomplished in two steps. First, the field produced by a rectangular radiating surface is calculated under the far -field assumptions. Second, the field due to a single element is then appropriately modified to account for the geometrical arrangement of the array elements. It is this latter expression that is used to compute the radiating pattern of the NxN array.

A rectangular radiating surface is assumed to vibrate in the plane (x,y) perpendicular to the Z axis. The surface velocity is assumed uniform time-harmonic as described in the previous section. Figure 4.3a) illustrates the geometry of the considered element. The field produced by this rectangular source at an arbitrary point p(x,y,z) is given by

$$P(r,t) = \frac{j\rho c}{\lambda} \int_S u\, e^{-j\omega t} \frac{e^{-jkr}}{r} ds \qquad (4.15)$$

$$r = \sqrt{(x-x_0)^2 + (y-y_0)^2 + z^2} \qquad (4.16)$$

where (x_0,y_0) is the center of the elementary surface $(ds = dx_0dy_0)$ and the constant $(\frac{j\rho c}{\lambda})$(for a given frequency) is as defined in the previous section. By using the far field assumptions of the previous section, Eq. (4.15) becomes

$$P(x,y,z) = A \int_{-\frac{h}{2}}^{\frac{h}{2}} \int_{-\frac{w}{2}}^{\frac{w}{2}} u \exp^{-j\frac{kxx_0}{R}} \exp^{-j\frac{kyy_0}{R}} dx_0\, dy_0 \qquad (14.17)$$

with $$A = \frac{j\rho c}{\lambda}\frac{e^{-jkR}}{R} \qquad (14.18)$$

and $$|x_0| \leq \frac{w}{2}, \quad |y_0| \leq \frac{h}{2} \qquad (14.19)$$

Equation (4.17) is the far-field approximation of the field produced by a rectangular element of width w and high h at point p(x,y,z). The far-field pattern of a square element of width w is obtained by substituting h by w in Eq. (4.17). To obtain the field produced by a rectangular element S_{im} centered at point $(x_0\text{-}id,y_0\text{-}md)$ (see Figure 4.3b)), it is adequate to substitute x_0 and y_0 by x_0-id and y_0-md, respectively, as shown below

$$P_{im} = A\ U_{im}\, e^{jk\frac{xid}{R}} e^{jk\frac{ymd}{R}} \int_{-\frac{w}{2}}^{\frac{w}{2}} \int_{-\frac{w}{2}}^{\frac{w}{2}} e^{-jk\frac{xx_0}{R}}\, e^{-jk\frac{yy_0}{R}}\, dx_0\, dy_0 \qquad (4.20)$$

where P_{im} is the field produced by the array element S_{im} at point P and U_{im} is the surface velocity associated with that element. The complex surface velocity is assumed uniform for simplicity.

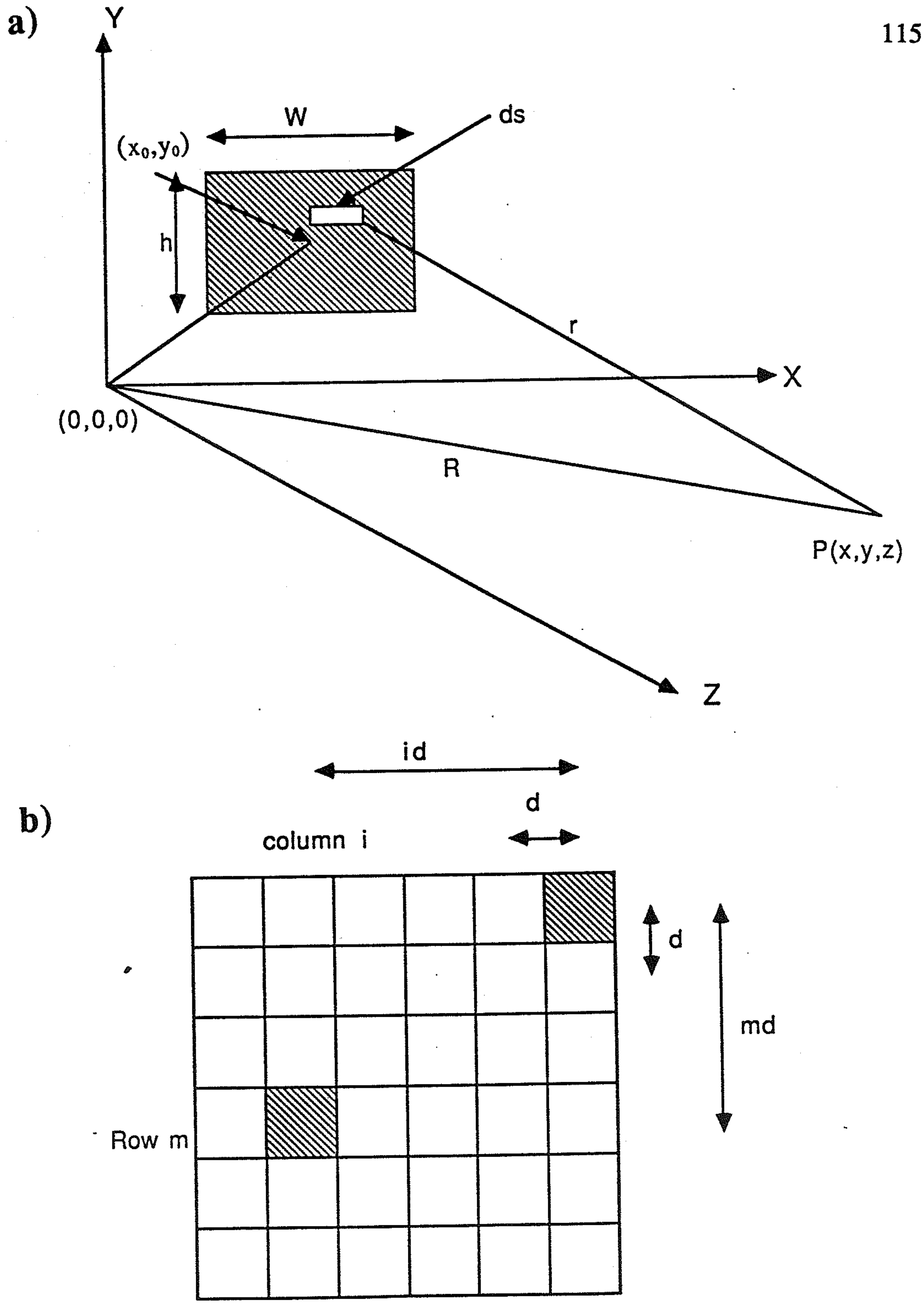

Figure 4.3. Geometry considered for the calculation of the far-field pattern of an NXN array. a) Schematic of the position of the point P (where the pattern is to be evaluated) with respect to the rectangular element. b) Geometry of the array where the square element mn is shaded.

The two integrals of Eq. (4.22) can be evaluated independently and the expression becomes

$$P_{im} = A\, U_{im}\, w^2\, e^{jk\frac{xid}{R}} e^{jk\frac{ymd}{R}}\, F_1(\theta,\phi) \tag{4.21}$$

with $F_1(\theta,\phi) = \mathrm{sinc}(\frac{\pi w}{\lambda}\sin\theta)\ \mathrm{sinc}(\frac{\pi w}{\lambda}\sin\phi)$ (4.22)

and $\theta = \sin^{-1}(\frac{x}{R})$ and $\phi = \sin^{-1}(\frac{y}{R})$ (4.23)

For simplicity, the surface velocity of all array elements will be assumed uniform and equal to U_0 in the remainder of this section.The far-field expression of the NxN square-element array can be evaluated by adding the contributions of all elements S_{im} ($1 \le i,m \le N$) as follows

$$P = A\, w^2\, U_0\, F_1(\theta,\phi) \sum_{i=1}^{N} e^{(\frac{j\pi id}{\lambda}\sin\theta)} \sum_{m=1}^{N} e^{(\frac{j\pi md}{\lambda}\sin\phi)} \tag{4.24}$$

Equation (4.24) can be evaluated by performing the discrete summation over i and m independently. Finally, the resulting far-field radiation pattern can be written as

$$P = A\, U_0\, (\frac{d}{D})^2 \exp(\frac{j\pi d}{\lambda}(N+1)\ (\sin\theta + \sin\phi))\ F_1(\theta,\phi)\ F_2(\theta,\phi) \tag{4.25}$$

with $F_2(\theta,\phi) = \dfrac{\mathrm{sinc}\,(\frac{\pi D}{\lambda}\sin\theta)}{\mathrm{sinc}(\frac{\pi d}{\lambda}\sin\theta)}\ \dfrac{\mathrm{sinc}(\frac{\pi D}{\lambda}\sin\phi)}{\mathrm{sinc}(\frac{\pi d}{\lambda}\sin\phi)}$ (4.26)

and $D = Nd$ (4.27)

It is worth mentioning that Eq. (4.25) contains two independent factors F_1 and F_2 such as the first describes the directivity of a square element of width w and the second describes that of an NxN array of point sources. This remark confirms that the directional factor of an array is the product of the directional factor of an array of the same geometry but with simple sources at the locations of its original elements by the directional factor of an element of the array [33].

To examine the validity of this analytical expression, the pressure field was evaluated using the far field approximation of Eq. (4.25) and compared to that calculated using numerical technique (rectangular radiator). For these simulations, an array of 20X20 elements each of 1.5 λ with an operating frequency of 500 kHz was assumed. The attenuation of the medium was neglected and a sound velocity of 1500 m/s was considered. The far field constant C of the rectangular radiator method was taken to be 16 in all simulations.

As expected, simulations show perfect agreement when the far-field assumptions are well verified (roughly for $z \geq \frac{D^2}{4\lambda}$). Figures 4.4 and 4.5 illustrate the resulting patterns at z=1200 and z=2000 mm, respectively. The surface plots of Figures 4.4a) and 4.5a) are obtained using Eq. (4.25) while those of Figures 4.4b) and 4.5b) are obtained via the rectangular radiators method. As observed from the simulations, the analytical expression is quite accurate and leads to results similar to those obtained by the numerical method. However, when the computations are performed near or within the near-field limit ($z \leq \frac{D^2}{4\lambda}$), the expression is no longer valid and its use cannot be justified. In fact, the Frensel diffraction effect (which is not accounted for in the derivation) becomes important and hence, the numerical technique is more accurate, as seen in Figures 4.6 and 4.7, which compare the patterns obtained using Eq. (4.25) with those obtained from the numerical method when the planes of calculation are at 800 and 500 mm from the applicator, respectively.

4.5 The Time-Averaged Intensity Profiles Associated with Diffuse Heating Patterns

Two different methods are proposed to produce diffuse intensity profiles that can be used for heating. The two techniques are the electronic scanning of an intense focal spot

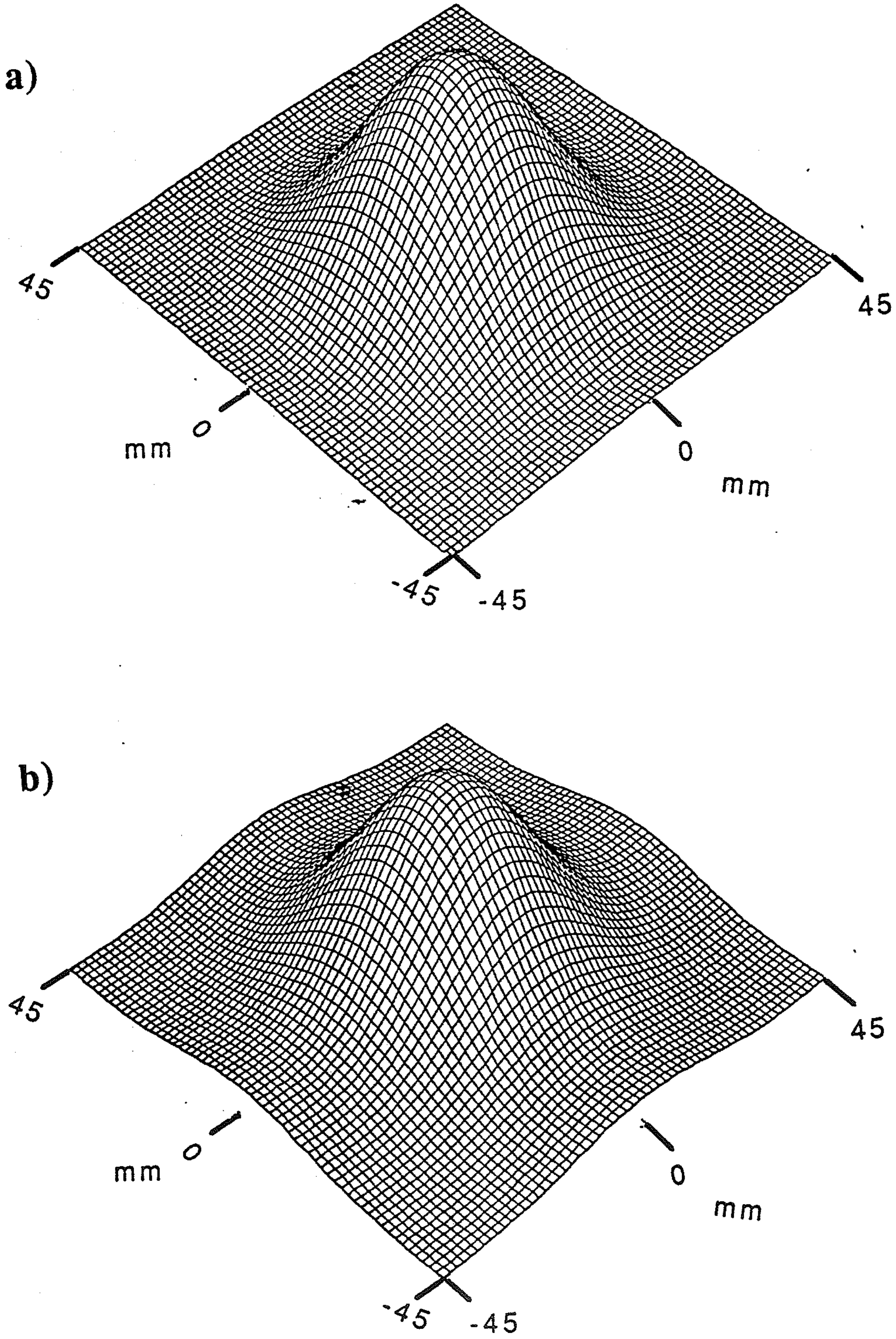

Figure 4.4. A surface plot of the radiation pattern in a transverse plane (z=1200 mm). a) the field calculations are done using Eq. (4.25) and b) the calculations are done using the rectangular radiators method.

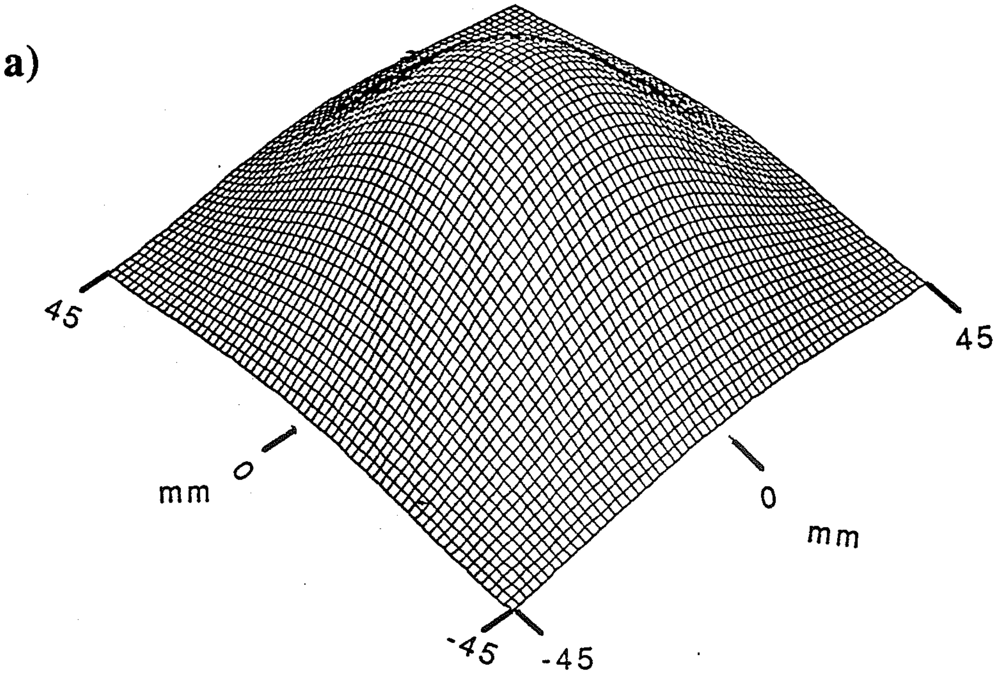

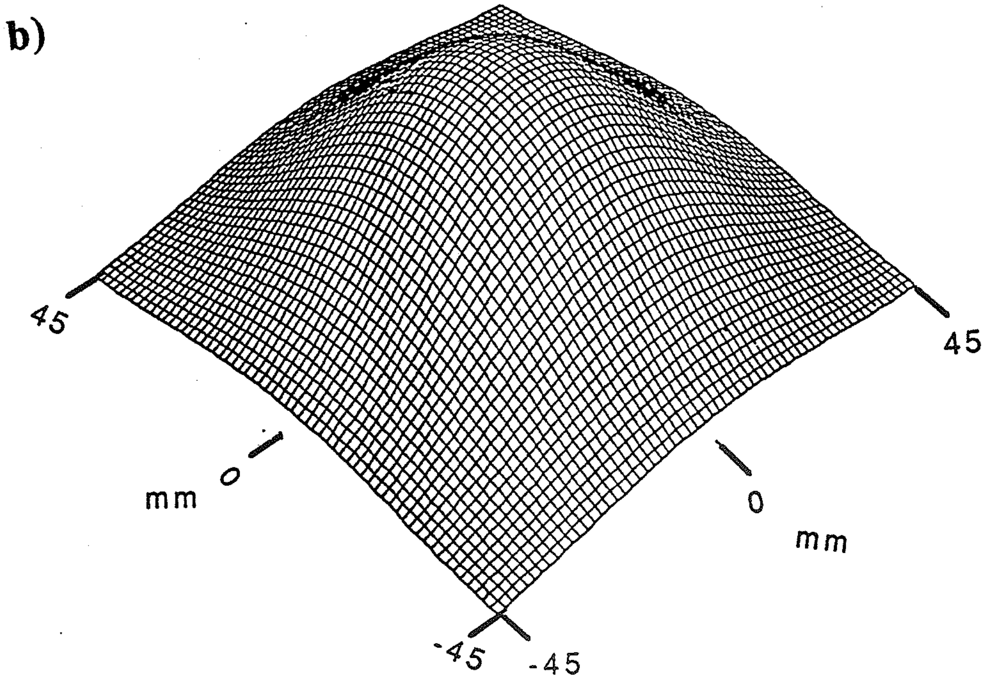

Figure 4.5. A surface plot of the radiation pattern in a transverse plane (z=2000 mm). a) calculations are done via Eq. (4.25) and b) via the rectangular radiator method.

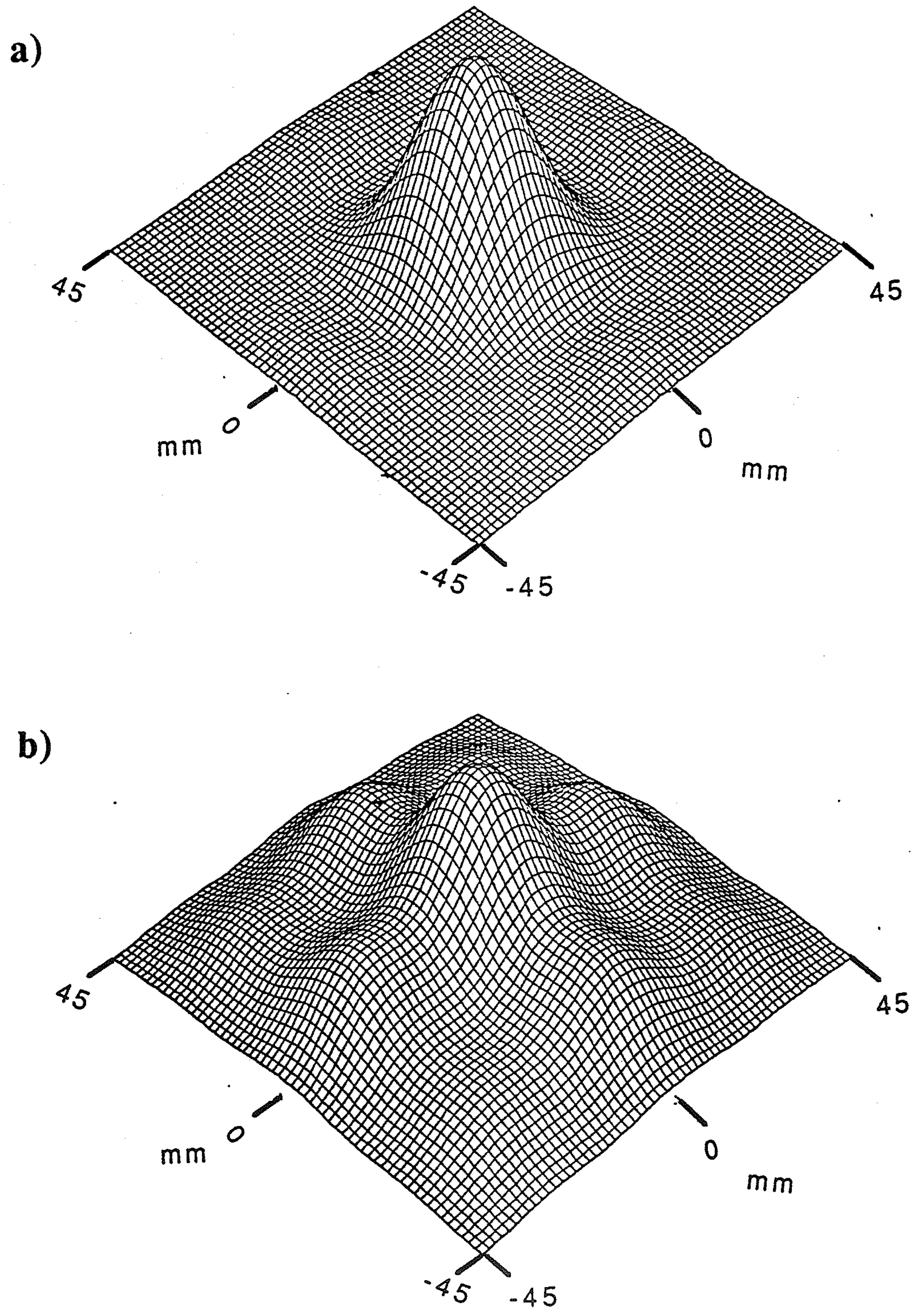

Figure 4.6. A surface plot of the radiation pattern in a transverse plane (z=800). a) calculations are done via Eq. (4.25) and b) via the rectangular radiator method.

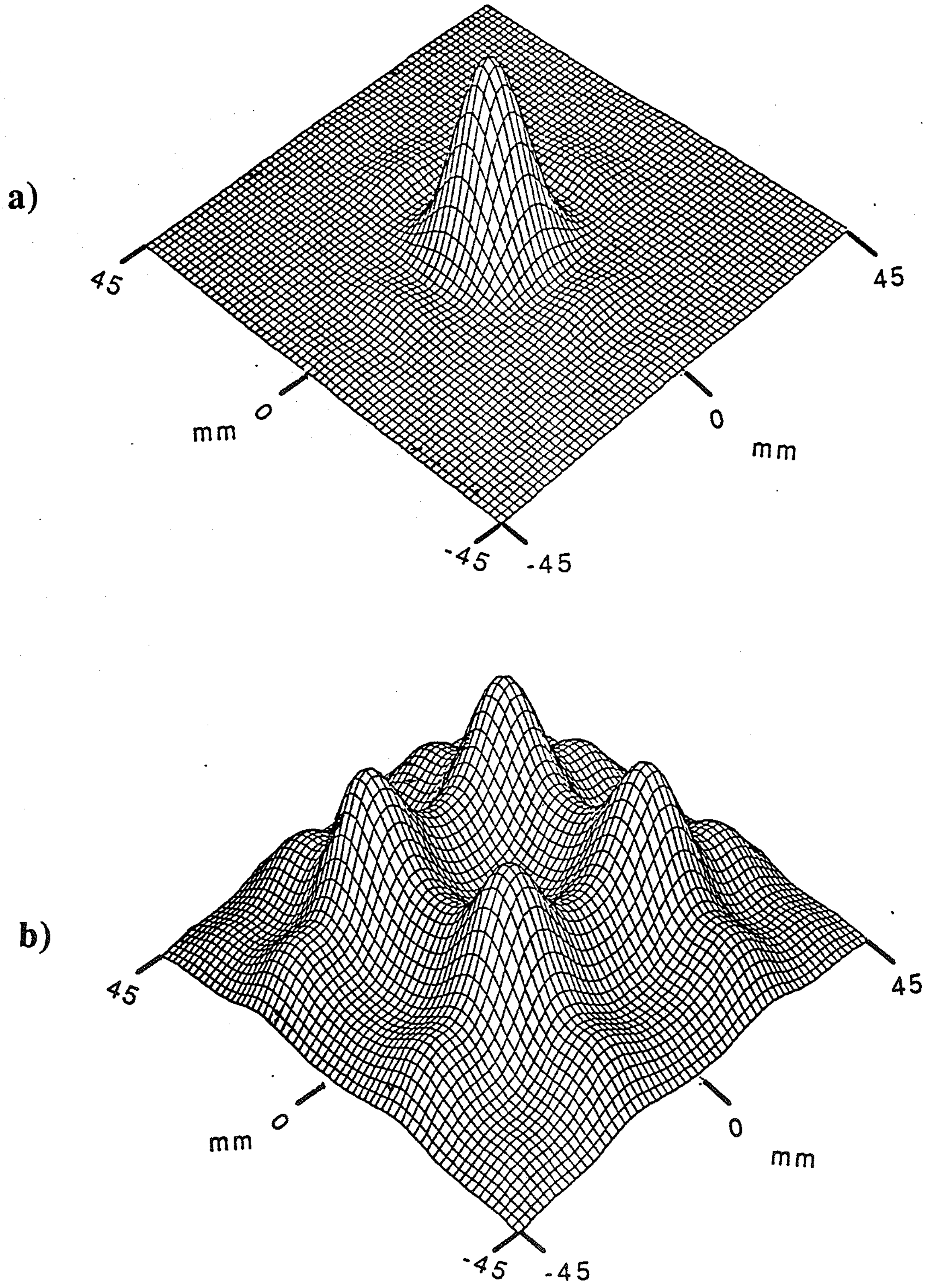

Figure 4.7. A surface plot of the radiation pattern in a transverse plane (z=500). a) Calculations are done via Eq. (4.25) and b) via the rectangular radiator method.

and the direct synthesis of heating patterns using the RFCM (see Chapter 2). Electronic scanning consists of producing a focal spot which is then swept over a predetermined trajectory (or surface) while the RFCM consists of simultaneously focusing at different points along a desired path (or surface). The two techniques will be investigated through computer simulations in Sections 4.6 through 4.9, and their produced intensity profiles will be compared and analyzed. Chapter 6 will focus on the temperature distributions associated with the different heating patterns. However, it is necessary at this point to define the scanned field intensity that results from sweeping a focal spot over a desired scan trajectory and the time averaged intensity which results from the direct synthesis of diffuse heating patterns. These definitions will be helpful in comparing the techniques and will prove useful for the analysis of the resulting thermal response in Chapter 6.

The scanned field intensity $I_{sc}(x,y,z)$ which will equivalently be called the time-averaged field intensity that results from sweeping a focal spot over N points distributed over a scan trajectory is defined as

$$I_{sc}(x,y,z) = \frac{\sum_{i=1}^{N} I_{i0}(x,y,z)\ t_i}{\sum_{i=1}^{N} t_i} = \frac{1}{T}\sum_{i=1}^{N} I_{i0}(x,y,z)\ t_i \tag{4.28}$$

where $I_{i0}(x,y,z)$ is the stationary field intensity profile resulting from focusing at point i, t_i is the time spent at point i (dwell time), and T is the scan period (time necessary to come back to point i after sweeping all the other points).

For the direct synthesis technique, the RFCM is used to simultaneously focus at different points along the scan trajectory. The technique results in a stationary diffuse field intensity profile (annular, elliptical, etc.) which does not require electrical or mechanical scanning. Because of the stationary nature of the resulting pattern, it is only necessary to multiply the time-averaged intensity profiles (same as temporal-peak for this case) by 2 α

where α is the pressure absorption coefficient (see Chapter 6) and to input the resulting power deposition pattern into the bioheat transfer equation. The maximum field intensity in the focal plane will be evaluated for all simulated profiles and serve as a characteristic of the directly synthesized heating patterns.

For all the directly synthesized heating patterns discussed in the remainder of this chapter, except that of Figure 4.11, the maximum field intensity evaluated in the focal plane is also the SPTP value associated with the pattern. As will be demonstrated, this SPTP value is substantially lower than those required by electrical and mechanical (see Chapter 3) scanning techniques.

4.6 Direct Synthesis of Field Intensity Profiles

Demonstrated in this section, is the ability of the FCM, when appropriately applied, to generate a variety of diffuse beam profiles that might prove useful in different ultrasonic applications. Besides their potentials in hyperthermia applications, laterally diffuse beams might be useful in other ultrasonic applications such as beam shaping and bioeffects experimentations [43]. The FCM is very well suited for the production of virtually any focal intensity profile. A variety of focal shapes ranging from very simple focal spots to the most diffuse elliptical or annular patterns are demonstrated. The goal of this section is to demonstrate the flexibility of the method to produce regular or irregular intensity profiles at different depths. Section 4.7 will focus on the possibility of using some of these profiles in hyperthermia applications. While this section is mainly concerned with the resulting pattern in the focal plane, Section 4.7 will investigate the behavior of the patterns in different planes as well. In particular, the formation of undesired secondary foci proximal or distal to the focal plane will be investigated. In addition, the time-averaged intensity gain in the focal plane will be computed to determine if enough therapeutic gain can be produced at the desired location.

Figure 4.8a) is a surface plot of an annular field profile at 100 mm depth. This pattern was synthesized by assuming an annular shaped source of 22.5 mm radius centered at (0, 0) in the plane z= 100 mm. The time-average intensity gain evaluated in the focal plane was found to be 3.9 dB. Figure 4.8b) illustrates the synthesis of a diffuse focal spot obtained by simultaneously focusing at (0, 10) and (0, 20) in the plane z= 100 mm. The synthesis of three simultaneous focal spots at (8, 8), (0, 0), and (-8, -8) in the plane z= 100 mm is shown in Figure 4.8c). The field intensity gain of the latest pattern evaluated in the focal plane was 6.1 dB.

Figure 4.9a) is a surface plot of an elliptical focal pattern at z=100 mm from the applicator surface. This pattern was produced by assuming 120 point sources distributed over the periphery of an ellipse of equation $(\frac{x}{12})^2+(\frac{y}{18})^2=1$. Two annular rings were also simultaneously produced by assuming two annular rings centered at (15, 15) and (-15, -15), respectively, in the plane z= 100 mm. The resulting pattern in the focal plane is shown in Figure 4.9b). Figure 4.9c) illustrates the synthesis of four simultaneous focal spots by assuming four small disk shaped sources at points (20, 20),(-20, 20),(-20, -20), and (20, -20) in the plane z= 100 mm.

A variety of spatially diffuse intensity profiles can also be produced by appropriately distributing the assumed sources in the focal plane. As a demonstration, a " line foci" was produced by assuming eight sources appropriately placed over the x-axis as shown in Figure 4.10a). More diffuse pattern can be generated by simultaneously synthesizing two or more crossing line foci as shown in Figures 4.10b) and c). Figure 4.10b) was obtained by simultaneously synthesizing two identical "line foci" over the X and the Y axis, respectively. Figure 4.10c) was obtained by uniquely varying the amplitudes of the different foci of the pattern of Figure 4.10b).

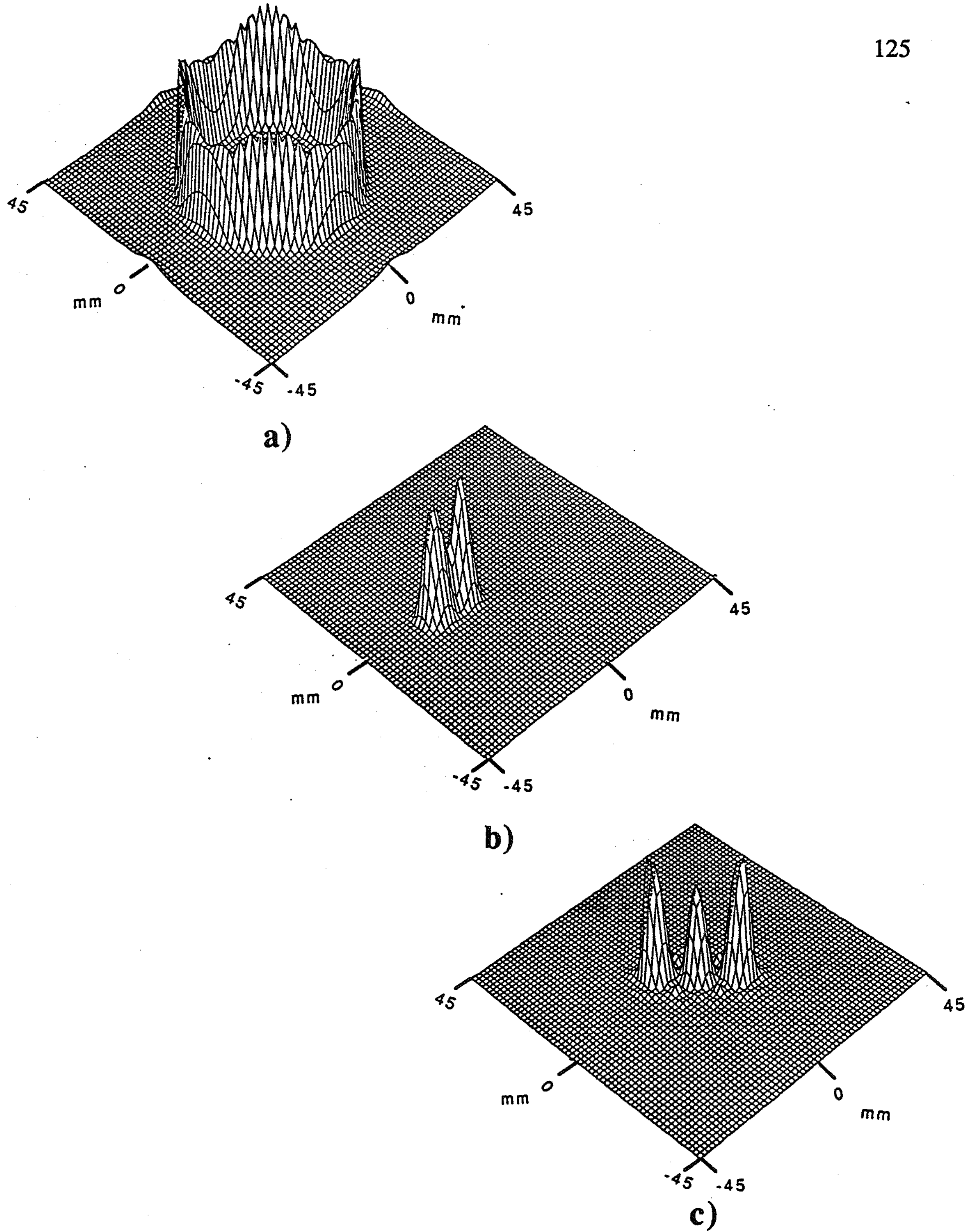

Figure 4.8. Direct synthesis of arbitrary field intensity profiles in the focal plane. a) Annular pattern. b) Broadened foci. c) Three simultaneous foci.

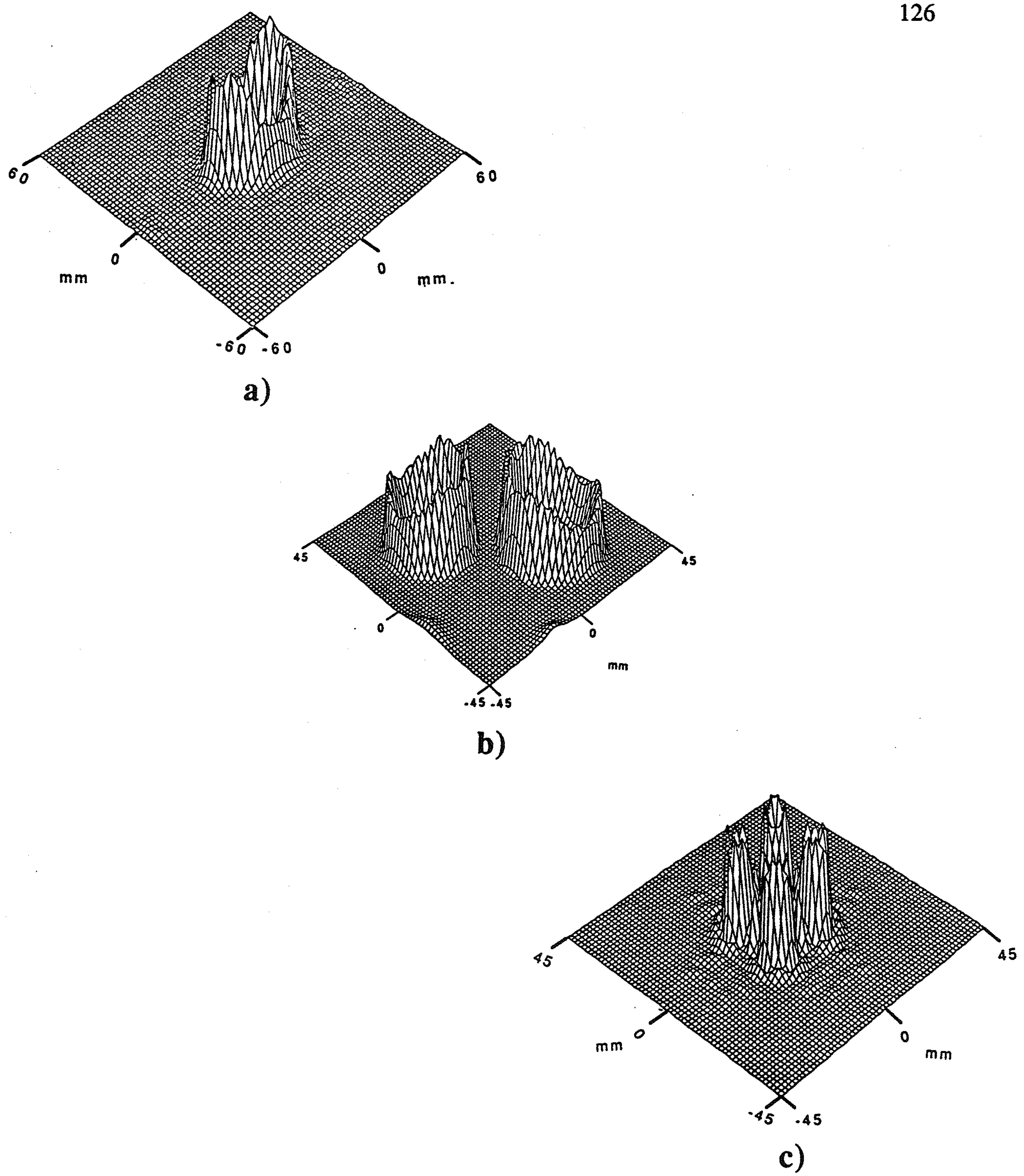

Figure 4.9. Direct synthesis of arbitrary field intensity profiles in the focal plane. a) Elliptical pattern. b) Two annular pattern in the same plane. c) Four simultaneous foci.

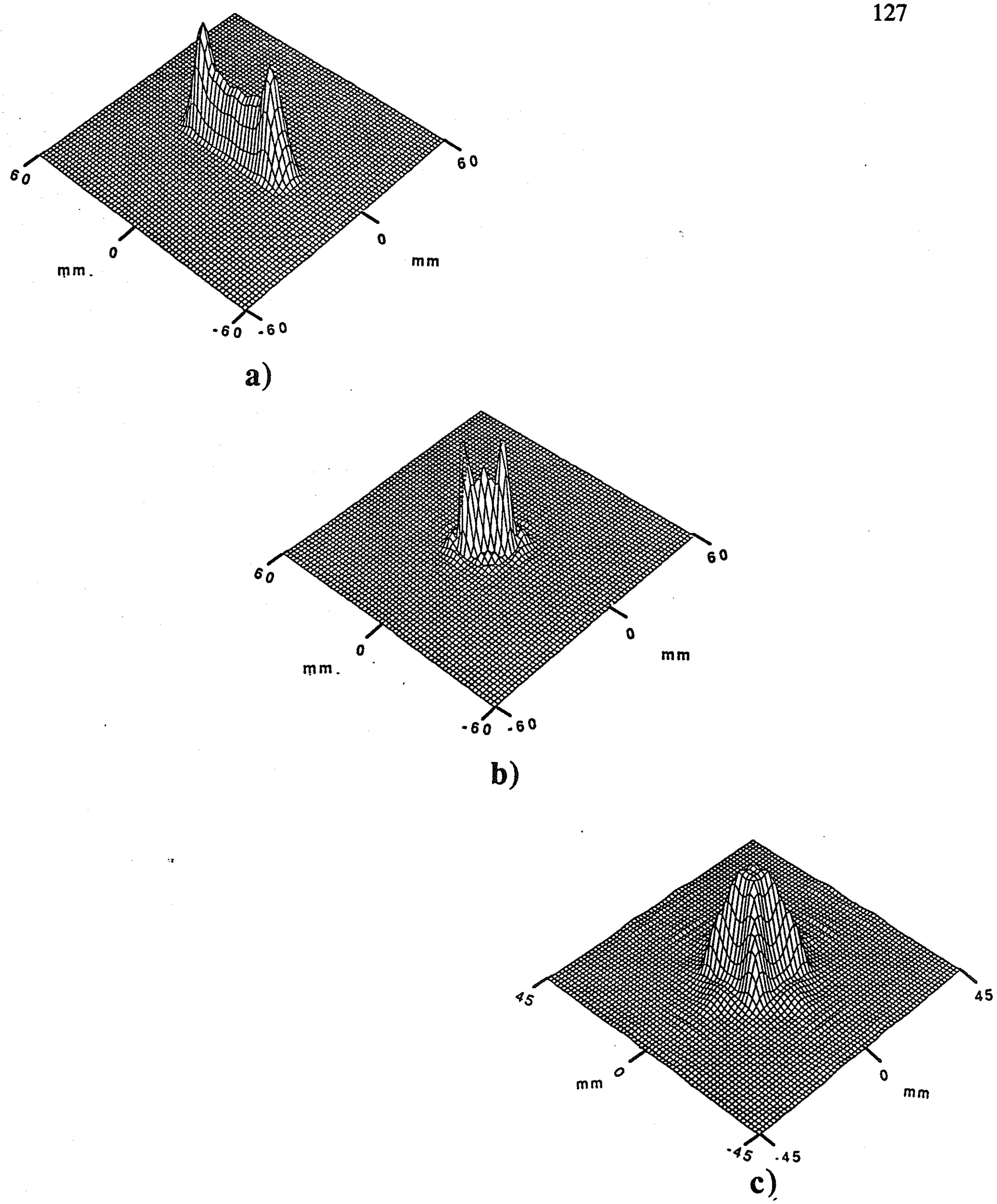

Figure 4.10. Direct synthesis of arbitrary field intensity profiles in the focal plane. a) " Line foci" produced by simultaneously focusing at eight focal points (see text). b) " Cross foci" produced by combining two line foci. c) A diffuse foci produced by combining line foci (see text).

4.7 Analysis of the Direct Synthesis of Heating Patterns

The capability of the FCM to tailor the focal intensity profile to virtually any desired shape was demonstrated in the preceding section. However, the question of usefulness of those patterns in hyperthermia applications was not addressed. For a hyperthermia treatment to be successful, the resulting temperature within the tumor should be higher than a minimum therapeutic temperature (i.e., 42^0 C) while the normal tissue temperature should remain under a certain safe temperature (i.e., 39^0C). The issue of the associated temperature distributions will be addressed in Chapter 6, where the 3-D bioheat transfer equation is solved and the resulting thermal response is discussed. This section will focus on the analysis of the power deposition patterns which are used as inputs to the bioheat transfer equation.

Figure 4.11a) shows an annular pattern of 45 mm diameter 100 mm depth from the applicator surface. This pattern was produced by assuming an annular ring of the same size centered at (0, 0) in the focal plane. Although the pattern is very well behaved in the focal plane(z=100 mm), a relatively strong secondary foci is developed on the axis of symmetry near the applicator surface as described in [29]. Figure 4.11b) is a surface plot of the power deposition pattern in a traverse plane near the array surface (z= 35 mm) where the maximum intensity is about 2.1 dB higher than that of the annular focus. As mentioned in Chapter 3, this problem can be partially resolved by accounting for the secondary foci to fall within the coupling medium (bolus). Another alternative is to use the RFCM to eliminate the secondary foci by appropriately phasing the different assumed sources (see Chapter 2). To synthesize an annular heating pattern, 22 fictitious sources were distributed over the periphery of a circle of diameter 45 mm in the plane z= 100 mm. The assumed sources were small disks of a 4 mm radius, and their excitation phase and amplitude were as described in Chapter 2. Figure 4.12 shows the resulting pattern in five transverse planes at depths ranging from 20 to 180 mm from the applicator surface. The time-averaged intensity gain evaluated in the focal plane is 4.92 dB. The time averaged intensity gain is

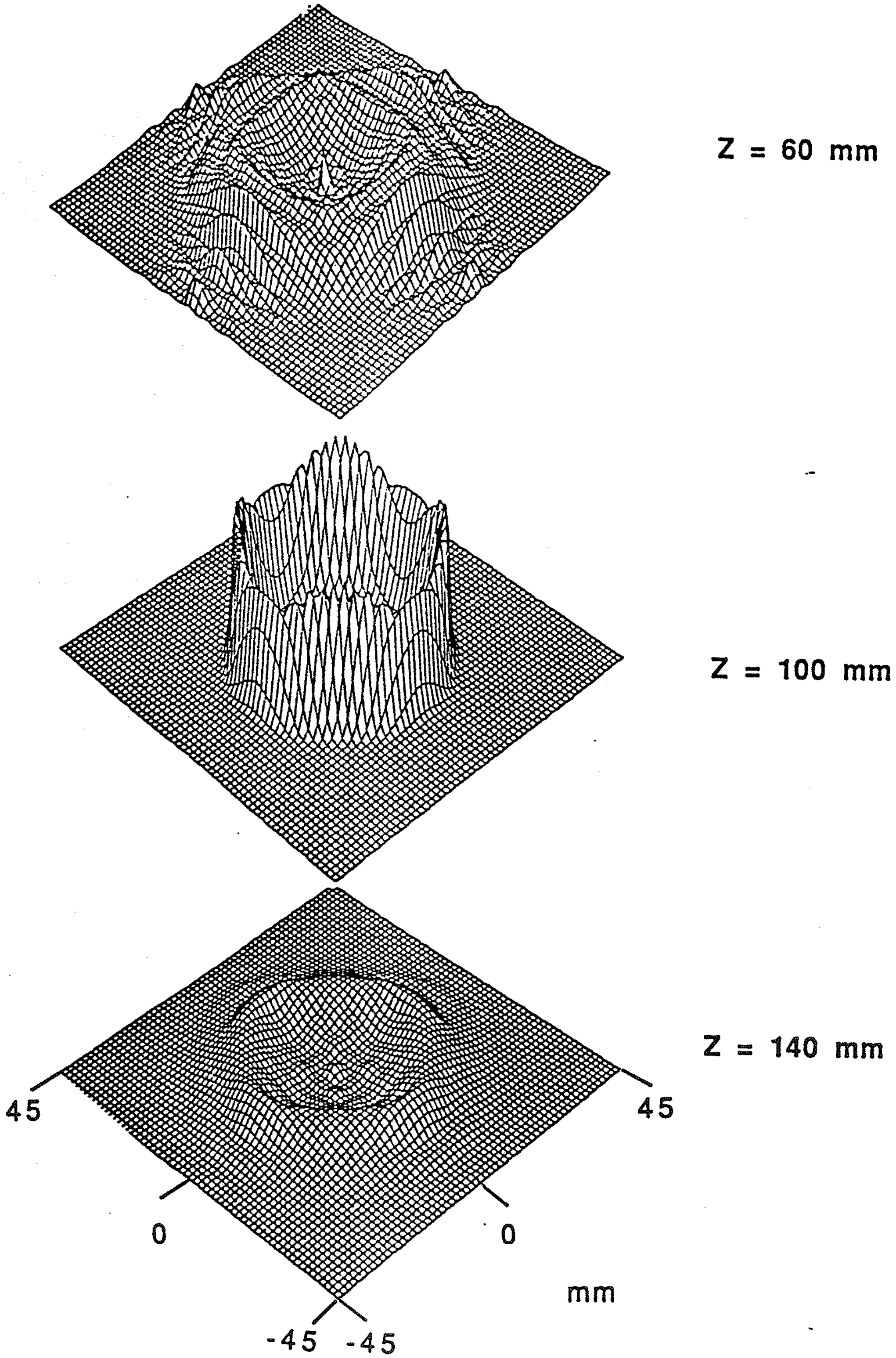

a)

Figure 4.11. Annular heating pattern of 25 mm radius at 100 mm depth synthesized using the FCM. a) A surface plot of the pattern in different transverse planes.

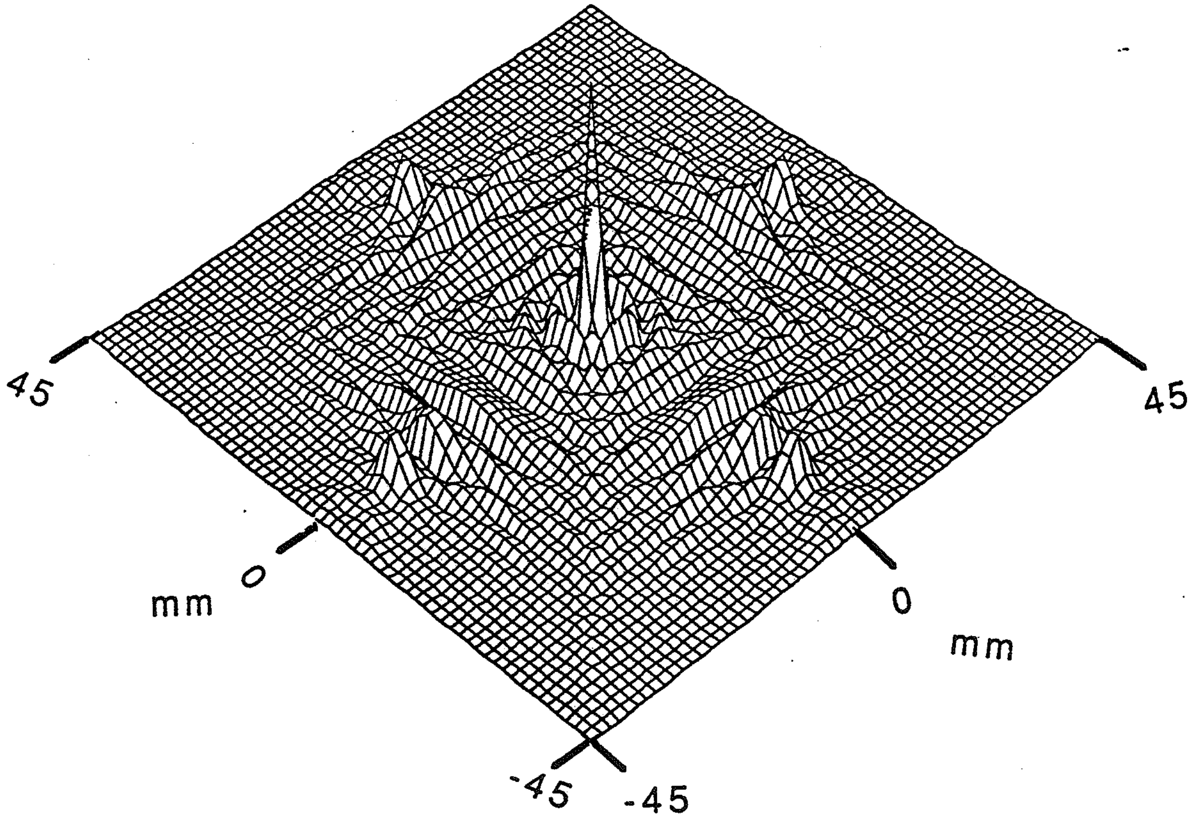

(b)

Figure 4.11. b) A surface plot of the pattern in a transverse plane at a proximity of the transducer surface (z=35 mm). The secondary foci intensity is about 2 dB higher than that evaluated in the focal plane.

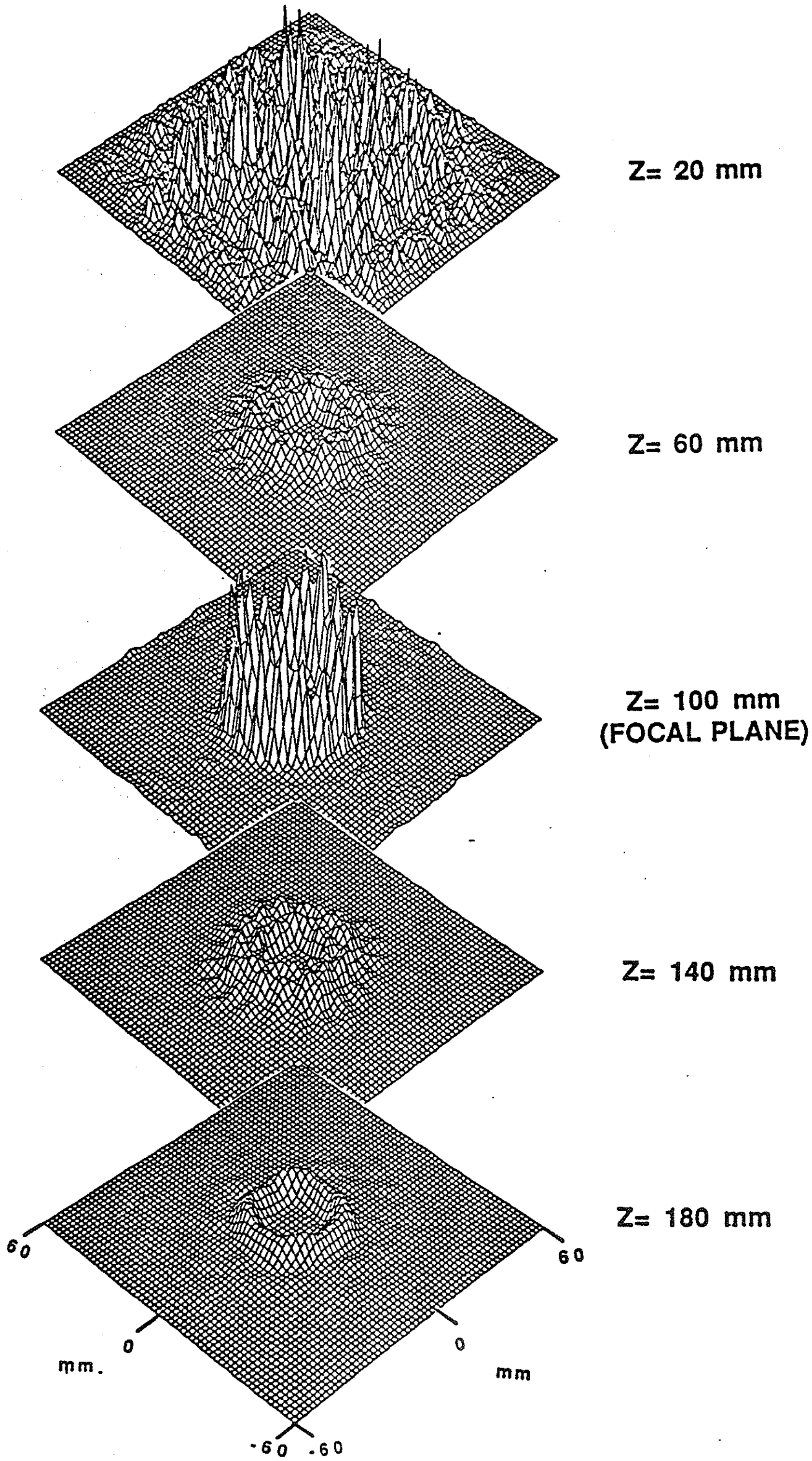

Figure 4.12. Annular heating pattern of 22.5 mm radius at 100 mm depth synthesized using the RFCM. Surface plot of the pattern in different transverse planes at different depths.

defined as the ratio of the maximum time-averaged intensity evaluated in the focal plane to the maximum intensity evaluated at the array surface. This time-averaged intensity gain, in the case of direct synthesis, is equivalent to the scanned field intensity defined customarily for scanning techniques.

The synthesis of an annular pattern of 21 mm diameter is illustrated in Figure 4.13. This pattern was synthesized by assuming eight sources (disk of 4 mm radius) over an annular path of a 10.5 mm radius centered at (0, 0) in the plane z= 100 mm. The resulting pattern is shown in different transverse planes, including the focal plane (z= 100 mm). The time-averaged intensity gain at the focal site is 8.11 dB. It has been shown in Chapter 3 that the direct synthesis technique would result in secondary foci far beyond the focal plane in some cases. In particular, the secondary focus intensity might exceed that of the annular foci especially when the synthesis of a small radius annular pattern was attempted. However, Figures 4.12 and 4.13 demonstrate that the appropriate use of the RFCM allow one to eliminate these unwanted foci prior or beyond the focal plane. The time-averaged intensity gain evaluated in the transverse planes at z= 140 and 180 mm are about 7.4 and 13 dB, respectively, less than that evaluated in the focal plane.

A larger size annular pattern was synthesized using 15 assumed sources distributed over the circumference of a 33 mm diameter circle at a 100 mm depth. Figure 4.14 is a surface plot of the resulting pattern in five transverse planes at different depths. The time-averaged intensity gain evaluated at the focal site was found to be 5.71 dB. A maximum time-averaged field intensity of 14.8 W/cm^2 would be produced in the focal plane if the array elements were able to deliver 4 W/cm^2 at their radiating surface.

From the different patterns simulated in this section, it is obvious that the appropriate use of the RFCM does not lead to secondary foci along the axis, a problem often associated with this kind of direct power deposition using specially designed lenses [20] or phased arrays [17].

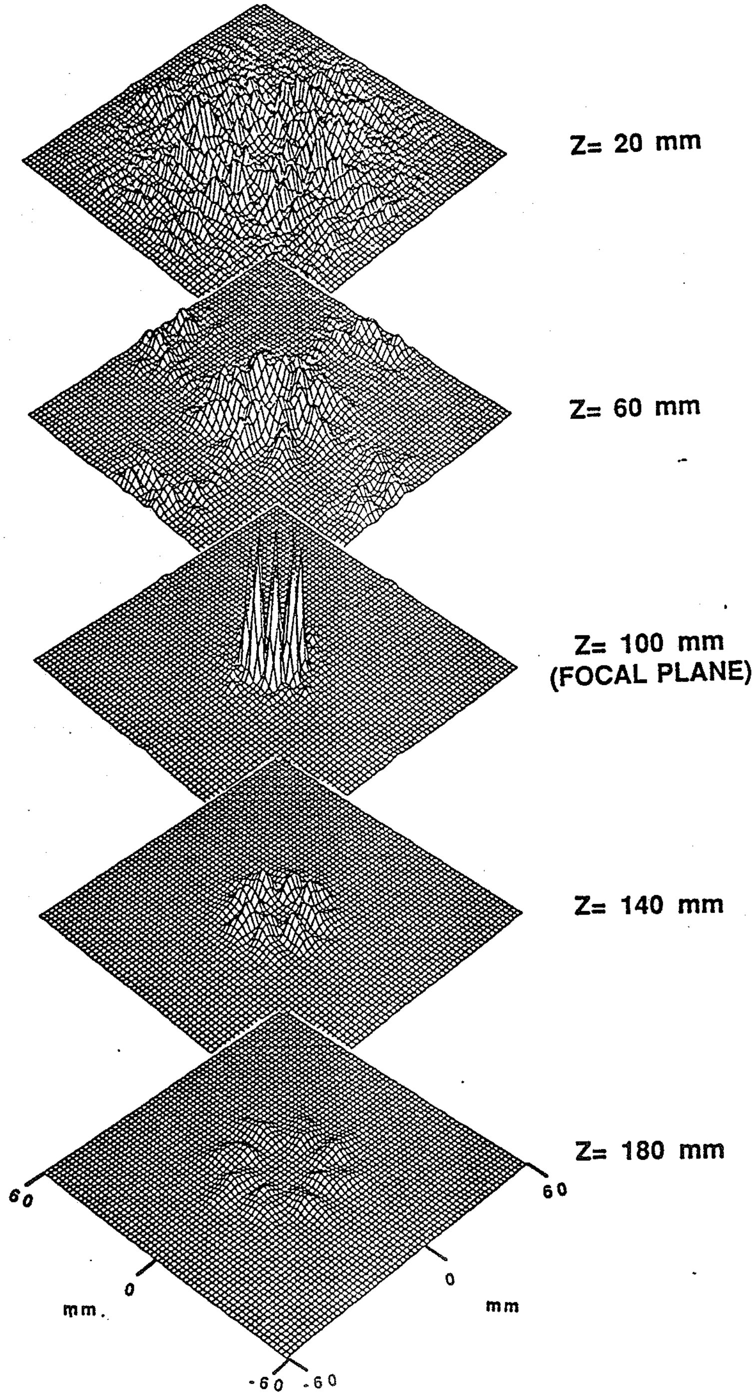

Figure 4.13. Annular heating pattern of 10.5 mm diameter at 100 mm depth synthesized using the RFCM. A surface plot of the pattern in different transverse planes including the focal plane.

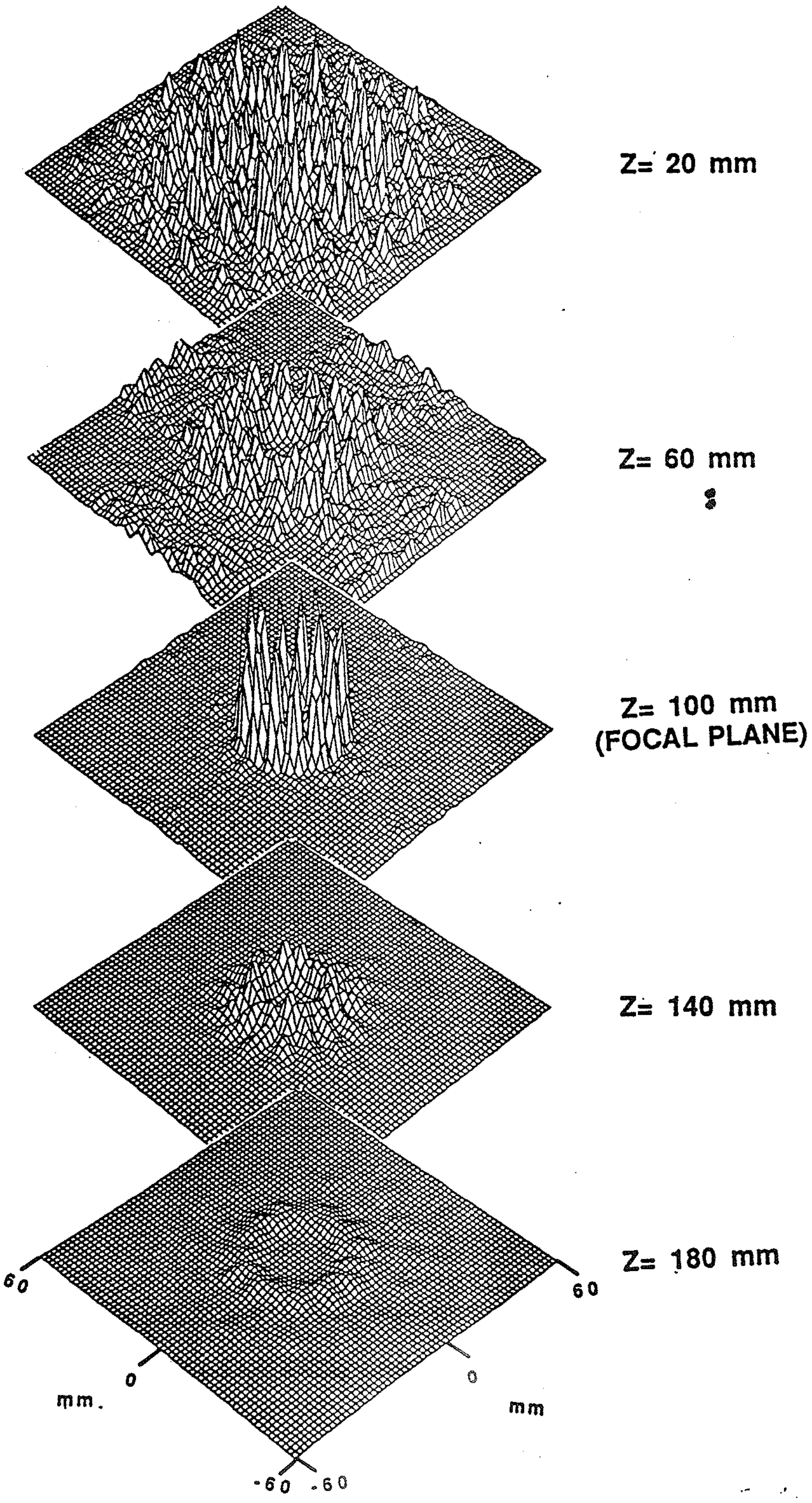

Figure 4.14. Annular heating pattern of 33 mm diameter at 100 mm depth synthesized using the RFCM. A surface plot illustrating the pattern in different transverse planes at different depths.

4.8 Electronic Scanning Versus Direct Synthesis of Heating Patterns

Both the FCM and the RFCM were shown to be able to directly synthesize diffuse heating patterns of different types. In particular, it was demonstrated that annular heating patterns could by synthesized by assuming a suitable number of fictitious sources appropriately distributed over the periphery of the desired pattern to be synthesized. This technique can be used as an alternative to the electronic scanning of an intense focal spot. Scanning is usually proposed as a means of producing diffuse heating patterns.

In this section, the direct synthesis and the electronic scanning techniques are used to synthesize some desired power deposition patterns and the resulting patterns are compared. While the comparison will be uniquely based on power deposition concepts in this section, Chapter 6 will focus on the resulting temperature distributions associated with the two techniques.

Two tumor models, different only by their cross-sectional diameters, are considered for simulations. A small tumor model of 13 mm diameter and a large one of 45 mm diameter are used for comparison. It is desired to deposit the ultrasonic energy around the periphery in annular fashion by using the RFCM and the electronic scanning method, respectively. The RFCM is first used to synthesize an annular pattern of radius equivalent to that of the model to be heated. To make a valid comparison, the number of scanning points (points needed to produce an annular pattern by electronic scanning) is taken equal to the number of fictitious sources required by the RFCM. In addition, the electronic scanning SPTP focal intensity is adjusted to achieve a scanned field intensity gain equivalent to the time-averaged intensity gain produced by the the first approach (RFCM) in the focal plane.

To synthesize an annular pattern of a 13 mm diameter at a 100 mm depth, it was necessary to assume five sources (disk shaped of 4 mm radius) around the periphery of the model. The surface plot of the resulting pattern is shown in Figure 4.15a). The time-

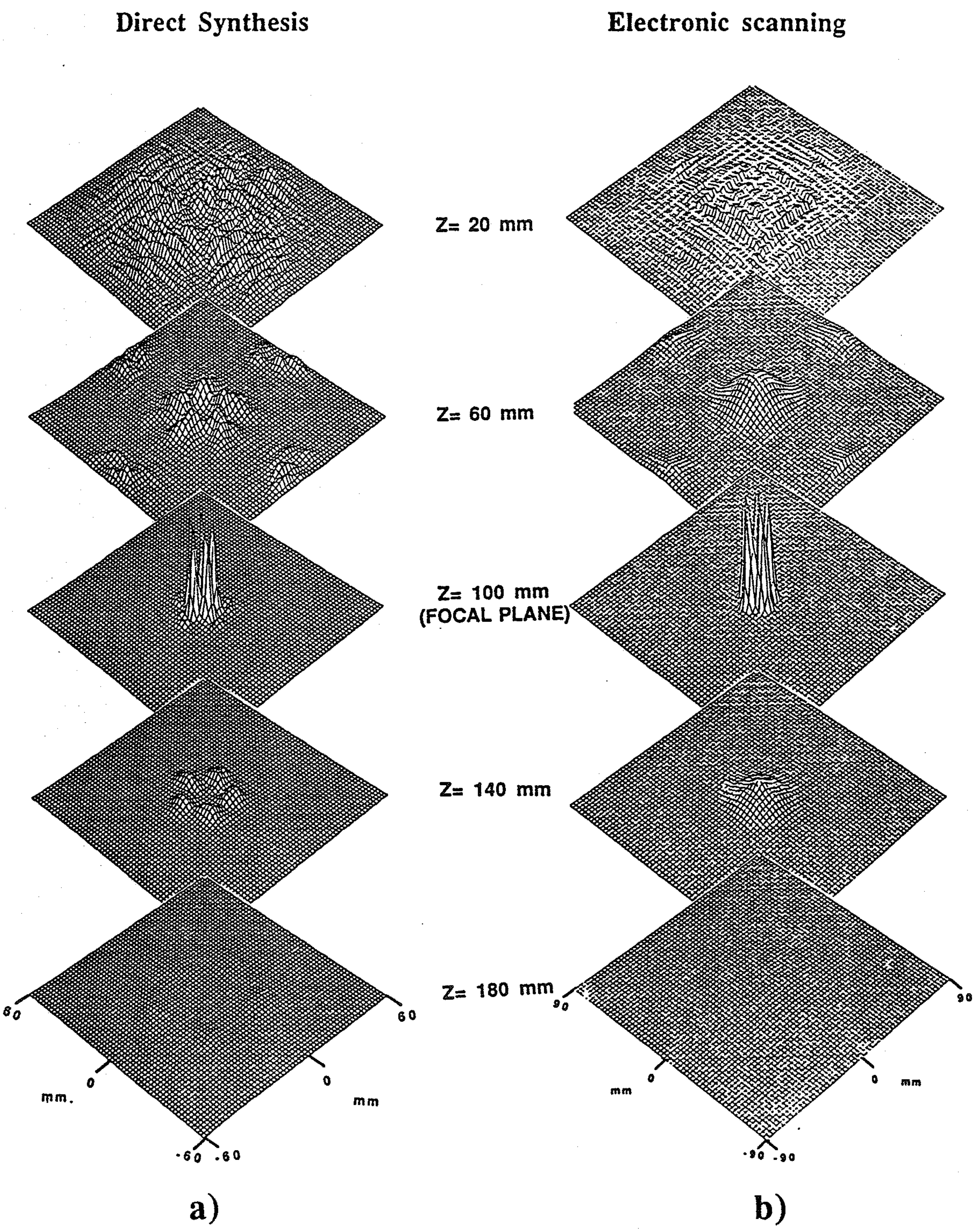

Figure 4.15. Comparison between the synthesis of a 13 mm diameter annular pattern at 100 mm depth using different methods. a) Pattern synthesized using the RFCM and b) the same pattern synthesized by electronic scanning.

averaged intensity gain evaluated in the focal plane was 10.1 dB. Figure 4.15a) illustrates the pattern in five transverse planes at different distances from the applicator. The electronic scanning was achieved by producing a focal spot that was then swept over five points, around the periphery, by adjusting the excitation signals of the individual elements. The locations of scan point were chosen to coincide with that of the assumed sources of the RFCM synthesis. Figure 4.15b) shows the resulting pattern in five transverse planes identical to those shown in Figure 4.15a). To obtain a scanned field intensity gain of 10.1 dB, it was necessary to use an SPTP focal intensity gain of 17.14 dB.

The direct synthesis of an annular pattern of a larger radius was achieved in similar fashion. The field intensity profiles resulting in different transverse planes are shown in Figure 4.16a). To produce this pattern, it was necessary to assume 20 sources distributed uniformly over the model periphery. The time-averaged field intensity gain, in the focal plane (z=100 mm), was 4.45 dB. This pattern would result in a maximum time-averaged intensity of 11.04 W/cm^2 when the array elements were assumed to vibrate at their maximum tolerable surface velocity (corresponding to a maximum intensity of 4 W/cm^2 at the array surface). Figure 4.16b) illustrates the pattern produced by electronically scanning an intense focal spot over the model periphery. For the sake of comparison, the scan point locations were chosen to coincide with those of fictitious sources assumed in the first approach. To achieve a scanned field intensity gain of 4.45 dB, it was required to use an SPTP focal intensity gain of 17.6 dB. The SPTP focal intensity required to result in a scanned intensity of 11.04 W/cm^2 was approximately 220 W/cm^2.

From the above simulations, it is obvious that both electronic scanning and direct synthesis can be equivalently used to achieve intensity gain at depth. Spatially diffuse power deposition patterns can be produced either by synthesizing a focal spot which is then translocated electronically over a desired trajectory or by establishing the driving phase and

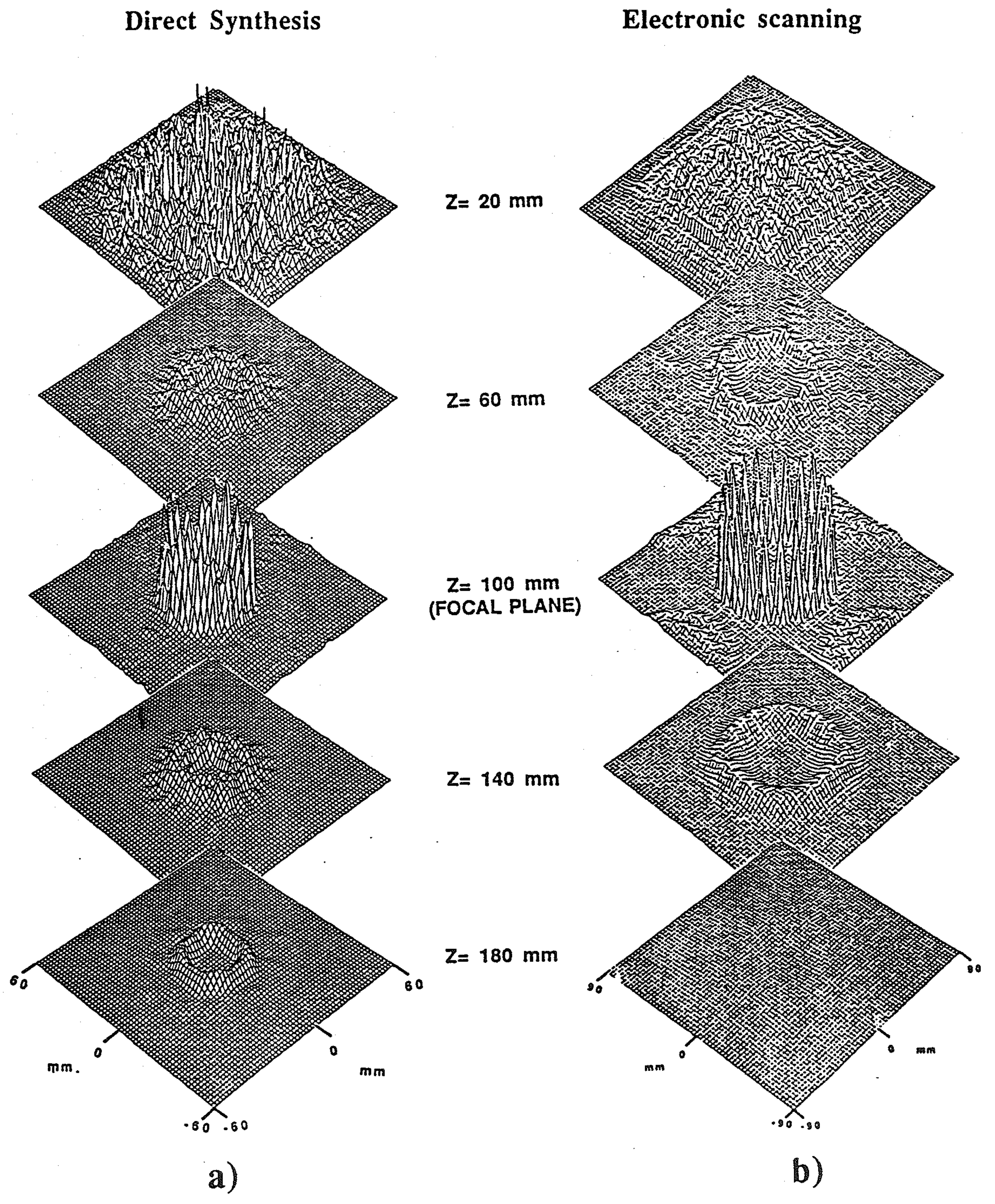

a) b)

Figure 4.16. Comparison between the synthesis of a 45 mm diameter annular pattern at 100 mm depth using different methods. a) Pattern synthesized via the RFCM and b) the same pattern synthesized by electronic scanning.

amplitude distributions for the direct synthesis (RFCM). The two techniques lead to similar power deposition patterns, as can be seen from Figures 4.15 and 4.16. However, the electronic scanning technique requires a substantially higher SPTP focal intensity, than those used generally in the direct synthesis technique, to produce the same time-averaged intensity necessary to induce therapeutic effects. The use of the direct synthesis technique might be preferable when nonthermal undesired effects (i.e., cavitation) are of concern [30]. Both techniques lead to very well behaved power deposition patterns at different depths (i.e., no secondary foci near the transducer or far beyond the focal plane) as could be seen from the different simulations. However, the direct technique seems to result in a relatively long depth of field (longitudinal extension of the 3 dB focal region) in the case of large annular pattern synthesis. While the time-averaged focal intensity drops sharply beyond the focal plane (more than 6 dB in less than 35 mm), the 3 dB focal region seems to extend to about 40 mm toward the transducer (a drop of 2 dB only at z= 65 mm). This elongation might be desirable in some cases, such as heating large cylindrically shaped tumors.

4.9 Electronic Scanning at Reduced SPTP Focal Intensity

By simultaneously focusing on two or more locations at a certain depth, it is possible to produce a diffuse power deposition pattern that can be scanned electronically to heat a large tumor tissue volume. The advantage of this technique is to reduce the number of the required scan points compared to those needed for conventional scanning and, hence, to use a relatively reduced SPTP focal intensity. The multiple focusing feature allows one to split the focused beam intensity among the different foci and consequently, the focused energy is distributed over a larger cross section. This feature might be used to avoid the occurrence of some nonthermal effects such as cavitation and nonlinear saturation. In the following, two different methods are proposed as a means of electronically scanning at reduced SPTP focal intensity. The associated temperature distributions are discussed in Chapter 6.

The first method consists of the temporal scanning of two or more annular power deposition patterns. While depositing the ultrasonic energy around the periphery of a small tumor might be adequate for heating, heating larger tumors might require some additional power deposition towards the tumor core. To obtain a uniform heating of a tumor, the scan period can be divided appropriately among the different annular patterns leading to the desired diffuse heating pattern. To demonstrate, an annular pattern of 33 mm diameter was synthesized by assuming 15 sources (4 mm radius disks) as described in Section 4.7. Figure 4.14 illustrates the resulting pattern at different depths. The time averaged intensity gain evaluated in the focal plane was 5.71 dB. To heat uniformly a tumor of 33 mm diameter, it might be necessary to deposit some ultrasonic energy close to the tumor center in addition to that deposited around the periphery. To accomplish this, this pattern was temporally scanned with the pattern of Figure 4.13 (annular pattern of 21 mm radius). Figure 4.17 illustrates the scanned field intensity obtained by the procedure. A time-averaged intensity gain of 5.5 dB was evaluated in the focal plane. To obtain this pattern, 0.62 of the scan period was spent on the larger annular pattern while the remaining fraction was spent on the smaller one. To produce a time-averaged intensity of approximately 10 W/cm^2 (within the 3 dB region), it was necessary to use an SPTP focal intensity of 25.4 W/cm^2 for this kind of scanning. This value of focal intensity is still substantially lower than typical values used in conventional scanning (Section 4.7).

Another method consists of producing multiple focal spots at different locations in the focal plane. These foci are then swept simultaneously by adjusting the driving electronics. Figures 4.18 and 4.19 illustrate the direct synthesis of three and four simultaneous foci in the focal plane (z= 100 mm). Figure 4.18 is the surface plot of the synthesis of three foci in different transverse planes ranging in depth from 20 to 180 mm

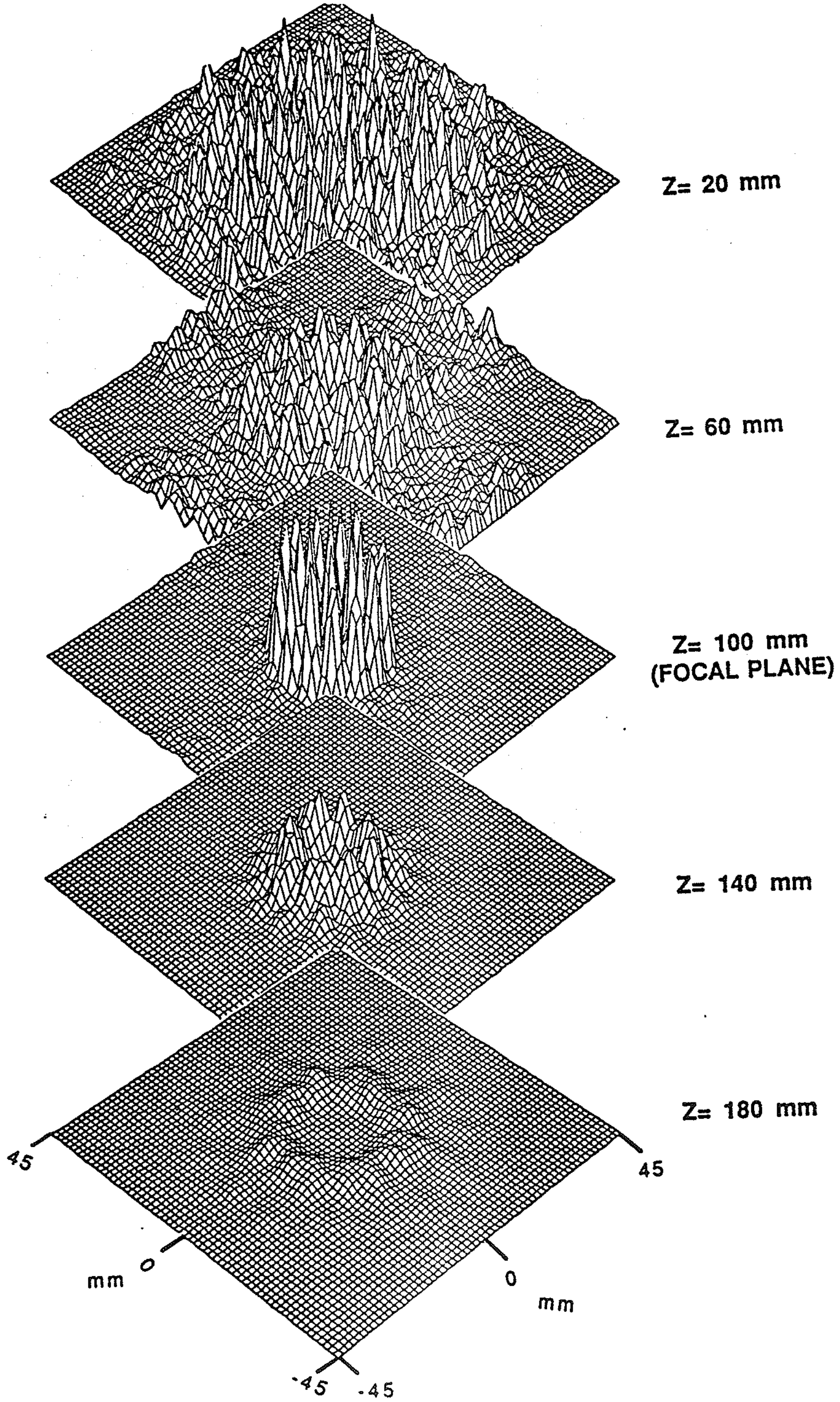

Figure 4.17. Temporal scanning of two directly synthesized annular patterns. A surface plot of the pattern resulting from temporally scanning a 33 and a 21 mm diameter annular patterns.

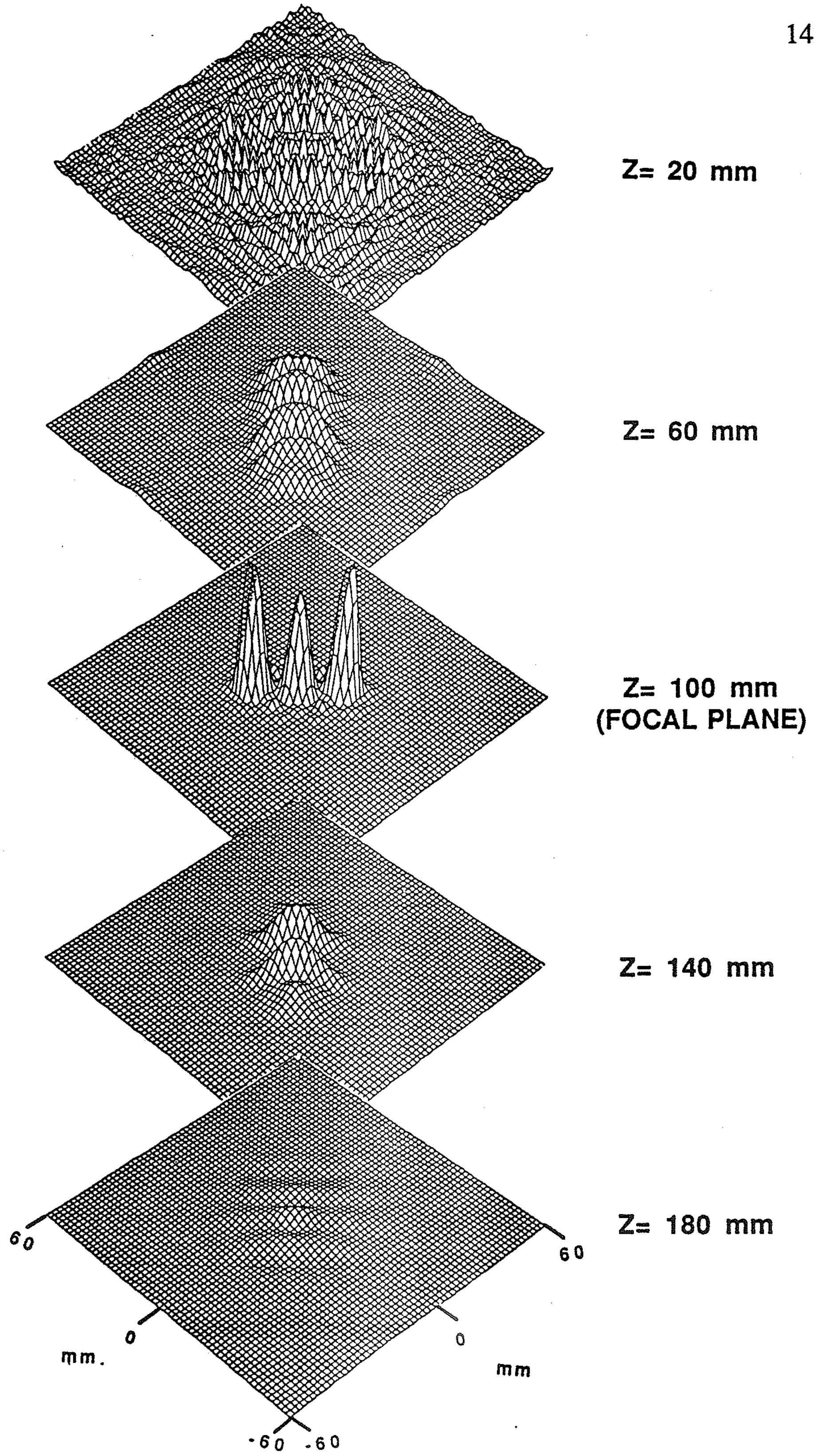

Figure 4.18. Multiple focusing synthesis of heating patterns. A surface plot of a field intensity pattern produced by simultaneously focusing at (8,8),(0,0), and (-8,-8) at 100 mm depth.

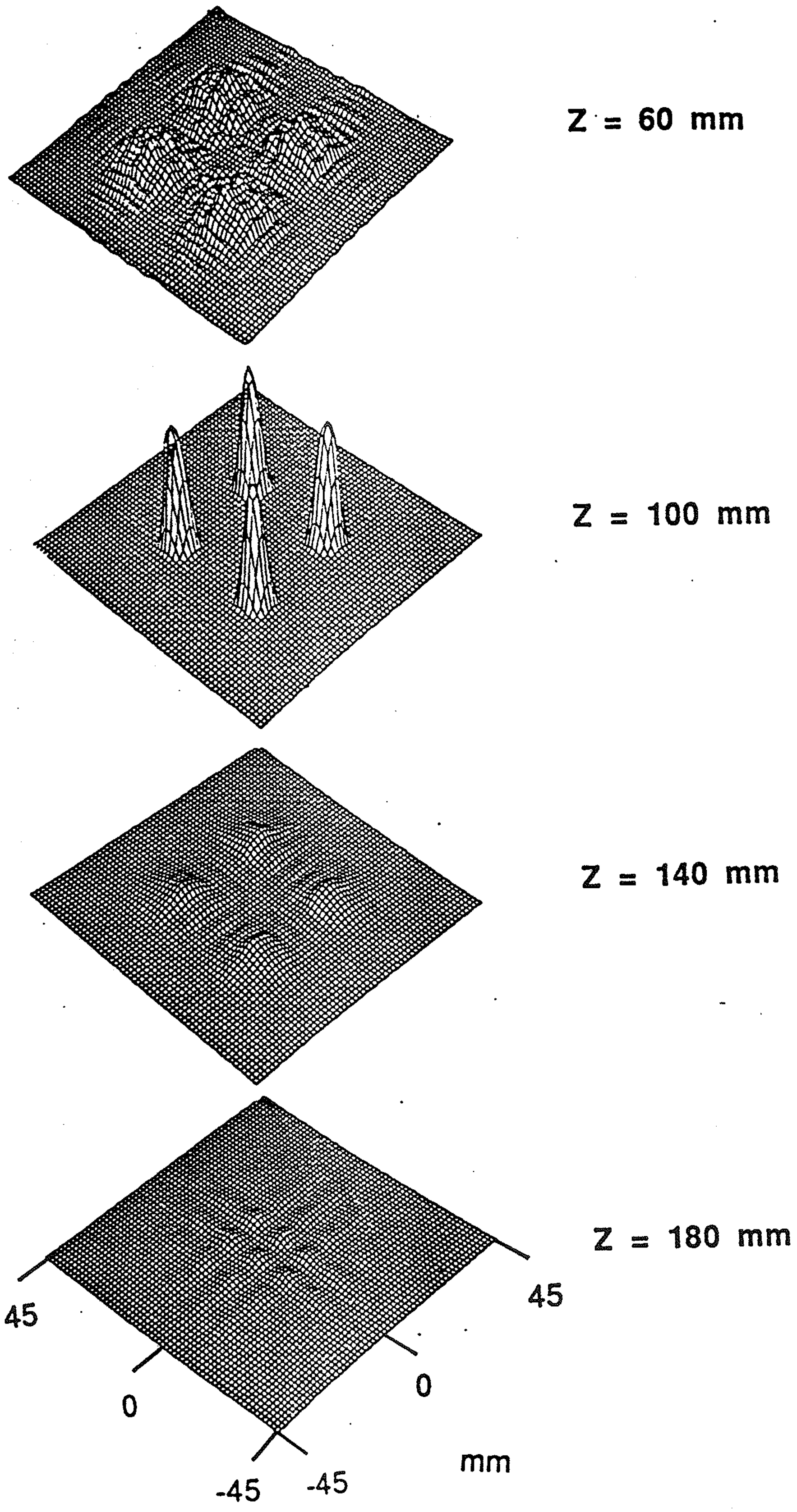

Figure 4.19. Multiple focusing synthesis of heating patterns. A surface plot of the pattern produced by simultaneously focusing at 4 points in the plane z=100.

from the applicator surface. This pattern was synthesized by assuming three disk shaped sources each of a 4 mm radius at (8, 8), (0, 0), and (-8, -8) in the plane z= 100 mm. The view of the pattern in the focal plane was rotated by 90° to show the relative amplitude of the different foci. Figure 4.19 is a surface plot of the synthesis of 4 simultaneous focal spots at a 100 mm depth. This pattern was achieved by assuming four simultaneous vibrating sources at (20, 20), (20, -20), (-20, -20) and (-20, 20), respectively. A time-averaged intensity gain of 4.15 dB was evaluated in the focal plane.

The method consists of directly synthesizing a diffuse focal pattern (multiple focal spots) which is then swept over a carefully designed scan trajectory. Examples of possible scan trajectories for the patterns shown in Figures 4.18 and 4.19 are illustrated in Figure 4.20a) and b), respectively..

As a demonstration, three simultaneous foci were synthesized at points (0, 7), (0, 0), and (0, -7) as shown in Figure 4.21a) which is a contour plot of the resulting pattern in the focal plane. The time-averaged field intensity gain evaluated in the focal plane (z= 100 mm) was 11.79 dB. By rotating the "line foci" of Figure 4.21a) by 45^0 counter clockwise, the diffuse pattern of Figure 4.21b) resulted. To scan a larger area, The line was temporally rotated by 135 ^{0} with uniform intervals of 45^0 and the resulting contour plot is shown in Figure 4.21c). To achieve a time-averaged intensity of approximately 10 W/cm^2 in the focal plane (3 dB region), it was necessary to use an SPTP focal intensity of 40 W/cm^2. However, if conventional scanning were to be used, an SPTP focal intensity of 90 W/cm^2 would have been needed. In conclusion, combining the direct synthesis and the electronic scanning techniques might prove useful in hyperthermia applications.

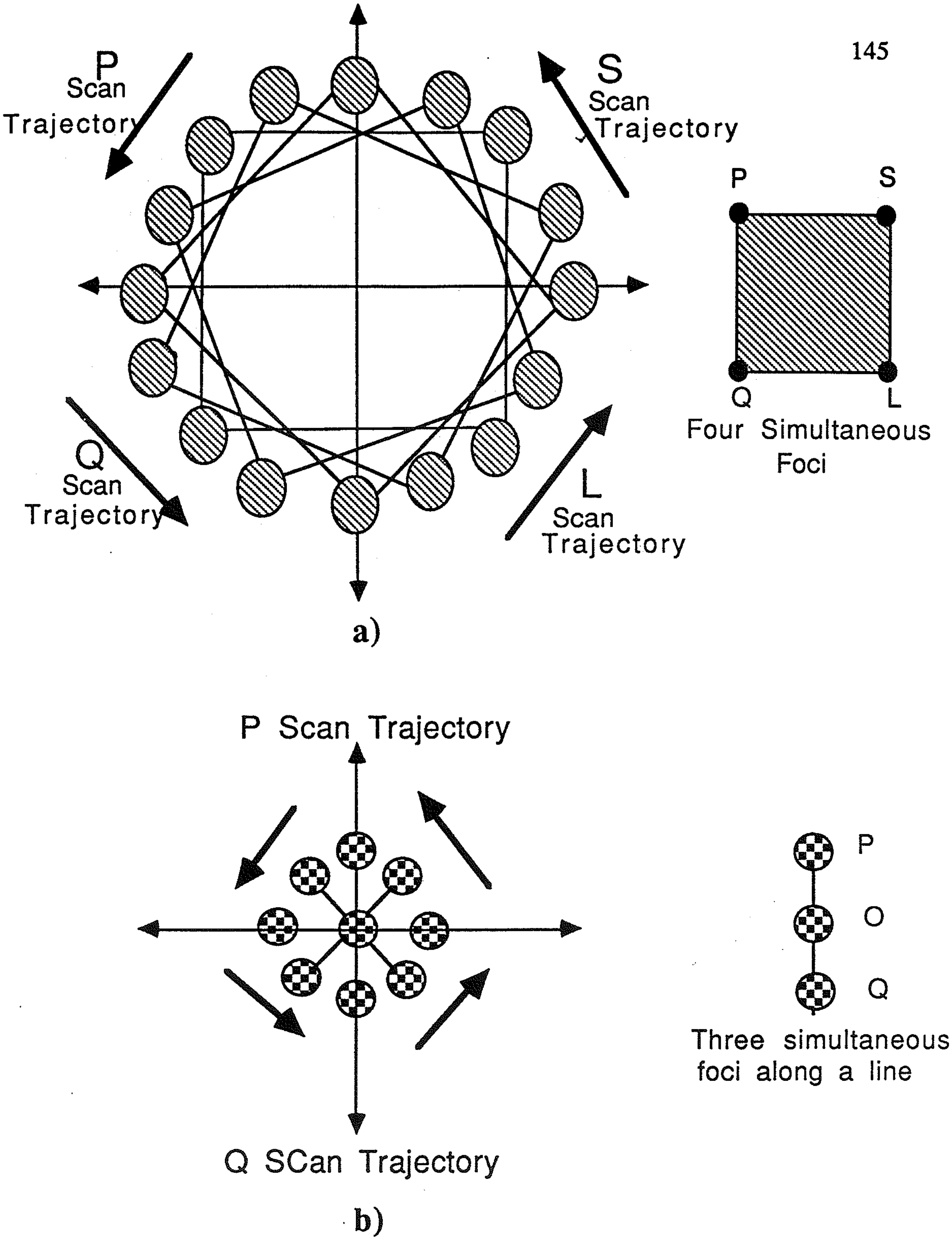

Figure 4.20. Scan trajectories. a) a schematic of a scan path that could be used for the pattern of Figure 4.19 and b) a scan trajectory that might be used for the pattern of Figure 4.18 (see text).

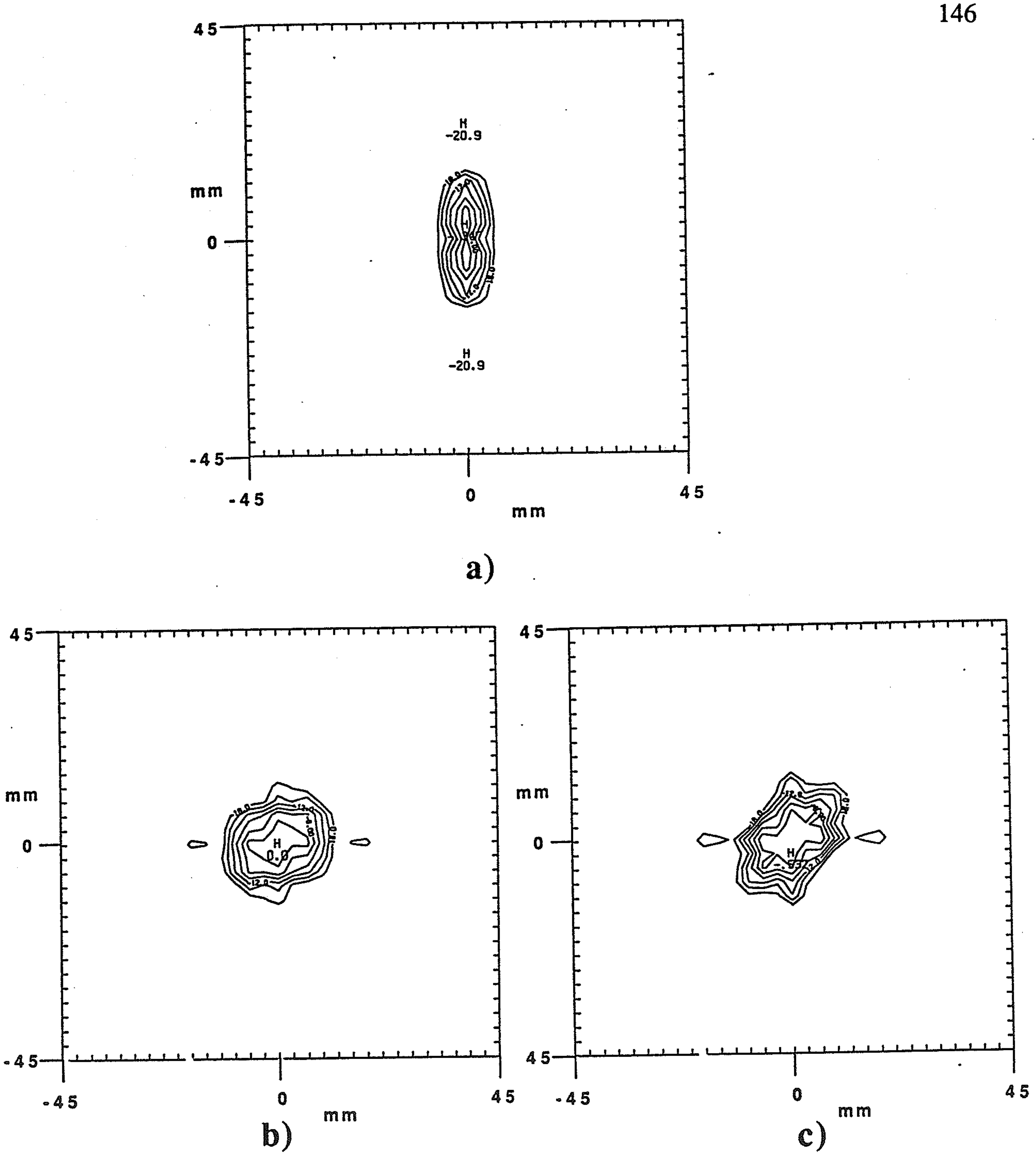

Figure 4.21. Temporal scanning of directly synthesized patterns. a) A contour plot of the focal pattern resulting from simultaneously focusing at (0,7),(0,0), and (0,-7) in the plane z=100 mm. b) A diffuse foci resulting from temporally scanning the "line foci" of a) over two positions and c) over three positions (see text).

4.9 Conclusions

In this chapter, a comprehensive investigation of the FCM and the RFCM was conducted. The geometry of the NxN square-element array allowed the production of different field intensity profiles that were not achievable using the CRA geometry. Besides their possible potential in hyperthermia applications, the different diffuse intensity profiles might be candidates for other ultrasound applications as well. Synthesis of field intensity profiles of regular and irregular shapes were shown to be possible. In particular, annular patterns of different sizes were synthesized using the RFCM. While this type of annular foci was shown to result in undesired secondary foci along the axis (Chapter 3), the phase rotation property of the RFCM allows the complete elimination of such secondary foci in the case of the NxN applicator. In addition, the production of small radius annular patterns was shown to be possible without the complexity of developing a serious secondary foci far beyond the focal plane as described in Chapter 3.

The comparison between direct synthesis and the electronic scanning techniques lead to the conclusion that the direct synthesis of small diffuse annular patterns (of diameter less than 20 mm) can be used as an alternative to scanning. However, the direct synthesis of larger annular foci might lead to a larger depth of field compared to that produced by electronic scanning. The direct synthesis allows the use of substantially reduced SPTP focal intensity compared to those typically used in electronic scanning. In addition, the possibility of combining electronic scanning with the direct synthesis techniques was also discussed.

The temperature distributions associated with some of the investigated power deposition patterns will be discussed in Chapter 6. The 3-D bioheat equation will be solved numerically, and conclusions concerning the method and the applicator performance will be made.

CHAPTER 5

SIMULATED TEMPERATURE DISTRIBUTIONS ASSOCIATED WITH HEATING BY A CONCENTRIC-RING APPLICATOR

5.1 Introduction

The power deposition patterns produced by a CRA were investigated in Chapter 3. Different power deposition patterns, ranging from simply focusing on the axis of the array to producing multiple annular foci, were demonstrated. Chapter 3 was limited to the synthesis of field intensity profiles, the formation of secondary foci, and to the comparison of the resulting patterns with those produced by other techniques. The temperature distributions associated with those power deposition patterns were purposely left out to allow for a complete investigation of the direct synthesis technique. Moreover, a temperature study at that point would imply that the use of the direct synthesis technique was limited to hyperthermia applications. Although the ultimate goal of this thesis is to investigate the analysis and design of hyperthermia applicators, the scope of Chapters 3 and 4 might include other applications, such as beam shaping, imaging, and tissue characterization [42]. Chapter 3 also emphasized the differences between several synthesis techniques and discussed some geometrical limitations of the applicator (CRA).

This chapter will focus on the simulated temperature distributions associated with the different patterns investigated in Chapter 3. The purpose of this study is to test the potential of the synthesized patterns, or at least some of them, in hyperthermia cancer therapy. The design of phased arrays in hyperthermia depends strongly on the produced temperature distribution in the body. While the temperature inside the treated volume must be raised above a certain minimum therapeutic temperature, the normal tissue temperature should not exceed a specified maximum temperature for safe treatment. Furthermore, while a very high temperature within the tumor might limit the treatment due to pain, cold spots within the treatment volume might contribute to even accelerating the tumor growth rather than to its regressing [43]. The bioheat transfer equation provides a means of evaluating the performance of the CRA, or any other hyperthermia applicator, and allows one to judge the relative ability of different applicators to satisfy the different requirements of a safe and effective treatment.

In this chapter, the power deposition patterns produced by the CRA are used as inputs to the bioheat transfer equation which is then solved numerically for the temperature distribution. An evaluation of the CRA as a means of inducing hyperthermia based on the temperature distributions is then given. The temperature distributions associated with the synthesis of multiple foci along the axis and those resulting from annular intensity patterns are discussed. The mechanical scanning of the CRA, suggested in Section 3.7, is evaluated as a means of heating moderate and deep seated tumors.

5.2 The Steady State Bioheat Transfer Equation (BHTE)

Because of the cylindrical symmetry of the array, and hence the resulting power deposition pattern, it is convenient to use the bioheat transfer equation in cylindrical coordinates given by

$$\frac{\delta^2 T}{\delta r^2}+\frac{1}{r}\frac{\delta T}{\delta r}+\frac{1}{r^2}\frac{\delta^2 T}{\delta \phi^2}+\frac{\delta^2 T}{\delta z^2}+\frac{W_b C_b}{K}(T_b-T)+\frac{Q(r,z)}{K}=\frac{1}{K}\frac{\delta T}{\delta t} \tag{5.1}$$

where K is the conductivity (W/m/°C), (r,z,ϕ) is the cylindrical coordinates system, T is the temperature (° C) at the point (r,z,ϕ), W_b is the blood perfusion in Kg/m^3/s, C_b is the blood heat capacity (J/Kg/° C), T_b is the arterial blood temperature, and Q is the power deposition density (W/m^3) defined as $2\alpha I(r,z)$ where α is the pressure absorption coefficient (cm^{-1}) and $I(r,z)$ is the field intensity (W/cm^2) [44,45].

The time dependency of Eq. (5.1) can be dropped, as a first approximation, because most of the treatment time is spent in providing enough heat to maintain the temperature and because of the stationary nature of the input (which is generated by the direct synthesis). Furthermore, because of the radial symmetry of the power generated by a CRA and by choosing a cylindrical anatomical model, Eq. (5.1) can be simplified to give

$$\frac{\delta^2 T}{\delta r^2} + \frac{1}{r}\frac{\delta T}{\delta r} + \frac{\delta^2 T}{\delta z^2} + \frac{Q(r,z)}{K} + \frac{W_b C_b}{K}(T_b - T) = 0 \tag{5.2}$$

Equation (5.2) can be solved using numerical techniques such as finite difference or finite elements. However, the choice between these two techniques is mainly governed by the nature of the considered anatomical model and the regularity of the boundary conditions of the problem. These different issues will be discussed in the following sections.

5.2.1 Thermal anatomical model

A model similar to that proposed by Roemer et al. [38] is considered for the computation of the temperature distributions. The model consists of four normal tissue layers, each characterized by its own thickness, thermal conductivity, and blood perfusion. The layers are skin, fat, muscles, and viscera, respectively. Moreover, the medium is assumed homogeneous and strong reflectors such as bones and gas cavities are excluded. The tumor itself, embedded in the viscera, consists of three concentric regions which can have different blood perfusion rates (w_1, w_2, w_3). Figure 5.1 illustrates the considered anatomy. The values of the thermal conductivity and thickness of the different layers are given in Table 5.1. The tumor volume and depth will be varied to allow the investigation of different design parameters of the CRA. A uniform blood perfusion rate, both in normal and tumor tissue, will be assumed. The tumor conductivity is assumed to be that of the viscera. The radial and axial extents of the model are considered infinite, and the temperature at the walls of the 2-D grid can be identified with the body temperature (37 °C). The skin temperature is assumed to be 25 °C. However, the effect of cooling the skin by circulating cold water through the coupling medium might be simulated by assuming lower skin temperature.

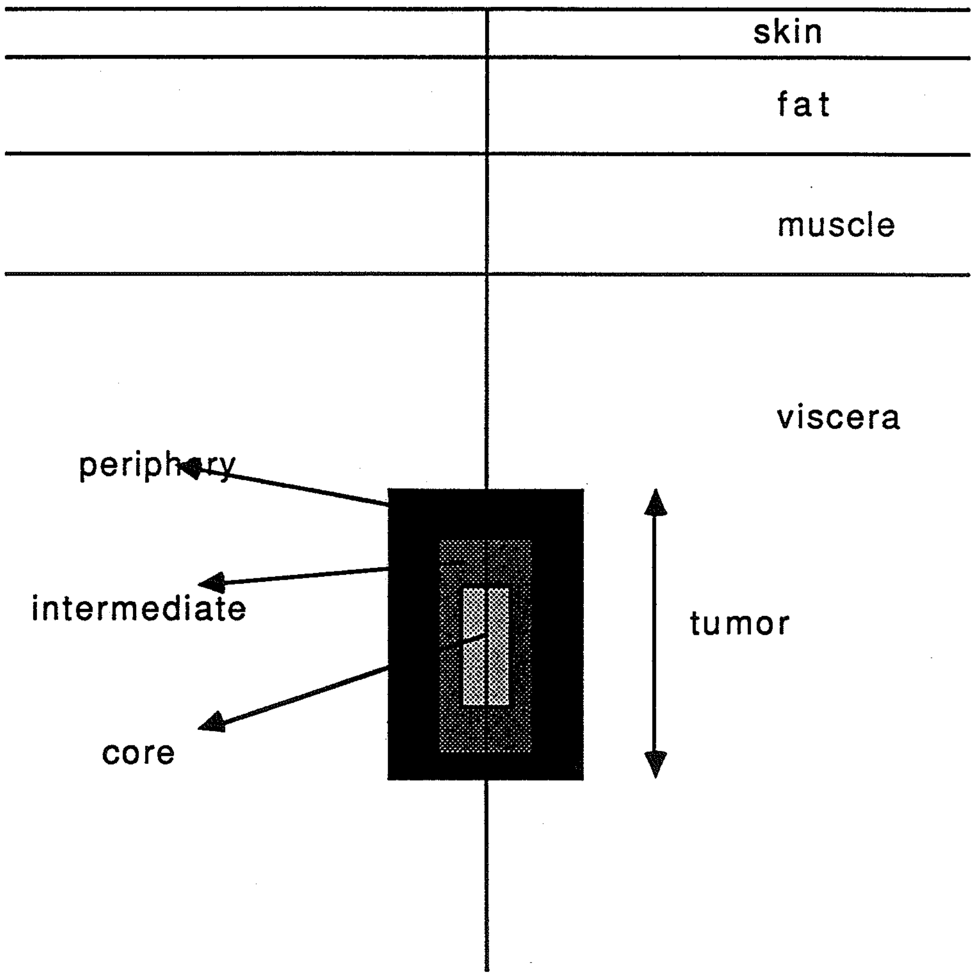

Figure 5.1. A cross section of a geometrical model of the tumor and the surrounding tissue .

Table 5.1

Properties and Dimensions of Normal Tissue (from Reference [11])

Tissue Type	Thickness (cm)	Conductivity (W/m/° C)
Skin	0.4	0.21
Fat	2.0	0.16
Muscle	3.0	0.42
Viscera	15.9	0.55

The choice between finite differences and finite elements is mainly governed by factors such as the complexity of the anatomical model, the nature of the boundary conditions, and the homogeneity of the medium. Due to the simple geometry of our adopted model, to the assumed homogeneity of the medium, and to the regularity of the boundary conditions, the method of finite difference seems adequate for our purpose.

5.2.2 The finite difference formulation of the bioheat transfer equation (BHTE)

The finite difference method consists of approximating the differential elements by an equivalent difference form. As an illustration, the x direction (in a 1-D problem) is divided into equally spaced nodes as shown by Figure 5.2a). The first and second derivatives at node m can be approximated as follows:

$$\left(\frac{dy}{dx}\right)_m = \frac{y_{m+1} - y_m}{\delta x} \qquad \text{(forward difference)} \qquad (5.3)$$

$$\left(\frac{dy}{dx}\right)_m = \frac{y_m - y_{m-1}}{\delta x} \qquad \text{(backward difference)} \qquad (5.4)$$

with $\delta x = x_{m+1} - x_m$

a more accurate expression is obtained by combining Eq. (5.3) and Eq. (5.4)

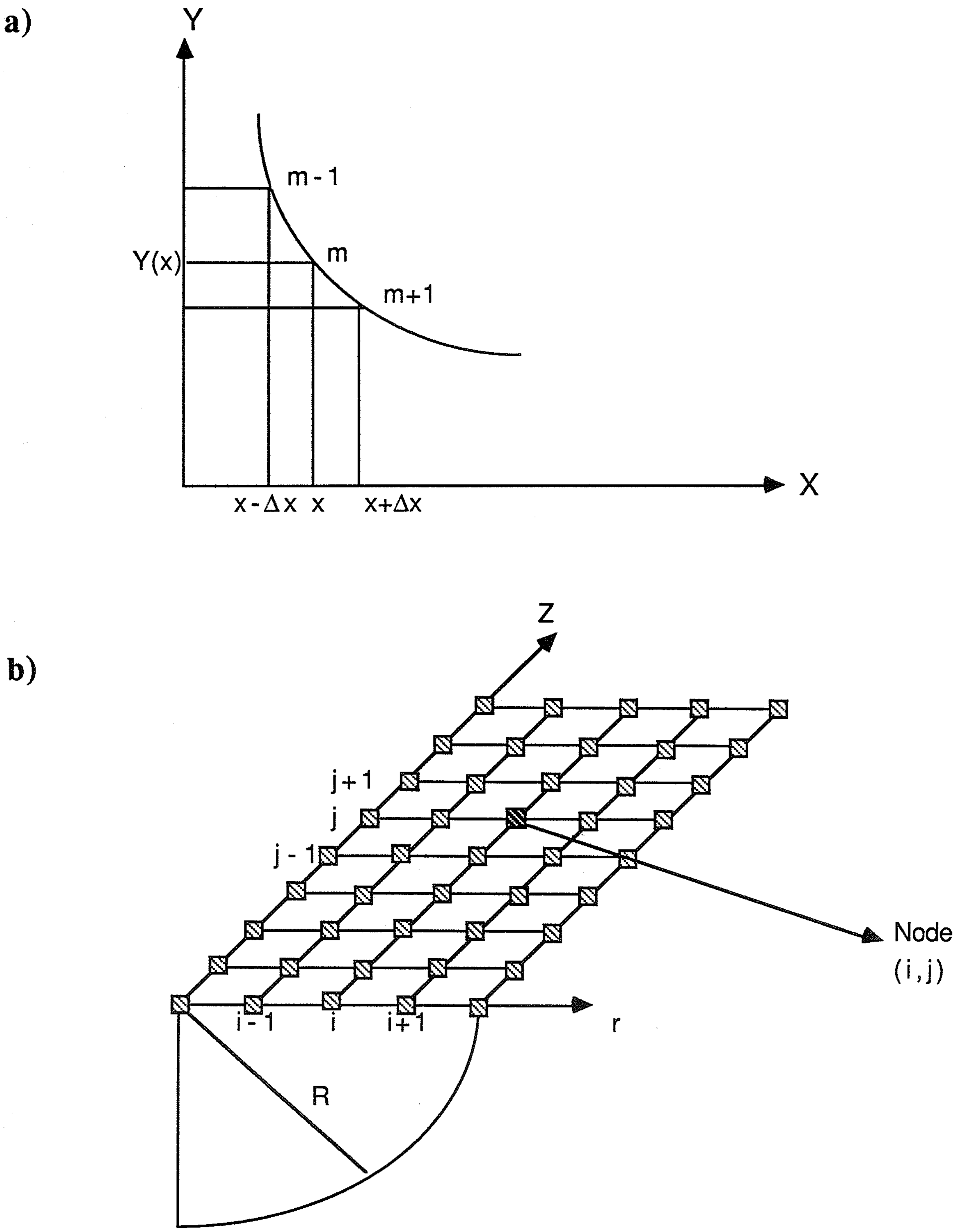

Figure 5.2. The geometry used in solving the bioheat transfer equation. a) In a 1-D problem and b) in a cylindrical radially symmetric 2-D problem.

$$(\frac{dy}{dx})_m = \frac{y_{m+0.5} - y_{m-0.5}}{\delta x} = \frac{y_{m+1} - y_{m-1}}{2\delta x} \tag{5.5}$$

where $y_{m+0.5}$ means the variable y evaluated at half distance between node m and node m+1. Similarly, an expression for the second derivative is derived as follows:

$$(\frac{d^2y}{dx^2})_m = \frac{(\frac{dy}{dx})_{m+0.5} - (\frac{dy}{dx})_{m-0.5}}{\delta x} = \frac{y_{m+1} - 2\,y_m + y_{m-1}}{(\delta x)^2} \tag{5.6}$$

Equations (5.5) and (5.6) can also be derived using a slightly different method. By using Taylor series expansion of y(x+δx) in the neighborhood of y(x), an estimate of the first and second derivatives will result as shown below. The advantage of this approach is that an upper bound of the error associated with the finite difference approximation can easily be evaluated. In fact, the finite difference method is based on approximating the differential elements $(\frac{dy}{dx}, \frac{d^2y}{dx^2})$ by finite difference expressions. These difference expressions are rather valid and will lead to the same result as the differential elements if the difference step size becomes infinitesimally small (δx--- 0). Taylor series expansion of y(x+δx) for a small δx can be written as

$$y(x+\delta x) = y(x) + \frac{\delta x}{1}(\frac{dy}{dx})_x + \frac{(\delta x)^2}{2!}(\frac{d^2y}{dx^2})_x + \frac{(\delta x)^3}{3!}(\frac{d^3y}{dx3})_x + \frac{(\delta x)^4}{4!}(\frac{d^4y}{dx^4})_x + 0(\delta x)^5 \tag{5.7}$$

and by substituting x by x_i and x+dx by x_{i+1}, Eq. (5.7) becomes

$$y_{i+1} = y_i + \frac{\delta x}{1}(\frac{dy}{dx})_{x_i} + \frac{(\delta x)^2}{2!}(\frac{d^2y}{dx^2})_{x_i} + \frac{(\delta x)^3}{3!}(\frac{d^3y}{dx^3})_{x_i} + \frac{(\delta x)^4}{4!}(\frac{d^4y}{dx^4})_{x_i} + 0(\delta)^5 \tag{5.8}$$

in addition, by substituting x by x_i and x_{i-1} by x-δx, the expression becomes

$$y_{i-1} = y_i - \frac{\delta x}{1}(\frac{dy}{dx})_{x_i} + \frac{(-\delta x)^2}{2!}(\frac{d^2y}{dx^2})_{x_i} + \frac{(-\delta x)^3}{3!}(\frac{d^3y}{dx^3})_{x_i} + \frac{(-\delta x)^4}{4!}(\frac{d^4y}{dx^4})_{x_i} + 0(\delta x)^5 \tag{5.9}$$

and by subtracting Eq. (5.9) from Eq. (5.8), one gets

$$y_{i+1} - y_{i-1} = 2\frac{\delta x}{1}\left(\frac{dy}{dx}\right)_{x_i} + \frac{(\delta x)^3}{3}\left(\frac{d^3y}{dx^3}\right)_{x_i} + 0(\delta x)^5 \qquad (5.9')$$

which can be rearranged, after neglecting the terms of order equal to or greater than three, to give

$$\left.\frac{dy}{dx}\right)_{x_i} = \frac{y_{i+1} - y_{i-1}}{2\delta x} \qquad (5.10)$$

which is same as Eq. (5.5). By adding Eqs. (5.9) and (5.8), one gets

$$y_{i+1} - 2y_i + y_{i-1} = \frac{(\delta x)^2}{1}\left(\frac{d^2y}{dx^2}\right)_{x_i} + \frac{(\delta x)^4}{6}\left.\frac{d^4y}{dx^4}\right)_{x_i} + 0(\delta x)^4 \qquad (5.10')$$

which is finally written as

$$\left.\frac{d^2y}{dx^2}\right)_{x_i} = \frac{y_{i+1} - 2y_i + y_{i-1}}{(\delta x)^2} \qquad (5.11)$$

It is noticed that Eq. (5.11) was obtained by neglecting the terms of 4th or greater order in the previous expression From the above analysis, it is obvious that the maximum error associated with the approximation is of third order in δx.

In conclusion, the method accuracy can be improved to any desired extent by choosing a smaller grid step size (grid volume in case of 3-D problems). However, a smaller size grid increment would also increase the required computation time.

5.2.3 The radially symmetrical BHTE in a finite difference form

Figure 5.2b) illustrates the geometry of the 2-D grid considered to solve the BHTE. The index i describes the node variation in the r direction while j describes that in the z direction. The second derivatives with respect to r and z are approximated by

$$\left.\frac{d^2T}{dr^2}\right)^i_j = \frac{T^{i+1}_j - 2T^i_j + T^{i-1}_j}{(\delta r)^2} \qquad (5.12)$$

$$\left.\frac{d^2T}{dz^2}\right)^i_j = \frac{T^i_{j+1} - 2T^i_j + T^i_{j-1}}{(\delta z)^2} \qquad (5.13)$$

and

$$\left.\frac{dT}{dr}\right)^i_j = \frac{T^{i+1}_j - T^{i-1}_j}{2\delta r} \qquad (5.14)$$

To solve the BHTE given by Eq. (5.2), the differential elements are substituted by the difference forms derived above. As obvious from Eq. (5.2), the case r= 0 requires special attention, as the equation is singular along the axis of symmetry due to the term $\frac{1}{r}\frac{dT}{dr}$. First, the equation is solved for $r \neq 0$ as follows:

$$\frac{T^{i+1}_j - 2T^i_j + T^{i-1}_j}{(\delta r)^2} + \frac{1}{2r_i}\frac{T^{i+1}_j - T^{i-1}_j}{\delta r} + \frac{T^i_{j+1} - 2T^i_j + T^i_{j-1}}{(\delta z)^2} + \frac{Q(r_i,z_i)}{K} + \frac{W_bC_b}{K}(T_b - T^i_j) = 0 \qquad (5.15)$$

and by considering $\delta r = \delta z = \delta$, Eq. (5.15) becomes

$$T^{i+1}_j - 2T^i_j + T^{i-1}_j + \frac{\delta}{2r_i}(T^{i+1}_j - T^{i-1}_j) + (T^i_{j+1} - 2T^i_j + T^i_{j-1}) + \frac{Q(r_i,z_i)\delta^2}{K} + \frac{W_bC_b\delta^2}{K}(T_b - T^i_j) = 0$$

which is rearranged to give

$$T_j^i = C_0\{(1+\frac{\delta}{2r_i})\, T_j^{i+1} + (1-\frac{\delta}{2r_i})\, T_{j+1}^i + T_{j+1}^i + T_{j-1}^i + \frac{W_b C_b \delta^2}{K} T_b + \frac{Q(r_i,z_i)\delta^2}{K}\} \qquad (5.16)$$

with $C_0 = \frac{1}{(4+\frac{W_b C_b \delta^2}{K})}$

As mentioned earlier, this final expression is valid everywhere but at r= 0. Along the axis (r= 0), Eq. (5.2) should be manipulated further because of the term $\frac{1}{r}\frac{dT}{dr}$ which can be evaluated by applying L'hopital's rule

$$\lim \frac{\frac{dT}{dr}}{r} = \frac{\frac{d}{dr}(\frac{dT}{dr})}{\frac{d}{dr}(r)} = \frac{\delta^2 T}{\delta r^2} \qquad (5.17)$$

and Eq. (5.2) becomes

$$2\frac{\delta^2 T}{\delta r^2} + \frac{\delta^2 T}{\delta z^2} + \frac{Q(r,z)}{K} + \frac{W_b C_b}{K}(T_b - T) = 0 \qquad (5.18)$$

by substituting Eqs. (5.12)-(5.14) into Eq. (5.18), the following difference expression results:

$$2\frac{T_j^{i+1} - 2T_j^i + T_j^{i-1}}{(\delta r)^2} + \frac{T_{j+1}^i - 2T_j^i + T_{j-1}^i}{(\delta z)^2} + \frac{Q(r_i,z_i)}{K} + \frac{W_b C_b}{K}(T_b - T_j^i) = 0 \qquad (5.19)$$

Taking into consideration the circular symmetry at r= 0 (i.e., $T_j^{i+1} = T_j^{i-1}$) and equating the step size in the r and z direction (i.e., $\delta r = \delta z = \delta$), one gets

$$T_j^i = C_1\{4\, T_j^{i+1} + T_{j+1}^i + T_{j-1}^i + \frac{W_b C_b \delta^2}{K} T_b + \frac{Q(r_i,z_i)\delta^2}{K}\} \qquad (5.20)$$

with $C_1 = \dfrac{1}{(6+\dfrac{W_bC_b\delta^2}{K})}$

Finally, the finite difference form of the BHTE is given below:

for $r \neq 0$

$$T_j^i = C_0\{aT_j^{i+1} + b\,T_{j+1}^i + T_{j+1}^i + T_{j-1}^i + \frac{W_bC_b\delta^2}{K}T_b + \frac{Q(r_i,z_i)\delta^2}{K}\} \qquad (5.20')$$

and for $r = 0$

$$T_j^i = C_1\{4\,T_j^{i+1} + T_{j+1}^i + T_{j-1}^i + \frac{W_bC_b\delta^2}{K}T_b + \frac{Q(r_i,z_i)\delta^2}{K}\} \qquad (5.20'')$$

with

$a = (1+\frac{\delta}{2r})$, $b = (1-\frac{\delta}{2r})$, C_0 and C_1 are as specified above.

5.2.4 Iterative method: finite difference with over-relaxation

The finite difference equation can be solved iteratively using the Gauss-Seidel technique. The technique starts by guessing a value for each unknown $(T_j^i)^0$. A new value $(T_j^i)^1$ is then calculated using the above difference equation, and the procedure is repeated until the convergence of the solution is achieved.

A disadvantage of the Gauss-Seidel technique is its slow rate of convergence. However, the convergence rate can be improved by using a weighting term w known as the relaxation factor. The modified technique is known as the finite difference with over-relaxation. The iteration equation is then modified as follows:

$$(T_j^i)^k = f(T_{SG})w + (1-w)\,(T_j^i)^{k-1} \qquad (5.21)$$

where k is the number of iterations, $f(T_{SG})$ is the Gauss-Saddle iterative equation, and w is the relaxation factor. The role of the relaxation factor can be illustrated by considering the following cases:

Case 1: $w = 0$, the new value will always be equal the old one (i.e., $T^k = T^{k-1}$) and no convergence is achieved.

Case 2: $w = 1$, The iterative equation becomes that of Gauss-Seidel and the convergence rate is slow.

Case 3: $0 < w < 1$, the method iterates between the old value and the Gauss-Seidel one and consequently, the convergence is even slower. This is known as the under-relaxed case.

Case 4: $w \geq 2$, the iterative procedure will not converge for this range of values.

Case 5: $1 < w < 2$, the iterations extrapolate beyond the Gauss-Seidel value, and hence, the convergence is improved. This is known as the finite difference with over-relaxation.

The value of w depends on the problem, and an optimum value needs to be determined in order to achieve convergence with the smallest number of iterations. For the simulations included in this chapter, a value of 1.42 was determined to be optimum and the number of iterations was kept less than 26 for most cases. A listing of a Fortran program (RIGHTTEMP) to solve the cylindrical BHTE is given in Appendix B. The computation time on the Cray X-MP48 for a grid of 70x47 point size is less than a second. The program offers the option of calculating an absolute or a difference temperature rise (T or $(T-T_{ref})$). In some cases, calculating the temperature rise ($T-37^0$) is more appropriate.

In the following sections, a normal blood perfusion rate of 8.3 $kg/m^3/s$ [38] is assumed. The tumor blood flow will be assumed uniform and equal to that of normal tissue ($W_1 = W_2 = W_3 = W_n$) unless otherwise specified where W_1, W_2, and W_3 are the blood perfusion rate in the core, intermediate, and peripheral layer of the tumor, respectively. However, the effect of blood perfusion on the temperature distributions will be investigated in Section 5.6 where the blood perfusion will be varied and a parametric study will be provided. The maximum surface velocity of the transducer material was computed based on an appropriate maximum intensity of 4 W/cm^2 delivered at the transducer surface, and the tissue characteristic coefficients are taken from Table 5.1.

5.3 Heating Associated with Simple and Multiple Focusing along the Applicator Axis

In Chapter 3, the FCM was used to generate focal spots along the axis by assuming a point source (or a small disk shape) at the desired location. The method results in amplitude shading of the required signal characterized by strong amplitudes towards the center and relatively low amplitudes toward the outer elements of the array. Figure 5.3a) illustrates the amplitude distribution resulting from the synthesis of a focal spot at 80 mm from the array surface. Due to the particular geometry of the CRA, the effective radiated surfaces of the outer elements are substantially larger than those of the inner ones and consequently, a very high amplitude shading factor results. To improve the amplitude shading factor, the logarithmic scaling procedure is used, as outlined in Section 2.4. The amplitude distribution resulting from applying the procedure to the previous distribution is shown in Figure 5.3b).

In the following simulations, unless specified otherwise, the amplitude distributions are logarithmically scaled while the phase distributions are kept the same as computed by the FCM. Simulations also showed that the synthesis of single foci (simple or annular) can be achieved using a uniform amplitude control instead of the one resulting from the FCM.

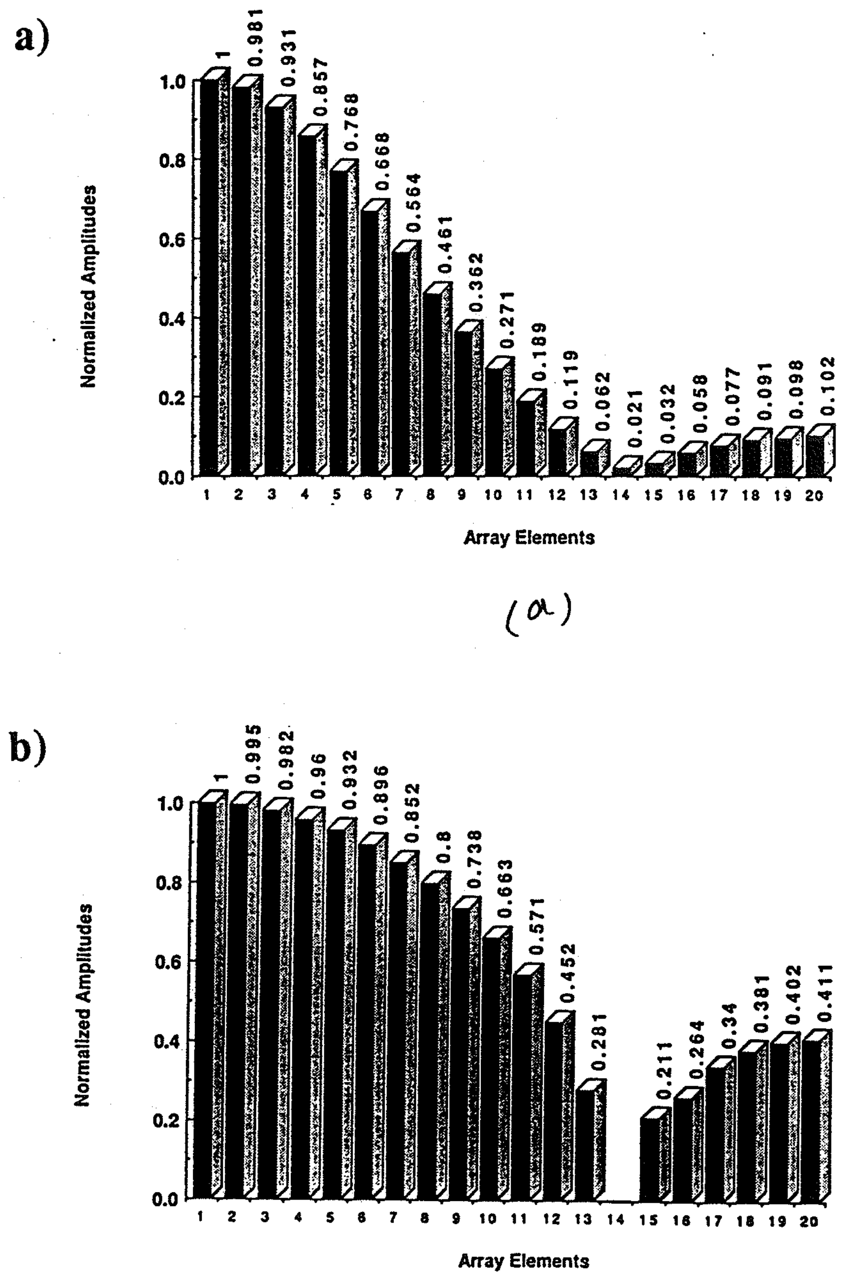

Figure 5.3. Improvement of the shading factor. a) The normalized driving amplitude as resulting from the application of the FCM. b) The normalized driving amplitude after applying the procedure of 5.3.

In Chapter 3, the array was focused at (0, 0, 70) along its axis and the resulting field intensity profile was illustrated in Figure 3.29. The intensity gain evaluated at the focal site is found to be 22.3 dB. The temperature distribution associated with the pattern of Figure 3.29 is shown in Figure 5.4. The maximum intensity was adjusted in order for the maximum temperature not to exceed 60^0 C. It can be noticed that therapeutic heating ($\geq 42^0$ C) is confined to a very small volume as illustrated in Figure 5.4. Huu and Hartemann showed similar temperature distributions associated with focusing the CRA on a point along its axis. Their conclusion was that volume heating can be achieved by focusing the array along its main axis. However, it is obvious that the volume to be heated must be extremely small, and hence, this type of focusing cannot be used for tumor heating without some manipulation. In Section 5.5, multiple focusing on the axis combined with a simple mechanical movement is proposed as a means of heating deep seated tumors.

An elongated focus can also be produced by focusing simultaneously at z=80 and 105 mm, respectively. Figure 5.5a) is a contour plot of the resulting pattern in the (r,z) plane. This technique could reduce the spatial-peak temporal-peak focal intensity, especially when used for scanning, as will be shown. As could be seen from Figure 5.5a), the 3dB-focal region is larger than that in Figure 3.29, and hence, an SPTP of 303.12 W/cm^2results as compared to 648 W/cm^2 of the previous case. One can conclude that multiple focusing can be used to smooth out the power deposition pattern by splitting the focal intensity over a larger region, a desired result that is usually achieved by scanning a focal spot over a predetermined trajectory. The temperature distribution that results from inputting the power deposition pattern of Figure 5.5a) to the BHTE is given in Figure 5.5b). Figure 5.5b) demonstrates that the temperature of a volume of approximately 2.3 cm^3 can be raised to therapeutic level ($\geq 42^0$C). It is also possible to produce a more elongated foci by simultaneously focusing at three points, as was discussed in Chapter 3. The power deposition pattern of focusing simultaneously at 65, 90, and 130

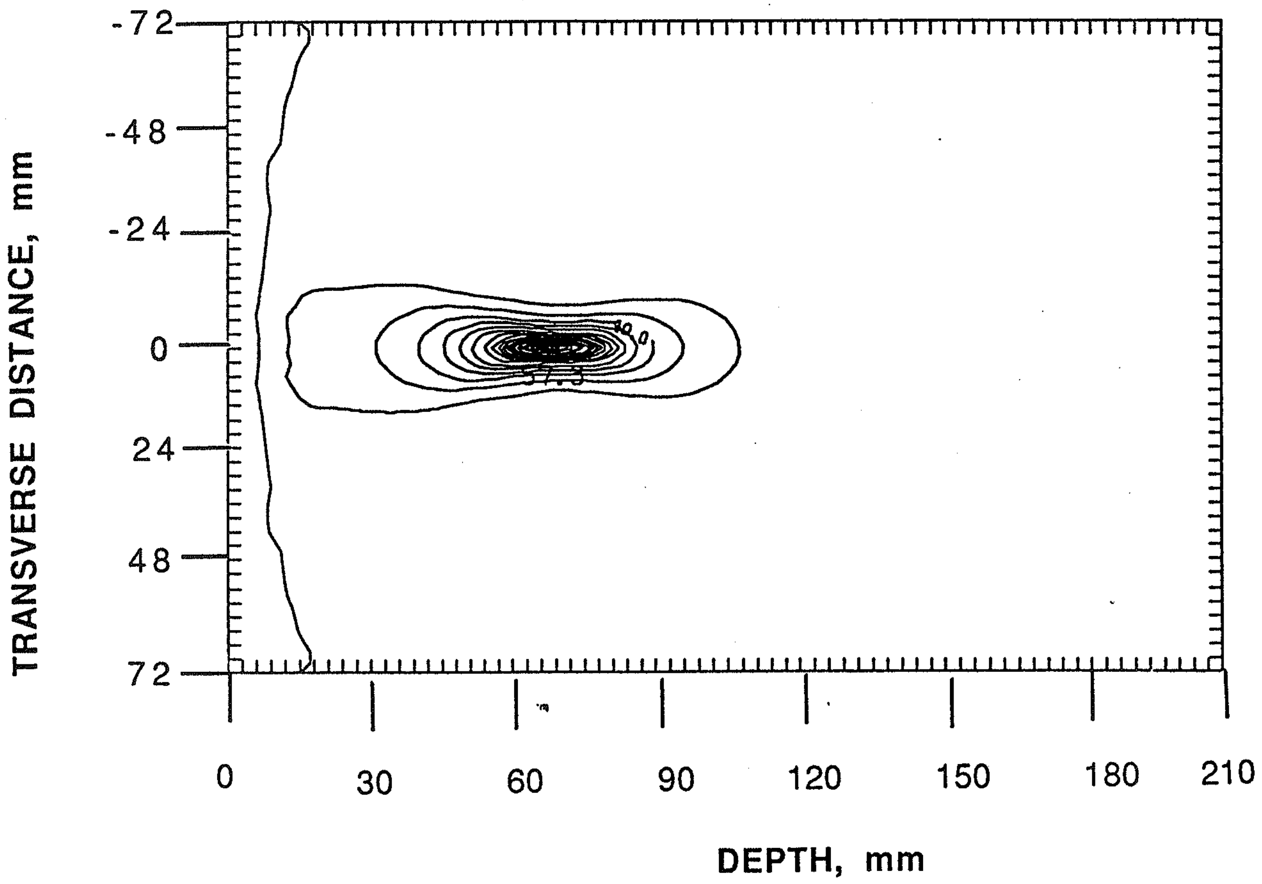

Figure 5.4. Thermal response associated with a simple focus along the axis . The lowest contour level is 37 ⁰ and contours are given at 1 ⁰ interval.

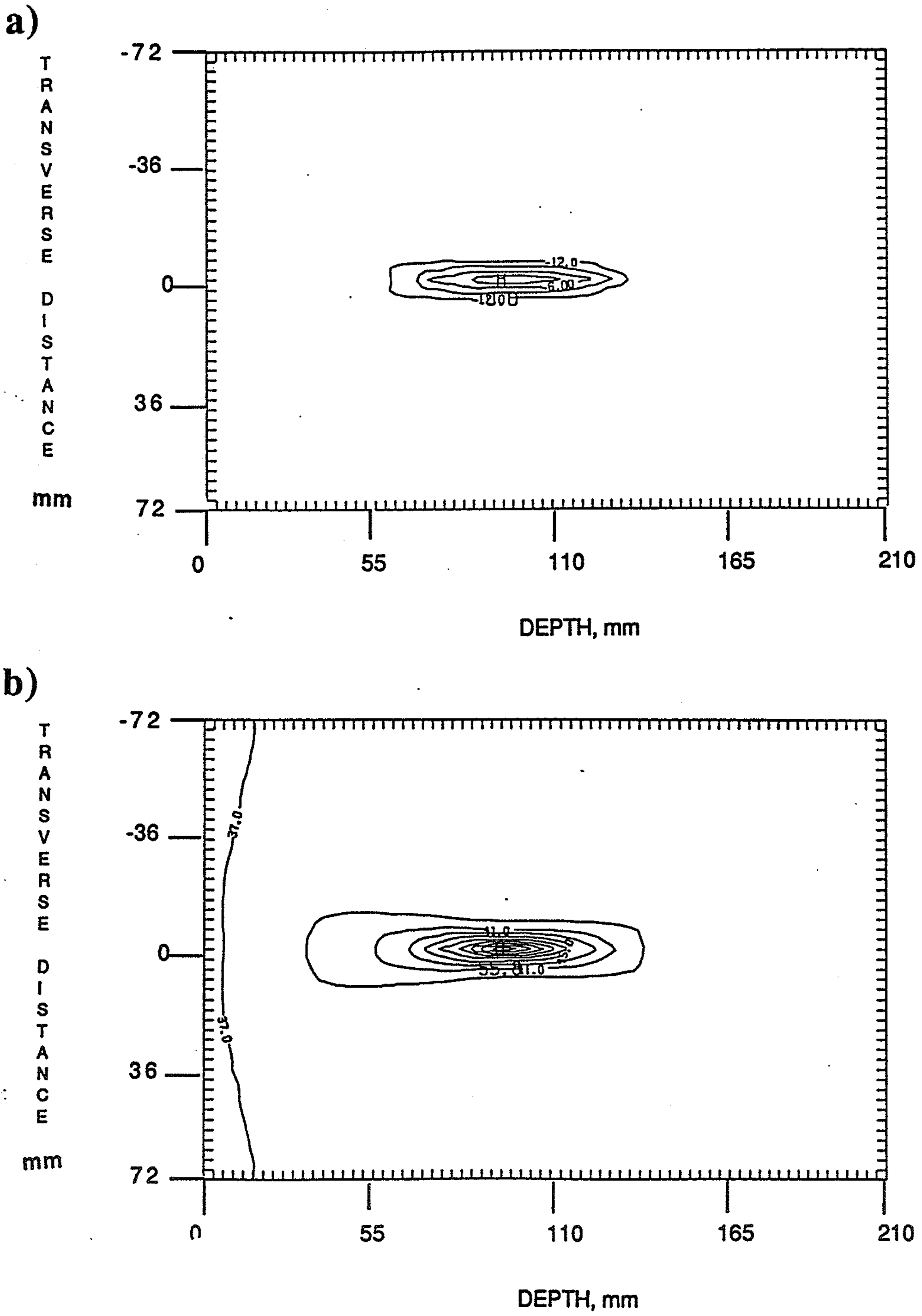

Figure 5.5. Thermal response due to an elongated foci along the axis. a) An intensity profile produced by simultaneously focusing at (0,0,85) and (0,0,100), respectively. b) Temperature distribution resulting from the pattern of a). The lowest contour level is 37^0 and contours are given at intervals of 1 ^{0}C.

respectively, was inputted to the BHTE, and the resulting temperature distribution is shown in Figure 5.6. These elongated foci will prove more useful in Section 5.5, where a simple mechanical movement is combined with multiple focusing to produce more diffuse heating patterns.

The power deposition pattern resulting from the simultaneous focusing at 65, 130, and 178 mm from the applicator surface is illustrated in Figure 5.7a). Although this pattern might not be useful for any practical situation, it is only meant to demonstrate the flexibility of the multiple focusing feature of the FCM. An intensity gain of 12.2 dB was evaluated at the nearest focal site. The intensity gain evaluated at the second and third foci are within 3 db from the first one. The temperature distribution associated with this pattern is shown in Figure 5.7b), which demonstrates the possibility of heating three separate volumes at different depths by simply adjusting the electronic control of the array.

5.4 Heating Associated with Annular Intensity Patterns

In Chapter 3, the synthesis of annular intensity profiles was demonstrated. It was shown that a particularly strong secondary foci (far beyond the focal plane) would result from the attempt of synthesizing small annular rings. In particular, the problem was more severe if the synthesis of "rings" of radii smaller than a characteristic radius (R_s) was attempted. In addition, because of the circular symmetry, a strong secondary foci can appear near the applicator. In summary, the prospect of using the CRA to generate annular heating patterns useful in hyperthermia was not very optimistic. In this section, it is demonstrated that annular intensity patterns, while possible to be synthesized, might have somewhat limited usefulness in hyperthermia cancer therapy. However, a more efficient method will be proposed in the next section.

The temperature distribution associated with the synthesis of an annular pattern of 40 mm radius at 80 mm depth (see Figure 3.9) is shown in Figure 5.8a). The tumor to be treated is assumed to be of cylindrical shape of a cross-sectional radius of 40 mm and a

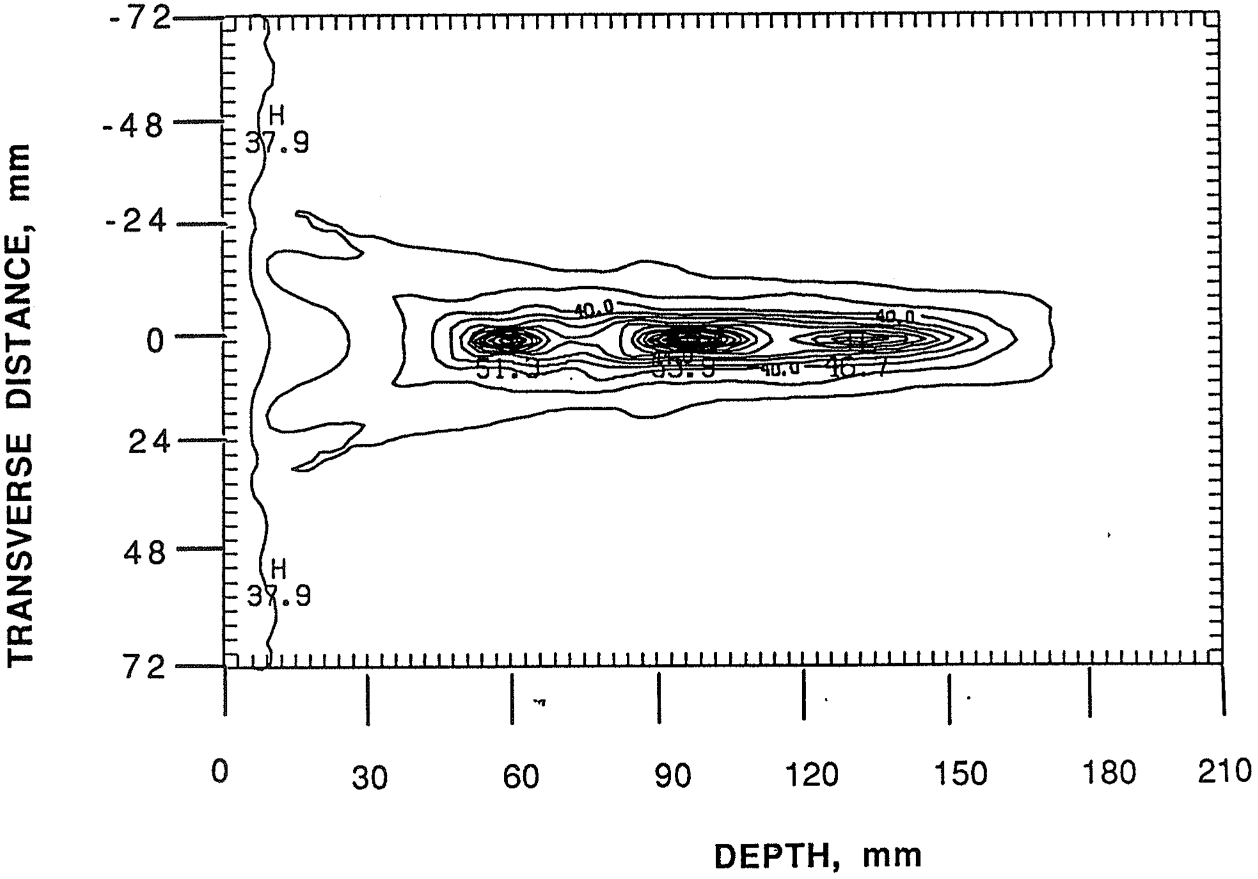

Figure 5.6. Temperature distribution associated with multiple focusing along the axis. A contour plot of the temperature distribution resulting from simultaneously focusing at (0,0,65), (0,0,90), and (0,0,130) along the axis. The lowest contour level is 37 ^{0} and contours are given at 10 C intervals.

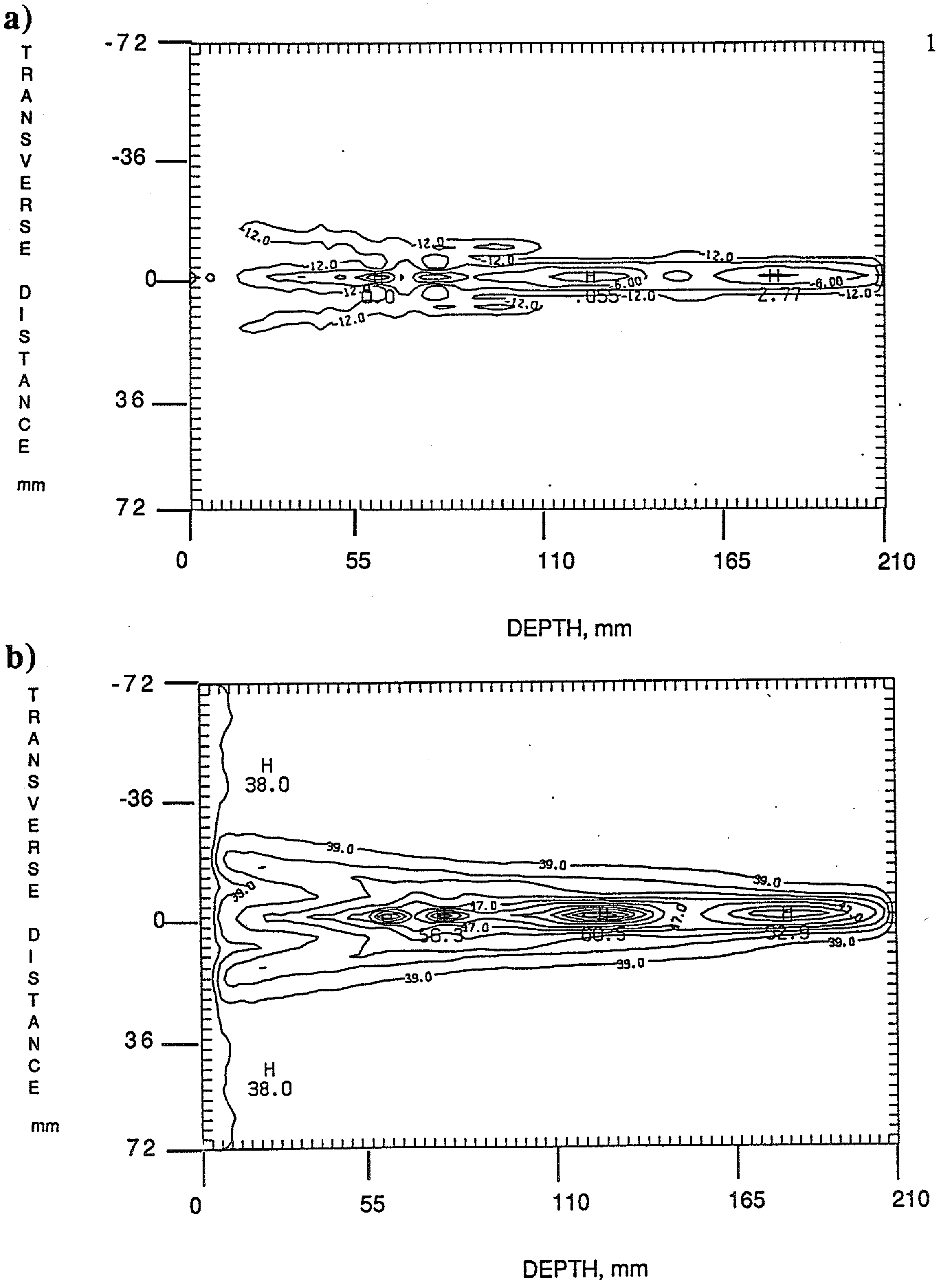

Figure 5.7. Temperature distribution associated with multiple focusing along the axis. a) Field intensity profile resulting from simultaneously focusing at (0,0,65), (0,0,130), and (0,0,178) along the axis. Contours are given at intervals of 3 dB. b) Temperature distribution associated with the pattern of a).

length of 50 mm. The tumor center is assumed to coincide with the center of the synthesized ring. The time-averaged intensity gain evaluated in the focal plane is 2.545 dB. A maximum time-averaged intensity of 7.13 W/cm^2 would result in the focal plane if the annular electrode can deliver 4 W/cm^2. It can be seen from Figure 5.8a) that although therapeutic temperatures are easily reached at the edges of the tumor, the core of the tumor was not heated, even when a poorly perfused tumor is assumed. For example, Figure 5.8b) is the temperature distribution associated with the intensity profile of Figure 3.9 for a blood perfusion rate of 4.0 kg/m^3/s and ($W_1 = W_2 = 0$). The same conclusion is reached when the pseudo-direct method was used for synthesis as seen from Figure 5.8c). A much more severe problem is observed in the case of the synthesis of annular rings with smaller radii. Figures 5.9a) and b) illustrate the temperature distributions resulting from the attempt of synthesizing annular rings of 30 and 20 mm radii, respectively. A severe hot spot far beyond the focal plane appears in both cases and seems to be a serious limitation. It is observed from Figures 5.9a) and b) that it would be impossible to raise the temperature of the tumor to a therapeutic level without dangerously increasing the temperature of the hot spot at depth. This result was predicted in Chapter 3 based on geometrical considerations.

To resolve the problem associated with the synthesis of large radius rings, namely to raise the temperature of the tumor core to a therapeutic level, one option is to temporally scan between a large and a small radius annular patterns. However, this approach is complicated by the severity of the hot spot associated with the synthesis of smaller annular patterns.

In conclusion, the results of this section confirm those of Chapter 3, which were purely based on power deposition analysis. The direct synthesis of annular intensity profiles, which can be easily achieved using a CRA, may have limited usefulness for cancer therapy. The following section will investigate the possibility of using the patterns produced in Section 3.7, by combining mechanical and electrical means, to heat tumors at different depths.

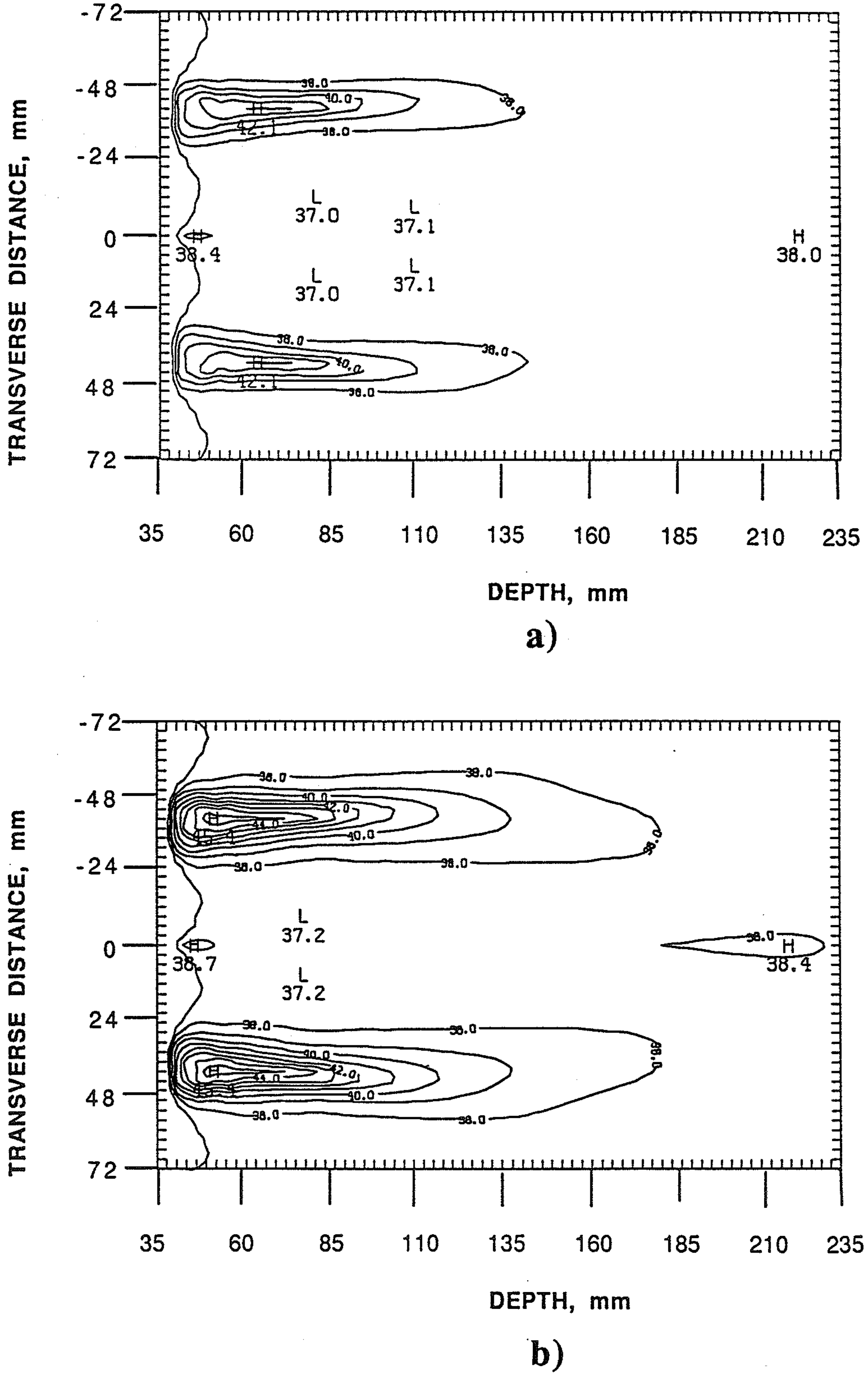

Figure 5.8. Thermal response associated with annular heating patterns. a) A contour plot of the temperature distribution associated with the intensity profile of Figure 3.9 for a blood perfusion of 8.3 kg/m^3/s. b) The temperature distribution associated with the same intensity profile but with a blood perfusion of 4 kg/m3/s. The tumor core and intermediate layer perfusion rate is assumed zero.

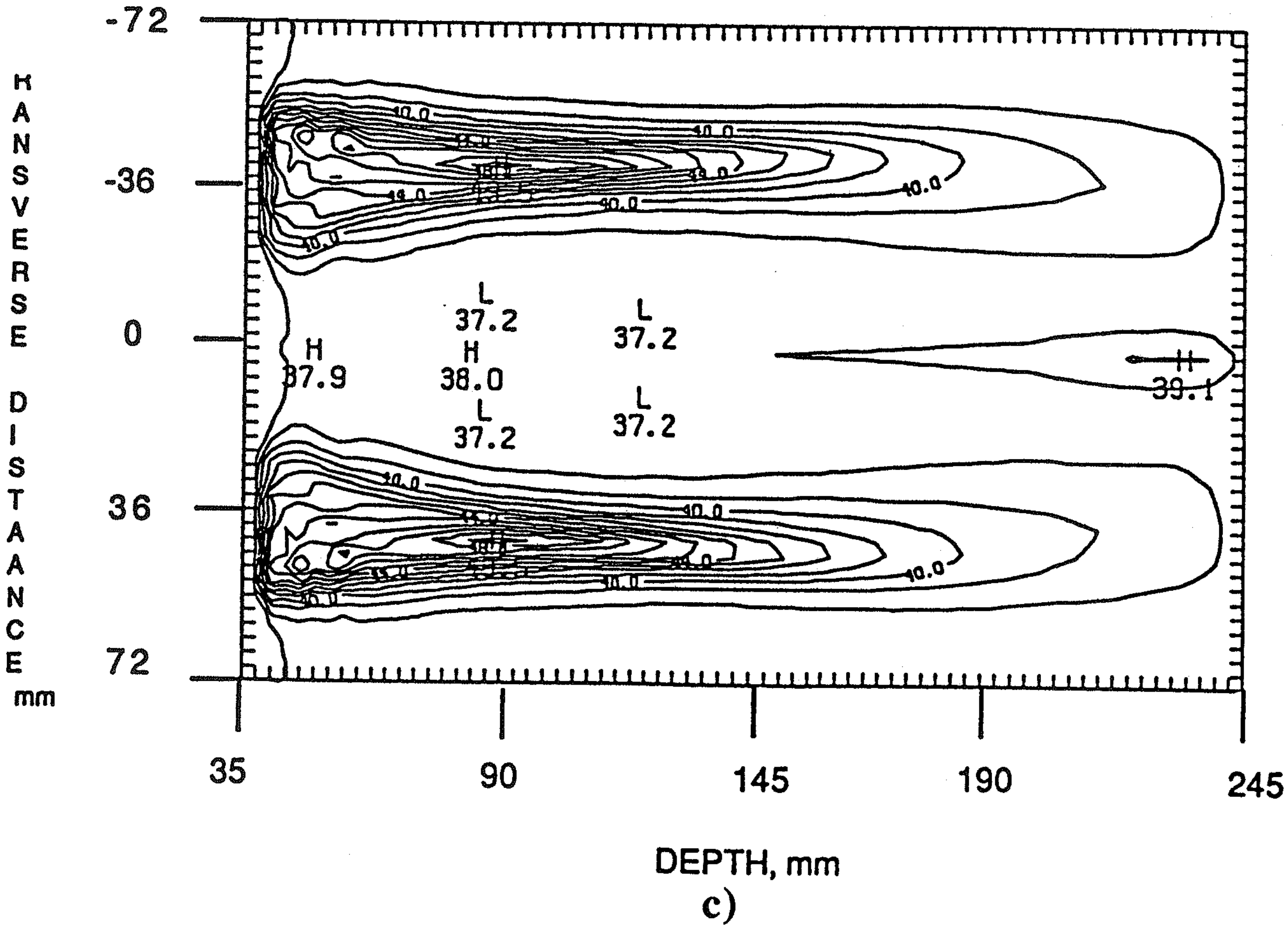

Figure 5.8. c) A contour plot of the temperature distribution associated with the intensity profile of Figure 3.18b which was synthesized using the pseudo-direct method. The maximum temperature is 49.5 and the contours are given at intervals of 1 ^{0}C.

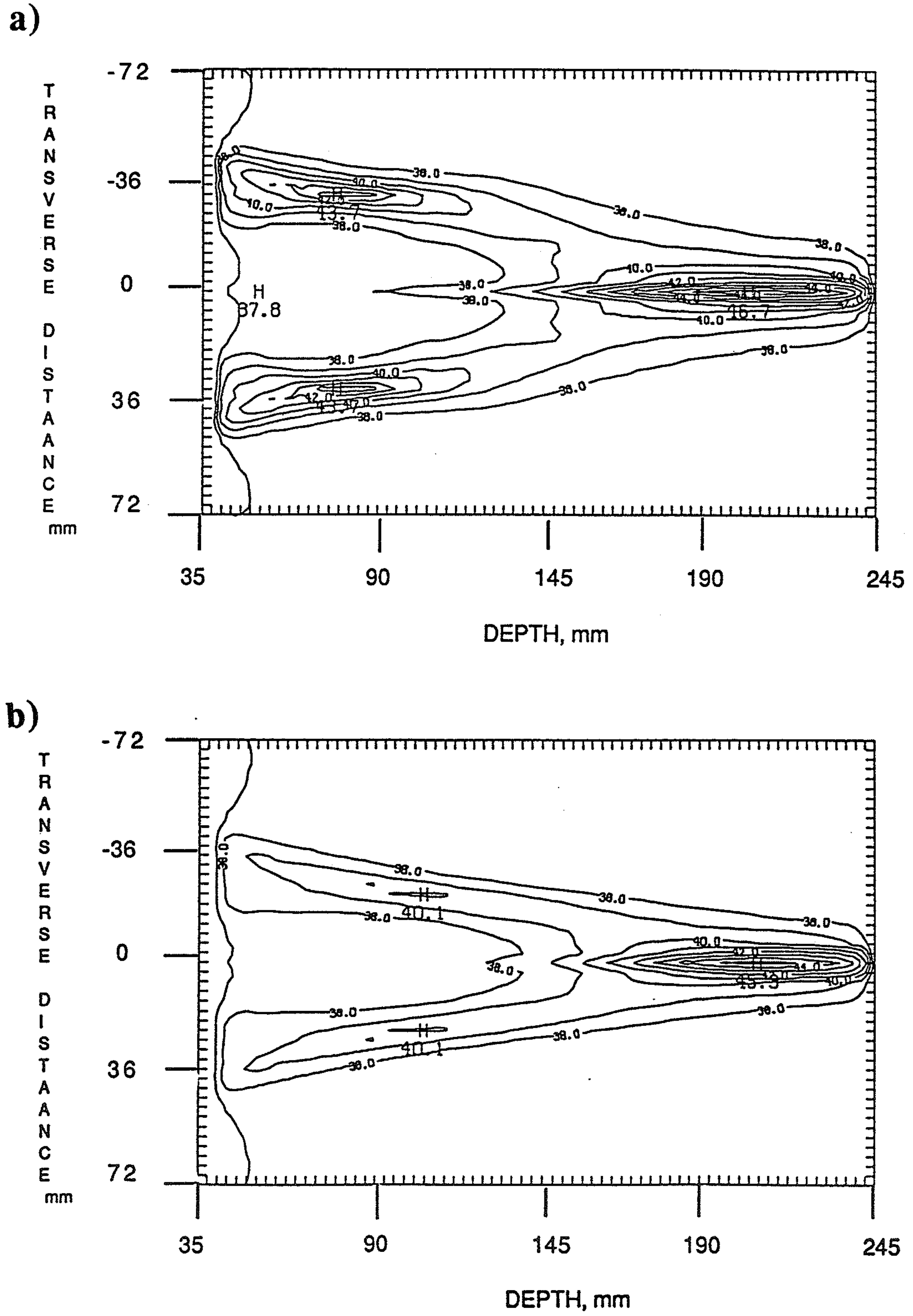

Figure 5.9. Thermal response associated with annular heating patterns. a) A contour plot of the temperature distribution associated with a 30 mm radius annular pattern at 80 mm depth. b) The temperature distribution associated with a 20 mm radius annular pattern at 80 mm depth.

5.5 Heating Associated with the Mechanical Scanning of the CRA

It was demonstrated that simple mechanical movement of the transducer, when combined with simple and multiple focusing along the array axis, would lead to unique power deposition patterns that cannot eventually be produced by either form of scanning separately. In particular, the possibility of heating the back as well as the front of a tumor, by appropriately placing the tumor between two simultaneous focal spots which are then scanned mechanically was demonstrated. In addition, it was shown that scanning can effectively be done at reduced SPTP focal intensity (which is often a concern) by simultaneously focusing at different sites or by the generation of elongated foci. In this section, the temperature distributions associated with these patterns are investigated.

The power deposition pattern resulting from the synthesis of a single focus at z= 70 mm along the main axis of the array was shown in Figure 3.29. As demonstrated earlier, the temperature distribution associated with this pattern is too small and might only be adequate to heat an extremely small tumor (see Figure 5.4). The scanned field intensity profile resulting from mechanically scanning the focal spot of Figure 3.29 over a disk of a 35 mm radius was illustrated in Figure 3.30a). The mechanical scanning was simulated by evaluating the convolution integral over an appropriate surface (see Section 3.7). The time-averaged intensity gain of the scanned pattern is 5.91 dB. This time-averaged gain is adequate to raise the temperature of a cylindrical volume of almost 68 cm^3 to a therapeutic level as illustrated in Figure 5.10. However, when the focal spot of Figure 3.29 was mechanically scanned over an annular ring of inner and outer radii of 9 and 15 mm, respectively, the annular pattern illustrated in Figure 3.30b) was produced. The time-averaged intensity gain is evaluated at the focal site and found to be 15.09 dB. By inputting the power deposition pattern of Figure 3.30b) to the BHTE, the temperature

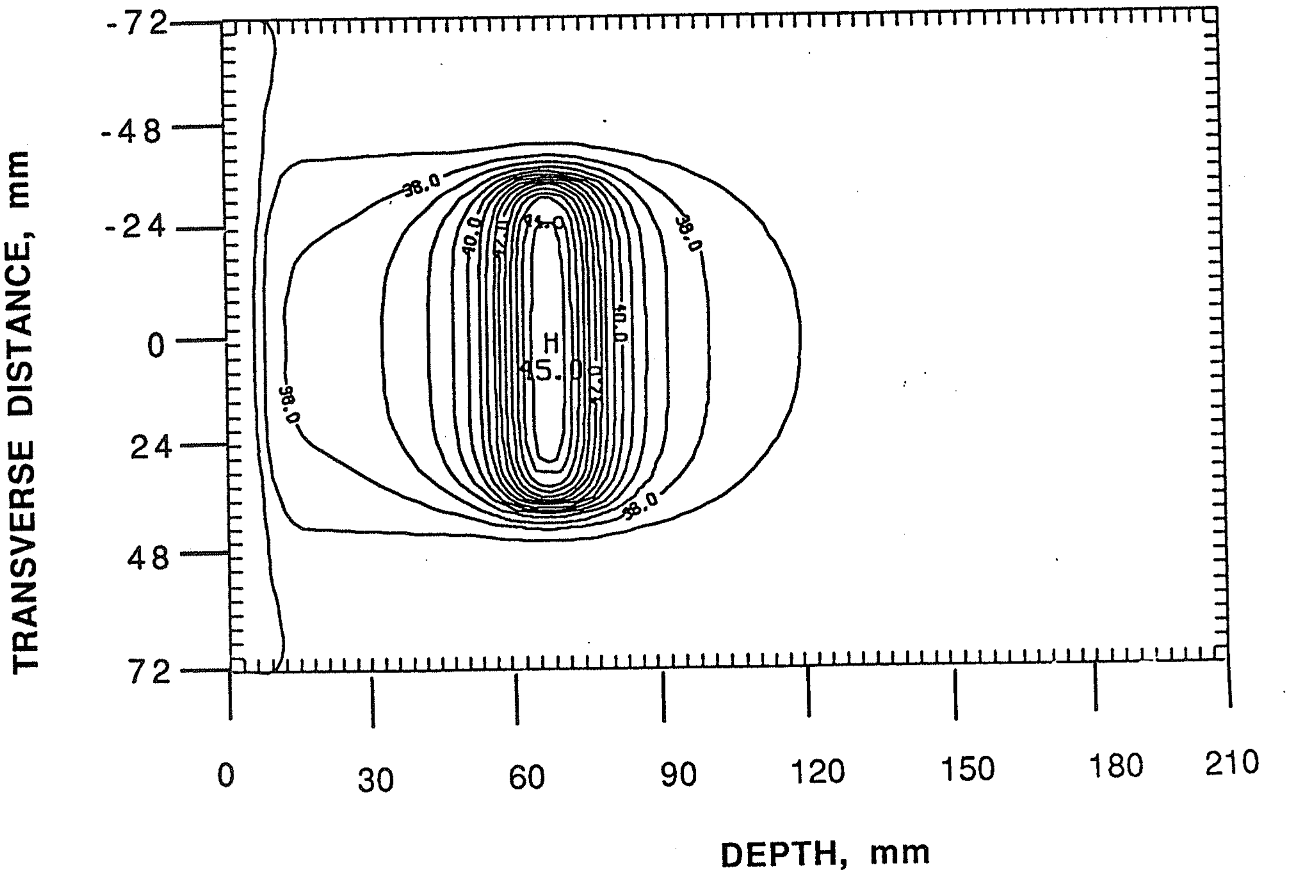

Figure 5.10. Simulated temperature distribution associated with mechanical scanning. A contour plot resulting from mechanically scan the pattern of Figure 3.28 over a disk of 35 mm radius. The lowest contour level is 37⁰C and contours are given at intervals of 1⁰C.

distribution illustrated in Figure 5.11 results. It can be seen from Figure 5.11 that while the temperature at the edges of the heated volume is well above 42^0, the tumor core is not adequately heated ($\leq 39\ ^0$C) and hence, scanning should be over a complete disk or at least over a multiple concentric annular path.

An elongated focus was also generated by simultaneously focusing at 60 and 80 mm (along the axis) from the array surface, and the resulting pattern was illustrated in Figure 3.31a). The scanned field intensity profile (time-averaged intensity) pattern, using the elongated foci, over a disk of 30 mm radius was also shown in Figure 3.31b). The time averaged intensity gain relative to Figure 3.31b) is 6.64 dB. The temperature distribution resulting from inputting this pattern to the BHTE is illustrated in Figure 5.12. A cylindrical volume, extending over 39 mm in the z-direction, is heated to a therapeutic level. The heated volume is approximately 82 cm^3. The SPTP focal intensity used for the scanning is 432 W/cm^2 compared to the 648 W/cm^2 used in the previous simulation. It is also demonstrated that depositing the energy around the edges of a tumor of a 17 mm radius is inadequate to obtain therapeutic temperature throughout the whole tumor as illustrated in Figure 5.13a). However, by scanning the focal spot over a smaller radius annular path, the core of the tumor could be heated as well. The temperature distribution resulting from scanning a 10 mm radius annular ring is illustrated in Figure 5.13b).

The pattern obtained by simultaneously focusing at 60, 68, and 90 mm is scanned over a disk of an 18 mm radius, and the resulting pattern was shown in Figure 3.32. It is interesting to note that the SPTP focal intensity used to achieve this pattern is 187.77 W/cm^2 compared to over 400 W/cm^2 used in the previous cases. This technique might allow heating a moderate size tumor by placing it appropriately between the foci. The advantage of the method is the use of lower SPTP focal intensity which is often a concern with mechanical or electrical scanning. By inputting the pattern of Figure 3.32 to

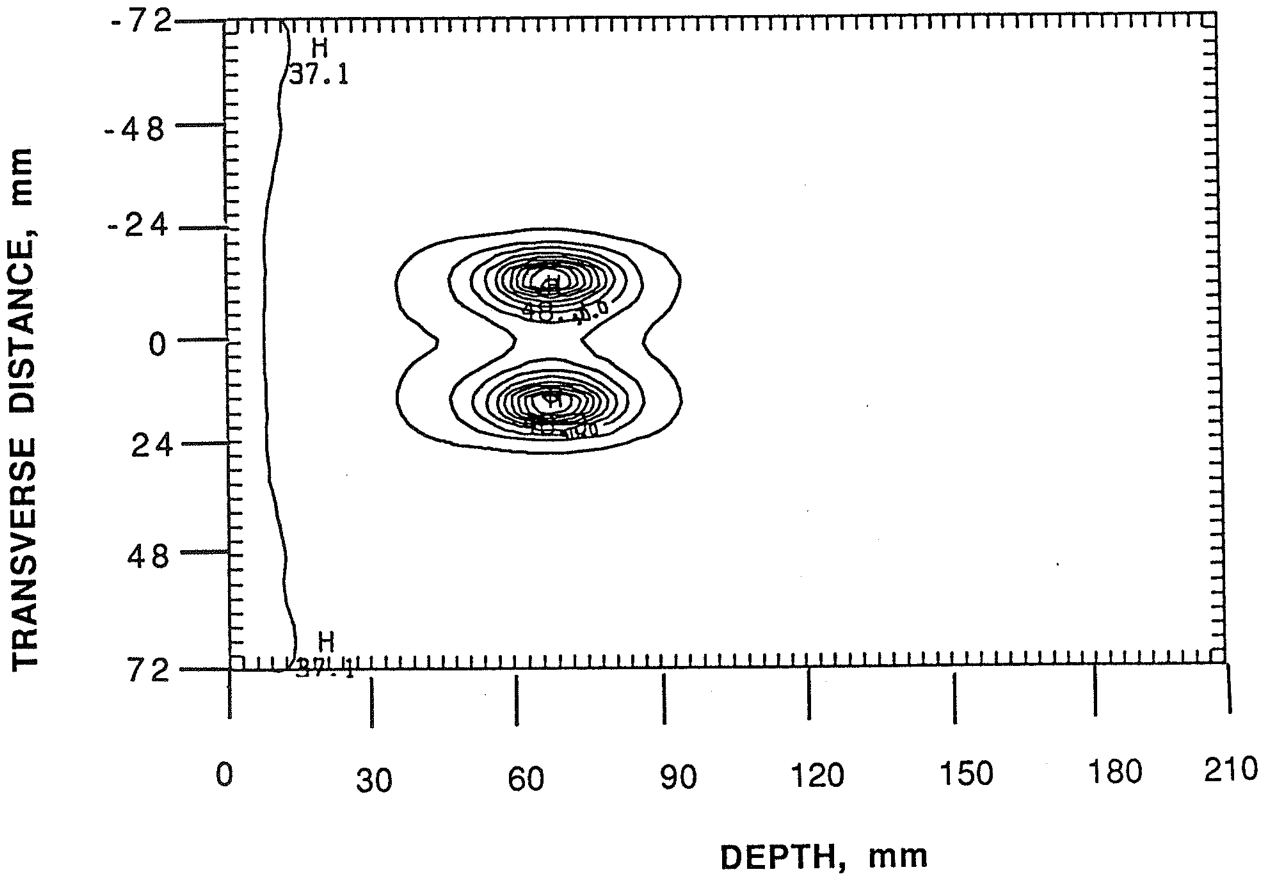

Figure 5.11. Simulated temperature distribution associated with mechanical scanning. A contour plot of the temperature distribution resulting from scanning the pattern of 3.28 over an annular surface of inner and outer radius of 9 and 15 mm, respectively.

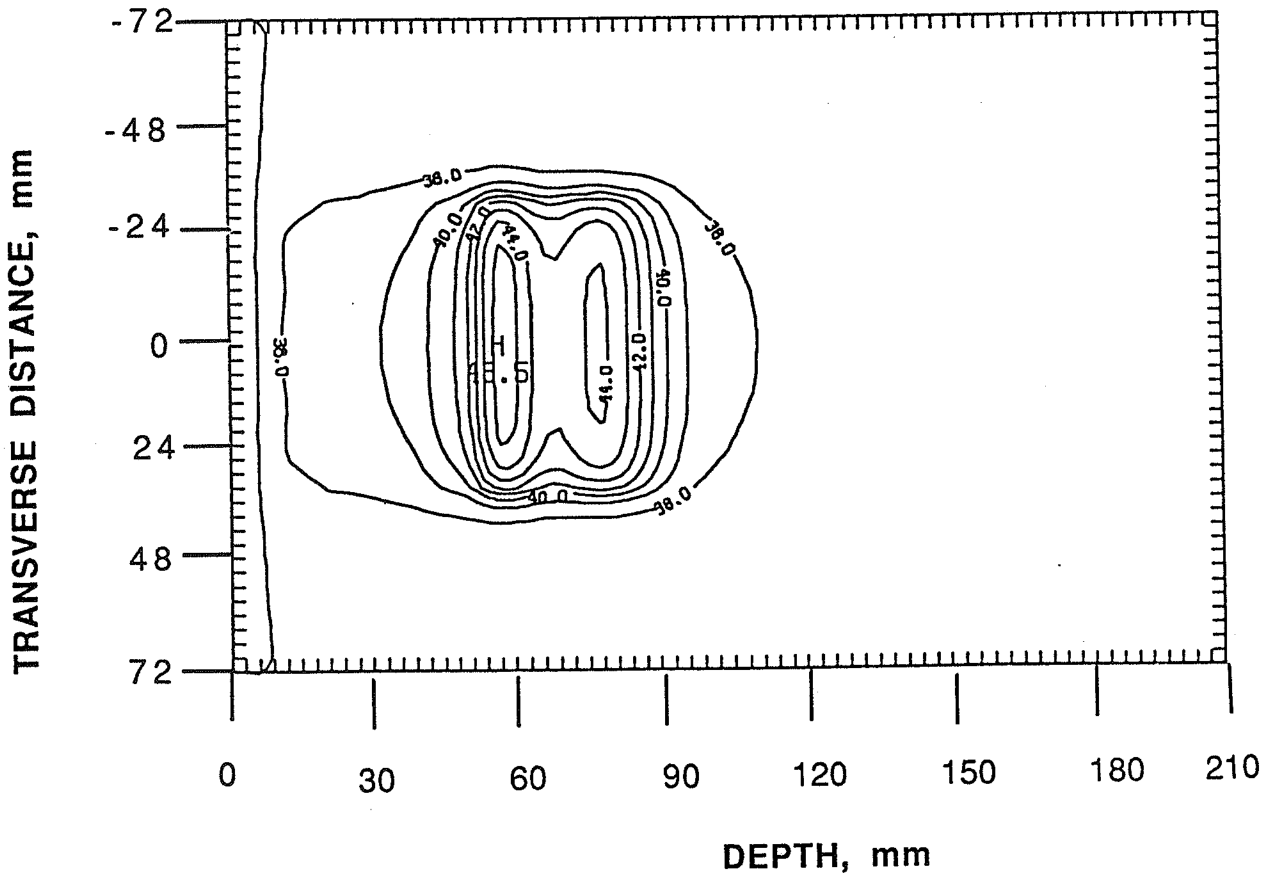

Figure 5.12. Simulated temperature distribution associated with mechanical scanning. A contour plot of the temperature distribution resulting from scanning an elongated focus (see Figure 3.31b) over a disk of 30 mm radius. Contours are given at intervals of 1^0C.

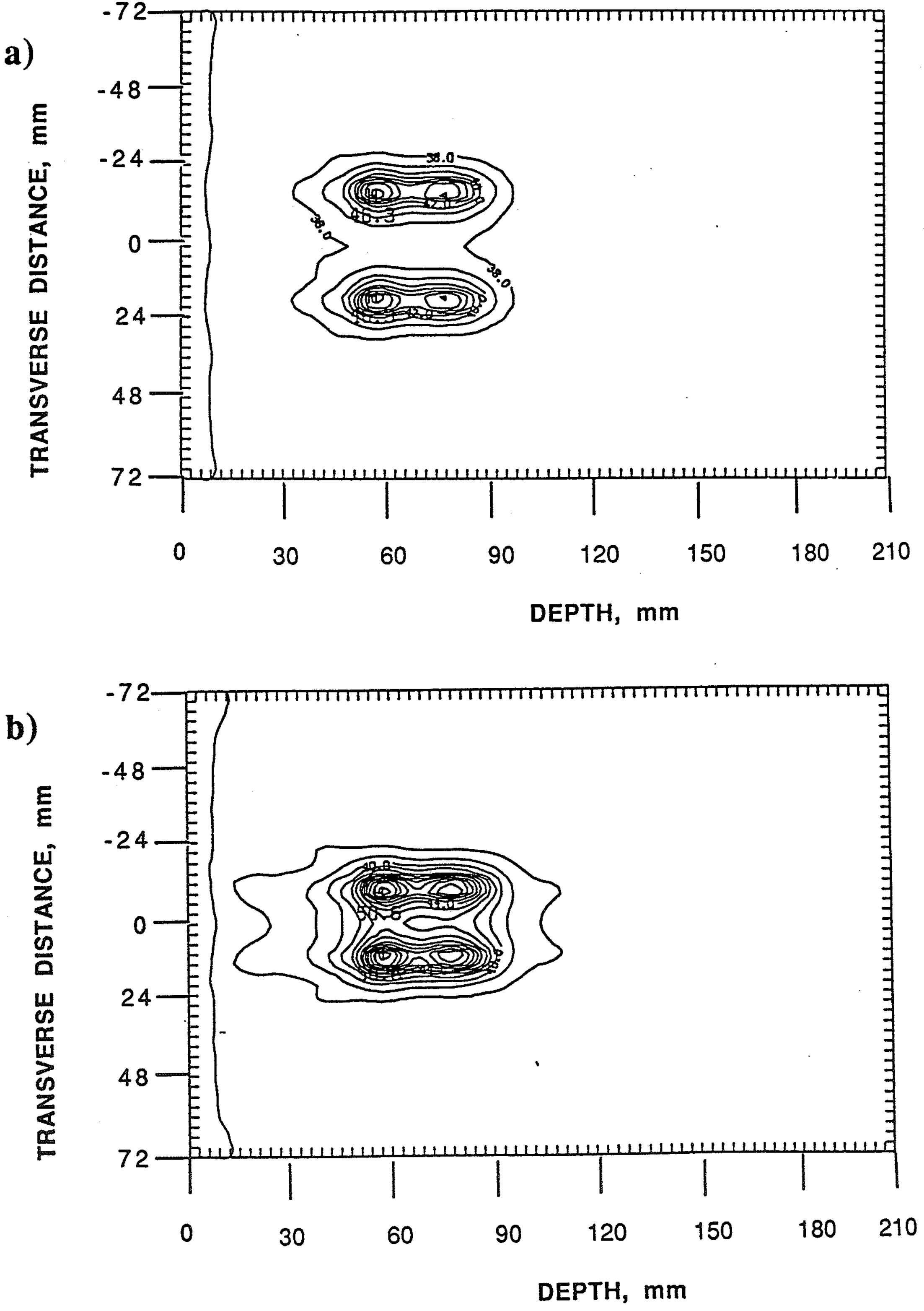

Figure 5.13. Simulated temperature distribution associated with mechanical scanning. a) A contour plot of the temperature distribution resulting from from scanning an elongated foci over an annular ring of radius greater than 12 mm and b) is the temperature distribution resulting from scanning over a 10 mm radius annular ring.

the BHTE, the contour plot of the resulting temperature distribution is shown in Figure 5.14, which shows that the temperature of a volume of almost 58.5 cm^3 is raised to a therapeutic level.

The possibility of heating simultaneously different volumes (i.e., back and front of a large tumor) is also demonstrated. By simultaneously focusing at 48, 72, and 90 mm (from the array surface) and scanning the resulting pattern over a disk of 25 mm radius, the power deposition pattern of Figure 5.15a) is produced. The SPTP focal intensity used to realize this pattern is 130.77 W/cm^2. The scanned field intensity gain in the focal planes is approximately 3 dB. The temperature distribution associated with the pattern of Figure 5.15a is shown in Figure 5.15b).

Finally, heating tumors at greater depths is investigated. The array is first focused at a point 180 mm from its surface along the main axis. The resulting pattern is shown in Figure 5.16a). By scanning the pattern of Figure 5.16a) over a disk of a 10 mm radius (by performing the convolution integral), the scanned field intensity profile of Figure 5.16b resulted. The large depth of field of the stationary pattern (see Figure 5.16a)) is due to the large F-number of the pattern $\left(\text{F-number} = \frac{\text{focal depth}}{\text{radius}}\right)$ which can be adjusted by varying the number of annular elements (effective radius of the applicator).

5.6 The Effect of Blood Perfusion Rate on the Synthesized Heating Patterns

In this section, the effect of blood flow on the tissue thermal response to hyperthermia induced heating will be investigated. The goal of this investigation is to demonstrate the importance of modifying the heating pattern, in some cases, to adapt to biological changes in the treated region such as blood flow. In fact, an important advantage of phased arrays over fixed focus hyperthermia systems is their ability to modify the heating pattern during the treatment. This flexibility, which makes phased arrays more versatile than mechanical scanning, would allow the therapist to modify the shape,

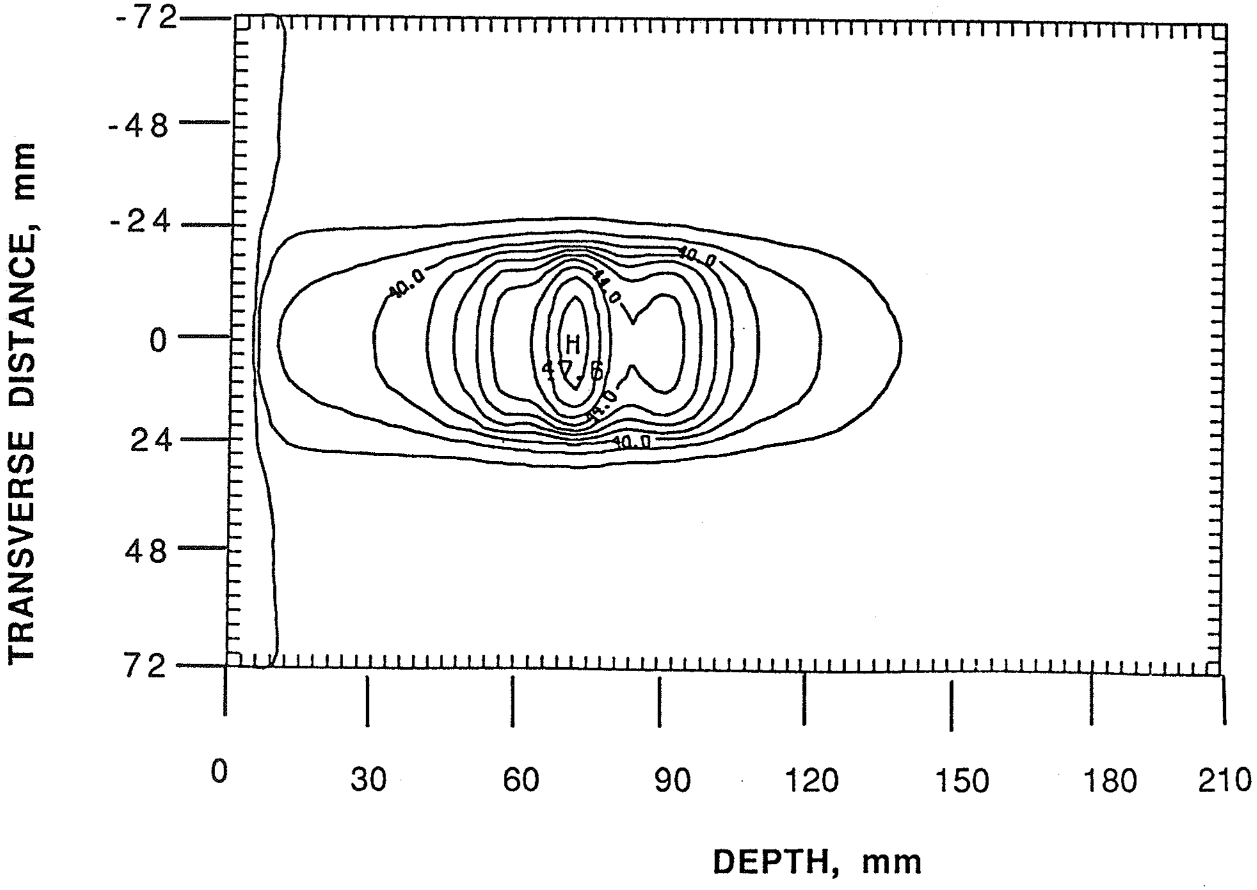

Figure 5.14. Simulated temperature distribution associated with mechanical scanning. A contour plot of the temperature distribution resulting from inputting the pattern of Figure 3.32 to the BHTE. Contours are given at intervals of 1°C.

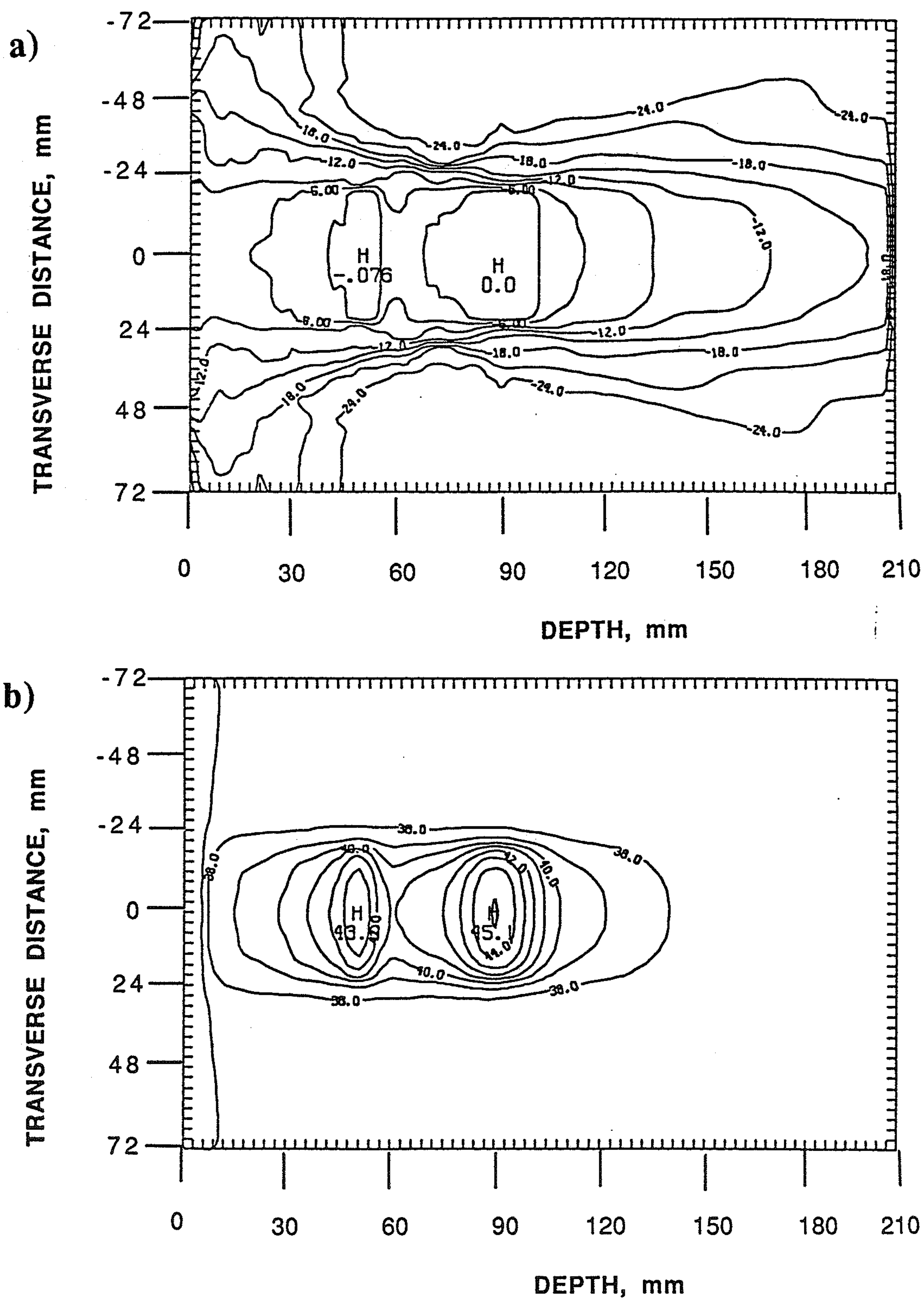

Figure 5.15. a) A contour plot of the field intensity profile resulting scanning three simultaneous foci (see text) over a disk of 25 mm radius. All Normalized intensities of less than -24 dB are truncated and contours are given at intervals of 3 dB. b) Temperature distribution resulting from (a).

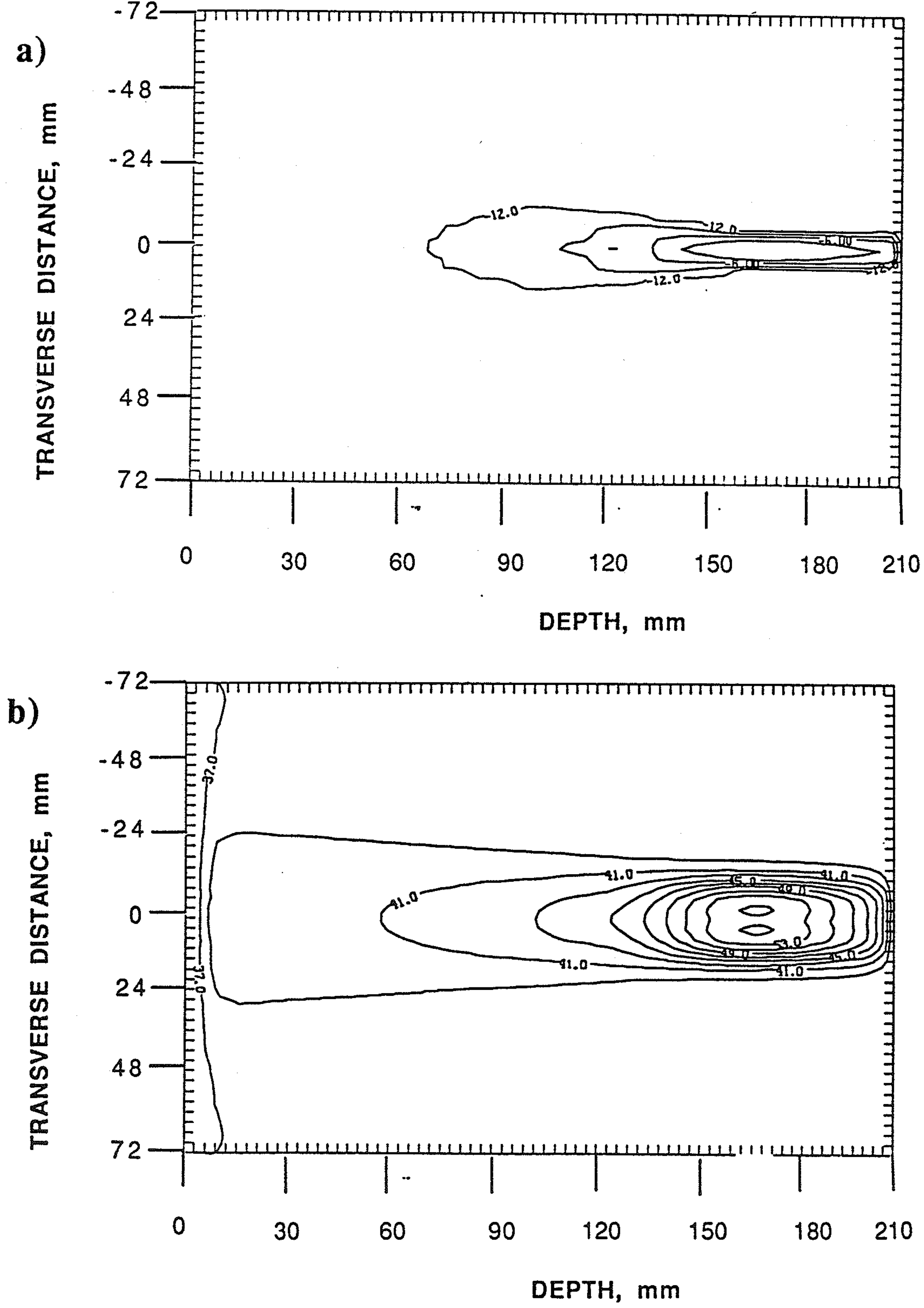

Figure 5.16. Heating of deep seated tumors. a) A contour plot of the field intensity profile resulting from focusing at (0,0,180) along the array axis and b) is the temperature distribution resulting from scanning the pattern of (a) over a disk of 10 mm radius.

intensity, and depth of the synthesized pattern by adjusting the electronic control as demonstrated in Chapters 3 and 4.

Although noninvasive measurements of tissue temperature and/or blood flow are still very difficult if not impossible, an ultimate hyperthermia system should have a means of determining the volume distribution of both temperature and blood perfusion. Understanding the effect of variations in blood perfusion on the temperature distribution might be very helpful in the design of adaptive control algorithms for the ultimate hyperthermia system.

Two series of simulations were conducted for this investigation. In a first series, the field intensity pattern of Figure 3.29 was scanned over a disk of a 25 mm radius. The resulting time-averaged intensity profile is illustrated in Figure 5.17. A time-averaged gain of 8.35 dB was evaluated in the focal plane (z= 70 mm). The maximum time-averaged intensity in the focal plane was adjusted to 12.5 W/cm^2 and kept constant for all simulations. The blood perfusion rate was varied between 1 and 10 kg/m^3/s and the BHTE was solved for each case. Figure 5.18 illustrates the resulting temperature distribution for blood perfusion of 8, 6, 4, and 2 kg/m^3/s, respectively. It is noticed that the maximum temperature reached inside the tumor is a strong function of blood flow. Figures 5.19a) and b) illustrate the effect of blood flow on the maximum temperature and on the number of iterations necessary to solve the BHTE, respectively. It should be noted that an over-relaxation factor of 1.42 was used for all simulations. This value was found to be optimum for a blood perfusion rate of 8.3 kg/m^3/s. However, it would be necessary to determine a more suitable value to minimize the required cpu time if the study of different blood perfusion rate is intended.

In a second series of simulations, the elongated focus of Figure 3.31 was scanned over a disk of 25 mm radius. The resulting scanned field intensity profile is shown in Figure 5.20a) . The scanned field intensity gain was found to be 5.96 dB as evaluated in the focal plane. It is desired to raise the temperature of a cylindrical tumor model of 25 mm

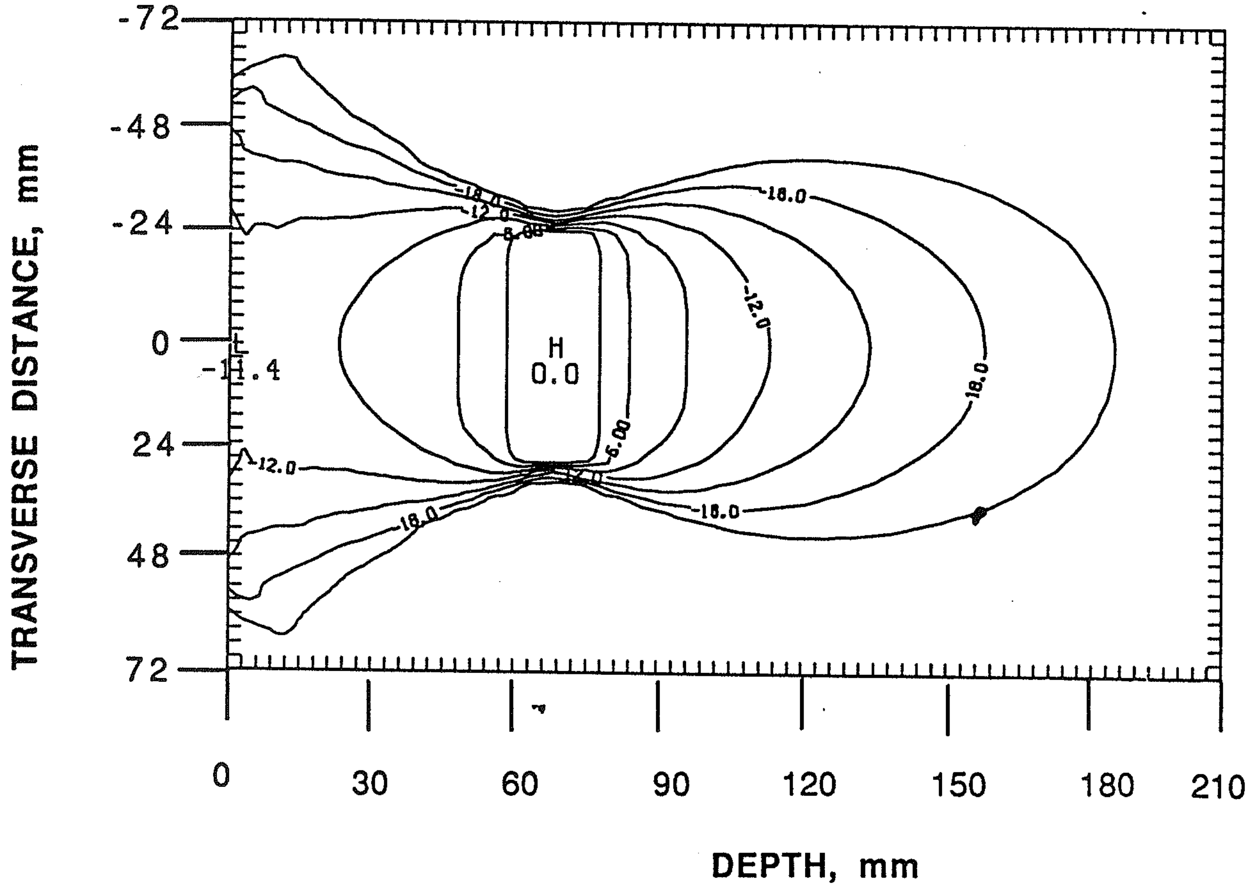

Figure 5.17. The scanned field intensity profile resulting from scanning the pattern of Figure 3.29 over a disk of 25 mm radius. Contours are given at intervals of 3 dB.

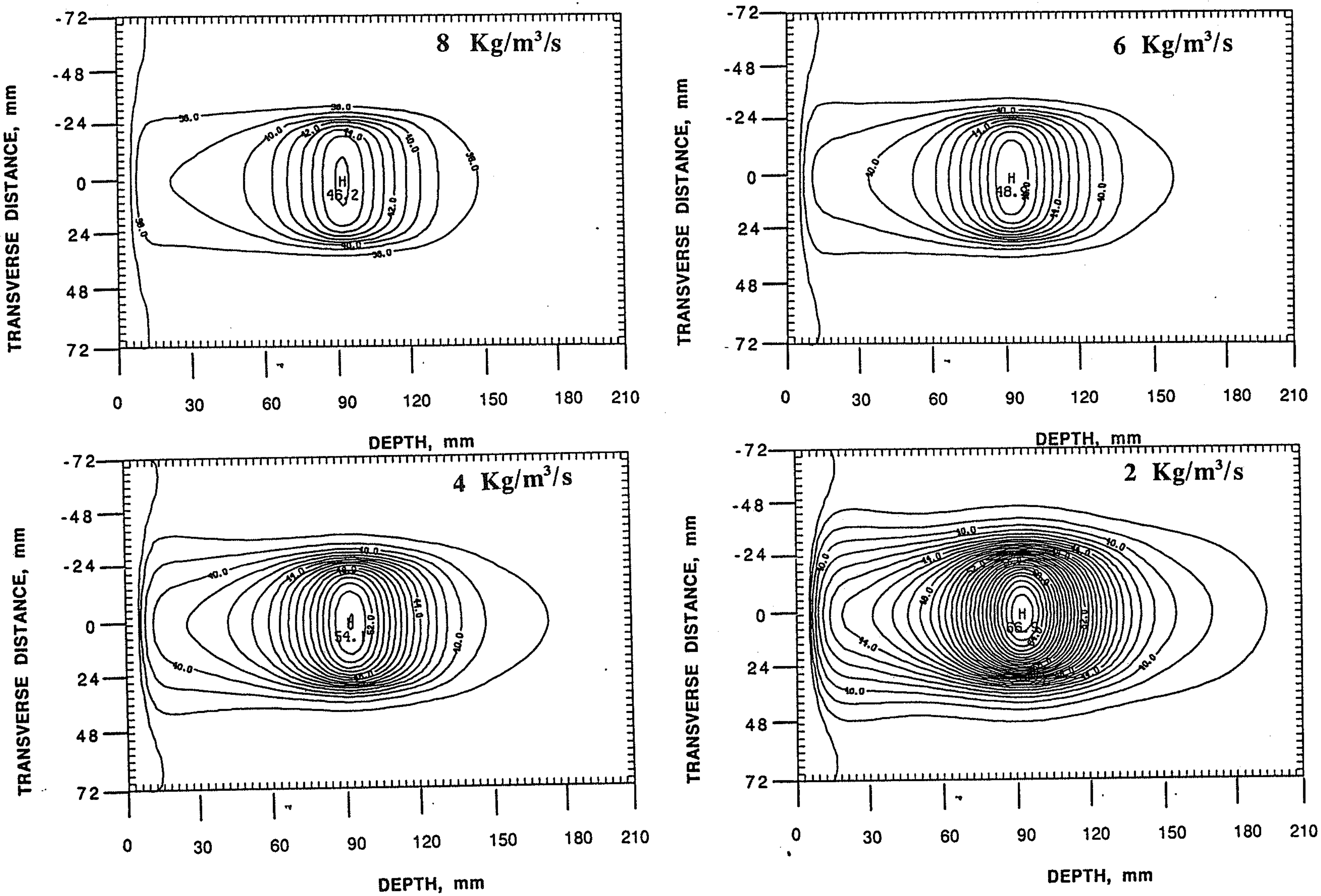

Figure 5.18. Temperature distributions associated with the intensity profile of Figure 5.17 for different blood flow rates as shown above. Contours are given at intervals of 1 ^{0}C.

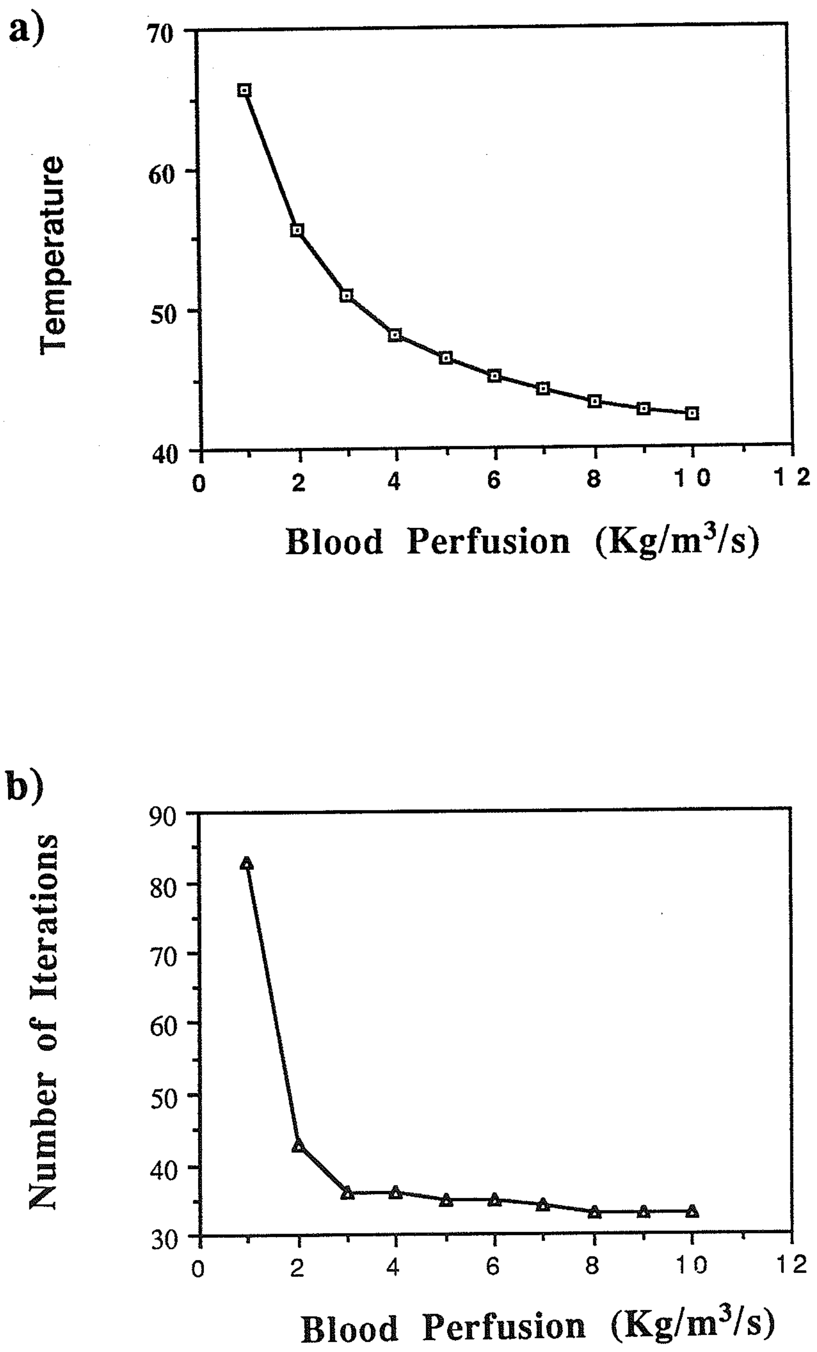

Figure 5.19. a) A plot of the maximum temperature inside the tumor as a function of blood flow. b) A plot of the number of iterations required to solve the BHTE for different Blood perfusion rates. In both cases, the time averaged intensity was kept constant (12.5 W/cm^2) for different blood perfusion rates.

radius and 28 mm length to a therapeutic level (≥ 42^0 C). Figure 5.20b) illustrates the temperature distribution resulting by adjusting the time-averaged intensity to 15.6 W/cm^2 and assuming a highly perfused model (8 kg/m^3/s). Figure 5.20b) shows that the therapeutic heating is confined to the tumor model (volume to be heated). However, if the blood perfusion rate suddenly drops or if this heating pattern is designed for a poorly perfused model (≤ 4 kg/m3/s), therapeutic heating might extend to normal tissue as illustrated in Figure 5.21, which shows the effect of blood flow on the temperature distribution within tumorous and normal tissue by considering a blood flow of 8, 6, 4, and 2 kg/m^3/s, respectively. While the maximum temperature inside the tumor increases substantially with lower blood flow (see Figure 5.19a)), the extension of the heated volume increases (for constant power) to eventually exceed the tumor boundaries as demonstrated for w_n = 4 kg/m^3/s in Figure 5.21. The problem might become more serious for lower blood perfusion rate as can be seen from Figure 5.21 (w_n = 2 kg/m^3/s).

These simulations demonstrate the importance of blood flow to hyperthermia treatment planning. The knowledge of the perfusion rate within the treatment region (tumor and surrounding tissue) will prove very useful as a feedback for optimal control algorithms for phased array hyperthermia systems which are capable of modifying their synthesized heating patterns accordingly.

5.6 Conclusions

This chapter concentrated on investigating the CRA as a tool for inducing therapeutic heat in cancer therapy. The FCM was used to synthesize different intensity patterns which had been multiplied by 2α (α being the tissue absorption coefficient) and then inputted to the cylindrical BHTE. The BHTE was then solved numerically, using a finite difference with over-relaxation technique.

It is shown that focusing on the axis results in a very sharp localized power deposition pattern. However, the small size of the resulting 3 dB focal region makes it

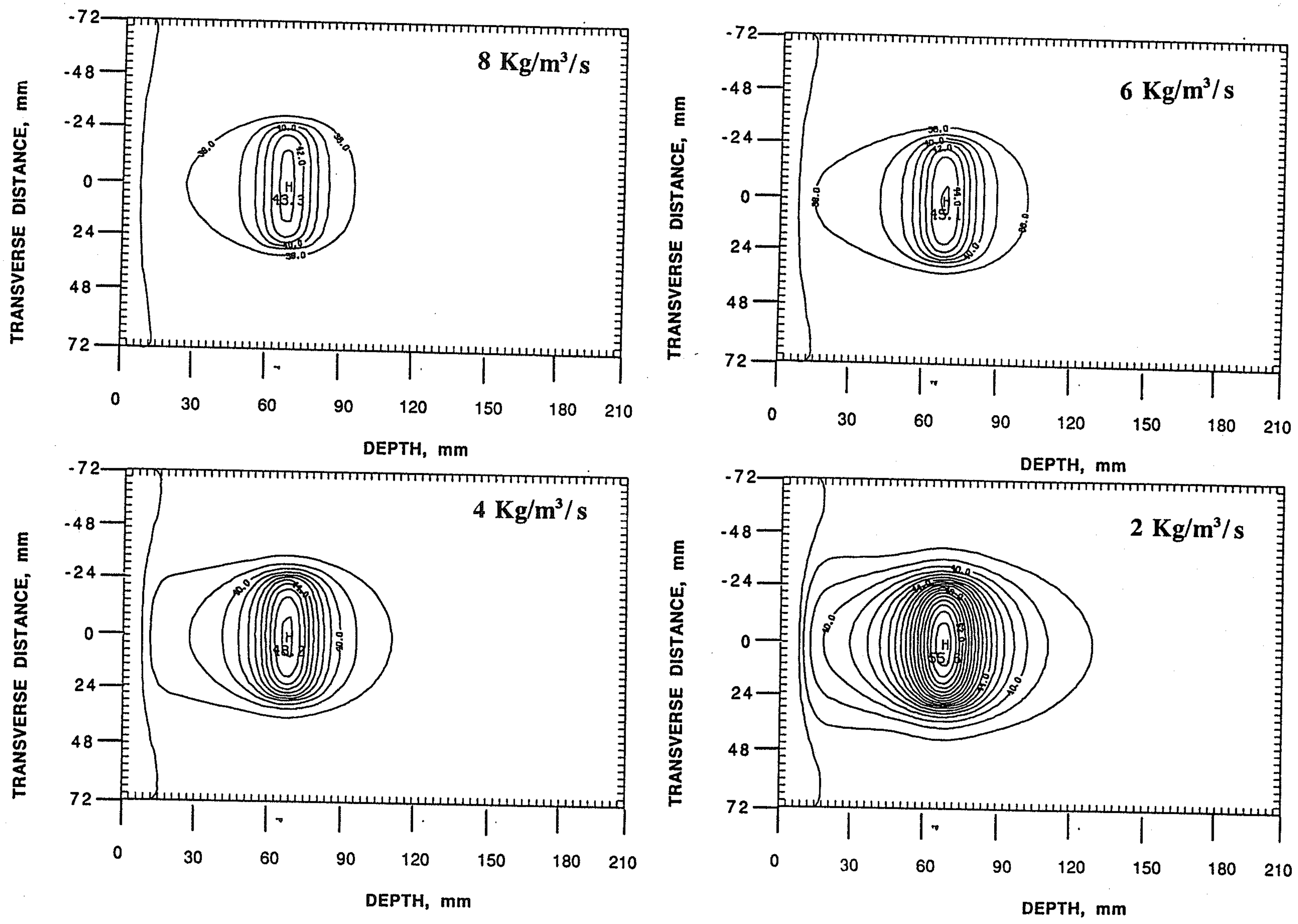

Figure 5.21. The temperature distribution associated with the pattern of Figure 5.20a) for different values of blood perfusion rates as shown above. Contours are given at intervals of 1^0C.

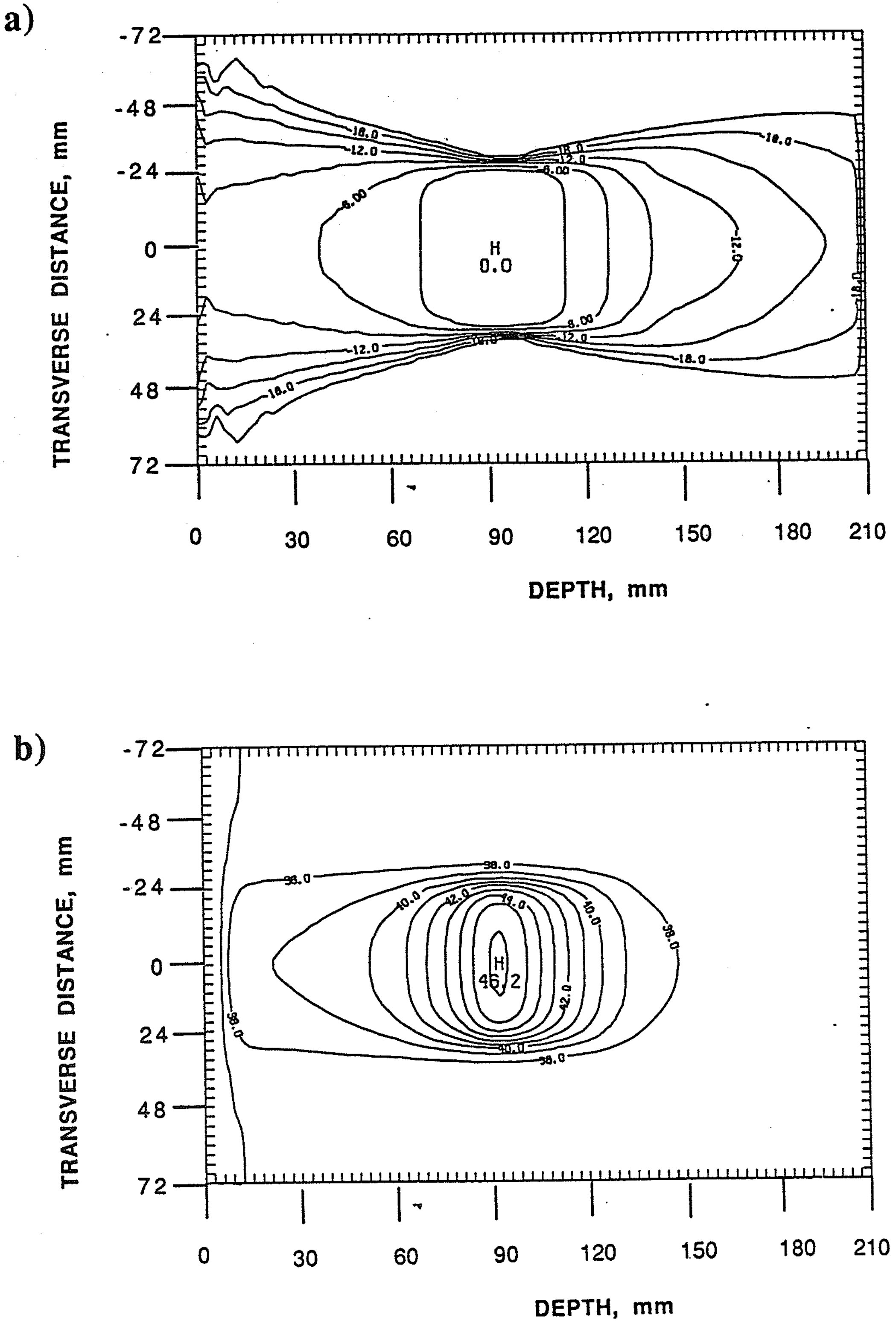

Figure 5.20. a) The scanned field intensity profile resulting from scanning the pattern of Figure 3.31 over a disk of 25 mm radius (see text). b) The associated temperature distribution for a blood perfusion of 8.0 kg/m^3/s.

inadequate to heat even very small tumors without some manipulation. Elongated foci might lead to larger focal volumes, but the special shape of these volumes (elongated ellipses) would severely limit practical applications. It is also shown that while the direct synthesis of annular patterns is very simple, their use as a means of heating tumors is not promising. It is then demonstrated that the combination of a simple mechanical movement with the electronically controlled multiple focusing (along the axis of the array) leads to virtually any desired heating pattern. Finally, the effect of blood flow on the resulting temperature distributions is investigated and discussed.

CHAPTER 6

THE SIMULATED TEMPERATURE DISTRIBUTIONS ASSOCIATED WITH THE NXN SQUARE-ELEMENT ARRAY

6.1 Introduction

The power deposition patterns produced by the NxN square-element array were studied in Chapter 4. The application of the rotating field conjugation method to the synthesis of annular patterns was shown to produce well-behaved patterns without secondary foci proximal or distal the focal plane. The RFCM was compared to the electronic scanning of an intense focal spot. In addition, simulations were conducted to demonstrate the possibility of combining the direct synthesis technique with the electronic scanning to obtain different power deposition patterns. The advantage of the combination is to reduce the number of scanning points while using a relatively low level SPTP focal intensity.

Chapter 4 was restricted to the different aspects of the power deposition, such as the intensity gain and the possible formation of secondary foci. However, the potential for use of these patterns in hyperthermia cancer therapy can only be judged by their associated temperature distributions within the tumor and the surrounding normal tissue. To simulate these distributions, the field intensities were multiplied by the tissue absorption coefficient and then inputted to the steady-state bioheat transfer equation (BHTE) which was then solved numerically for the tissue thermal response.

Demonstrated in this chapter, is the capability of the NxN array to induce heating at different depths. In particular, some diffuse patterns synthesized in Chapter 4 are used as inputs to the BHTE, and the resulting thermal responses are discussed. A thermal anatomical homogeneous model is adopted and used for the computation of the temperature distributions in tissue-like media. A summary of the finite difference with over-relaxation is given as a reference. The resulting temperature distributions are used to evaluate the

NxN phased array as a hyperthermia applicator. The evaluation is based on the possibility of raising the tumor temperature above a certain minimum therapeutic temperature (i.e., ≥ 42 °C) while keeping the normal tissue temperature below a certain specific temperature (i.e., 40 °C).

6.2 The 3-D Steady-State Bioheat Transfer Equation (BHTE)

In Chapter 5, the steady-state bioheat equation was analyzed, and an iterative solution in cylindrical coordinates, with angular symmetry, was discussed. The iterative solution was based on the finite difference with over-relaxation technique. Unlike the patterns produced by the CRA, those produced by the NxN are generally nonsymmetrical and require the solution of the 3-D BHTE. A three-dimensional anatomical model is proposed for the computation of the temperature distributions. The finite difference technique is used to solve the BHTE in rectangular coordinates. Details of the numerical technique and an estimate of the error associated with the approximation were given in Chapter 5 and will not be repeated here. In this section, the 3-D anatomical model is illustrated followed by a formulation of the BHTE in a finite difference form which is used in the different simulations discussed in the following sections.

6.2.1 Thermal-anatomical model

A thermal anatomical model of the tumor and the surrounding tissue is assumed in order to simulate the tissue thermal response to the ultrasonic power deposition. The model is similar to that adopted in Chapter 5, except for the geometry of the tumor which is assumed to be spherical in shape. Figure 6.1 illustrates the assumed geometry in the (y,z) plane. All parameters are assumed to be constant in the second transverse direction (x) outside the tumor. The model consists of four layers of the same thickness and conductivity as those of the cylindrical model (see Table 5.1). The blood perfusion rate in

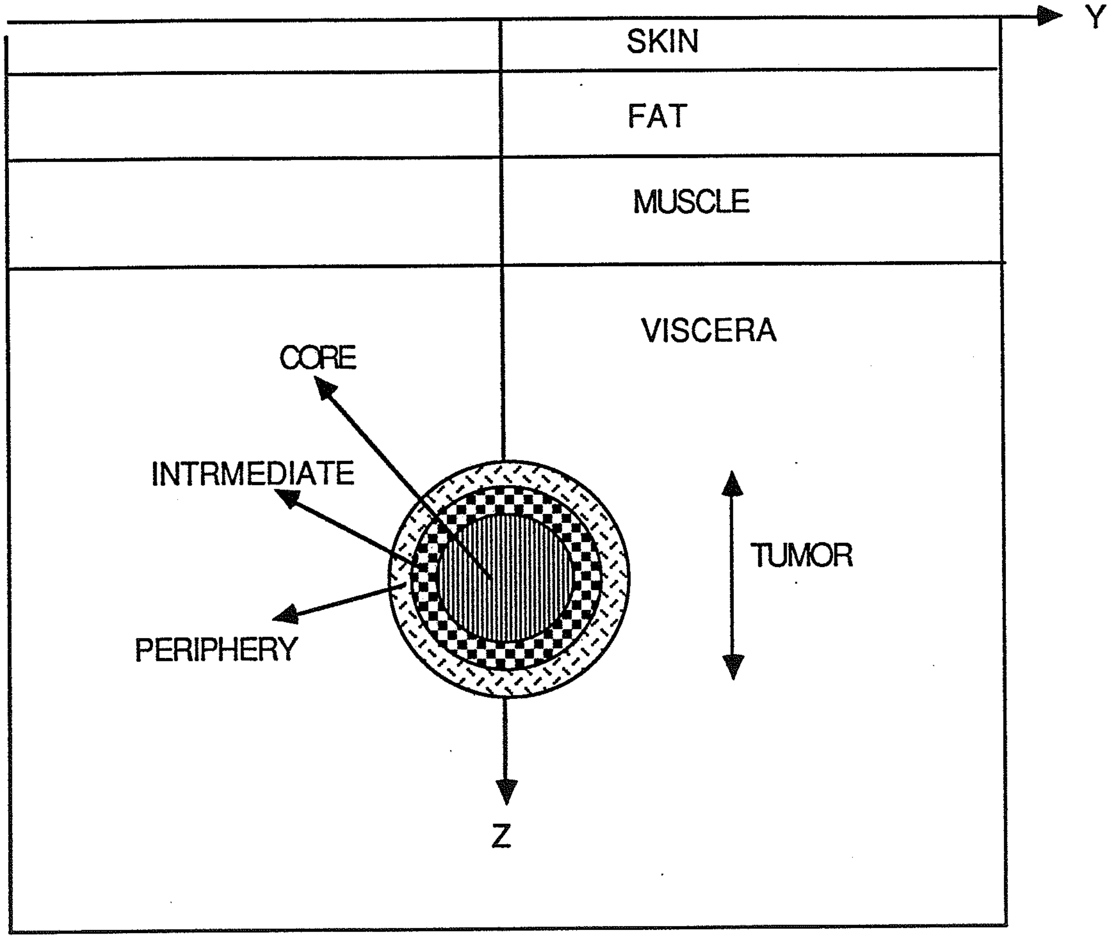

Figure 6.1. Thermal anatomical model of the tumor and the surrounding tissue. The tumor, embedded in the viscera, consists of three concentric spheres which can have different blood perfusion rates.

normal tissue is assumed to be 8.3 $Kg/m^3/s$ for the simulations. The tumor model, embedded in the viscera, consists of three concentric spherical layers which can have different blood perfusion rates. However, the tumor blood perfusion will be identified with that of normal tissues (8.3 $Kg/m^3/s$) through this chapter. The effect of blood perfusion on the thermal response was studied in Chapter 5 and will not be repeated here. The conductivity of the tumor tissue is identified with that of the viscera, and the tumor depth is varied to allow the investigation of heating at different depths. The skin temperature is assumed constant and equal to 25 ^{0}C. The temperature at the wall of the 3-D grid is identified with that of the body (37 ^{0}C). Finally, the model is assumed homogeneous, and strong reflectors such as gas cavities and bones are excluded.

6.2.2 The finite difference formulation

The general form of the steady-state bioheat equation in rectangular coordinates is given by

$$-K\left(\frac{\partial^2 T}{\partial x^2}+\frac{\partial^2 T}{\partial y^2}+\frac{\partial^2 T}{\partial z^2}\right)+w_b\, c_b\,(T - T_b) - Q(x,y,z)= 0 \qquad (6.1)$$

where K is the thermal conductivity ($W/m/^0 C$), Q is the power deposition rate (W/m^3), w_b is the blood perfusion rate ($Kg/m^3/s$), c_b is the blood specific heat ($J/kg/^0 C$), T is the tissue temperature (^{0} C), and T_b is the arterial blood temperature.

Equation (6.1) can be put in a finite difference form by using the approximate difference expression of the second-order partial derivative as shown below:

$$\frac{\partial^2 T}{\partial x^2}=\frac{T_{(n+1)mp} - 2\,T_{nmp} + T_{(n-1)mp}}{\Delta^2} \qquad (6.2)$$

where T_{nmp} is the temperature at node nmp and Δ is the incremental size in the three directions (i.e., $\Delta= \Delta x= \Delta y= \Delta z$). Figure 6.2a) shows the considered geometry.

a)

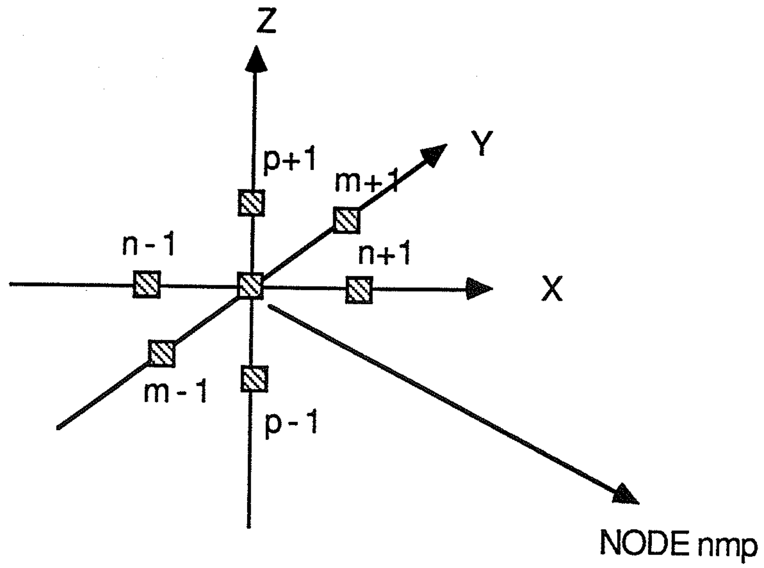

b)

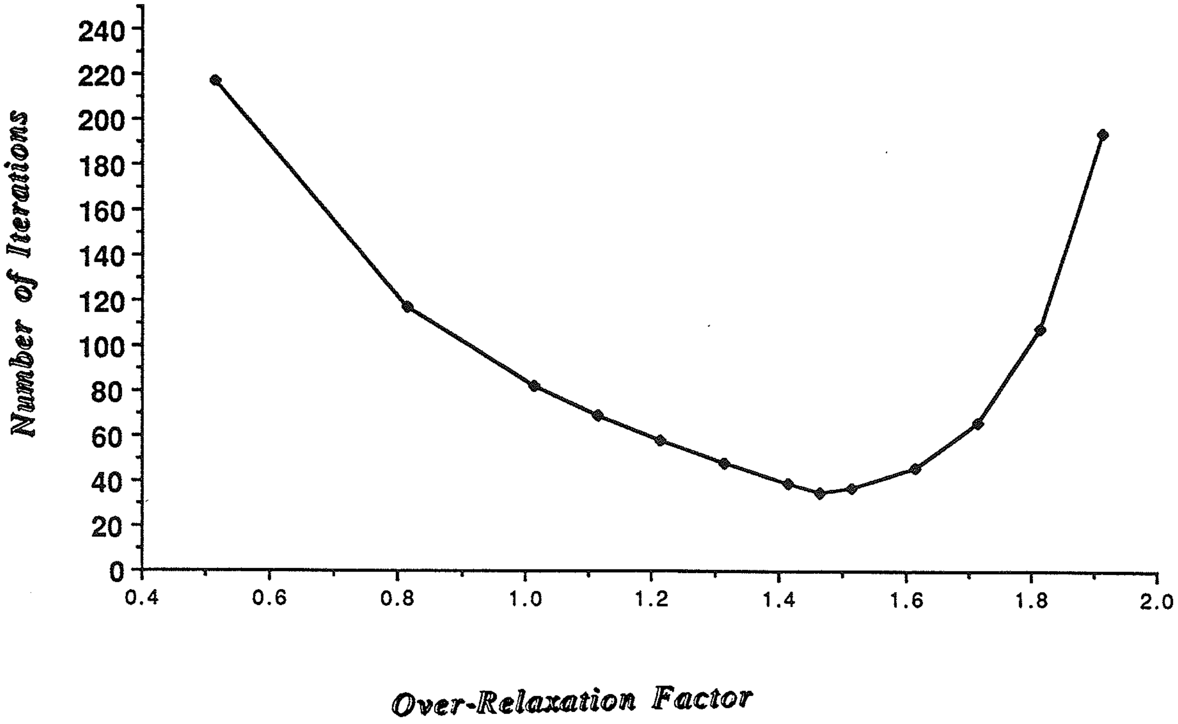

Figure 6.2. a) Geometry used for the finite difference formulation. b) Plot of the number of iteration as a function of the over-relaxation factor for a typical run of the BHTE program.

It can be seen that Eq. (6.2) is simply the 3-D version of Eqs. (5.12) and (5.13) derived in the preceding chapter. The partial derivatives with respect to y and z can similarly be written in a finite difference form as below:

$$\frac{\partial^2 T}{\partial y^2} = \frac{T_{n(m+1)p} - 2\,T_{nmp} + T_{n(m-1)p}}{\Delta^2} \qquad (6.3)$$

$$\frac{\partial^2 T}{\partial z^2} = \frac{T_{nm(p+1)} - 2\,T_{nmp} + T_{nm(p-1)}}{\Delta^2} \qquad (6.4)$$

and by using these approximations in Eq. (6.1), the nodal temperature can easily be derived as follows

$$T_{nmp} = f(T_{nods}) = \frac{1}{6K_{nmp} + \Delta^2 w_{bnmp}\, c_b\, T_b}\,[K_{nmp}\, T_{nods} + w_{bnmp}\, c_b\, w_b] \qquad (6.5)$$

where K_{nmp} and w_{bnmp} are the conductivity and the blood perfusion rate at node nmp. T_{nods} is defined as follows

$$T_{nods} = T_{(n+1)mp} + T_{(n-1)mp} + T_{n(m+1)p} + T_{n(m-1)p} + T_{nm(p+1)} + T_{nm(p-1)} \qquad (6.6)$$

and it is Eq. (6.5) that is used in the iterative form of the finite difference with over-relaxation

$$(T_{nmp})^{new} = W\, f(T_{nods})^{new} + (1-W)\,(T_{nmp})^{old} \qquad (6.7)$$

where the superscript gives the order of iteration and W is the over-relaxation parameter.

A series of simulations were conducted to determine an optimum value for the over-relaxation parameter W which depends, among others, on the anatomical model parameters and on the chosen grid size. A typical power deposition pattern was used as an input to the bioheat transfer equation, which was solved for differnt values of W. The relaxation factor was varied between 0.5 and 1.95 while keeping all other parameters fixed. Figure 6.2b) illustrates the effect of W on the required number of iterations. A value of 1.45 was determined to be optimum and was used in all the following simulations. For this value of W, the number of iterations was typically between 35 and 41 for a grid of (31X31X50). The cpu run time for the same grid size was approximately 6.3 second on the CRAY X-MP48. A listing of a Fortran program used to solve the 3-D BHTE is given in Appendix C.

6.3 Temperature Distributions

The ultrasonic field intensity patterns, produced by the NxN array in Chapter 4, were multiplied by 2 α (α is the pressure absorption coefficient) to compute the time-averaged rate at which heat is produced per unit volume. This rate Q is then used as an input to the 3-D BHTE which is solved numerically for the tissue thermal response.

In the following simulations, the blood perfusion rate inside the tumor is identified with that of normal tissue (8.3 Kg/m^3/s). The array elements were assumed to be capable of delivering a maximum intensity of 4 W/cm^2 at their surface. The tissue attenuation and the speed of sound were assumed to be 1 dB/cm/MHz and 1500 m/s, respectively. The skin temperature is assumed constant (25 ^{0}C). The time-averaged intensity gain of the different patterns is adjusted in order for the temperature not to exceed 50 ^{0}C. The method of direct synthesis (FCM and RFCM) is used to produce simple, multiple, and laterally diffuse focusing at different sites. The patterns are then inputted to the BHTE and the resulting temperature distributions are discussed.

The array is also used to produce an intense focal spot which is then swept over a predetermined scanning trajectory, a technique known as electronic scanning. The temperature distributions associated with the electronic scanning are compared with those associated with the direct synthesis deposition technique, and preliminary conclusions are drawn.

6.3.1 Temperature distributions associated with the direct synthesis technique

The capability of the array to produce enough therapeutic gain at depth is first simulated. The array was first used to produce an intense focal spot along its main axis at 130 mm depth. The intensity gain evaluated at the focal site is 15.1 dB. The focal intensity is adjusted to 15 W/cm^2 and the resulting temperature distribution is shown in Figures 6.3a) and b). Figure 6.3a) is the temperature profile in the (y,z) plane while Figure 6.3b) is a temperature contour plot in the focal plane (z= 130 mm). The field conjugation method is then used to produce a focus at 160 mm from the array surface. A fictitious disk shaped source of a 5 mm radius was assumed at the desired location (0, 0, 160). The field intensity gain evaluated at the focal location is 12.08 dB. With this intensity gain, the array is capable of producing an SPTP focal intensity of 64.3 W/cm^2 at the focal site. However, the focal intensity was adjusted to 14.2 W/cm^2 and inputted to the BHTE. The resulting thermal response is illustrated in Figure 6.4.

A more diffuse focus can be produced by assuming five fictitious sources around the periphery of a tumor of a radius of 6.5 mm. The resulting power deposition was analyzed in Section 4.7 and the resulting intensity profile was shown in Figure 4.15a). A time-averaged intensity gain of 10.4 dB was evaluated at the focal site. The temperature distribution associated with this pattern is shown in Figure 6.5. To obtain this distribution, a maximum time-averaged intensity of 6.4 W/cm^2 was used in the simulation. It is worthwhile mentioning that the direct synthesis method requires an SPTP focal intensity of the same order as the maximum time-averaged intensity (6.4 W/cm^2 in this case). A larger tumor model is also assumed at 130 mm from the applicator surface. The assumed tumor

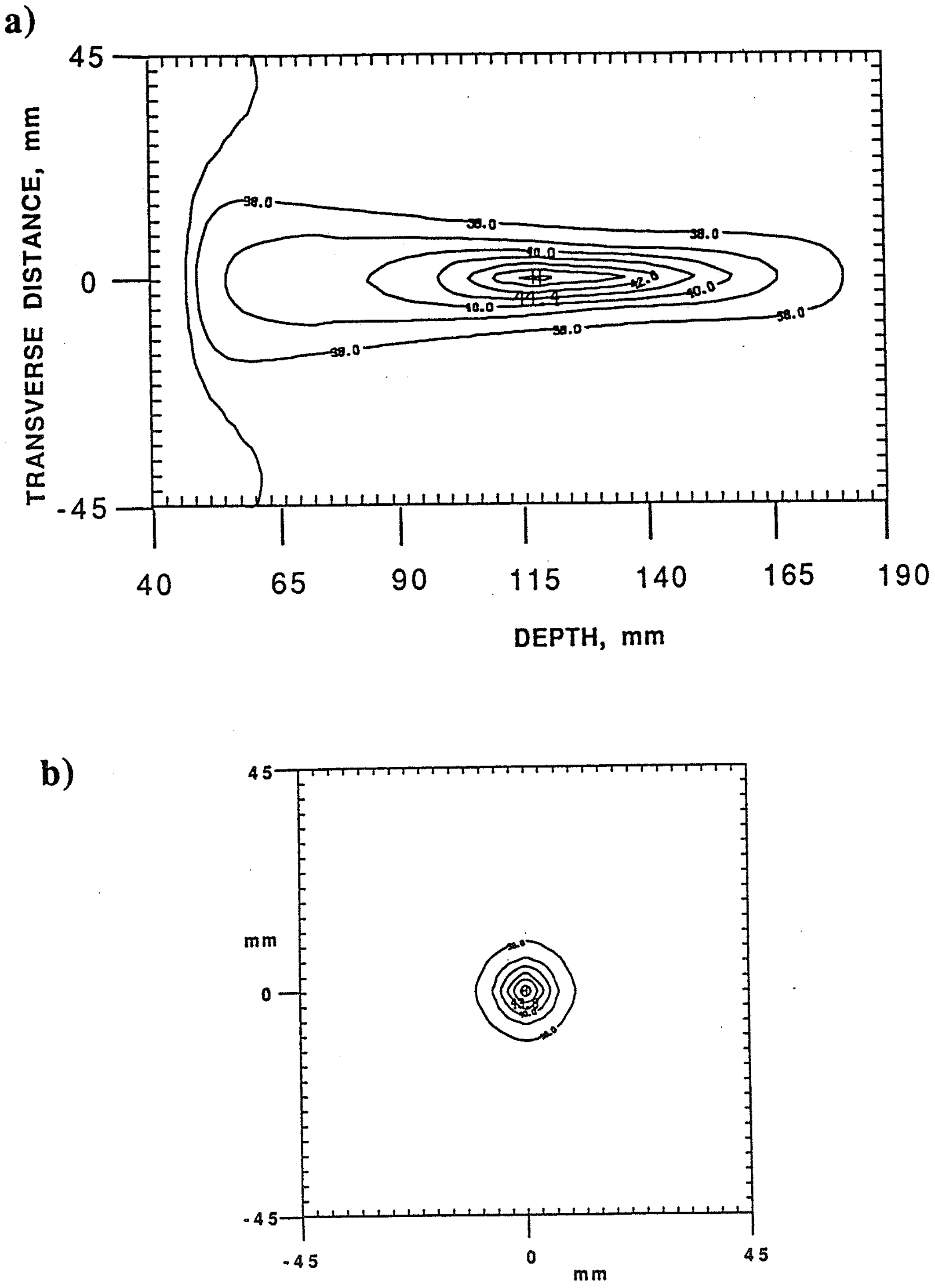

Figure 6.3. Temperature distribution associated with a simple focus. a) A contour plot (in the x-z plane) of the temperature distribution resulting from focusing the array at (0,0,130) and b) is the temperature profile in the focal plane (z=130). Contours are given at intervals of 1^{0}C.

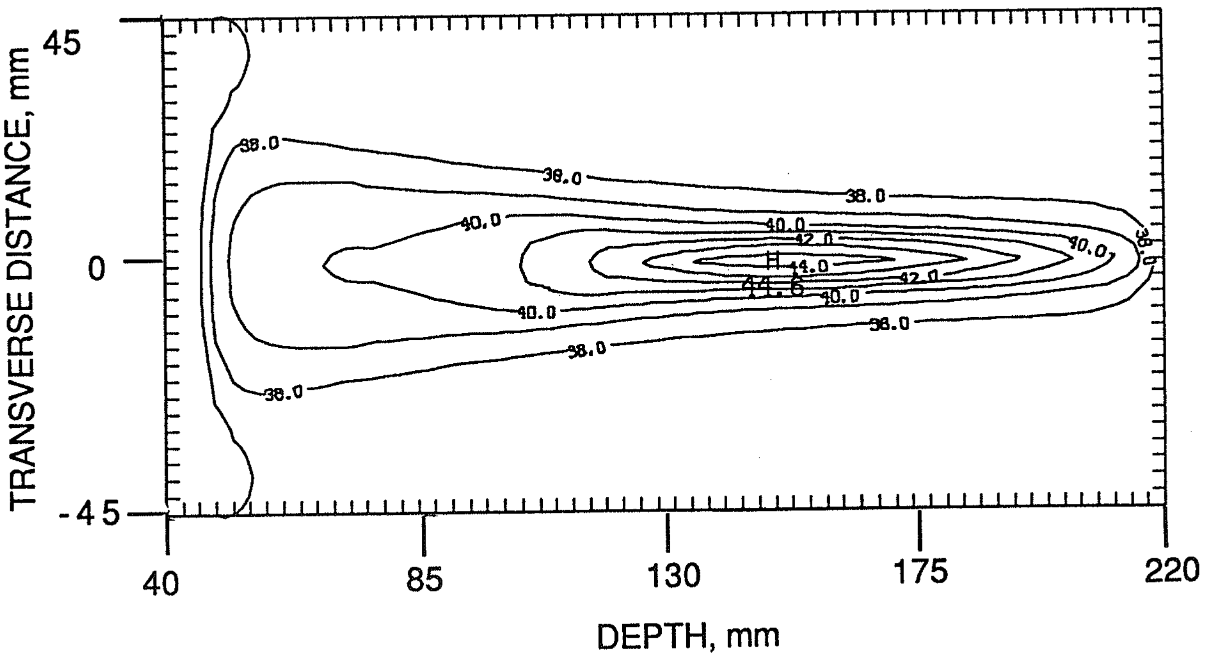

Figure 6.4. Temperature distribution associated with a simple foci at (0,0,160). The pattern was synthesized by assuming a source of 5 mm radius at (0,0,160). Contours are given at intervals of 1^{0}C.

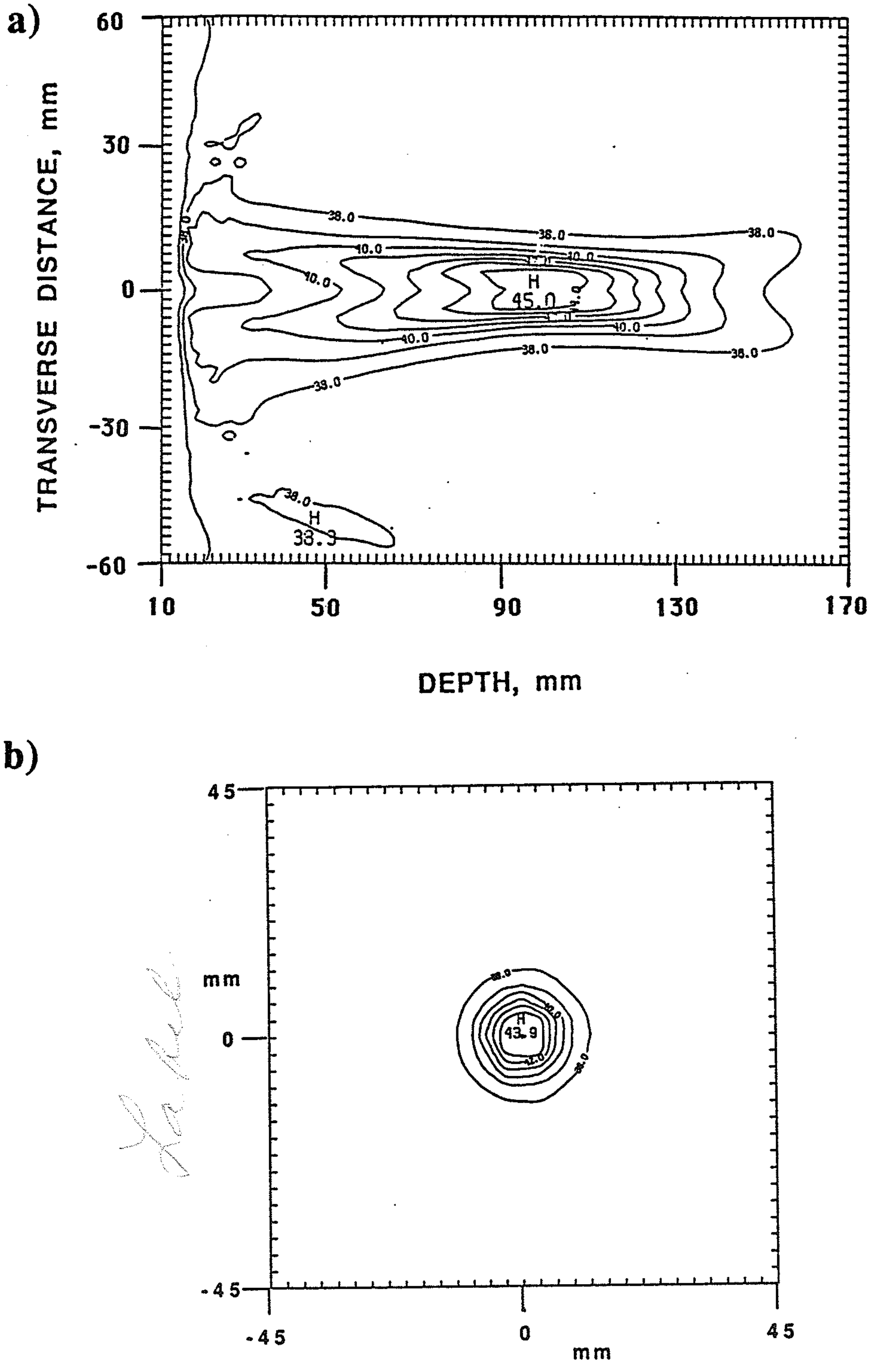

Figure 6.5. Temperature distribution associated with a diffuse focal region. a) Temperature profile in the (x,z) plane resulting from using the pattern of Fig.4.13 as input to the BHTE and b) is the temperature profile in the focal plane (z=100 mm).

model is of a 17.5 mm diameter centered at (0, 0) in the plane z= 130 mm. It was necessary to use seven assumed sources uniformly distributed around the model periphery. The time-averaged intensity gain of the pattern evaluated in the plane z=130 mm was 8.47 dB. The temperature distribution associated with this pattern is illustrated in the contour plots of Figures 6.6a) and b). The maximum time-averaged intensity (also SPTP focal intensity) was adjusted to 9.4 W/cm^2 in order to obtain the response of Figure 6.6. It is noticed that for small tumor models (diameter smaller than 20 mm), the direct deposition of power around the periphery is adequate to raise the temperature of the whole tumor to a therapeutic temperature.

To investigate the possibility of heating larger size tumors by uniquely depositing the ultrasonic energy around the tumor periphery, the power deposition pattern of Figure 4.14 was used as an input to the BHTE. This pattern was synthesized by assuming 15 sources around a tumor of a 33 mm diameter. The resulting temperature distribution is shown in Figure 6.7. The maximum time-averaged intensity in the simulations was adjusted to 7.5 W/cm^2. It is seen that while it is possible to achieve therapeutic heating at the edges of the model, the model core is not heated as shown in Figure 6.7a).

Finally, a tumor model of a radius of 22 mm at a 100 mm depth is considered. The RFCM was used to synthesize an annular heating pattern of this size in Chapter 4. Twenty assumed sources were distributed around a ring of the appropriate size, and the pattern of Figure 4.12 was obtained. The power deposition pattern of Figure 4.12 was used as input to the 3-D BHTE and the resulting temperature distribution is shown in Figure 6.8, which demonstrates the possibility of raising the tumor periphery temperature to a therapeutic level (42.7 °C) while the tumor core is far below the therapeutic threshold.

In conclusion, the different temperature distributions demonstrate the capability of the array to produce therapeutic gain at depth. Annular focal patterns seem to be adequate

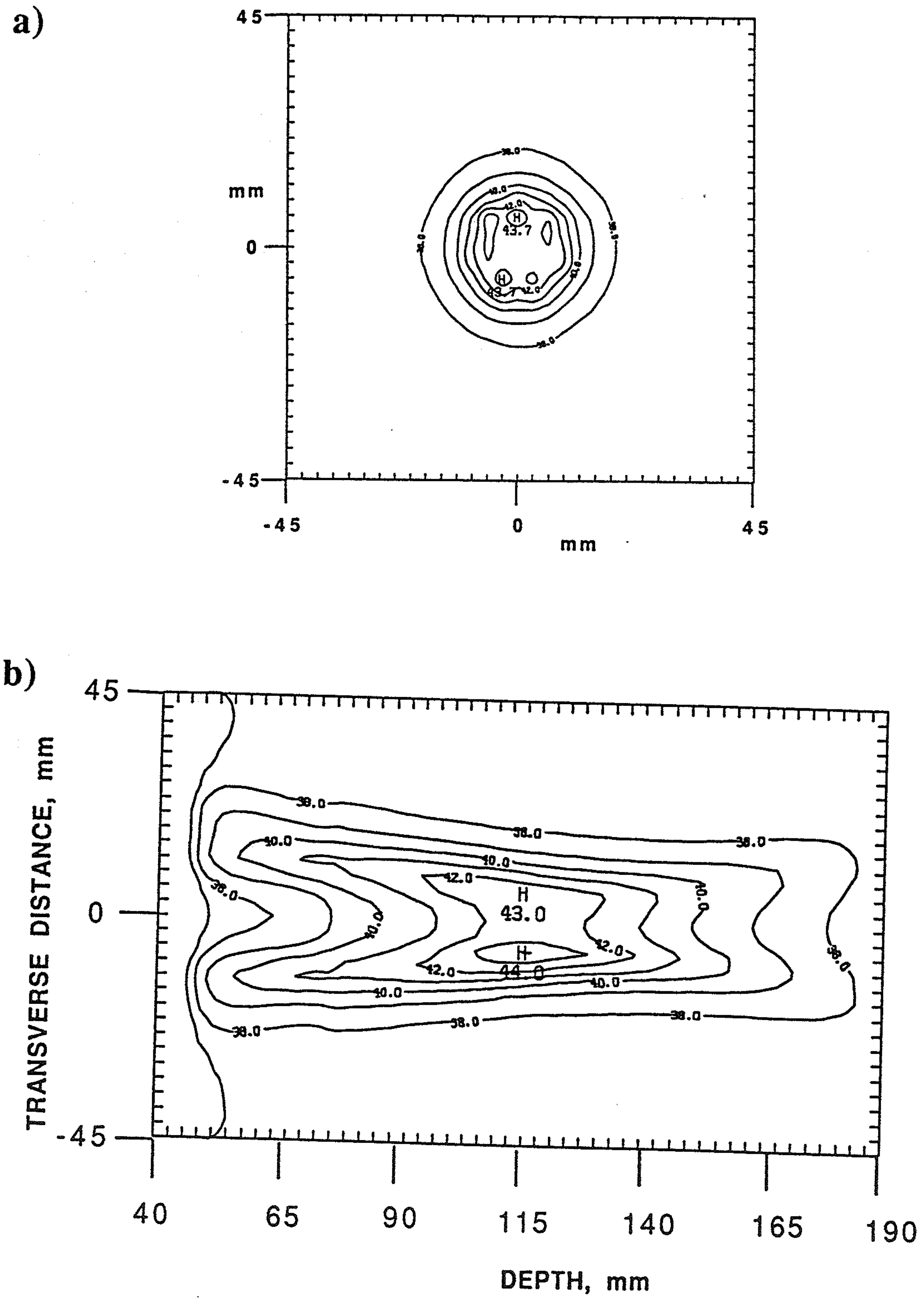

Figure 6.6. Heating associated with annular patterns. Temperature distribution produced by simultaneously focusing at seven points around the periphery of a 17 mm diameter model. a) Temperature distribution in the focal plane (z=130 mm) and b) in the plane (x,z). Contours are given at intervals of 1°C.

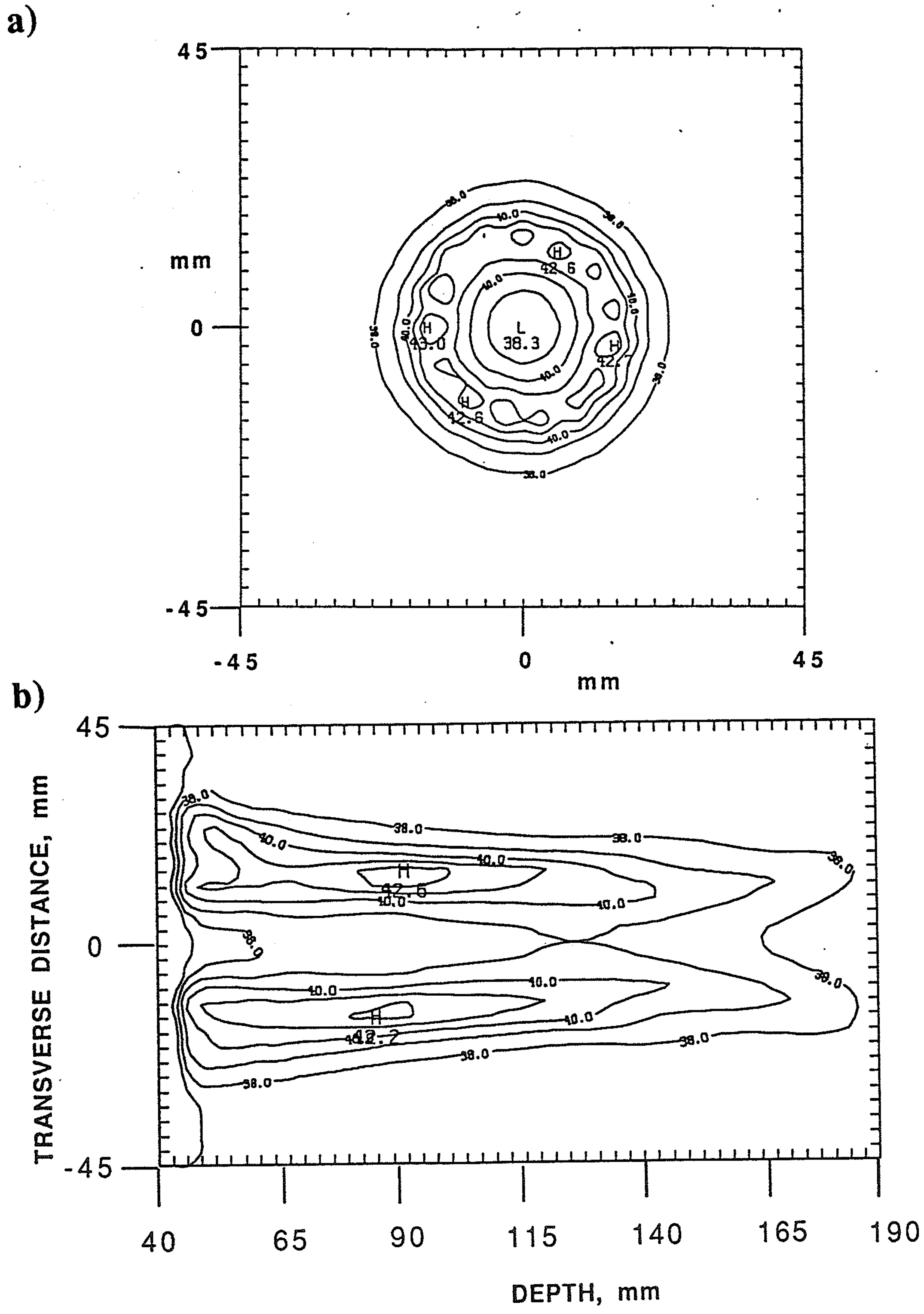

Figure 6.7. Heating associated with annular power deposition patterns. Temperature profiles in a) the focal plane (z=100 mm) and b) a longitudinal plane (y=0) resulting from inputting the pattern of Fig. 4.14 to the BHTE. Contours are given at intervals of 1°C.

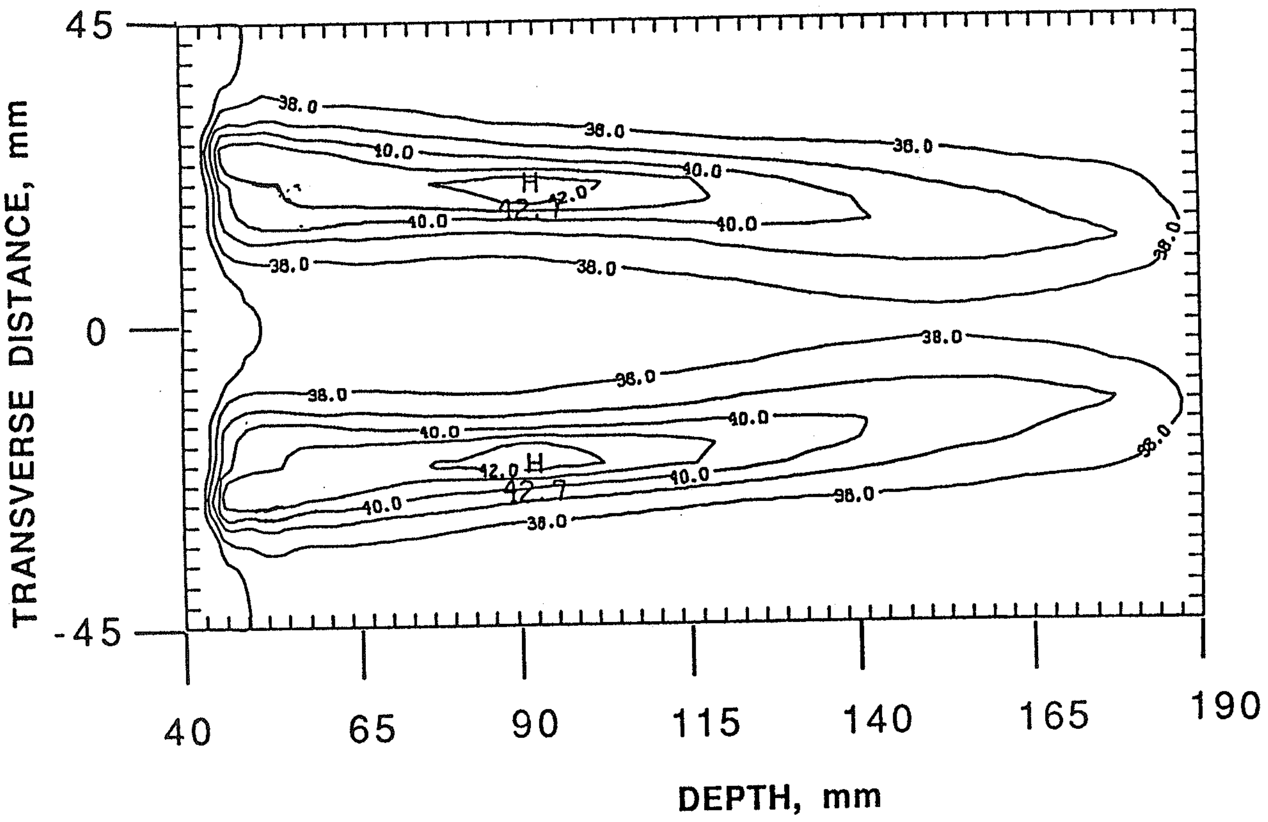

Figure 6.8. Heating associated with annular power deposition patterns. A contour plot of the temperature distribution in the (x,z) plane produced by the annular pattern of Fig. 4.12. Contours are given at intervals of 1^0C.

to heat small size tumors (diameter < 20 mm). However, depositing the ultrasonic energy uniquely around the tumor periphery is inadequate for larger tumors. In fact, while the therapeutic temperature is easily reached at the model edges, the model core seems insensitive to this modality of power deposition and some ultrasonic energy deposition toward the model center might be required, as suggested in [9].

6.3.2 Temperature distributions associated with electronic scanning

The electronic scanning technique was compared to the direct synthesis method in Chapter 4. The electronic scanning technique consists of producing an intense focal spot which is then moved over a predetermined path by adjusting the electronic control. In this section, two different size annular patterns are first synthesized using the electronic scanning technique. These patterns are then used as inputs to the 3-D BHTE and the resulting temperature distributions are discussed.

To heat a small tumor of a 13 mm diameter at a 100 mm depth, a focal spot was produced and then electronically translocated over an annular trajectory around the model periphery. The resulting power deposition pattern was discussed in Section 4.7 and its intensity profile was shown in Figure 4.15b). The pattern of Figure 4.15b) was inputted to the BHTE and the resulting temperature distribution is shown in Figures 6.9. This thermal response was obtained by adjusting the SPTP focal intensity to 30 W/cm^2. Figure 6.9a) is a contour plot of the resulting temperature in the (x,z) plane (y = 0), while Figures 6.9b) and c) are the temperature profiles in two transverse planes at 75 and 100 mm, respectively. The simulations demonstrate that a therapeutic temperature can be achieved at the tumor site (z=100). However, Figure 6.9b) shows that temperatures higher than those achieved in the focal plane are produced along the axis prior to the focal plane (z=75) due to ultrasonic beams overlapping as suggested by Lele [35].

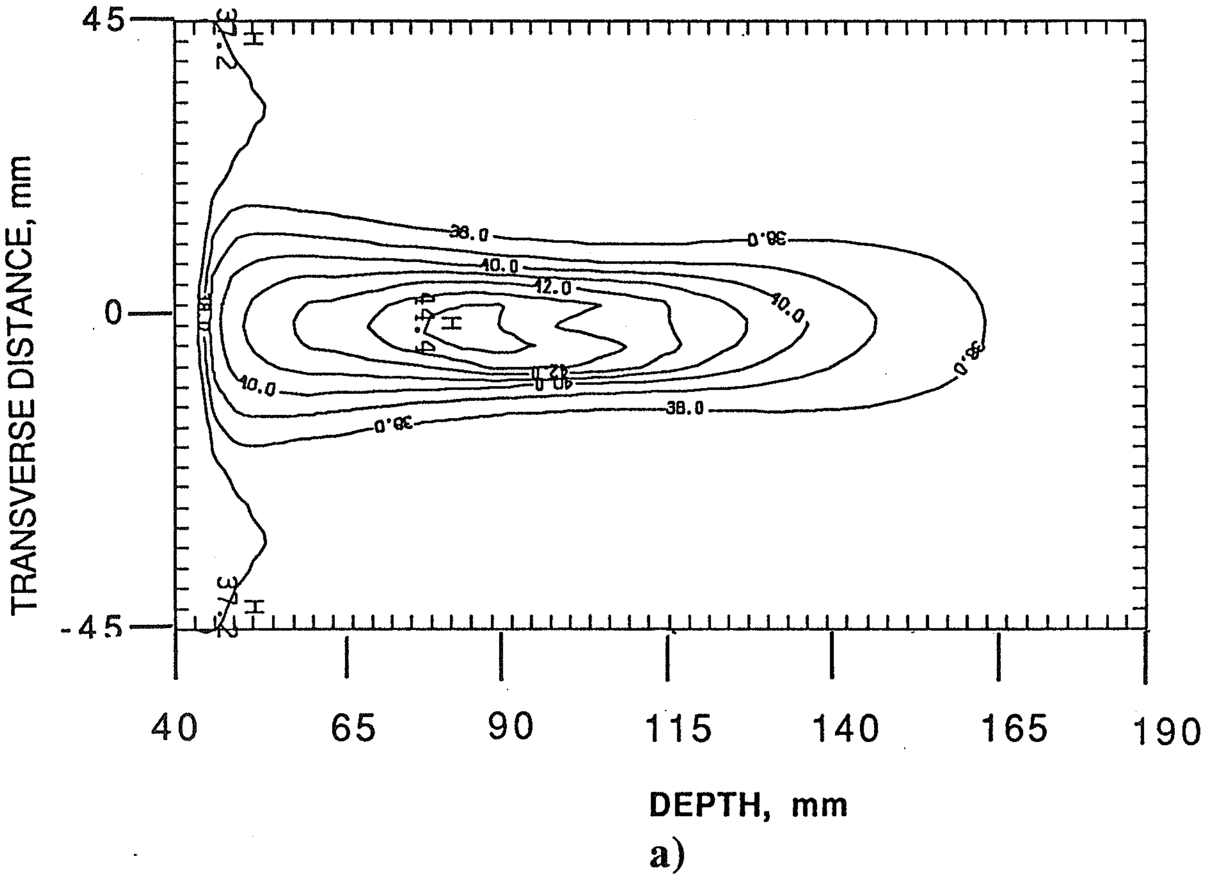

Figure 6.9. Thermal response resulting from electronic scanning. a) A contour plot of the temperature distribution produced by the pattern of Figure 4.15. Contours are given at intervals of 1^0C.

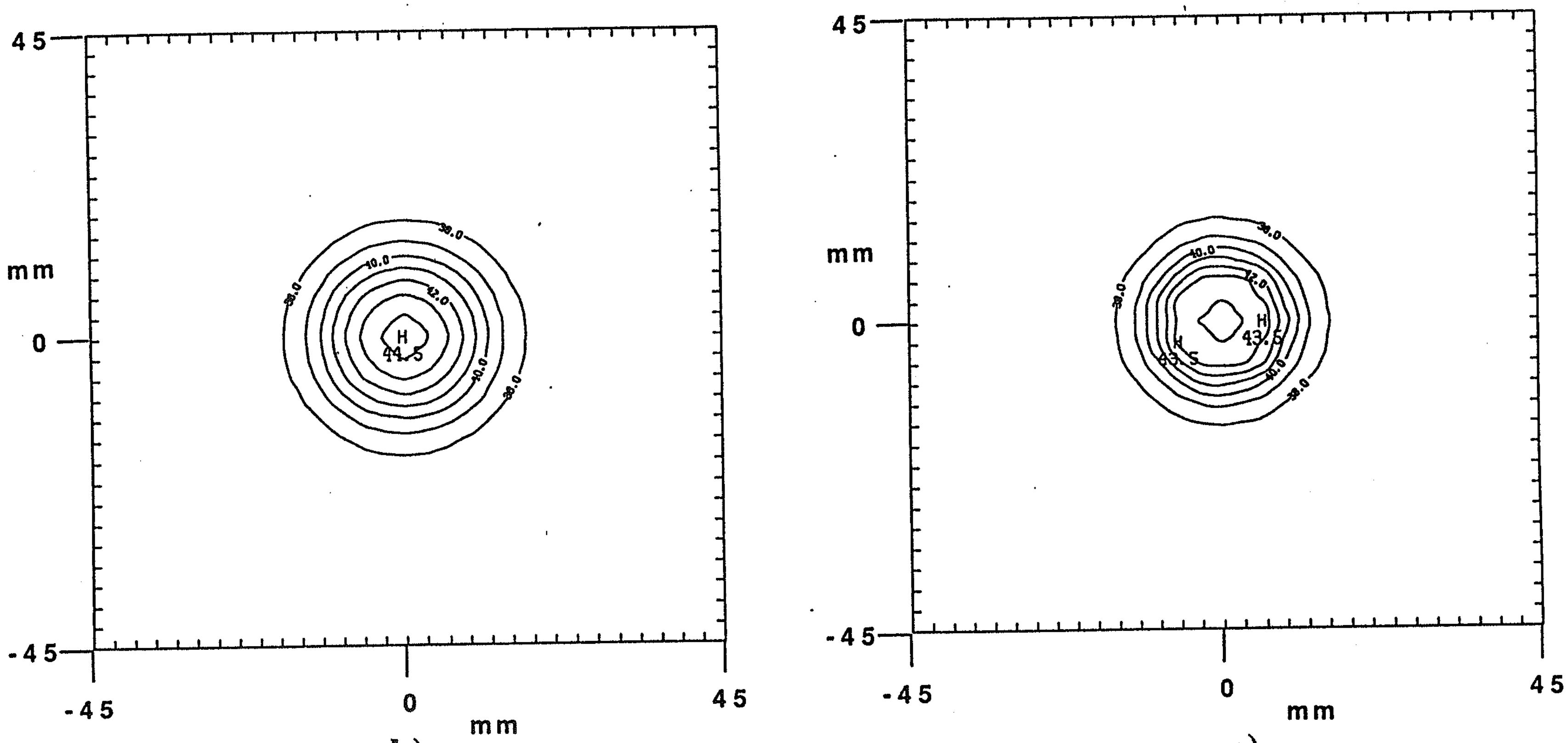

b) c)

Figure 6.9. b) Temperature distribution in the transverse plane (z=75) and c) temperature distribution in the focal plane (z=100).

A larger model of a 17 mm diameter at a 140 mm depth was also considered. To produce an annular pattern of this size, it was necessary to electronically scan the focal point over seven points uniformly distributed over the periphery. The SPTP focal intensity gain evaluated in the focal plane was 15.2 dB. The SPTP focal intensity was adjusted to 35 W/cm^2, and the power deposition pattern was inputted to the 3-D BHTE. The resulting temperature profiles are shown in Figures 6.10a) and b). It is noticed again that temperatures higher than those obtained at the focal site are produced prior to the focal plane (z=105 mm).

It is interesting to note that the electronic scanning leads in general to an elongated heated region. This elongation is due to a relatively large depth of field of the power deposition pattern resulting from scanning. In Chapter 4, a similar conclusion was reached for patterns produced by direct synthesis. These remarks suggest that the large depth of field is due to the planar surface of the applicator and not to the phasing technique (i.e., direct or scanning).

6.5 The Simulated Temperature Associated with the Temporal Tcanning of Directly Synthesized Heating Patterns

It can be concluded from Section 6.3 that depositing the ultrasonic energy around the periphery of a tumor of a diameter larger than 20 mm was not adequate to heat the whole tumor volume. Therapeutic temperatures were easily reached at the periphery while the model core temperature was not adequately raised, as could be seen from Figure 6.8. However, when the power deposition pattern of Figure 6.8 is temporally scanned with a smaller size annular pattern (technique described in Section 4.9), the temperature distribution of Figure 6.11 results. This temperature distribution suggests that larger size tumors (diameter ≥ 20 mm) could appropriately be heated by temporally scanning two or more annular patterns.

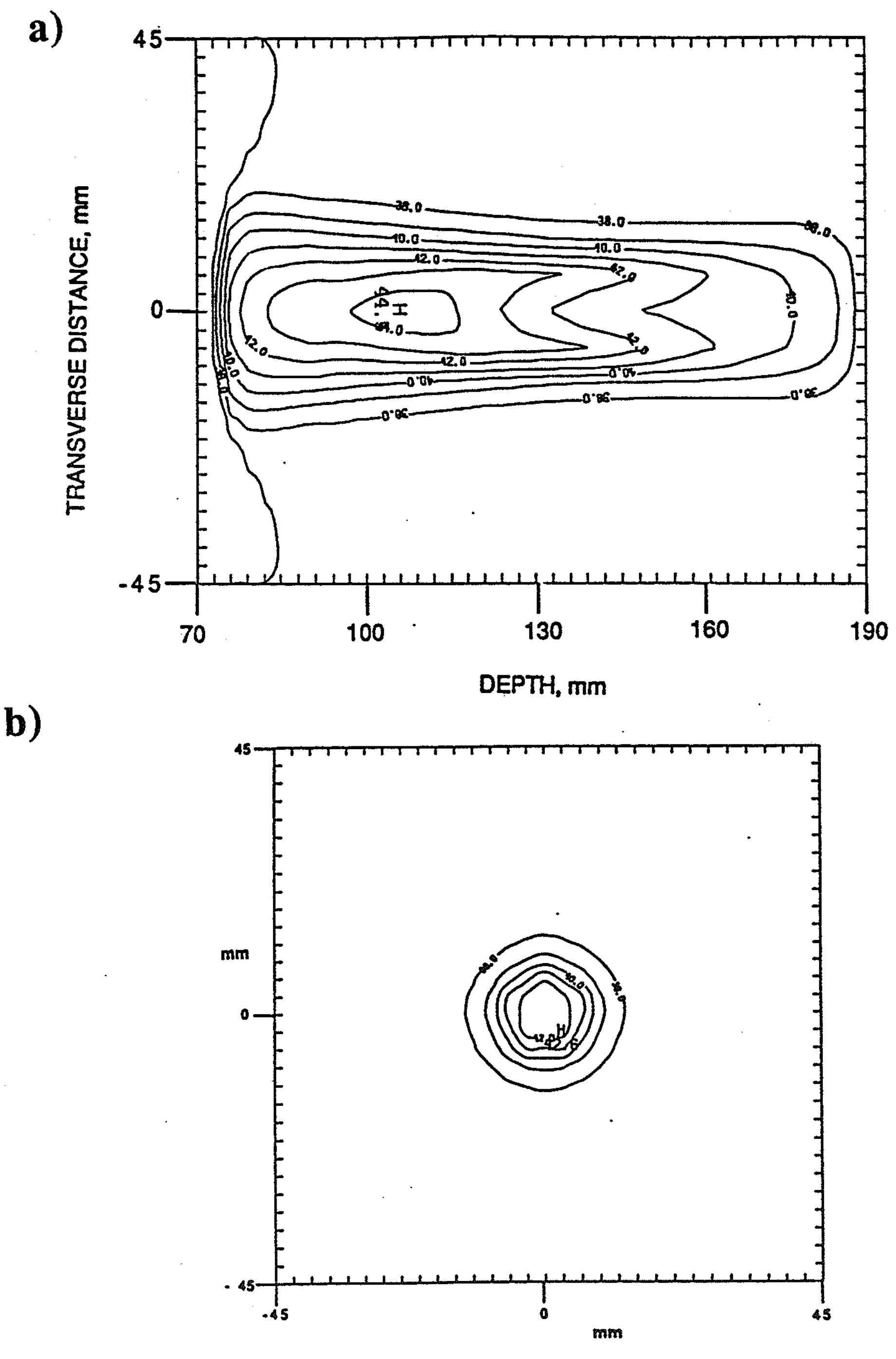

Figure 6.10. Thermal response resulting from electronic scanning. a) A contour plot of the temperature distribution in the (x,z) plane and b) the temperature distribution in the focal plane. The pattern was produced by translocating the focal spot over 7 points around the model periphery (see text). Contours are given at intervals of 1°C.

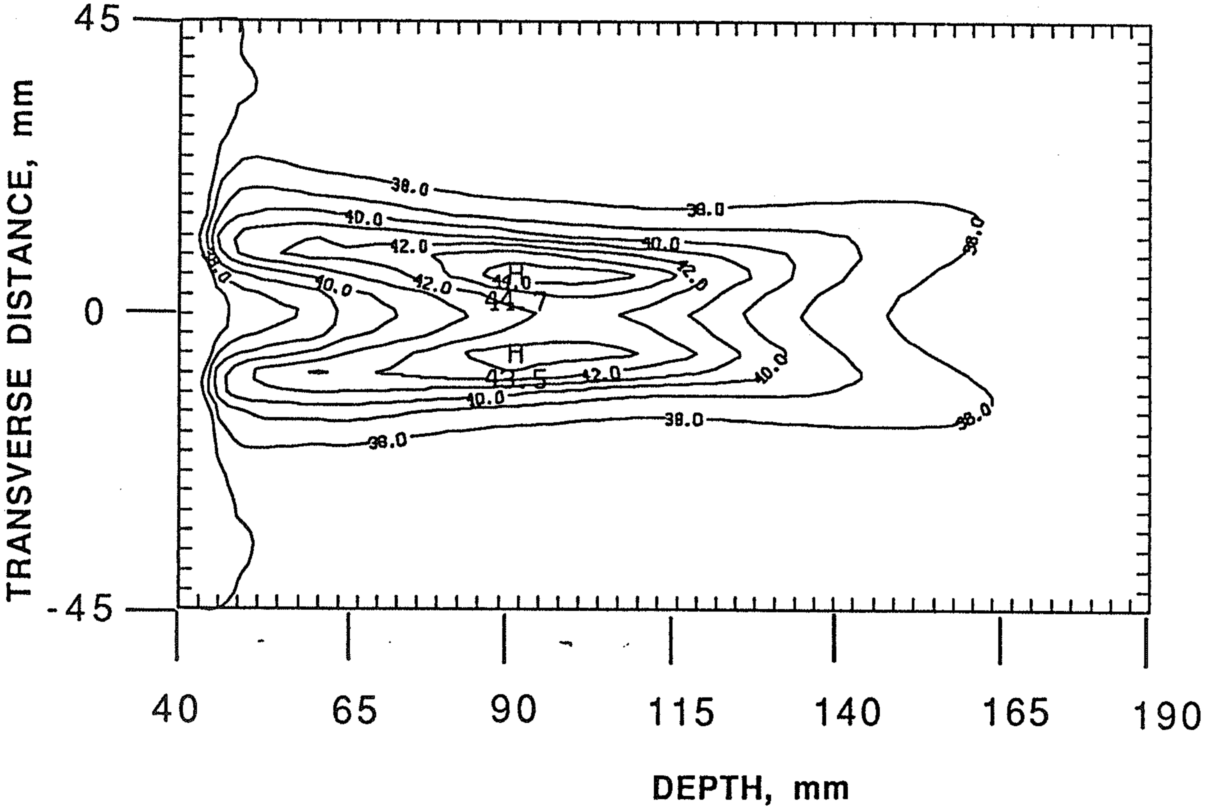

Figure 6.11. Temporal scanning of directly synthesized heating patterns. A contour plot of the temperature distribution resulting from temporally scanning the pattern of Figure 4.17 with a 17 mm diameter annular pattern. Contours are given at intervals of 1 °C.

Different heating patterns can be produced by simultaneously focusing at different sites in the focal plane. These directly synthesized patterns can then be electronically scanned leading to a more diffuse heating pattern, and consequently, larger heated volumes.

As an illustration, the FCM was used to synthesize simultaneously two foci at (0, 5) and (0, -5) at 100 mm depth. A time-averaged intensity gain of 12.4 dB was evaluated in the focal plane. The maximum time-averaged intensity was then adjusted to 10 W/cm^2 and the power deposition pattern inputted to the BHTE leading to the temperature distributions of Figures 6.12. Figure 6.12a) is the temperature profile in the transverse plane z= 100 mm while Figures 6.12b) and c) are the simulated temperatures in longitudinal planes perpendicular to the applicator surface and passing through the two foci (planes y= 5 an y= -5, respectively). It is clear from Figure 6.12a) that this pattern leads to two separately heated regions, each associated with one focal spot. It is also possible to synthesize an elongated focus (designated "line focus" in Chapter 4) by simultaneously producing a third focal spot at (0, 0) in the focal plane. The time-averaged intensity gain of the resulting pattern evaluated in the focal plane is 11.3 dB. The simulated temperature associated with this pattern is shown in Figures 6.13a) and b). The resulting heated region is elongated, as can be seen from Figure 6.13a). The temperature profile in a plane perpendicular to the applicator surface (y= 0) is shown in Figure 6.13b). A third pattern was synthesized by simultaneously focusing at (5, 0) and (-5, 0), respectively. This pattern results in a temperature distribution symmetrical to that of Figure 6.12 over the x axis. Figures 6.14a) and b) illustrate the temperature profile in the focal plane and in a longitudinal plane crossing the two foci (y= 0).

A more diffuse heating pattern can be produced by temporally scanning the patterns of Figures 6.12 and 6.14, as was described in Section 4.8. The temperature distribution associated with the temporal scanning is illustrated in Figures 6.15a) and b). The temperature profile resulting in the focal plane is shown in Figure 6.15a), while the temperature distribution resulting in the plane y = 0 is illustrated in Figure 6.15b). It is

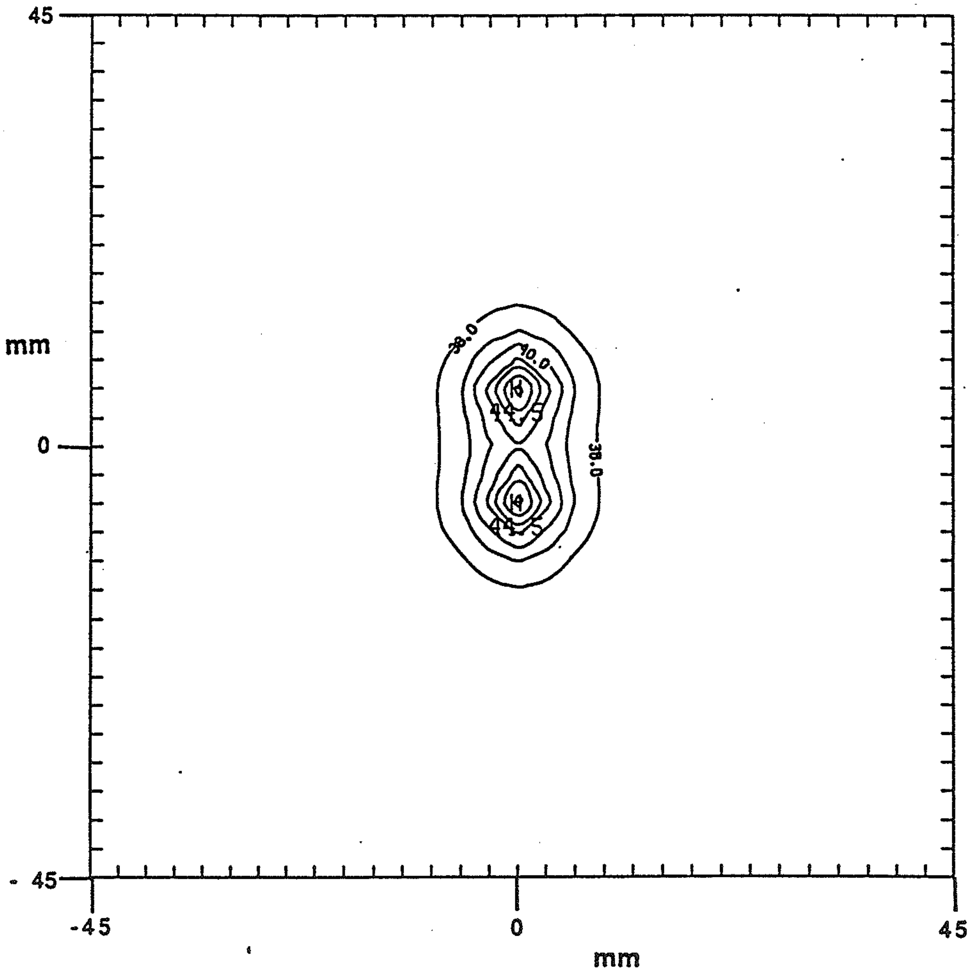

a)

Figure 6.12. Temperature distribution associated with multiple focusing. a) A temperature profile in the focal plane (z= 100 mm) resulting from simultaneously focusing at (0, 5) and (0, -5) in the plane z= 100 mm.

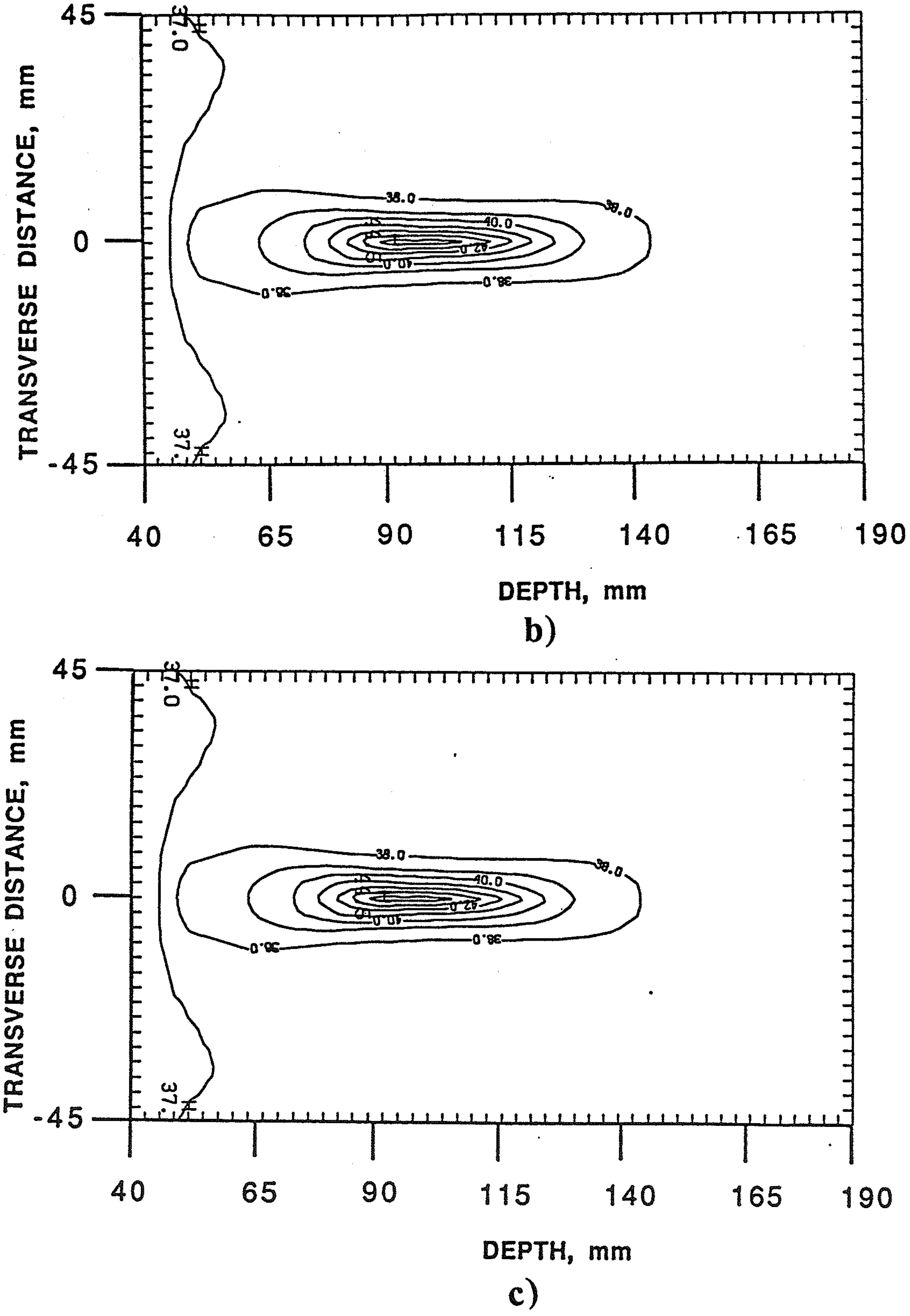

Figure 6.12. b) Temperature profile resulting from the pattern described in (a) in the plane y = 5 and c) in the plane y = -5 mm. Contours are given at intervals of 1°C.

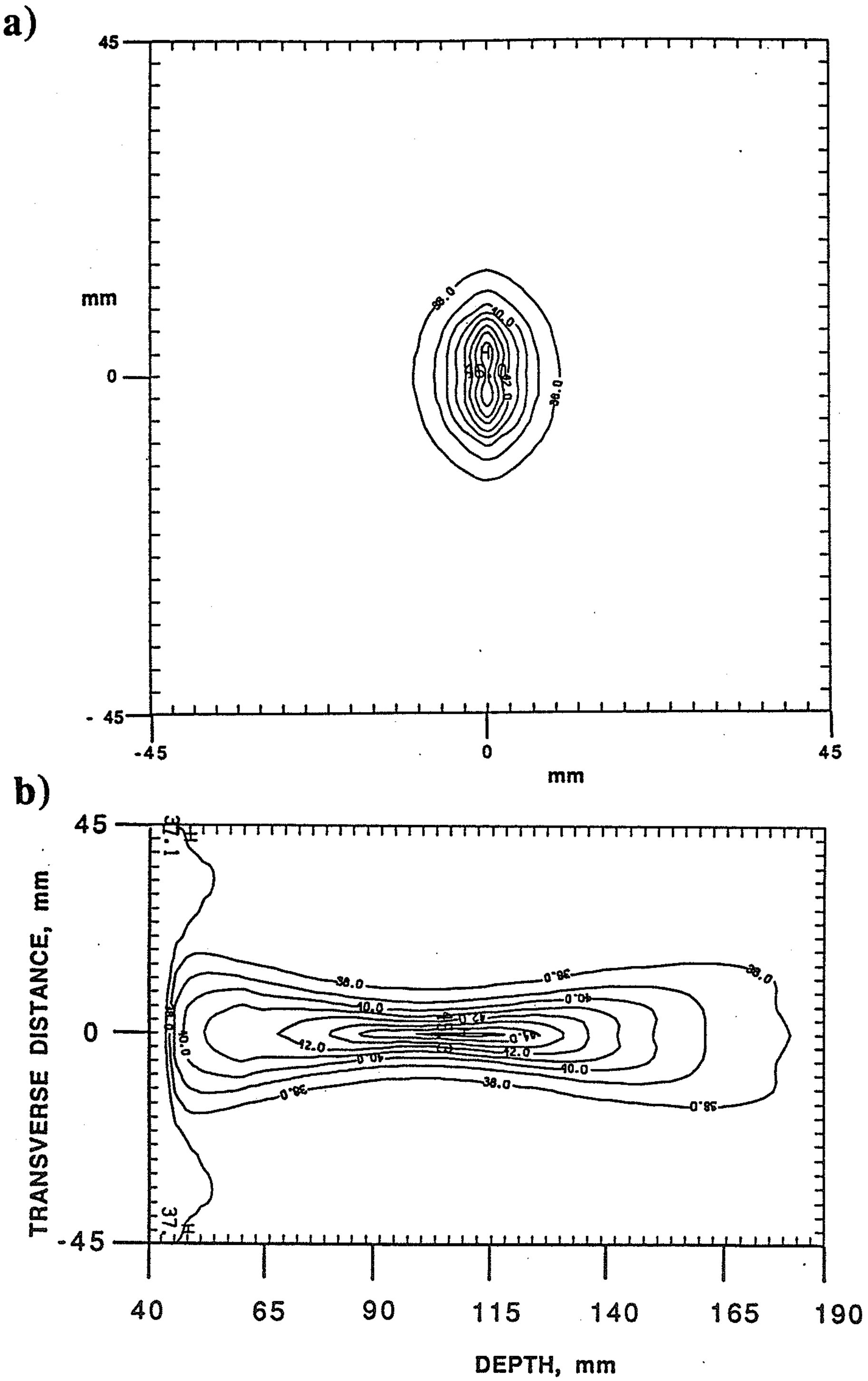

Figure 6.13. Temperature distribution associated with multiple focusing. a) A contour plot, in the focal plane, of the temperature distribution associated with simultaneously focusing at (0,5), (0,0), and (0,-5), respectively, and b) in a longitudinal plane (y = 0. Contours are given at intervals of 1°C.

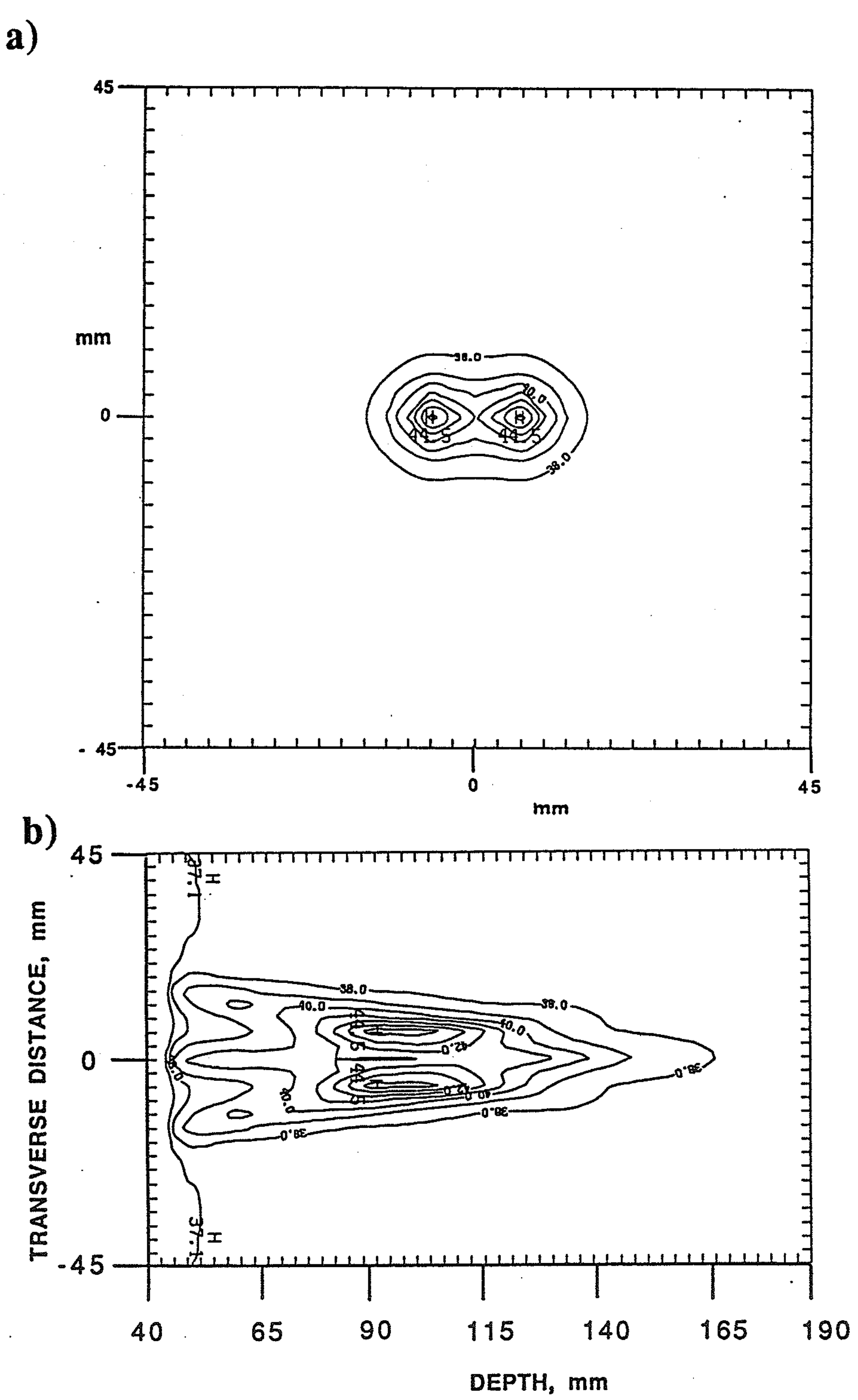

Figure 6.14. Temperature distribution associated with multiple focusing . Temperature profiles resulting from simultaneously focusing at (5,0) and (-5,0) at 100 mm depth a) in the focal plane (z=100 mm) and b) in the plane (y=0). Contours are given at intervals of 1°C.

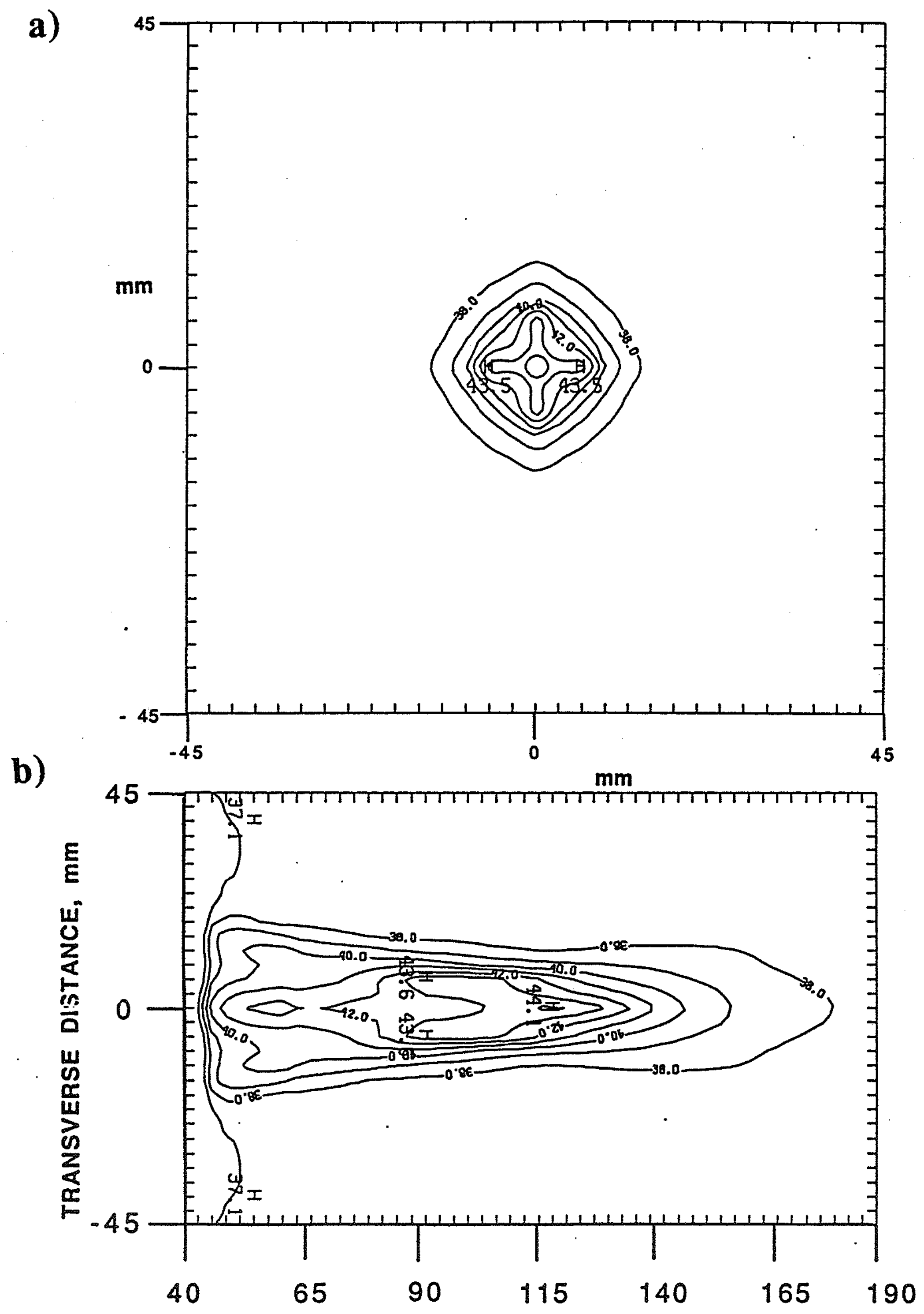

Figure 6.15. Thermal response associated with temporal scanning. a) A contour plot of the temperature profile resulting from temporal scanning (see text) in the focal plane and b) in a longitudinal plane (y= 0). Contours are given at intervals of 1 °C.

seen that the heated volume extends to beyond the focal plane where a temperature higher than those reached in the focal plane results (44.1 ^{0}C). This extension is due to the formation of a secondary foci along the axis beyond the focal plane. The secondary focus intensity can be reduced by appropriately phasing the assumed sources as described in Chapter 2. However, it might be possible to heat larger tumors by placing them carefully between the different focal planes.

6.6 Conclusions

Throughout this chapter, the simulated temperature distributions associated with different heating patterns were investigated. The investigation goal was to evaluate the phasing technique as well as the applicator geometry for hyperthermia applications. Furthermore, the direct synthesis technique was compared to the electronic scanning, and some relevant simulations were shown.

It was demonstrated that the direct synthesis method (RFCM) could be used to heat tumors of different geometry at different depths. In some cases, the resulting heating pattern might have a large depth of field. However, the same observation was made concerning the electronic scanning technique. This might suggest that the elongation is due to the planar geometry of the applicator rather than to the synthesis method. It was also demonstrated that the direct synthesis method required a much lower SPTP focal intensity compared to those required by the electronic scanning. This property might prove valuable to avoid some undesired nonthermal effects such as cavitation.

CHAPTER 7

PRELIMINARY EVALUATION OF A PROTOTYPE SQUARE-ELEMENT ARRAY

7.1 Introduction

Although the theory of ultrasound phased arrays is well established, their fabrication is by no means trivial. This chapter will attempt to describe an NxN square-element phased array prototype and to present some preliminary testing results. The prototype element size is substantially larger than the size considered for the simulations of Chapter 4. This particular size (8.3 mmx 8.3 mm) was chosen to minimize the number of required electronic control circuits and to test some details of the fabrication procedure (i.e., piezoelectric cutting, bonding, matching, etc.). These tests are believed to pave the way for the fabrication and testing of an array with a larger number of elements (element size 4.5 mm x 4.5 mm) which is intended for evaluation after the termination of this initial study. At the time of these measurements, the electronic control circuits (Section 7.4) were not yet ready and hence, a broad band power amplifier was used to drive the different elements (no phasing). The experimental data will include measurements of the frequency response of the individual elements, experimental determination of the fundamental thickness mode, and the measurement of the acoustic field (in water) resulting from single or multiple elements driven by the same RF signal. The fabrication procedure and the experimental setups will be discussed in detail.

7.2 Array Fabrication

The array, an 8x8 structure with square elements each of 8.3 mm width was made using a PZT-8 square plate of 68 mm width. To minimize the interelements cross coupling, the ceramics wafer was mounted on glass using RTV silicon rubber, and a 0.25 mm thick diamond saw was used to cut all the way through the PZT thickness. The diamond saw was adjusted to cut an extra millimeter through the glass to assure complete separation between the array elements. Bonding the segmented PZT plate to a quarter wavelength matching layer was done using conducting epoxy. However, a prior attempt to bond the element to a quarter wavelength aluminium matching layer using a very thin layer of nonconducting epoxy (ECOBOND 285 by EMERSON) failed. After applying the epoxy to the contact surface, a very high pressure was applied to achieve good contact between the ceramic elements and the aluminium plate which was then used as a common electrical ground. After 24 hours, the curing time recommended by the epoxy manufacturer, the element impedance was recorded and found to be generally higher than 2500 ohm, and the elements failed to resonate in the frequency interval of interest (500-700 KHz). This was probably due to the insufficiency of the applied pressure to make the epoxy layer thin enough and to the existence of small air pockets within the epoxy and, consequently, a very thin layer of conducting epoxy (CHO-BOND 584 by CHOMERIC) was then used to bond the ceramics to a quarter wavelength magnesium layer. The magnesium was chosen because of its suitable matching characteristics (characteristic impedance = $5.3\ 10^6\ Kg/m^2\ s$). The glass plate was then removed using a chemical solvent, and the PZT surface was very carefully cleaned using different chemical cleaning agents. A 50-ohm coaxial cable was then attached to the electrically positive surface of each element using conducting epoxy. The segmented plate was then mounted in a water tight plexiglas housing (12 cmX12 cmX7 cm) with a 3 cm radius plexiglas tube to protect the coaxial cables.

7.3 Frequency Characteristics

The electrical impedance of each square element was measured over a wide band of frequencies. The goal was to determine an optimum driving frequency and to study the behavior of the transducer elements near the fundamental thickness resonance mode (f_r). The measurements were carried using an automated system consisting of a vector impedance meter (HP 4193A) interfaced with a signal synthesizer, a plotter (HP 7470), and an HP9816 computer as shown in Figure 7.1. A Fortran program was used to convert the impedance readings into magnitude, phase, resistance, and conductance. The different quantities were

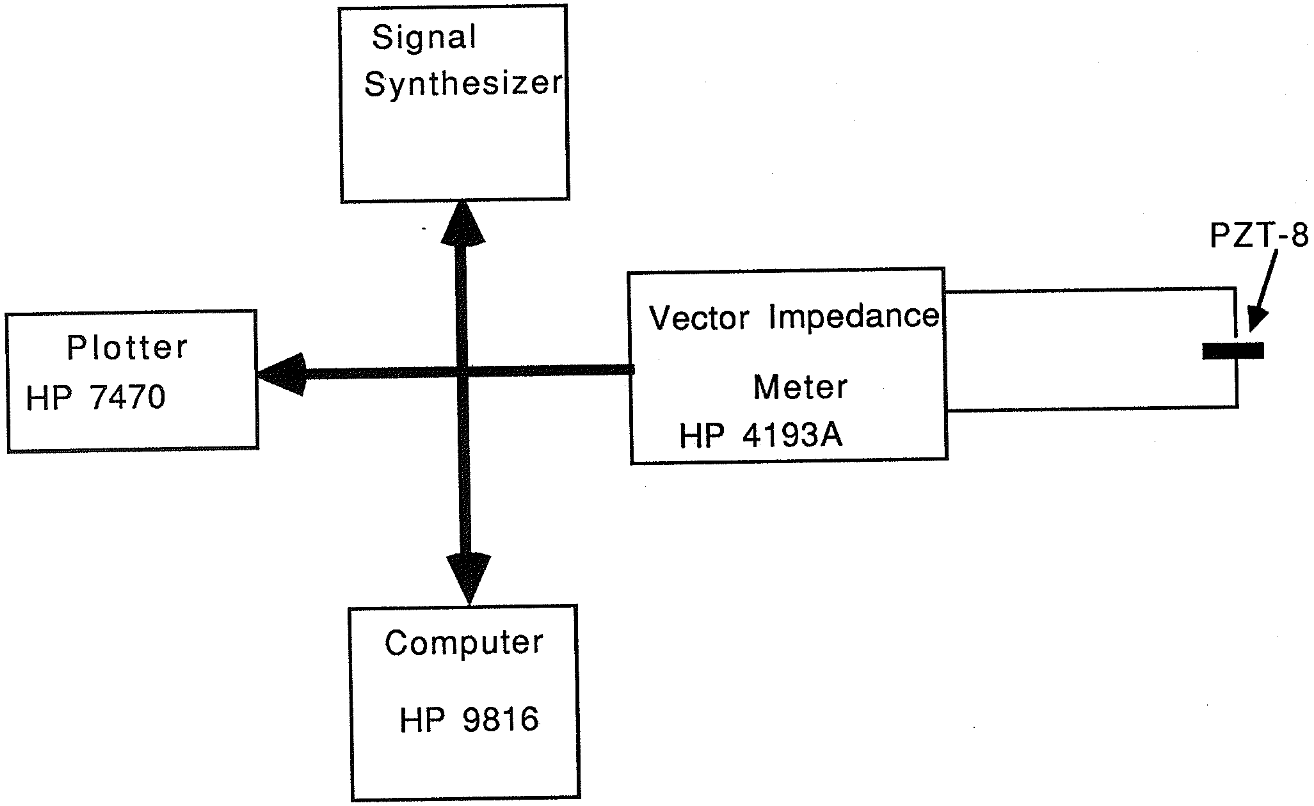

Figure 7.1. A schematic of the impedance measurement setup.

then plotted as a function of frequency to determine the frequency characteristics of each element.

Figures 7.2a) and b) illustrate the impedance magnitude and phase measured for a typical transducer element. It was observed that the resonance frequency of the elements, with matching layer, was generally between 636 and 668 kHz. The antiresonance frequency is typically 15-23 kHz above that of the resonance. More variation was also observed with respect to the magnitude of impedance at resonance. The magnitude varies between 380 to 745 ohm for the 64 elements. These observations suggest the necessity of electrical matching circuit for each element (see Section 7.5).

Different characteristics of importance can be determined based on the measured frequency response of the array elements. The electromechanical coupling can be determined from the experimental values of the resonance and antiresonance frequencies. The electromechanical coupling is a measure of the degree of energy conversion from electrical to mechanical (acoustical) based on the following relation [46]

$$K^2 = 1 - \left(\frac{f_r}{f_a}\right)^2 \tag{7.1}$$

where f_r and f_a are the resonance and antiresonance (maximum magnitude) frequency, respectively. By taking the average values (64 elements) of these two measured quantities, the value of K was found to be 0.25.

The mechanical quality factor can be determined from [46]

$$Q = \sqrt{\frac{|Z_{max}|}{|Z_{min}|}\,\frac{\sqrt{1-K^2}}{K^2}} \tag{7.2}$$

where Z_{max} and Z_{min} are determined experimentally and K from Eq. (7.1). By taking the average values of Z_{max} and Z_{min} and the determined value of K, the mechanical Q was determined to be 33.2.

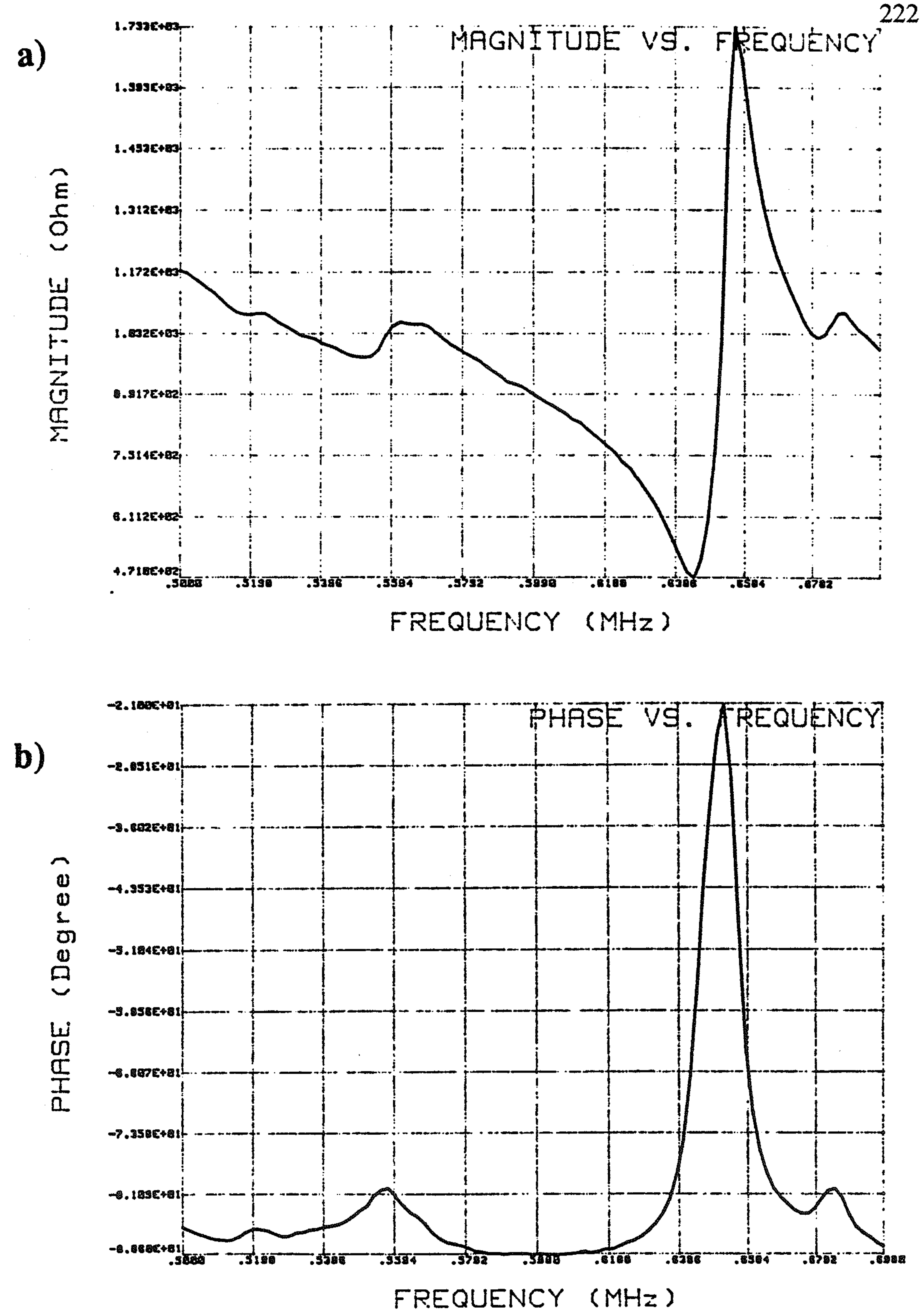

Figure 7.2. The frequency response of a square-element PZT-8 transducer. a) the impedance magnitude as a function of frequency and b) the phase plot as a function of the frequency.

The power factor can also be determined from the relation

$$\text{Cos}\ \phi = \frac{1}{\sqrt{1 + (\omega_r\ C_0\ R_r)^2}} \qquad (7.3)$$

where C_0 and R_r are the values of the clamped capacitance (roughly the capacitive conductance at resonance) and the resonance resistance including the load resistance which can be evaluated from the collected data. For an average value of the measured quantities (R_r = 479 ohm and $(C_0\omega_r)^{-1}$= 381.2 ohm), the power factor is evaluated to be 0.619. The power factor is a measure of the active output power and hence, needs to be maximized.

In conclusion, it is necessary to provide a matching circuit that will improve the power factor and, consequently, to maximize the output power at the operating frequency (f_r). Moreover, although all transducer elements have the same size, their resonance impedances are different and hence, the matching circuit components should be calculated for every individual element.

7.4 The Driving Electronic Circuit

The driving electronic circuitry should provide every element with the appropriate phase and amplitude signal necessary for focusing. A digital circuit using two digital counters of 4 bits each was designed for this purpose. A 10.5 MHz clock circuit is used to provide a 650 kHz signal at the output of the divided by 16 counter groups. The output of the digital circuit is obtained by using the two-digital counter outputs (most significant bit) as inputs to a logical NOR gate. The signal phase is governed by varying the initial states between counter groups. The amplitude of the signal is controlled by adjusting the duty cycle of the NOR gate output which is controlled by varying the initial states of the two digital counters. A schematic of the complete circuit (with the power amplifier) is illustrated in Figure 7.3. A derivation of the relative amplitude and phase as functions of the initial states of different counters using Fourier analysis of the output signal is given in Reference [37].

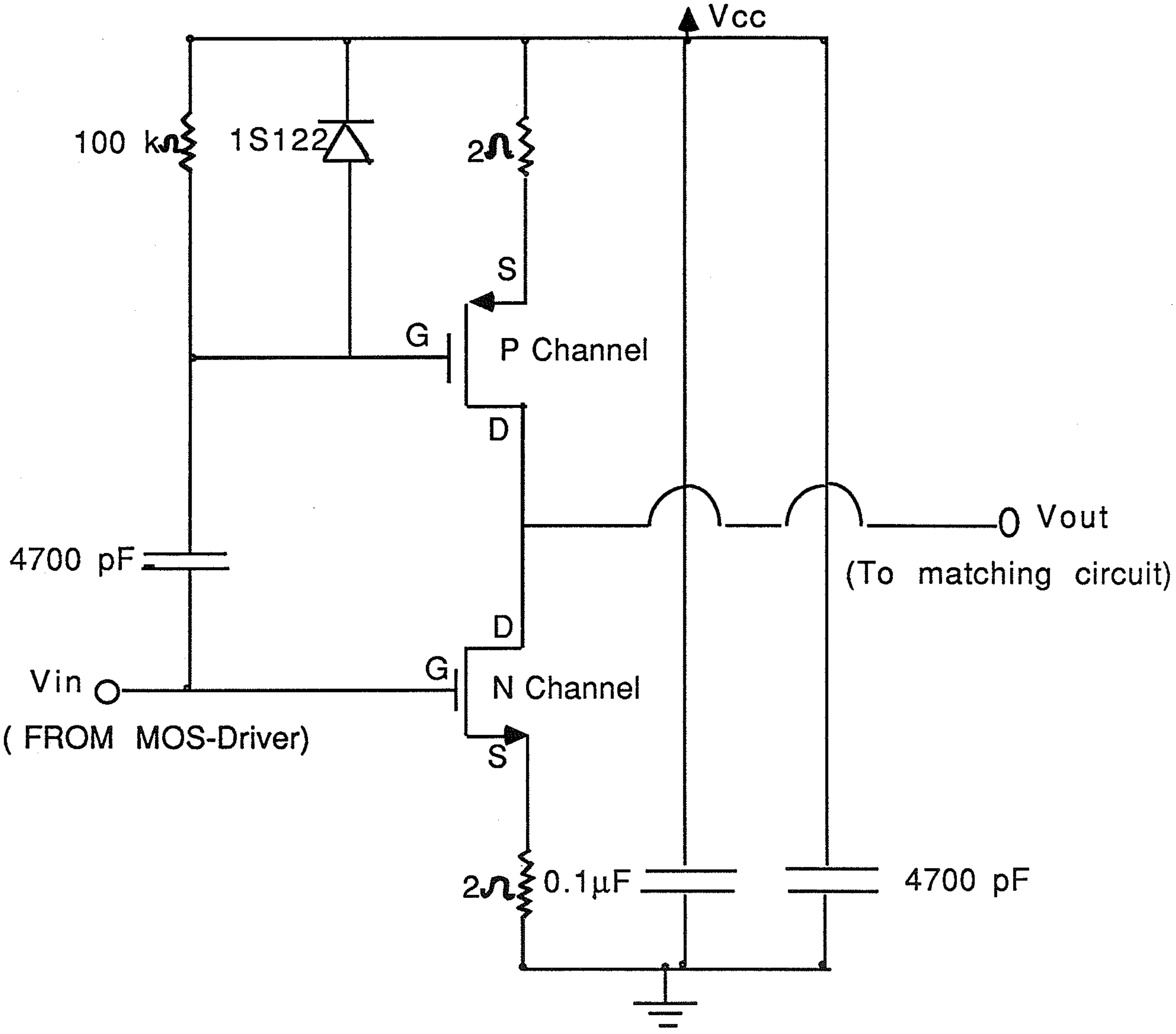

Figure 7.3. A schematic of the driving electronic circuits for a square-element of the NxN array.

The digital circuit output is connected to a power amplifier which consists mainly of a complementary pair of power MOS FETs which are designed to provide more than 100 watts each.

7.5 Impedance Matching Circuit

As described in Section 7.3, the impedance of each array element including a 2 m length 50-ohm coaxial cable was measured and an optimum operating frequency was determined. Based on these measurements, an optimum frequency of 650 kHz was chosen for the driving signals. The impedance measurements also demonstrated the need for an individual matching circuit for every element. The matching circuit role is to maximize the output electrical power and hence, the acoustical extracted energy.

The matching circuit is required to eliminate (minimize) the imaginary part of the element impedance at resonance which is essentially capacitive due to the large piezoelectric clamped capacitor at resonance [44]. The circuit quality factor Q needs to be small to provide a wide 3 dB frequency bandwidth. A Q of approximately 2.0 was chosen for the matching circuit. The designed matching circuit was a simple T filter consisting of an inductor, ceramic capacitor, and a large resistor as shown in Figure 7.4. A fine adjustment capacitor is added at the output to ensure a fine tuning to achieve a maximum power output.

7.6 Preliminary Results

The acoustic field measurements were conducted in an automated plexiglas water tank filled with degassed water. The water tank is computer-controlled, capable of 3-D scanning with an adjustable step size. Measurements were collected from the array using a 21-channel Marconi PVDF membrane hydrophone. The water tank sides were lined with absorbing rubber to minimize the effect of reflection. The 21 hydrophone outputs were preamplified and were selected one at a time by a multiplixer circuit which is interfaced with a PDP11 microcomputer. The selected channel output is fed to an RMS digital meter and its

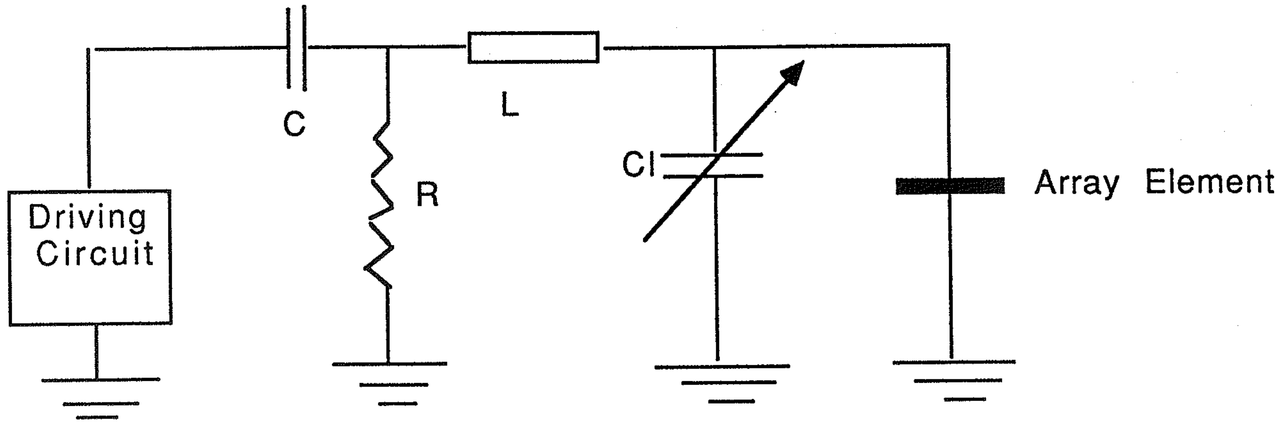

Figure 7.4. Electrical matching circuit for an individual element of the NxN array.

d.c. output converted to a 10-bit digital signal using a 25 kHz A-to-D converter. Figure 7.5 is an illustration of the experimental setup.

To determine experimentally the resonance frequency for a square element, the element was excited using a broadband power amplifier and its response (in degassed water) was measured using a hydrophone for several frequencies. The hydrophone was scanned transversely in a plane parallel to the transducer surface until the location of the maximum output voltage (for a fixed input voltage and frequency) was determined. The hydrophone was then fixed and the input RF frequency was varied. The output voltage for different frequencies was recorded while keeping the element input voltage constant. However, it was very difficult to keep the input voltage constant for different frequencies (output impedance is a function of frequency) and an attenuator was used for the adjustment. This adjustment, while very crude, makes it possible to keep the input voltage value within 15% of the desired fixed value (12.5 V). The hydrophone output voltage was then measured for frequencies between 150 and 980 kHz and the resulting plot is given in Figure 7.6, which shows that a maximum output voltage is recorded for a frequency of 652 kHz. This value of resonance frequency agrees perfectly with the averaged value determined using the vector impedance meter.

A square element was excited using an input voltage of 90 V (RMS) between its electrically positive surface and the ground. To check the interelement coupling between adjacent elements, the induced voltage on the immediate neighboring elements was measured using a digital oscilloscope. This voltage was generally of about -22 dB compared to the voltage of the excited element. However, this increased slightly when four elements (2x2) were simultaneously excited but remained less than -20 dB. These results indicate that the interelement electrical coupling is reasonably low and could be ignored compared to the input voltage level.

A single element was then driven using an RF frequency of 652 kHz with an input voltage of 90 V, and the resulting field was measured using the Marconi system described

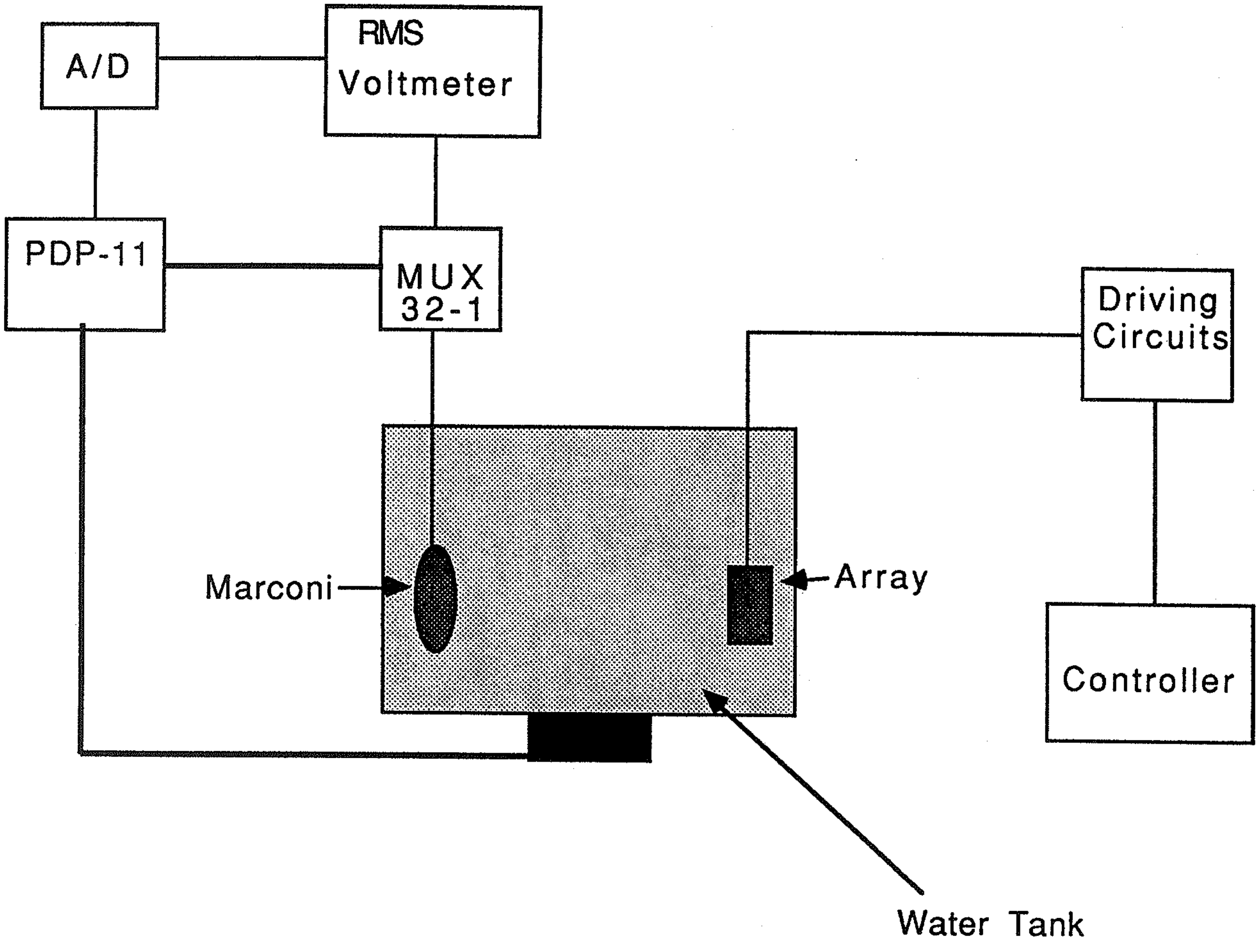

Figure 7.5. A schematic of the experimental setup of the Field measurement.

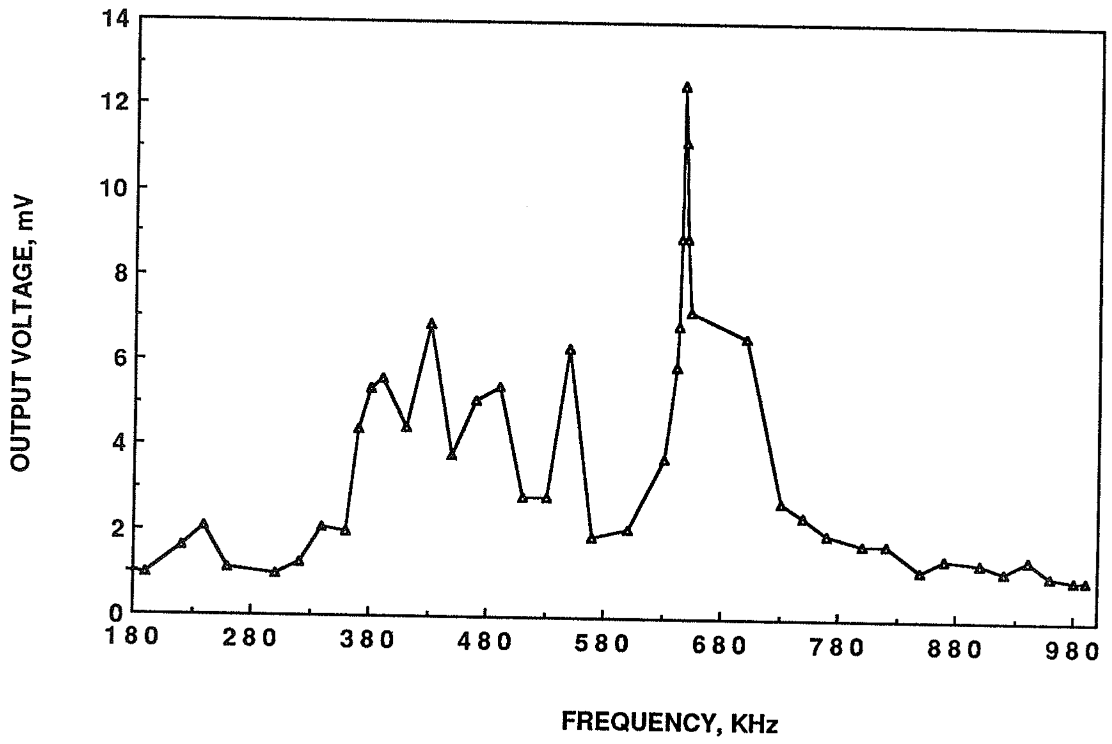

Figure 7.6. Determination of the resonance frequency of a square-element transducer. The output voltage of a measurement hydrophone is plotted as a function of the operating frequency of the input signal. The input voltage was kept approximately at 12.4 V RMS.

earlier. The measurements were conducted at 32 and 62 mm from the radiating surface, and a surface plot of the resulting field pattern is shown in Figure 7.7a). Figure 7.7b) illustrates the comparison between the measured and the computer simulated normalized field using the rectangular radiator numerical method. As could be seen from Figure 7.7b), a reasonable agreement is observed between the simulated results and those measured in the water tank in spite of the lack of matching circuit (see Section 7.5).

Four square elements (2x2) were then simultaneously driven by the same signal described above, and the field was measured in transverse planes at different distances from the applicator. The measurements were conducted at 32, 55, and 100 mm from the array surface, and the resulting surface plot is shown in Figure 7.8a). Figure 7.8b) illustrates the comparison the computer simulated normalized fields and those measured in the tank. As concluded in the previous experiment, there is a good agreement between the measured and theoretically predicted plots. A comparison between the 3 dB width of the measured and theoretically predicted pattern indicates a slightly larger width in case of measurement as illustrated in Table 7.1. This might be because of some larger effective size due to the matching layer.

Table 7.1

Comparison between the 3 dB width of the simulated and measured patterns

distance from the array, mm	measured 3 dB pattern width, mm	predicted 3 dB pattern width, mm
32	25	16.5
55	29	18.0
100	34	27.0

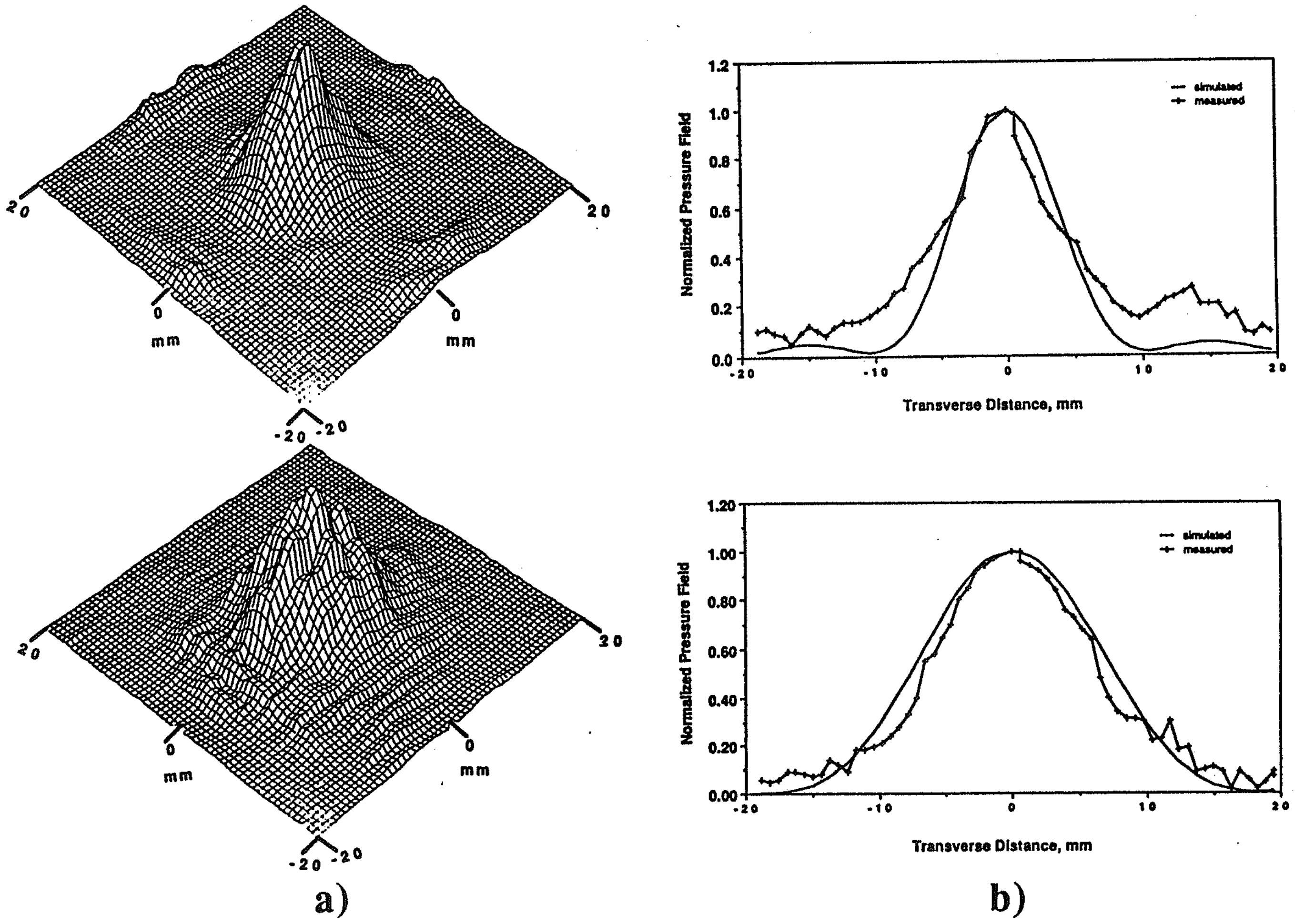

Figure 7.7. a) A surface plot of the measured pressure field due to a single element driven by a 90 V RMS at 625 kHz. b) Comparison of the theoretical and experimental relative field corresponding to (a). The measurements were done at 32 and 62 mm from the array surface, respectively.

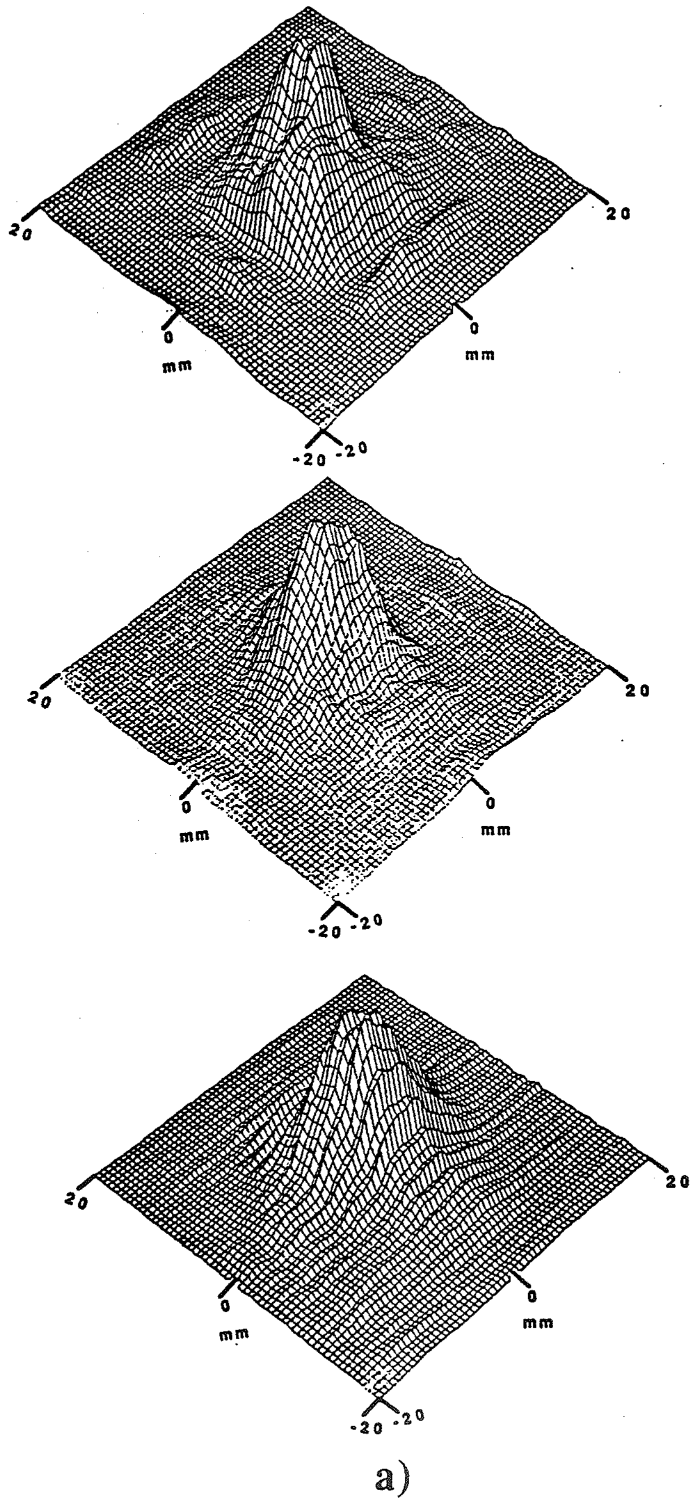

Figure 7.8. a) A surface plot of the measured pressure field due to 4 elements (2x2) simultaneously driven by the same signal (90 V RMS at 625 kHz). The transverse planes are at 32, 55, and 100 mm from the array surface, respectively.

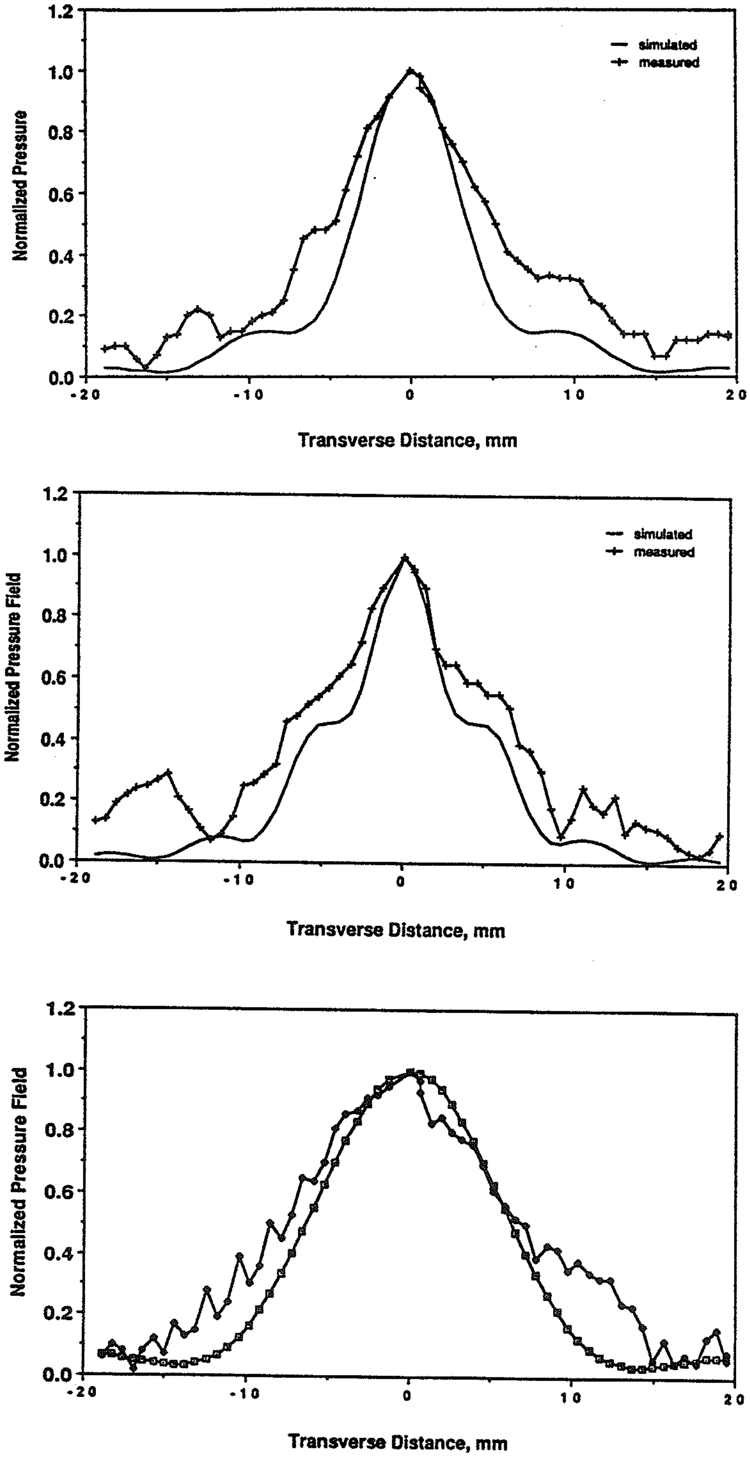

b)

Figure 7.8. b) Comparison of the theoretical and experimental relative field corresponding to (a). The transverse planes are at 32, 55, and 100 mm from the applicator surface, respectively.

In a last series of measurements, a group of four elements, arranged in a linear fashion, was also driven using the same signal of the previous cases. The resulting field was measured in a transverse plane at 100 mm from the array surface, and a surface plot of the measured values with a comparison between theoretically predicted and measured field patterns are given in Figure 7.9a) and b), respectively. The measurements seem to follow closely the predicted pattern as shown in Figure 7.9. However, a 3 dB width of 49 results as opposed to 43 in the case of computer simulations.

7.7 Conclusions

An 8x8 PZT-8 square-element phased array prototype was fabricated and some preliminary field measurements were conducted in degassed water. While the element size was substantially larger than those considered for computer simulations (see Chapter 4), the goal was to check the fabrication procedure (i.e., PZT cutting, bonding, matching, etc.). Simple experiments were conducted to measure the pressure field produced by a single and multiple square elements driven by the same RF signal (no phasing). The experimental results obtained in this chapter agree reasonably with the computer predicted simulations. Important practical parameters such as the electromechanical coupling and the mechanical Q were determined experimentally. These measurements will be the base for a more extensive set of measurements to evaluate the applicator as a phased array upon the completion of the driving circuit.

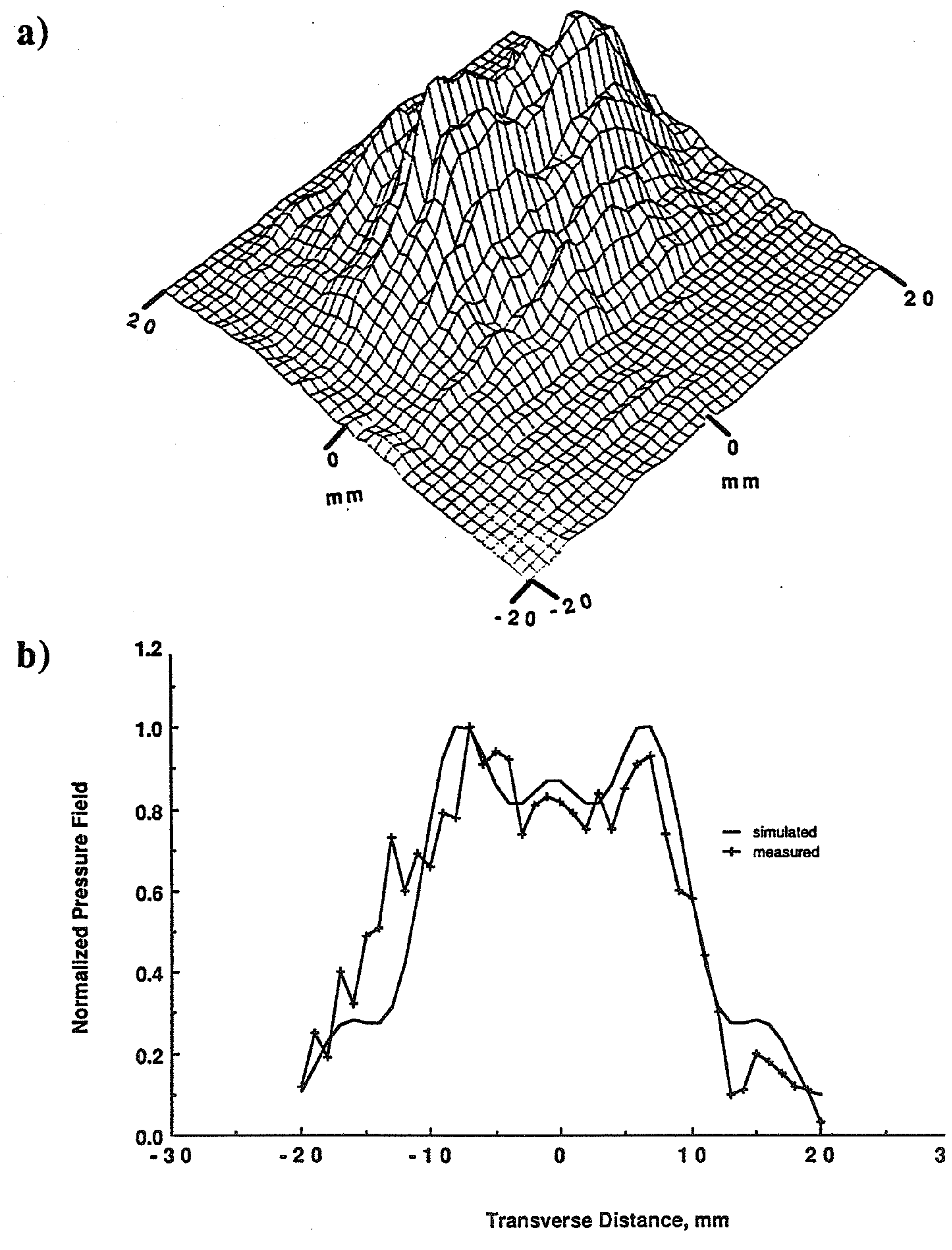

Figure 7.9. a) A surface plot of the measured field due to four elements, arranged in linear fashion, simultaneously driven by the signal of Figure 7.7. b) Comparison of the theoretical and experimental relative field associated with a). The field was measured at 100 mm from the array surface.

CHAPTER 8

RECOMMENDATIONS FOR FUTURE RESEARCH

Computer simulations discussed herein have demonstrated the potential of the field conjugation method as a means of directly synthesizing different heating patterns useful in hyperthermia cancer therapy. The method consists of assuming a desired pattern in the focal plane and of establishing the required excitation signal for each array element. While it is generally possible to tailor the power deposition pattern to any tumor geometry by only specifying the desirable pattern in one plane (focal plane), it would be useful to have some degree of control over the resulting pattern in other planes as well. In particular, it is important to investigate the inverse problem of going from specified pattern characteristics in more than one transverse plane (i.e., near or distal to the focal plane) to establishing the necessary array phase and amplitude distributions to achieve a more optimum overall heating pattern. This might lead to heating patterns which would not excessively heat the surrounding normal tissue or bone structures distal to the tumor location. While the synthesis of annular heating patterns leads, in many cases, to the formation of undesired secondary foci proximal or distal to the focal plane, these undesired hot spots can be eliminated by combining the field conjugation method with a particular phasing technique (RFCM). However, more research is still needed to generalize the procedure to other heating patterns as well.

The FCM consists of assuming a vibrating source and evaluating its effect at the center of each array element. The computed fields are then used to establish the required phase and amplitude of the driving signals. The driving signal determination procedure deals with the array elements as if they were point sources placed at the center of each array element which is a fair assumption for very small transducers ($< \lambda$). However, this assumption might need to be reconsidered for relatively large size elements ($> \lambda$). The directivity of the array elements might be improved by computing the field, produced by a fictitious source, at several locations over the element surface and using some weighted average of these computed field values to determine the phase and amplitude of the signal necessary to drive each array element. This modified procedure might prove useful when larger elements are considered to minimize the total number of array elements and associated driving electronics.

The use of the field conjugation method in conjunction with the bioheat transfer equation might also be possible. More precisely, the inverse problem of going from a desired steady-state temperature distribution to determining the necessary power deposition pattern should be investigated [47]. This power deposition pattern can then be used to decide the shape, number, spacing, and phasing of the fictitious sources required for the application of the RFCM. These specifications can then be used to establish the optimum phase and amplitude distributions necessary to drive the array elements. Ultimately, the shape, number, and distribution of fictitious sources can be automatically adjusted (updated) using temperature (and eventually blood flow) feedback measurements as a part of an adaptive control algorithm for a phased array hyperthermia system.

An 8x8 square-element phased array prototype was manufactured and some initial experimental data were reported. The experimental data included frequency characteristics of the array elements, the electromechanical conversion coefficient, the mechanical quality factor, and some simple field measurements (no phasing). Although all transducers were cut to the same size and were similarly handled through the first phase of fabrication (cleaned, bonded, etc.), a substantial variation in frequency characteristics (i.e., impedance magnitude at resonance, resonance frequency, etc.) among elements was observed. These variations might be due to the nonuniformity of the conducting epoxy layer and/or to variations in the thickness of the matching layer. Additional research is still needed to determine the reason for the variations and to decide if modifications to the fabrication procedure are needed before attempting to fabricate an array with a larger number of elements.

The synthesis of diffuse heating patterns results, in some cases, in a large half power length which might be undesirable for some hyperthermia applications (i.e., heating with bones distal to the tumor). This problem might be solved by using an array with a larger effective surface. However, the size of a hyperthermia applicator is usually limited by practical considerations such as the available body portal (acoustic window). Another alternative could be the use of nonplanar phased arrays [16]. In particular, heating patterns produced by nonplanar phased arrays should be simulated and compared with those produced by planar applicators. The comparison would be valuable for the implementation of a clinical hyperthermia system.

APPENDIX A

NxN SQUARE-ELEMENT ARRAY FIELD PROGRAM

```
      PROGRAM NBYN(NCARMC,INPUT=TTY,OUTPUT=TTY,RESA,
     * TAPE7=RESA,DADA,TAPE17=DADA,TAPE10=NCARMC)
C
C     PROGRAM TO CALCULATE THE FIELD PRODUCED BY AN NxN
C     SQUARE-ELEMENT ARRAY.
C
      PARAMETER (NXX=61,NYY=61,NZ=90)
      DIMENSION FMAG(NXX,NYY,NZ),WORK(15000),FFMAG(NXX,NYY)
      COMPLEX XINTEN(40,40)
      COMPLEX PARTIAL,JI,CMPCON,CMP
      REAL LAMDA,K
      COMMON JI,CMPCON,LAMDA,FREQ,IND
      DATA PI,S/3.1415926536,1500./
      PRINT*,'NUMBER OF ELEMENTS'
      READ (17,*)NE
      PRINT*,'SPACING BETWEEN ELEMENTS IN MM'
      READ (17,*)SPACE
      PRINT*,'WIDTH OF ELEMENT IN MM'
      READ (17,*)WIDTH
      PRINT*,'OPERATING FREQUENCY IN KHZ'
      READ (17,*)FREQ
      PRINT*,'ATTENUATION CONSTANT IN NP/MHZ/MM'
      READ (17,*)ALPHA
      PRINT *,'A-RADIUS OF THE TUMOR'
      READ (17,*)A
      PRINT*,'ENTER B-RADIUS OF THE TUMOR'
      READ (17,*)B
      PRINT *,A
      CONF=2*PI*A
      LAMDA=S/FREQ
      NS=INT(CONF/(2.*LAMDA))
      PRINT *,'SUGGESTED NUMBER OF SOURCES',NS
      PRINT *,'ENTER THE NUMBER OF SOURCES'
```

```
      READ (17,*)NS
      PRINT *,NS
      PRINT *,'X-COORDINATE OF THE TUMOR'
      READ (17,*)XT
      PRINT *,'YCOORDINATE OF THE TUMOR'
      READ (17,*)YT
      PRINT *,'Z-COORDINATE OF THE TUMOR'
      READ (17,*)ZT
       PRINT *,'XT=',XT,'YT=',YT,',ZT=',ZT
      PRINT *,'NUMBER OF ROTATIONS'
      READ (17,*)MOD
      PRINT *,MOD
      PRINT *,'NUMBER OF FRAMES IN THE Z-DIRCTION'
      READ (17,*)NFRAM
      PRINT *,NFRAM
      PRINT *,'ENTER ZERO FOR POINT SOURCE OR ENTER SOURCE RADIUS'
      READ (17,*)SD
C
C       RECTANGULAR RADIATOR PARAMETERS
C
      PRINT*,'ENTER STEP AS FRACTION OF WAVELENGTH'
      READ (17,*)STEP
      PRINT*,'RECTANGLE AREA CONSTANT'
      READ (17,*)FAR
      WIDTH2=WIDTH/2.
       HGT2=HGT/2.
      LAMDA=S/FREQ
      K=2*PI/LAMDA
      JI=(0.,1.)
      IND=24
      ALPHA=ALPHA*(FREQ/1000.)**1.1
      CMPCON=CMPLX(-K,ALPHA)
      XMIN=1000.
      XMAX=0.0
      THETA=2.*PI/FLOAT(NS)
```

```
C
C     SET ROTATION
C
      DO 33 L=1,NS
        THETA1=(L-1)*THETA
      TH=2.*THETA1
      OMEGA= MOD*((A*A-B*B)*.25*K*COS(TH)+THETA1)
        XF=XT+A*COS(THETA1)
        YF=YT+B*SIN(THETA1)
        VERT=ZT*ZT
        XCNTR=-(NE+1)*SPACE/2.

C
C     EXCITATION CALCULATION
C
       DO 122 I=1,NE
       XCNTR=XCNTR+SPACE
       XX=XF-XCNTR
       YCNTR=-(NE+1)*SPACE/2.
       DO 122 II=1,NE
       YCNTR=YCNTR+SPACE
         YY=YF-YCNTR
       XLENG=SQRT(XX*XX+YY*YY)
       XXLENG=SQRT(XLENG*XLENG+VERT)
      IF(SD.EQ.0.0)THEN
       PARTIAL=CEXP(JI*K*XXLENG)/XXLENG
      ELSE
       CALL SYNTH(0,SD,VERT,XLENG,PARTIAL)
      ENDIF
      XINTEN(I,II)=XINTEN(I,II)+CONJG(PARTIAL)*CEXP(-JI*OMEGA)
      IF(XMIN.GT.CABS(XINTEN(I,II)))XMIN=CABS(XINTEN(I,II))
      IF(XMAX.LT.CABS(XINTEN(I,II)))XMAX=CABS(XINTEN(I,II))
122   CONTINUE
33    CONTINUE
C
C     SET LOGARITHMIC SCALE
```

```
C
      DO 277 I=1,NE
      DO 277 II=1,NE
        AMP=CABS(XINTEN(I,II))
        XINTEN(I,II)=ALOG10(AMP/XMIN)*XINTEN(I,II)/AMP
277   CONTINUE
      PRINT *,'XMIN=',XMIN,'XMAX=',XMAX
      XCAC=ALOG10(XMAX/XMIN)
      PRINT *,'STARTING Z'
      READ (17,*)Z
      ZSTART=Z
      PRINT *,Z
C
C     SET INCREMENTS
C
      PRINT *,'STEP IN Z-DIRECTION'
      READ (17,*)STEPZ
      PRINT *,'STEP IN Y AND X DIRECTION'
      READ (17,*)STEPY
      PRINT *,'STEP IN Z DIR=',STEPZ,'INCREM IN Y AND X=',STEPY
      STEPX=STEPY
C
C     FIELD CALCULATIONS
C
      XMAX=0.0
      XSTART=(NXX-1)*STEPX/2.
      XSTART=YSTART
      DO 1006 IZ=1,NFRAM
        Y=-(NYY-1)*STEPY/2.
      NX=1+INT(WIDTH/SQRT(LAMDA*Z/FAR))
      NY=1+INT(WIDTH/SQRT(LAMDA*Z/FAR))
      DELX=WIDTH/NX
      DELY=WIDTH/NY
      PRINT*,NX,DELX,NY,DELY
      DF=(DELX/2.)**2/LAMDA
      PRINT*,Z,DF
```

```
22     CONTINUE
       DO 1005 IY=1,NYY
       X=-(NXX-1)*STEPX/2.
       DO 1004 IX=1,NXX
10     CONTINUE
        PARTIAL=(0.,0.)
       XSTRT=-(NE+1)*SPACE/2.-WIDTH2
        DO 11 II=1,NE
        XSTRT=XSTRT+SPACE
        YSTRT=-(NE+1)*SPACE/2.-WIDTH2
        DO 11 JJ=1,NE
        YSTRT=YSTRT+SPACE
        CMP=CMPLX(DELX*DELY,0.)*XINTEN(II,JJ)/XCAC
        XN=XSTRT+DELX/2.
        DO 100 I=1,NX
        XD=X-XN
        YN=YSTRT+DELY/2.
        DO 200 J=1,NY
        YD=Y-YN
        R=SQRT(XD*XD+YD*YD+Z*Z)
        VAR=0.5*K/R
        XAR=VAR*XD*DELX
       YAR=VAR*YD*DELY
        SINX=1.
        SINY=1.
        IF(ABS(XD).GT. .00001) SINX=SIN(XAR)/XAR
        IF(ABS(YAR).GT. .00001) SINY=SIN(YAR)/YAR
        PARTIAL=PARTIAL+CMP*CEXP(JI*CMPCON*R)*SINX*SINY/R
200     YN=YN+DELY
100     XN=XN+DELX
11     CONTINUE
        FMAG(IX,IY,IZ)=PARTIAL*CONJG(PARTIAL)
        IF(XMAX.LT.FMAG(IX,IY,IZ))XMAX=FMAG(IX,IY,IZ)
1004    X=X+STEPX
1005       Y=Y+STEPY
1006      Z=Z+STEPZ
```

```
      WRITE(7,*)(((FMAG(I,J,L),I=1,NXX),J=1,NYY),L=1,NFRAM)
       L=INT(ZT/STEPZ+1)
       XMAX=0.0
       DO 499 I=1,NXX
       DO 499 J=1,NYY
         IF (XMAX.LT.FMAG(I,J,L))XMAX=FMAG(I,J,L)
499    CONTINUE
       DO 500 I=1,NXX
       DO 500 J=1,NYY
         FMAG(I,J,L)=FMAG(I,J,L)/XMAX
         IF (FMAG(I,J,L).LT..01)FMAG(I,J,L)=0.01
         FMAG(I,J,L)=10*ALOG10(FMAG(I,J,L))
       FFMAG(I,J)=FMAG(I,J,L)
500    CONTINUE
       PRINT *,'X AND Y STARTED AT',-XSTART,'TO',XTART
       PRINT *,'Z STARTED AT',ZSTART,'TO',Z,'WITH INCREMENT OF',STEPZ
        CALL CONREC(FFMAG,NXX,NXX,NYY,-21.,0.,-3.,0,0,0)
        CALL FLUSHA
        STOP
        END
       SUBROUTINE SYNTH(R1,R2,VERT,SIG,PARTIAL)
        COMPLEX J,K,PARTIAL
       REAL LAMDA
        COMMON J,K,LAMDA,FREQ,IND
        PARTIAL=(0.0,0.0)
        IF(SIG.GT.R2) Z=SIG-R2
             IF(SIG.LT.R1) Z=R1-SIG
             IF(SIG.GE.R1 .AND. SIG.LE.R2) Z=0.0
112     RI=SQRT(VERT+Z*Z)
        CALL STRIP(R1,R2,SIG,Z,LAMDA,IND,AREA)
        PARTIAL=PARTIAL+ CEXP(J*K*RI)*AREA/RI
        IF(Z.LT.R2+SIG) GOTO 112
        RETURN
        END
        SUBROUTINE STRIP(R1,R2,S,Z,XL,M,AREA)
C      SUBROUTINE TO CALCULATE THE AREA OF A CIRCULAR STRIP
```

```
C... CUTTING A RING
C
C    VARIABLES
C
C...  R1      INNER RADIUS OF THE RING
C...  R2      OUTER RADIUS OF THE RING
C...  S      ECCENTRICITY FROM AXIS
C...   Z      RADIUS OF THE STRIP
C...   XL     WAVELENGTH OF THE EXITATION SIGNAL
C...   M      INTEGER THAT DETERMINES THE WIDTH OF THE STRIP
C
C    INITIALIZE
C...   DETERMINE STRIP WIDTH
C
      F(R,VAR)=ACOS((VAR*VAR+S*S-R*R)/(2.*S*VAR))
      D=XL/M
      X=Z+D
      IF(S.EQ.0.0) THEN ! AXIAL POINT
            IF(X.GT.R2 .AND. Z.LT.R2) X=R2
                THETA1=0.0
      THETA2=ACOS(-1.)
      GOTO 1000
      ENDIF
      IF(S.LT.R2) GOTO 100
C   POINTS OUTSIDE OUTER RADIUS OF THE RING
       IF(X.GT.S-R1 .AND. Z.LT.S+R1) THEN! STRIP CUTS BOTH
           THETA2=F(R2,X)
       IF(Z.LT.S-R1) THEN
       X=S-R1
      THETA1=0.
      GOTO 1000
      ENDIF
            IF(X.GE.S+R1) THEN
           X=S+R1
           THETA1=F(R1,Z)
           GOTO 1000
```

```
          ENDIF
      THETA1=F(R1,X)
      GOTO 1000
      ELSE ! STRIP CUTS OUTER CIRCLE ONLY
          THETA1=0.0
       IF(X.GE.S+R2 .AND. Z.LT.S+R2) THEN
          THETA2=F(R2,Z)
          X=S+R2
      GOTO 1000
      ENDIF
      THETA2=F(R2,X)
      GOTO 1000
      ENDIF
100   CONTINUE
      IF(S.GT.R1) GOTO 200 ! POINTS BETWEEN R1 AND R2
C... POINTS BETWEEN 0.0 AND R1
      IF(S+R1 .LT. R2-S) GOTO 300
       IF(X.GT.R1-S .AND. Z.LT.R2-S) THEN
       IF(X.GT.R2-S) X=R2-S
      THETA2=ACOS(-1.)
      THETA1=F(R1,X)
      GOTO 1000
      ENDIF
       IF(X.GT.R1+S .AND. Z.LT.R2+S) THEN
      THETA1=0.0
       IF(X.GE.R2+S) THEN
      X=R2+S
      THETA2=F(R2,Z)
      GOTO 1000
      ENDIF
      THETA2=F(R2,X)
      GOTO 1000
      ELSE ! STRIP CUTS BOTH CIRCLES
      THETA2=F(R2,X)
       IF(X.GT.R1+S) THEN
      X=R1+S
```

```
      THETA1=F(R1,Z)
      GOTO 1000
      ENDIF
      THETA1=F(R1,X)
      GOTO 1000
      ENDIF
300   CONTINUE
       IF(X.GT.R1-S .AND. Z.LT.S+R1) THEN !STRIP CUTS INNER
      THETA2=ACOS(-1.)
       IF(X.GE.S+R1) THEN
       X=S+R1
      THETA1=F(R1,Z)
      GOTO 1000
      ENDIF
      THETA1=F(R1,X)
      GOTO 1000
      ENDIF
       IF(X.GT.S+R1 .AND. Z.LT.R2-S) THEN !NO CUTS
       IF(X.GT.R2-S) X=R2-S
      THETA2=ACOS(-1.)
      THETA1=0.0
      GOTO 1000
      ENDIF
C...      STRIP CUTS OUTER CIRCLE ONLY
      THETA1=0.0
       IF(X.GE.S+R2 .AND. Z.LT.S+R2) THEN
       X=S+R2
      THETA2=F(R2,Z)
      GOTO 1000
      ENDIF
      THETA2=F(R2,X)
      GOTO 1000
200   CONTINUE
       IF(R1.NE.0.0) GOTO 12
       IF(Z.LT.R2-S)  THEN
       IF(X.GT.R2-S) X=R2-S
```

```
      THETA1=0.
      THETA2=ACOS(-1.)
      GOTO 1000
      ELSE
      THETA1=0.
       IF(X.GT.R2+S) THEN
       X=R2+S
      THETA2=F(R2,Z)
      GOTO 1000
      ENDIF
      THETA2=F(R2,X)
      GOTO 1000
      ENDIF
12     CONTINUE
       IF(X.GT.S+R1 .AND. Z.LT.S+R2) THEN
      THETA1=0.
       IF(X.GE.S+R2) THEN
       X=S+R2
      THETA2=F(R2,Z)
      GOTO 1000
      ENDIF
       IF(X.LT.R2-S) THEN
      THETA2=ACOS(-1.)
      GOTO 1000
      ENDIF
      THETA2=F(R2,X)
      GOTO 1000
      ENDIF
       IF(S-R1.GT.R2-S) THEN
       IF(Z.LT.R2-S) THEN
      THETA1=0.0
      THETA2=ACOS(-1.)
      GOTO 1000
      ENDIF
       IF(X.GT.R2-S .AND. Z.LT.S-R1) THEN
       IF(X.GT.S-R1) X=S-R1
```

```
THETA1=0.0

 THETA2=F(R2,X)
GOTO 1000
ENDIF
 THETA2=F(R2,X)
  IF(X.GE.S+R1) THEN
 X=S+R1
 THETA1=F(R1,Z)
GOTO 1000
ENDIF
 THETA1=F(R1,X)
GOTO 1000
ENDIF
 IF(Z.LT.S-R1) THEN
  IF(X.GT.S-R1) X=S-R1
 THETA1=0.0
THETA2=ACOS(-1.)
GOTO 1000
ENDIF
  IF(X.GT.S-R1 .AND.Z.LT.R2-S) THEN
THETA2=ACOS(-1.)
 IF(Z.GE.R1+S) THEN
THETA1=0.0
GOTO 1000
ENDIF
  IF(X.GT.R2-S) X=R2-S
 THETA1=F(R1,X)
GOTO 1000
ENDIF
 THETA2=F(R2,X)
  IF(X.GT.S+R1) THEN
 X=S+R1
 THETA1=F(R1,Z)
GOTO 1000
ENDIF
```

```
      THETA1=F(R1,X)
1000  AREA=ABS(THETA2-THETA1)*(2.*Z*(X-Z)+(X-Z)*(X-Z))
      Z=X
      RETURN
      END
```

APPENDIX B
CYLINDRICAL BIOHEAT EQUATION PROGRAM

```
 PROGRAM BIOHEAT (INPUT=TTY,OUTPUT=TTY,DATA,TAPE6=DATA,RESULT,
   * TAPE15=RESULT,TEMP,TAPE9=TEMP,TEMPF,TAPE17=TEMPF,
   *NCARMC,TAPE10=NCARMC)
C
C     THIS PROGRAM CALCULATES THE TEMPERATURE DISTRIBUTION
C     ASSOCIATED WITH POWER DEPOSITION PATTERNS PRODUCED
C    BY A CRA. SPECIFICATIONS ARE READ FROM THE FILE DATA AND
C     INPUT IS READ FROM RESULT.
C
   DIMENSION T(100,100),X(100,100),WQ(100,100),TF(100,100)
   DIMENSION XK(100),W(100),CONS(100),CONS0(100)
   DATA XKS,XKF,XKM,XKV/.21,.16,.42,.55/
   DATA TS,TBS,CB,WN,EPS/25.,37.,4000.,8.3,.001/
   DATA ZS,ZF,ZM,ZV,HW1,HW2,HW3,TW1,TW2,TW3/
    * .004,.02,.03,.186,.02,.015,.01,
   * 0.02,0.015,.01/
C
   PRINT *,'ENTER THE RADIAL AND AXIAL EXTENT OF THE MODEL'
   PRINT *,'REMEMBER THAT EVERY ENTRY IS FOLLOWED BY A RETURN'
   READ(6,*)RMAX
   READ(6,*)ZMAX
   PRINT *,'ENTER 0 FOR OUTPUT IN TERM OF(T-TBS) OR 1 FOR T'
   READ (6,*)U
    PRINT *,'ENTER THE RELAXATION FACTOR'
    READ(6,*)RELAX
   PRINT *,'ENTER 1 FOR CHANGE IN LAYERD MODEL'
   READ (6,*)NC
   IF(NC.EQ.1)THEN
     PRINT *,'ENTER SKIN,FAT,AND MUSCLE THIKNESS IN M'
     READ(6,*)ZS
     READ(6,*)ZF
     READ(6,*)ZM
     ZV=ZMAX-(ZS+ZF+ZM)
```

```
       PRINT *,'ENTER TUMOR RADIAL EXTENT,HIGH,CORE WIDTH ,HIGH'
       READ (6,*)TW3
       READ (6,*)HW3
       READ (6,*)TW1
       READ (6,*)HW1
      ELSE
      ENDIF
      PRINT *,' ENTER THE DEPTH OF THE TUMOR'
      READ (6,*)DC
      PRINT *, ' ENTER STEP SIZE IN M'
      READ (6,*)DELTA
      DEL =DELTA*DELTA
      PRINT *,'ENTER THE CONVERGENCE CRITERIA'
      READ (6,*)EPS
      PRINT *,'ENTER CORE AND INTERMEDIATE BLOOD
     * PERFUSION AS A FRACTION OF WN'
      READ (6,*)FR3
      READ (6,*)FR2
       W1=WN
      W3 = FR3*WN
      W2 = FR2*WN
C
C      DIFFERENT LAYERS INDICES
C
C     CALCULATE THE DIFFERENT INDICES
      IMAX=ZMAX/DELTA+.5
      JMAX=RMAX/DELTA+.5
      IS=ZS/DELTA+.5
      IF=IS+ZF/DELTA+1
      IM=IF+ZM/DELTA+1
      I1=(DC-HW1)/DELTA+1.5
      I11=(DC+HW1)/DELTA+1.5
      I2=(DC-HW2)/DELTA+1.5
      I22=(DC+HW2)/DELTA+1.5
      I3=(DC-HW3)/DELTA+3.5
      I33=(DC+HW3)/DELTA+3.5
```

```
J3=TW3/DELTA+1.5
J1=TW1/DELTA+1.5
J2=TW2/DELTA+1.5
 PRINT *,'IMAX,JMAX,IS,IF,IM,I1,I11,I2,I22,I3,I33'
 PRINT *,IMAX,JMAX,IS,IF,IM,I1,I11,I2,I22,I3,I33
DO 22 I=1,IMAX
DO 22 J=1,JMAX
IF(I.LE.IS)THEN
  XK(I)=XKS
  W(I)=WN
  QUAN=WN*CB*DEL/XKS
  CONS(I)=1/(4.+QUAN)
  CONS0(I)=1/(6.+QUAN)
ENDIF
IF(I.GT.IS.AND.I.LE.IF)THEN
 XK(I)=XKF
  W(I)=WN
 QUAN=WN*CB*DEL/XKF
 CONS(I)=1/(4.+QUAN)
 CONS0(I)=1/(6.+QUAN)
ENDIF
 IF(I.GT.IF.AND.I.LE.IM)THEN
  XK(I)=XKM
  W(I)=WN
  QUAN=WN*CB*DEL/XKM
  CONS(I)=1/(4.+QUAN)
  CONS0(I)=1/(6.+QUAN)
 ENDIF
IF(I.GT.IM)THEN
 XK(I)=XKV
 W(I)=WN
 QUAN=WN*CB*DEL/XKV
 CONS(I)=1/(4.+QUAN)
 CONS0(I)=1/(6.+QUAN)
ENDIF
IF(I.GE.I1.AND.I.LE.I11)THEN
```

```
      IF(J.LE.J1)W(I)=W1
      IF(I.GT.I2.AND.J.LT.J2)W(I)=W2
      IF(I.LT.I22.AND.J.LT.J2)W(I)=W2
      IF(I.GE.I3.AND.J.LE.J3)W(I)=W3
      IF(I.LE.I33.AND.J.LE.J3)W(I)=W3
      ENDIF
22     CONTINUE
        PRINT *,'FINISHED LOOP 22'
C
C     READING THE DATA FROM FILE RESULT
      READ (15,*)((WQ(I,J),I=1,IMAX),J=1,JMAX)
      DO 24 I=1,IMAX
      DO 24 J=1,JMAX
       IF(WQ(I,J).LT.0.0)WQ(I,J)=0.0
        IF(XMAX.LE.WQ(I,J))XMAX=WQ(I,J)
24     CONTINUE
      DO 25 I=1,IMAX
      DO 25 J=1,JMAX
25     WQ(I,J)=WQ(I,J)/XMAX
C
C     INITIALIZING THE ARRAY
       DO 23 I=1,IMAX
       DO 23 J=1,JMAX
         T(I,J)=U*TBS
23      X(I,J)=U*TBS
      PRINT *,'ENTER ABSORPTION IN NP/M'
      READ (6,*)ALPHA
      PRINT *,'ENTER MAX. INTENSITY ALLOWABLE BY CERAMICS'
      READ(6,*)XI0
      PRINT *,'ENTER WAVELENGTH IN MM'
      READ(6,*)LAMDA
      GAIN=XMAX/(LAMDA*LAMDA)
      PRINT *,'INTENSITY GAIN OF THE PATTERN=',GAIN
      PEAK=2.*ALPHA*XI0*GAIN*1E06
      DO 26 I=1,IMAX
      DO 26 J=1,JMAX
```

```
26   WQ(I,J)=PEAK*WQ(I,J)
C
C    BOUNDARY CONDITIONS
    DO 27 J=1,JMAX
     T(1,J)=TS-(1-U)*TBS
27   T(IMAX,J)=TBS-(1-U)*TBS
    DO 28 I=2,IMAX
      T(I,JMAX)=TBS-(1-U)*TBS
28   CONTINUE
    INDEX=0
C
C    ITTERATION ON THE AXIS OF SYMMETRY
    ITT=0
1    ITT=ITT+1
     EPSKI=0.0
    DO 29 I=2,IMAX-1
      X(I,1)=T(I,1)
      TEM=CONS0(I)*(4*T(I,2)+T(I+1,1)+T(I-1,1)
   * +DEL*WQ(I,1)/XK(I)+U*W(I)*CB*TBS*DEL/XK(I))
    T(I,1)=(1-RELAX)*T(I,1)+RELAX*TEM
     EPSK=ABS(T(I,1)-X(I,1))
     EPSKI=EPSKI+EPSK
29   IF(EPSKI.GT.EPS)INDEX=INDEX+1
C
C    ITTERATIONS
    DO 30 I=2,IMAX-1
    DO 30 J=2,JMAX-1
      X(I,J)=T(I,J)
      R=(J-1)*DELTA
      RH01=1+DELTA/R/2.
      RH02=1-DELTA/R/2.
      TEM=CONS(I)*(RH01*T(I,J+1)+RH02*T(I,J-1)+T(I+1,J)
   *  +T(I-1,J)+(DEL/XK(I))*(WQ(I,J)+U*CB*W(I)*TBS))
     T(I,J)=(1-RELAX)*T(I,J)+RELAX*TEM
     EPSK=ABS(T(I,J)-X(I,J))
     EPSKI=EPSKI+EPSK
```

```
30     IF(EPSKI.GT.EPS)INDEX=INDEX+1
      PRINT *,'NUMBER OF ITTERATION=',ITT
       IF(EPSKI.GT.EPS)GO TO 1
       TMIN=100.
       TMAX=0.0
      DO 31 I=1,IMAX
      DO 31 J=1,JMAX
        IF(T(I,J).GT.TMAX)THEN
        TMAX=T(I,J)
          M=I
          L=J
        ENDIF
        IF(TMIN.GT.T(I,J))THEN
          TMIN=T(I,J)
            K=I
            P=J
         ENDIF
31         CONTINUE
        PRINT *,'OUT OF 31'
      WRITE(9,*)((T(I,J),I=1,IMAX),J=1,JMAX)
        DO 50 I=1,IMAX
        DO 50 J=2,JMAX
         TF(I,JMAX)=T(I,1)
          TF(I,JMAX-1+J)=T(I,J)
          TF(I,JMAX-J+1)=T(I,J)
50       CONTINUE
        PRINT *,'OUT OF 50'
         PP=2*JMAX-1
        WRITE(17,*)((TF(IX,JX),IX=1,IMAX),JX=1,PP)
        PRINT *,'TMIN=',TMIN,'FOR IAND J=',K,',',P
        PRINT *,'TMAX=',TMAX,'FOR I AND J=',M,',',L
      CALL CONREC(TF,PP,PP,IMAX,TBS,TMAX,-10.,0,0,0)
      STOP
      END
```

APPENDIX C
THREE-DIMENSIONAL BIOHEAT EQUATION PROGRAM

```
PROGRAM TWDIM(RESULT,TEMP,INPUT=TTY,OUTPUT=TTY,TAPE20=RESULT,
   * TAPE21=TEMP)
C
C     THREE DIMENSIONAL BIOHEAT EQUATION
C     WRITTEN 1/16/1987 BY E. EBBINI
C
      PARAMETER (NX=61,NY=91,NZ=61)
      IMPLICIT REAL (K,M)
      DIMENSION T(NX,NY,NZ),TO(NX,NY,NZ),KON(NX,NY,NZ),WB(NX,NY,NZ),
   * Q(NX,NY,NZ)
      DATA CB,TB,TSK,TVS,W,H/4000.,37.,25.,37.,1.6,2.E-3/
      DATA STH,FTH,MTH,VTH/.004,.02,.03,.126/
      DATA KS,KF,KM,KV/.21,.16,.42,.55/
      DATA WNORM,EPS/8.3,1.E-6/
 111  PRINT*,'CURRENT VALUE OF BLOOD FLOW IS',WNORM
      PRINT*,'ENTER 0 TO END OR ENTER NEW VALUE'
      READ*,WNORM
       IF(WNORM.EQ.0) STOP
     PRINT*,'SCALING FACTOR AS FRACTION'
     READ*,SFAC
C
C     SET LAYERS PARAMETERS
C
      DO 10 J=2,NY-1
      X=H*FLOAT(J)
      IF(X.LE. STH) THEN
      DO 20 I=2,NX-1
      DO 20 L=2,NZ-1
      KON(I,J,L)=KS
 20    WB(I,J,L)=WNORM
      ENDIF
      B2=STH+FTH
      IF(X.GT.STH.AND.X.LE.B2) THEN
      DO 30 I=2,NX-1
```

```
       DO 30 L=2,NZ-1
      KON(I,J,L)=KF
30     WB(I,J,L)=WNORM
      ENDIF
      B3=B2+MTH
      IF(X.GT.B2.AND.X.LE.B3) THEN
      DO 40 I=2,NX-1
      DO 40 L=2,NZ-1
      KON(I,J,L)=KM
40     WB(I,J,L)=WNORM
      ENDIF
      IF(X.GT.B3) THEN
      DO 50 I=2,NX-1
      DO 50 L=2,NZ-1
      KON(I,J,L)=KV
50     WB(I,J,L)=WNORM
      ENDIF
10       CONTINUE
C
C     READ POWER DEPOSITION FROM FILE RESULT
C
      READ(20,*)(((Q(I,J,L),I=1,NX),L=1,NZ),J=1,NY)
       FMAX=0.
      DO 52 I=1,NX
       DO 52 L=1,NZ
      DO 52 J=1,NY
      IF(FMAX.LT.Q(I,J,L)) FMAX=Q(I,J,L)
52     CONTINUE
      READ(20,*)XT,YT,RT
        PRINT*,'PEAK POWER DEPOSITION *1.E05 W/M**3'
        READ*,PEAK
      DO 55 I=1,NX
       DO 55 L=1,NZ
      DO 55 J=1,NY
      Q(I,J,L)=PEAK*1.E05*Q(I,J,L)/FMAX
55     CONTINUE
```

```
      YT=YT/1000.
       XT=XT/1000.
       RT=RT/1000.
      ZT=0.
      DO 60 I=2,NX-1
      XP=-H*(NX/2)+H*FLOAT(I)
      DO 60 J=2,NY-1
      YP=0.09-H*NY+H*FLOAT(J)
       DO 60 L=2,NZ-1
       ZP=-.06+H*FLOAT(L)
      RIJ=SQRT((XP-XT)**2+(YP-YT)**2+ZP**2)
      R1=0.8*RT
      R2=.9*RT
      IF(RIJ.LT.R1) WB(I,J,L)=WB(I,J,L)*SFAC
      IF(RIJ.GE.R1.AND. RIJ.LT.R2) WB(I,J,L)=2.*WB(I,J,L)*SFAC
60     CONTINUE
      ITER=0
C
C     START ITERATIONS
C
      DO 70 I=1,NX
      DO 70 L=1,NZ
70     T(I,1,L)=25.
      DO 80 I=1,NX
      DO 80 J=2,NY
      DO 80 L=1,NZ
80     T(I,J,L)=37.
14      ITER=ITER+1
       DO 90 I=2,NX-1
       DO 90 J=2,NY-1
      DO 90,L=2,NZ-1
90      TO(I,J,L)=T(I,J,L)
       DO 100 I=2,NX-1
       DO 100 J=2,NY-1
      DO 100 L=2,NZ-1
      KONS=KON(I,J,L)*W/(6.*KON(I,J,L)+H*H*WB(I,J,L)*CB)
```

```
      RES=H*H*(Q(I,J,L)+WB(I,J,L)*TB*CB)/KON(I,J,L)
      TOT=T(I+1,J,L)+T(I-1,J,L)+T(I,J+1,L)+T(I,J-1,L)+T(I,J,L+1)
      TOT=TOT+T(I,J,L-1)
      T(I,J,L)=KONS*(TOT+RES)+(1-W)*T(I,J,L)
 100  CONTINUE
      DO 110  I=2,NX-1
      DO 110  J=2,NY-1
       DO 110 L=2,NZ-1
      IF(ABS(TO(I,J,L)-T(I,J,L)).GT.EPS) GOTO 14
110    CONTINUE
      PRINT*,'CONVERGENCE ACHIEVED AFTER',ITER,' ITERATIONS'
      WRITE(21,*)(((T(I,J,L),I=1,NX),J=1,NY),L=1,NZ)
      GOTO 111
```

REFERENCES

[1] George M. Hahn,"Hyperthermia for the engineer: a short biological primer,"IEEE Trans.on Biomedical Engineering, Vol. BME-31,No. 1, 1984.

[2] John W. Strohbehn and Evan B. Douple,"Hyperthermia and cancer therapy: a review of biomedical contributions and challenges," IEEE Trans. on Biomedical Engineering, Vol. BME-31, No. 12, 1984.

[3] Leon C. Parks and George V. Smith," Systemic hyperthermia by extracorporeal induction: techniques and results," in Hyperthermia in Cancer Therapy edited by F. C. Storm (Boston: Hall Medical Publisher), pp. 407-446, 1981.

[4] A. Westra and W. C. Dewey," Variation in sensitivity to heat shock during the cell-cycle of Chinese hamster cells in vitro," Int. J. Radiat. Biol., Vol. 19: pp. 467-469, 1971.

[5] W. C. Dewey,W. G. Gerner L. E. Hopwood, S. A. Saporato, and L. E. Gerweck," Cellular responses to combination of hyperthermia and radiation," Radiology, Vol. 123, pp. 463-474, 1977.

[6] W.G. Corrner, E.W. Gerner, E, W, Miller," Human cancer therapy-II. Radiology, No.123, pp. 497-503.

[7] S. E. Field and L. E. Bleehenn ,"Hyperthermia in the treatment of cancer." Cancer Treatment Reviews, Vol. 6, 53-94.

[8] J. M. Larkin," A clinical investigation of total-body hyperthermia as cancer therapy," Cancer Research. Vol. 39, pp. 2252-2254, 1979.

[9] P. P. Lele," Hyperthermia by ultrasound," Proceedings of the International Symposium on Cancer Therapy by Hyperthermia and Radiation, Washington D.C., 1978.

[10] P. P. Lele," Local hyperthermia by ultrasound," in Physical Aspects of Hyperthermia, edited by G. H. Nussbaum (New York: American Association of Physicists in Medicine.publisher), pp. 393-440, 1982.

[11] Robert B. Roemer, W. Swindell, S. Clegg, and R. Kress," Simulation of focused, scanned ultrasonic heating of deep-seated tumors: the effect of blood perfusion,"IEEE Trans. Sonics and Ultrasonics, Vol.Su-31, No.5, pp. 754-768, 1984.

[12] R. J. Dikinson," An ultrasound system for local hyperthermia using scanned focused transducers," IEEE Trans. in Biomedical Engineering, Vol.31, pp. 126-135, 1984.

[13] P. P. Lele and K. J. Parker," Temperature distribution in tissue during local hyperthermia by stationary or steered beams of unfocused or focused ultrasound," Br. J. Cancer, Vol. 45, Suppl. V, 1982.

[14] L. A. Frizzell, P. J. Benkeser, K. B. Ochletree, and C. A. Cain,"Ultrasound phased arrays for hyperthermia,"Proc. 1985 UltrasonicSymposium, 1982.

[15] J. Huu and P. Hartemann," Deep and local heating by an ultrasound phased array applicators for ultrasound hyperthermia," Proc. 1982 Ultrasonic Symposium, pp. 735-738, 1982.

[16] E. Ebbini, S. Umemura, M. Ibbini, and C. Cain," A cylindrical-section ultrasound phased array for hyperthermia cancer therapy," IEEE Trans. Ultrasonics, Ferroelectrics, and Frequency Control, in press.

[17] C. Cain and S. Umemura," Concentric-ring and sector-vortex phased array applicators for ultrasound hyperthermia," IEEE Trans. MTT,Vol. 34, pp. 542-551, 1986.

[18] P. Fessenden, E. R. Lee, T. L. Anderson, J.W. Strohbehn, J. L. Mayer, T. V. Samulski, and J. B. Marmor, " Experience with a multitransducer ultrasound system for localized hyperthermia of deep tissues," IEEE Trans. Biomedical Engineering, Vol. 31, pp.126-135, 1984.

[19] P. P. Lele, " An annular-focus ultrasonic lense for production of uniform hyperthermia in cancer therapy," Letter to the editor, Ultrasound in Medicine and Biology, Vol.7, pp. 191-193, 1982.

[20] Ralph E. Beard, Richard L. Magin, Leon A. Frizzell, and Charles A. Cain," An annular focus ultrasonic lens for local hyperthermia treatment of small tumors," Ultrasound in Medicine and Biology, Vol. 8, No. 2, pp. 177-184, 1983.

[21] K. Hynynen," Design of ultrasonic transducers for local hyperthermia," Ultrasound in Medicine and Biology, Vol. 7, No. 4, pp. 397-402, 1981.

[22] K. B. Ochletree, P. J. Benkeser, L. A. Frizzell, and C. A. Cain," An ultrasonic phased array applicator for hyperthermia," IEEE Trans. on Sonics and Ultrasonics, Vol. Su-31, pp. 526-531, 1984.

[23] S. Child, B. Vives, K. Smachlo, W. Fridd, J. Hare, C. Linke, H. Davis, and E. Cartensen," Ultrasound treatment of tumors-III high intensity, low frequency exposure," Ultrasound in Medicine and Biology, Vol. 8, No. 1, pp. 41-44, 1982.

[24] R. A. Fisher, Optical Phase Conjugation, New York: Academic Press, 1983.

[25] J. Huingard, J. Harriot, and G. Rivet," Phase conjugation and spatial frequency dependence of wavefront reflectivity," Opt. Lett., Vol. 5, p. 102,1980.

[26] H. Ling and S. Lee," Focusing of electromagnetic wave through dielectric interphace," J. Opt. Soc. Am., Vol. 1, No. 9, 1985.

[27] R. C. Hansen," Focal region characteristcs of focused array antenna," IEEE Trans. Antenna Propagat. , Vol. Ap-33, No. 12, 1985.

[28] J. Loane, H. Ling, B. F. Wang, and S. W. Lee," Experimental investigation of a retro-focusing microwave hyperthermia applicator," IEEE Trans. on Microwave Theory and Technique, Vol. MTT-34, No. 5, 1986.

[29] Mohammed S. Ibbini and Charles A. Cain," A field conjugation method for direct synthesis of hyperthermia phased array heating patterns'" IEEE Trans. Ultrasonics, Ferroelectrics, and Frequency Control, in press.

[30] M. Ibbini, E. Ebbini, S. Umemura, and C. Cain," A new phasing technique based on the field conjugation method as an alternative to scanning," Proc. 1987 Ultrasonics Symposium, 1987.

[31] R. L. Pritchard'" Optimum directivity pattern for linear point arrays," J. Acoust. Am., Vol. 25, pp. 879-884, 1953.

[32] N. Davids, E. Thurston, and R. E. Menser," The design of optimum directivity acoustic array," J. Acoust. Soc. Am., Vol. 24, pp. 50-57, 1952.

[33 Lawrence Kensler, Austin Frey, Alan Coppens, James Sanders, Fundamentals of Acoustics, Wily Publisher, 1982.

[34] Kullervo Hynynen, " The effect of nonlinear prpagation and tissue interface on the temperature distribution during scanned , focused ultrasound hyperthermia," Proc. 1986 ultrasonics Symposium, 1986.

[35] Gerard E. Sleefe and Padmakar P. Lele," The limitation of ultrasonic phased arrays for the induction of local hyperthermia'" Proc. 1985 Ultrasonics Symposium, 1985.

[36] P. P. Lele ," Physical aspects and clinical study with ultrasound hyperthermia," in Hyperthermia Cancer therapy, edited by F. C. Storm (Boston: Hall Medical Publisher), pp. 333-367, 1983.

[37] P. J. Benkeser," Unfocused multielement and tapered phased array ultrasound transducers for hyperthermia treatment," Ph.D thesis, Univ. of Illinois, 1985.

[38] W. Swindell, R. Roemer, and S. Clegg," Temperature distribution caused by dynamic scanning of focused ultrasound transducers," Proc. 1982 Ultrasonic Symposium, pp. 750-753, 1982.

[39] Joe Zemanek," Beam behavior within the nearfield of a vibrating piston," J. Acoust. Soc. Am.,Vol. 49, No. 1, pp. 181-191, 1971.

[40] M. E. Lyons and K. J. Parker," Attenuation and absorption in soft tissue II-experimental results," Submitted to IEEE Trans. Ultrasonics, Ferroelectrics, and Frequency Control.

[41] K. B. Ochletree," Theoretical analysis of ultrasonic linear phased arrays for hyperthermia," M. S. thesis, Dep. Elec. Eng., Univ. of Illinois, 1984.

[42] George H. Harrison and Elisabeth K. Kubeczek," Single transducer electrode design for beam shaping in biomedical ultrasound," IEEE Trans. on Ultrasonics, Ferroelectrics, and Frequency Control, Vol. UFFC-33, No. 3, 1986.

[44] K. J. Parker," Ultrasonic attenuation and absorption in liver tissue," Ultrasound in Medicine and Biology, Vol. 9, No. 4, pp. 363-369, 1983.

[45] T. J. Cavicchi and W. D. O'Brien," Heat generated by ultrasound in an absorbing medium," J. Acoust. Soc. Am.,76: 124, 1984.

[46] T. F. Heuter and R. H. Bolt, Sonics, New York: Wiley, pp. 86-163, 1966.

[47] K. B. Ocheltree and L. A. Frizzell,"Determination of power deposition patterns for localized hyperthermia: a steady state analysis," International Journal of Hyperthermia, Vol. 3, pp. 269-279, 1987.

VITA

Mohammed Salameh Ibbini was born on March 15, 1954 in Ajloun, Jordan. He graduated from Irbid High School, Irbid, Jordan, in 1972.

In 1972, Mohammed attended the University of Grenoble, France, where he studied the french language. He began undergraduate studies at the ENSEEC, France, in 1973. After graduating from the ENSEEC in 1978 with a Dilplome in Electrical Engineering, Mr. Ibbini returned to Jordan where he worked as a power distribution engineer at the National Company of Electricity, Amman, Jordan.

Mr. Ibbini attended the University of Colorado at Boulder in the Fall, 1979 and graduated with M.S. degree in electrical engineering in December 1980. He then worked as a project manager at Bibars Industrial Establishment (branch of Calor-France), Amman, Jordan, until 1984. His duties included technical and commercial management and supervision.

In 1984, Mohammed attended the University of Illinois for his Ph.D degree. He worked under Professor Charles Cain as a research assistant in the analysis and design of phased arrays for hyperthermia cancer therapy. His appointments at the University of Illinois included a teaching assistantship in Systems area and a research assistantship in the Bioacoustics Research Laboratory.